Mass-Selected Infrared Multiple-Photon Dissociation as a Structural Probe of Gaseous Ion-Molecule Complexes

by

Richard Alexander Marta

A thesis

presented to the University of Waterloo

in fulfillment of the

thesis requirement for the degree of

Doctor of Philosophy

in

Chemistry

Waterloo, Ontario, Canada, 2009

Author's Declaration

I hereby declare that I am the sole author of this thesis. This is a true copy of the thesis, including any required final revisions, as accepted by my examiners.

I understand that my thesis may be made electronically available to the public.

Abstract

Mass-selected infrared multiple photon spectroscopy (IRMPD), Fourier transform ion cyclotron resonance (FT-ICR) kinetic experiments, RRKM and electronic structure calculations have been performed in order to propose a complex mechanism involving the formation of the proton-bound dimer of water ($H_5O_2^+$) from 1,1,3,3-tetrafluorodimethyl ether. It has been found that the reaction is facilitated by a series of sequential exothermic bimolecular ion-molecule reactions. Evidence for the dominant mechanistic pathway involving the reaction of CF_2H-O=CHF^+, an ion of *m/z* 99, with water is presented. The primary channel occurs *via* nucleophilic attack of water on the ion of *m/z* 99 (CF_2H-O=CHF^+), to lose formyl fluoride and yield protonated difluoromethanol (*m/z* 69). Association of a second water molecule with protonated difluoromethanol generates a reactive intermediate which decomposes *via* a 1,4-elimination to release hydrogen fluoride and yield the proton-bound dimer of water and formyl fluoride (*m/z* 67). The 1,4-elimination of hydrogen fluoride is found to be strongly supported by the results of both RRKM theory and electronic structure calculations. Lastly, the elimination of formyl fluoride occurs by the association of a third water molecule to produce $H_5O_2^+$ (*m/z* 37). The most probable isomeric forms of the ions with *m/z* 99 and 69 were found using IRMPD spectroscopy and electronic structure theory calculations. Thermochemical information for reactant, transition and product species was obtained using MP2/aug-cc-pVQZ//MP2(full)/6-31G(d) level of theory.

Ionic hydrogen bond (IHB) interactions, resulting from the association of ammonia and two of the protonated methylxanthine derivatives, caffeine and theophylline, have been

characterized using mass-selected IRMPD and electronic structure calculations at the MP2/aug-cc-pVTZ//B3LYP/6-311+G(d,p) level of theory. It was found that the formation of a proton-bound dimer (PBD) of caffeine and ammonia was elusive under the experimental conditions. The low binding energy of the caffeine and ammonia PBD is responsible for the perceived difficulty in obtaining an IRMPD spectrum. The IRMPD spectrum of the PBD of theophylline and ammonia was obtained and revealed bidentate IHB formation within the complex, which greatly increased the binding energy relative to the most stable isomer of the PBD of caffeine and ammonia. The IRMPD spectra of the protonated forms of caffeine and theophylline have also obtained. The spectrum of protonated caffeine showed the dominant existence of a single isomer, whereas the spectrum of protonated theophylline showed a mixture of isomers. The mixture of isomers of protonated theophylline resulted as a consequence of proton-transport catalysis (PTC) occurring within the PBD of theophylline and ammonia. All calculated harmonic spectra have been produced at the B3LYP/6-311+G(d,p) level of theory with fundamental frequencies scaled by 0.9679; calculated anharmonic spectra have also been provided at the same level of theory and were found to greatly improve the match with the IRMPD spectra obtained in all cases.

Ionic hydrogen bond (IHB) interactions, resulting from the association of caffeine and theophylline with their protonated counterparts, forming proton-bound homodimers, have been characterized using mass-selected IRMPD and electronic structure calculations at the MP2/6-311+G(2d,2p)//B3LYP/6-311+G(d,p) level of theory. It is found that the IRMPD spectra of the proton-bound homodimers of caffeine and theophylline are complicated

resulting from the existence of several pairs of enantiomers separated by a narrow range of relative Gibbs free energies (298 K) of 15.6 and 18.2 kJ mol^{-1}, respectively. The IRMPD spectrum of the proton-bound homodimer of theophylline is dominated by a unique isomer facilitated by formation of a bidentate IHB. Formation of this interaction lowers the relative Gibbs free energy of the ion to 9.75 kJ mol^{-1} below that of the most favourable pair of enantiomers. The IRMPD spectrum of the PBD of caffeine is complicated by the existence of at least two pairs of enantiomers with the strong likelihood of the spectral contributions of a third pair existing. The most favourable enantiomeric pair involves the formation of a $O-H^{+}\cdots O$ IHB. However, verification of a pair of enantiomeric PBDs containing a $N-H^{+}\cdots O$ IHB is also observed in the IRMPD spectrum of the PBD of caffeine due to the presence of three free carbonyl stretching modes located at 1731, 1751 and 1785 cm^{-1}.

The mass-selected IRMPD spectra of the sodium cation-bound dimers (SCBD) of caffeine and theophylline also have been obtained. Both the mass-selected IRMPD spectra and electronic structure calculations predict the most likely structure of the SCBDs of caffeine and theophylline to form by an efficient $O\cdots Na^{+}\cdots O$ interaction between C=O functional groups possessed by each monomer. The frequencies of the C=O-Na^{+} stretch are found to be nearly identical in the IRMPD spectra for both of the SCBDs of caffeine and theophylline at 1644 and 1646 cm^{-1}, respectively. However, the degenerate free C=O symmetric and asymmetric stretches for the SCBDs of caffeine and theophylline found at 1732 and 1758 cm^{-1}, respectively, demonstrating a red-shift for caffeine possibly linked to a steric interaction absent in theophylline. Free rotation about the $O\cdots Na^{+}\cdots O$ bond is found

to greatly decrease the complexity of the IRMPD spectra of the SCBDs of caffeine and theophylline and demonstrates excellent agreement between the IRMPD and calculated spectra. Electronic structure calculations have been done at the MP2(full)/aug-cc-pCVTZ/6-311+G(2d,2p)//B3LYP/6-311+G(d,p) level of theory using the aug-cc-pCVTZ basis set for Na^+ and all Na^+-interacting heterotatoms, and the 6-311+G(2d,2p) basis set for all non-interacting atoms within the SCBDs, in order to provide accurate electronic energies.

Currently, installation and implementation of a pulsed electrospray high pressure ion source mated to an existing high pressure mass spectrometer (HPMS) is underway. The new ion source will greatly increase the range of possibilities for the study of ion-molecule reactions in the McMahon laboratory. One of the unique features of the new design is the incorporation of a gas-tight electrospray interface, allowing for more possibilities than only the study of cluster-ion equilibria involving hydration ($H_2O_n\cdots S^+$), where S^+ is an ion produced by electrospray. Other small prototypical biological molecules such as amines and thiols can be used without concern for the toxicity of these species. Another unique design feature allows electrosprayed ions to associate with neutral solvent species in an electric field free reaction chamber (RC). This ensures that values of equilibrium constants determined are truly representative of ions in states of thermochemical equilibrium. The existing HPMS in the McMahon laboratory is limited to the study of small volatile organic molecules. The new ion source will permit the exploration of systems involving non-volatile species, doubly charged ions and many biologically relevant molecules such as amino acids, peptides, nucleobases and carbohydrates.

Acknowledgements

I would like to begin by thanking my supervisor, **Terry McMahon**, for his exceptional patience, kindness, generosity and trust! **Terry** is a true role model, who has never been too busy to answer my questions, has never made me feel like what I was talking about was nonsense (even if I was wrong), has always believed in me, is always up for a good conversation about chemistry (or life), and has always made me feel like I have had something to offer. **Terry**, I have learned so much from you and I greatly appreciate it. I would also like to thank **Terry** for giving me the opportunity to attend many excellent conferences and research trips, because I know that this is not something that he has to do, but wants to do for me. Finally, those who know me would know that I am high-strung, and I would like to thank **Terry** for his consistent ability to calm me down when I have been "freaking-out".

Over the past five years I have encountered several important and wonderful people whom must be acknowledged. I would like to begin by thanking **Jon Martens**, who is my best friend and an incredibly talented and creative scientist. I owe **Jon** infinitely for how much I have learned and improved working with him. We have also had amazing adventures that I will cherish. I would like to thank **Sabrina Martens**, who is also my best friend and my "pillar of strength". **Sabrina**, you have always been an excellent listener, always helped me when I was down and you are also amazingly fun! I will finish here by saying that I love both of you guys and that you are, and always will be a part of my family. Thank you for all that you have done for me.

I would like to thank my closest friends from the University of Waterloo, **Rob Nieckarz**, **Julie Goll** and **Mike Makahnouk**.

Rob, all that I can say is that you have always been my voice of wisdom. I arguably have had some of the most exciting and fun times in my life with **Rob,** and he has always been there for me through some very tough times. **Rob** and I had epic discussions about chemistry when we shared an office, and I will always value them. **Rob**, I believe the correct

answer to that one discussion we had is, effusion. I wish **Rob** the greatest success, he is and will always be a true friend and colleague.

Julie, thank you for being a wonderful friend and somebody I would call the "female version" of myself (ESTJ)! We have had some great times together and I greatly appreciate your kindness, excellent listening and caring over all of these years. I really enjoy our squash matches, enjoyed our yoga classes and who can ever forget about dodge ball! Go *Chemikazees*!

Mak, my "brother from another mother". Thank you for always being a person who will drop what they are doing to help me. I greatly appreciate and enjoy our mutual "venting" discussions and our classic video game sessions. I will never forget waking up at 6:00 am to go and "pump iron" with you, it was tiring, however a great experience. Thank you for your loyalty and support over all of these years, you are awesome.

I would like to continue by thanking the amazing group of individuals who make up my **PhD committee**. I have learned an incredible amount from all of you over the years. I have great respect and admiration for all of you as professors and scientists. I would never have made it this far without the knowledge and inspiration that you have given me. All of you are perfect examples of what being professors should be. I am honoured and appreciative that I was lucky enough to be taught by all of you. Finally, many thanks for choosing to be on my committee and reading this thesis.

I would like to thank all of the present and previous McMahon group members who have contributed to my life both professionally and personally, including, **Travis**, **Ronghu**, **Blake**, **Cveta, Matt (Fuzz)**, **Kris (Kelly)**, and **Chad**.

Travis, I will always consider you as a co-supervisor. You have taught me an incredible amount of things. You always took the time to help me and "push" me in the right direction. You are one of the most fun people to attend a conference with (Sumo match). I am eternally grateful.

Ronghu, you are one of the most respectful, considerate and supreme scientists I have ever met. You are the perfect example of hard work and dedication. I deeply enjoyed our

discussions during our marathon of work at CLIO. When I begin as a postdoc, I will try to emulate the strong example that you have set. You are an inspiration and great role model.

To the rest of the previous McMahon group members that I have not included specifically, thank you!

Thank you to Professor **Henryk Wincel** for his extraordinary hospitality and willingness to lend his advice during our (**Jon Martens** and I) visit to his laboratory to learn about his pulsed electrospray high pressure mass spectrometer.

Thank you to all of the staff at the University of Waterloo who have helped me over the years including **Cathy**, **Lisa**, **Janice**, **Bev**, **Jacek**, **Kruno**, **Harmen** and especially **Mike**. The new electrospray ion source could not have existed without **Mike's** talented skill and great ideas. There would have been no way to make it this far without all of you.

Thank you to all of my friends in Kitchener that I "grew up" with, many of whom have probably been wondering where I have been for the last five years!

Finally, I would like to thank my fantastic family for all of their unconditional love and support over all of these years of my life. I am profoundly lucky to have such an incredible family. You are all very important to me and I love you guys.

Dedication

« To My Parents & Grandparents »

Table of Contents

List of Figures

List of Tables

List of Acronyms and Abbreviations

ATD	arrival time distributions
C_1/C_2	skimmer cones
CB	copper block
CC	capillary cover
CCSD(T)	coupled cluster with direct single, double and perturbatively obtained triple excitations
CF	conflat
CGI	curtain gas inlet
CI	chemical ionization
CID	collision induced dissociation
CLIO	Centre Laser Infrarouge d'Orsay
CP	curtain plate
CRM	charge residue model
CW	continuous wave
DNA	deoxyribonucleic acid
DE	deflector electrode
EI	electron ionization
ES	exit slit
ESC	electrospray capillary
ESE	electrospray emitter assembly

FC/FCH	forechamber
FT-ICR	Fourier transform ion cyclotron resonance
FEL	free electron laser
$G_1/G_2/G_3$	grids
GCR	gas confinement region
H_1/H_2	resistive heating power inputs
HF	Hartree Fock
HJ	heating jacket
HPMS	high pressure mass spectrometry
HTC	heated transfer capillary
HVS	high voltage shield
ICR	ion cyclotron resonance
IEM	ion evaporation model
IHB	ionic hydrogen bond
IN/IP	interface plate
IR	infrared
IRMPD	infrared multiple-photon dissociation
IT	ion trap
IVR	intramolecular vibrational redistribution
LCAO	linear combination of atomic orbitals
LINAC	linear accelerator
MAD	mean absolute deviation
MICRA	mobile ion cyclotron resonance for analysis

MIKES	metastable kinetic energy spectrum
MP2	Møller-Plesset second order perturbation
MS	mass spectrometer
Nd:YAG	neodymium-doped yttrium aluminium garnet
OPO	optical parametric oscillator
PBD	proton-bound dimer
PEEK	polyetheretherketone
PL	pumping lead
PRC	pressure reducing capillary
QIT	quadrupole ion trap
RC/RCH	reaction chamber
RF	radio frequency
RGI_1	reactant gas inlet for reaction chamber
RGI_2	reactant gas inlet for capillary chamber
RGO_1	reactant gas outlet for reaction chamber
RGO_2	reactant gas outlet for gas confinement region
RRKM	Rice, Ramsperger, Kassel and Marcus
SB	source body
SCBD	sodium cation-bound dimer
SCF	self consistent field
SP	shielding plate
SS	stainless steel
TC	thermocouple
TFDE	1,1,3,3-tetrafluorodimethyl ether

ΔH_{298}°	change in enthalpy at 298 K
ΔG_{298}°	change in Gibbs free energy at 298 K
$\Delta\Delta G_{298}^{\circ}$	relative change in Gibbs free energy at 298 K
ΔS_{298}°	change in entropy at 298 K

Chapter 1
Introduction

1.1 Ionic-Hydrogen Bond Interactions in the Gas Phase

Knowledge of the intrinsic reactivity of gaseous ionic species is fundamental to the understanding of larger chemical systems. One of the principal intermolecular interactions in chemistry is the hydrogen bond.[1] When a hydrogen bond is formed during an ion-molecule association reaction, it is referred to as an ionic hydrogen bond (IHB) and there have been numerous studies related to IHB formation over the past four decades.[2-8] The typical range of bond energies for IHBs is 20 to 150 kJ mol^{-1},[6] with the high end of this range characterizing the IHB as a strong intermolecular interaction equivalent to some covalent bonds, such as F_2, which has a bond energy of 155 kJ mol^{-1}.[9] There are several examples of chemistry involving IHB formation including acid-base chemistry, electrolytes, ionic cluster formation and solvation, self-assembly in macromolecular chemistry and molecular crystals. The appearance of IHBs in biologically relevant chemical systems is prevalent and can include protein folding, enzyme active sites, membrane formation and proton-transport catalysis.[6] The presence of IHB formation in a plethora of chemical topics warrants a detailed study and understanding of this important intermolecular force.

The energetic and structural consequences associated with IHB formation cannot be intrinsically quantified in the condensed phase due to the complex nature of solvent effects.

However, the study of intermolecular forces in the gas phase is an immediate solution to the solvation problem. A representative system involving IHB formation in the gas phase is

$$M + MH^+ \longrightarrow M \cdots H^+ \cdots M \qquad \textbf{1.1}$$

where M is a neutral monomer species containing one or more Lewis basic heteroatoms. The association product on the right side of **Eq. 1.1** is referred to as a symmetric proton-bound dimer (PBD). The formation of symmetric PBDs involves the partial transfer of a proton from a donor to acceptor heteroatom with the bond strength correlated to the efficiency of the transfer. As the proton is transferred the partial positive charge on the proton increases while the partial negative charges of the donor and acceptor atoms increases. As the symmetric PBD is formed the $M - H^+$ bond length of the proton donor increases and charge is partially transferred to the acceptor atom. The symmetric PBDs share the proton efficiently due to the donor and acceptor molecules having identical proton affinities (PA). The PA is defined as the negative value of the enthalpy change for **Eq. 1.2**,

$$M + H^+ \longrightarrow MH^+ \qquad \textbf{1.2}$$

and therefore a more positive PA implies a more favourable protonation of the monomer M. It has been shown experimentally that in symmetric PBDs the strength of the IHB formed between the dimers is not proportional to the magnitude of the PA values of the monomer units.[4, 6, 10] If the association reaction given by **Eq. 1.1** involves IHB formation between two different heteroatoms (e.g. $N - H^+ \cdots O$) then the IHB bond strength decreases with a greater difference in PA between the donor and acceptor heteroatoms, resulting in the proton being shared disproportionately. For example, if the donor possesses a higher PA than the acceptor

heteroatom, then the proton will tend to favour the donor atom side of the IHB. Asymmetric PBDs can be formed under two circumstances: The first occurs when a monomer possesses more than one heteroatom with similar PAs, resulting in the possibility of multiple isomers being formed. The second is the formation of a heterodimer between two different monomer species (e.g. $CH_3OH\cdots H^+\cdots HOCH_2CH_3$). Both symmetric and asymmetric PBDs are always characterized by a large positive entropy of dissociation (80 to 130 J mol^{-1} K^{-1}) relative to covalent species due to retention of internal rotations and low frequency vibrations about the IHB of the PBD. The IHB bond strength is also affected by resonance stabilization. For example, if the formation of an IHB involves a perturbation to resonance stabilization in the monomer units, it can lower the overall exothermicity of the association reaction.[6]

Experiments involving the study of gaseous symmetric and asymmetric PBDs are perfectly suited to study using mass spectrometric techniques, since one of the principal criteria for performing mass spectrometry experiments is the existence of ionic species in the gaseous state.

1.2 Mass-Selected Infrared Multiple-Photon Dissociation Spectroscopy

Mass spectrometry can be a powerful method for the determination of the structure of molecules. Recently, there have been extensive studies coupling mass spectrometry with the use of laser-induced photoactivation, in order to provide the frequency-specific dissociation of isolated, gaseous ionic species.[7, 8, 11-19] The product ions of such dissociation processes are readily detected using various "trapped ion" mass spectrometric techniques, such as Fourier transform ion-cyclotron resonance (FT-ICR)[20] and ion trap (IT)[21] mass

spectrometry. Trapping of the ions is paramount to the success of laser-induced photoactivation since the ions must be confined to a space where they are exposed to the electromagnetic radiation provided by a laser for sufficiently long periods of time that multiple-photon activation can occur. Conventional forms of mass spectrometry, such as electron impact (EI) and chemical ionization (CI), rely on the identification and characterization of fragment ion intensities as a function of mass to charge ratio (*m/z*). Although the characterization of fragmentation patterns for small ionic species can be very useful, it is rare that the structure of larger ionic species can be elucidated solely from the information provided by a fragmentation mass spectrum. In modern mass-selected IRMPD spectroscopy, the principal mechanism for structural analysis, is the interpretation of an infrared (IR) consequence spectrum, where in this context, the mass spectrometer serves as a detection device only. In prototypical spectroscopy, the spectrum obtained shows the direct absorption or transmission of electromagnetic radiation as a function of photon energy. In consequence spectroscopy, the spectrum shows the efficiency of dissociation induced by the absorption of electromagnetic radiation as a function of photon energy. Therefore, consequence spectroscopy can be considered an indirect measure of the molecular absorption of electromagnetic radiation as a function of photon energy. A common way to express the vertical axis in a mass-selected IRMPD spectrum is as the IRMPD efficiency (**Eq. 1.3**)

$$IRMPD\ eff. = -\log\left(\frac{I_{parent}}{I_{parent} + \sum I_{fragments}}\right) \qquad \textbf{1.3}$$

where I_{parent} is the intensity of the isolated parent ion and $\sum I_{fragments}$ is the sum of the intensities of fragment ions produced following irradiation. The important similarity between conventional IR spectroscopy and IRMPD spectroscopy, is that both methods will provide a unique "chemical fingerprint" of the species of interest.

1.2.1 The IRMPD Process

The mechanism for the unimolecular dissociation of ions, based on the absorption of photons, is theoretically complex[22]; however, the following provides an essentially qualitative view in terms of a more physical description.

Consider a non-linear polyatomic molecule that contains 3N-6 modes of vibration, where N is the number of nuclei, all of which are coupled *via* electron density distributed throughout the molecule. Although, for mathematical simplicity, the vibrations of molecules are regularly treated as a collection of 3N-6 independent harmonic oscillators, real molecular vibrations are not harmonic, nor are they necessarily independent of each other. It is the coupling of molecular vibrations that makes IRMPD a possibility. In IR spectroscopy the excitation of a single oscillator within a molecule occurs by the absorption of photons and is often referred to as the "bright state." The "bright state" carries the initial oscillator strength for the selected spectroscopic transition and this energy will flow into the manifold of so-called "dark-state" oscillators which were not excited directly.[22] Some of the "dark states" are strongly coupled to the "bright state" oscillator and become excited, subsequently continuing to couple with oscillators that were not coupled directly with the "bright state." The energy is then effectively delocalized about the collection of oscillators within the

molecule and this process is referred to as intramolecular vibrational redistribution (IVR).[22-25] The lifetime of IVR is typically very short, at approximately 10 ps, i.e. near the time scale of molecular vibrations.[25] A consequence of IVR is that by the absorption of multiple quanta of photons, a molecule can rapidly have its total vibrational energy increased, in which case the dissociation threshold of the weakest bond within the species may be reached and fragmentation can ensue. The IVR process is considered a slow heating method due to the requirement of a molecule to absorb tens to hundreds of photons in order to promote dissociation.[26] A mole of 1000 cm^{-1} infrared photon equals approximately 12 kJ mol^{-1} of energy. This suggests that a typical covalent C-H bond, with a binding energy[27] of 414 kJ mol^{-1}, would require the absorption of approximately 35 photons in order to dissociate.

1.2.2 Applications of Mass-Selected IRMPD to Gaseous Chemical Systems

Recently, physical chemists have made mass-selected IRMPD a popular technique for the purpose of characterizing the structure of gaseous ionic species; however, the application of IRMPD to small chemical systems has existed for several decades.[28, 29] Over the years, the use of mass-selected IRMPD has produced many interesting studies. In 1985, Eyler and coworkers[30] were able to deduce different isomeric forms of the ion $C_4H_9O_2^+$ (*m/z* 89), which was generated following the mass-selected IRMPD of an assortment of oxygen-containing hydrocarbons including 1,4-dioxane and 2-(2-ethoxyethoxy)ethanol. In 1993, Osterheld and coworkers[31] used mass-selected IRMPD in order to study the dissociation of nitrobenzene radical cation with the purpose of comparing the experimental rates of dissociation with the predictions of microcanonical rate theory of Rice, Ramsperger, Kassel

and Marcus (RRKM).[32-36] One of the first examples of the use of mass-selected IRMPD in the study of dipeptides was performed using a FT-ICR mass spectrometer in 1991 by Zimmerman and coworkers.[37] This was a unique experiment at the time, since it first used a neodymium-doped yttrium aluminium garnet (Nd:YAG) laser to desorb a solid sample of dipeptide, followed by irradiation with an infrared CO_2 laser, in order to induce IRMPD of the gaseous dipeptide species. In 1994, large multiply charged bio-molecules such as bovine carbonic anhydrase (29 kDa), were partially sequenced using IRMPD/FT-ICR by Little and coworkers.[38] It was found that the mass-selected IRMPD could provide additional sequence information previously unavailable by the use of conventional collision-induced dissociation (CID) methods.

A feature common to all of the studies described above is that the type of laser used to perform the IRMPD analyses was either a continuous wave (CW) or pulsed CO_2 laser. The CO_2 laser is of relatively monochromatic wavelength, normally centered between approximately 9.5 and 10.6 μm in the infrared region. One disadvantage of using a monochromatic laser is that molecules must have sufficient vibrational frequencies coherent with the irradiation wavelength in order to initiate IRMPD. Another shortcoming of the use of monochromatic activation, is in the inability to produce a mass-selected IRMPD spectrum as a function of a broad range of photon energies. This form of mass-selected IRMPD provides an alternative to traditional CID methods, however it should not be considered spectroscopic since it does not provide a vibrational signature. For monochromatic IRMPD,

the information provided requires the interpretation of fragmentation intensities as a function of *m/z* ratios.

Many modern forms of mass-selected IRMPD differ from the use of traditional monochromatic laser techniques by incorporating the use of wavelength-tunable laser systems. The two most common tunable light sources currently used for mass-selected IRMPD spectroscopy include the free-electron laser (FEL)[39-41] and optical parametric oscillator (OPO).[42-46] The OPO is a useful tool for mass-selected IRMPD spectroscopy in the approximate range[47, 48] of 2000 to 4000 cm^{-1}. This thesis employs a FEL for the majority of spectra covering the spectral range of 1000 to 1900 cm^{-1}, encompassing the "fingerprint region" of vibrational frequencies. This region of the vibrational spectrum is particularly useful for studying the structural characteristics of ions containing carbonyl groups that may participate in IHB formation. For example in positive ions, free carbonyl stretches are found between approximately 1700 and 1800 cm^{-1} and protonated carbonyl stretches and proton bending modes are found between approximately 1600 and 1650 cm^{-1}.

In the present thesis, structural characterizations of the proton and sodium cation-bound homodimers of caffeine and theophylline, as well as the PBD of ammonia and theophylline have been made using mass-selected infrared multiple-photon dissociation (IRMPD) spectroscopy (1000 to 1900 cm^{-1}) and electronic structure calculations.

A unique mechanism for the generation of the proton-bound homodimer of water from successive bimolecular reactions involving water and 1,1,3,3-tetrafluorodimethyl ether at very low pressure (~ 10^{-9} Torr) is proposed. This work involved using mass-selected IRMPD

spectroscopy (600 to 1900 cm^{-1}), electronic structure and RRKM calculations as the methodology for describing a complex and multi-step mechanism.

Chapter 2
Experimental Considerations

2.1 The Free Electron Laser (FEL)

Several experimental and computational techniques have been implemented in the work presented in this thesis; however one common feature in each of the studies was the use of a FEL to perform mass-selected IRMPD spectroscopy. The FEL[39, 40, 49] is typically a linear accelerator (LINAC) based light source which can provide coherent, high-power radiation with the optical characteristics found in conventional laser systems. While a conventional laser uses the bound atomic or molecular states of solids and gases as its lasing medium, a FEL uses a relativistic electron beam. In a FEL, the electron beam passes through an undulator magnet assembly which results in the stimulated emission of light (**Figure 2.1**). The wavelength of the emitted light is determined by the electron beam energy and pulse characteristics, as well as the periodic magnetic field properties of the undulator. The FEL is excellent for providing high-average and high-peak power and is tunable over an extensive range of wavelengths including: X-rays, ultraviolet, visible, infrared and microwave. The wavelength of emitted light is strongly dependent on the relativistic electron beam energy and the ideal acceleration range for providing infrared photon emission is from 10 to 50 MeV. The details of the specific configuration of the FEL, as it was applied in the work presented here, will follow.

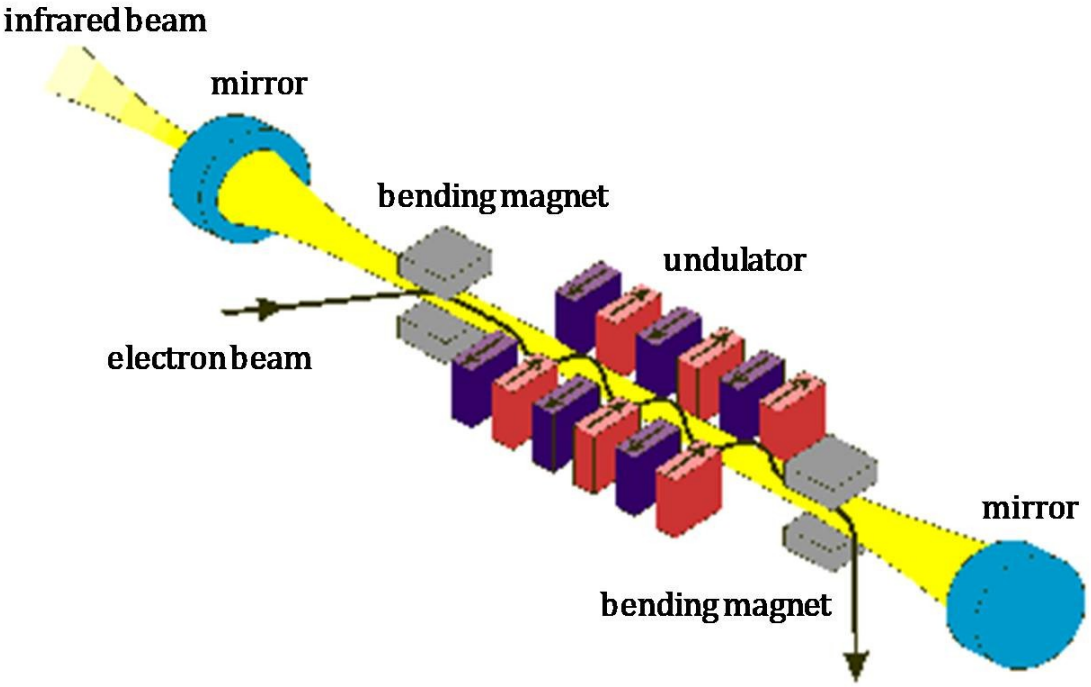

Figure 2.1: The periodic undulator magnet assembly responsible for altering the wavelength of light emitted by the inducing oscillation of a relativistic electron beam which is passed through the assembly.[49]

2.2 Fourier Transform Ion Cyclotron Resonance Mass Spectrometry

In 1949, Hipple and coworkers published the first ICR spectrum of a proton[50], followed by the ICR spectrum of H_2O^+. This early instrument had a *m/z* range of up to approximately 100 amu; however it was reliable up to only 28 amu.[51] Later, in 1974, Comisarow and Marshall published the first FT-ICR mass spectrum of CH_4^+. Using a single data acquisition of 25.9 ms, a signal-to-noise ratio of 8:1 and mass accuracy of approximately 0.005 amu was obtained.[52]

Since the inception of FT-ICR, the technology has evolved dramatically and modern instruments are capable of extraordinary resolution and mass range. For example, the LTQ FT Ultra Hybrid Mass Spectrometer by Thermo Scientific is claimed to have part-per-billion (ppb) resolution (± 0.000001 amu at 1000 amu). An impressive example of mass range capabilities was demonstrated by Chen and coworkers when they isolated coliphage DNA T4 ions of mass 10^8 amu.[53] It was estimated that the "stretched-out" length of the DNA molecule was approximately 10^8 pm, which is gigantic, in terms of a molecular frame of reference.

2.2.1 Theory of Fourier Transform Ion Cyclotron Resonance MS

The following is a brief description of how an FT-ICR functions as a mass spectrometer. The FT-ICR MS is equipped with a powerful permanent magnet and normally it is superconducting in nature. The FT-ICR MS used in one of the studies presented in this thesis, is equipped with a superconducting magnet possessing a field strength of 4.7 T. Current instruments have much stronger fields, such as the Bruker Daltonics Apex-Ultra series FT-ICR, which is equipped with a superconducting magnet at a field strength of 9.4 T.

An ion in the presence of a spatially uniform magnetic field is subjected to a force demonstrated by the Lorentz magnetic force equation,

$$\vec{F} = m\vec{a} = m\frac{d\vec{v}}{dt} = q\vec{v}\ x\ \vec{B} \qquad \textbf{2.1}$$

where m, q and $\vec{v}$ are the ion mass, charge and velocity, respectively. The cross product of $\vec{v}$ and $\vec{B}$ results in the magnetic component of the Lorentz force to be perpendicular to the plane determined by $\vec{v}$ and $\vec{B}$ and this is shown in **Figure 2.2**.

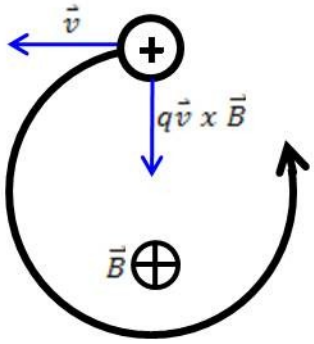

Figure 2.2: Ion cyclotron motion exhibited by a positive ion moving in the plane of the paper induced by the Lorentz magnetic force directing it inward, perpendicular to the direction of the applied magnetic field. A negative ion exhibits equal and opposite cyclotron motion.

The velocity of the ion in the xy-plane is defined as $v_{xy} = \sqrt{v_x^2 + v_y^2}$ and is perpendicular to the z-component of the magnetic field, B_z. Since the angular acceleration is

$$\left|\frac{dv_{xy}}{dt}\right| = \frac{v_{xy}^2}{r} \qquad \textbf{2.2}$$

then **Eq. 2.1** becomes

$$\frac{mv_{xy}^2}{r} = qv_{xy}B_z \qquad \textbf{2.3}$$

The angular velocity, ω (rad s^{-1}), about the axis of B_z is

$$\omega = \frac{v_{xy}}{r} \quad \textbf{2.4}$$

and therefore **Eq. 2.3** becomes

$$m\omega^2 r = qB_z \omega r \quad \textbf{2.5}$$

Since $q = Ze$, where Z is the charge number and e is the elementary charge constant, the characteristic "cyclotron" equation is obtained.

$$\frac{m}{z} = \frac{B_z e}{\omega_c} \quad \textbf{2.6}$$

The spectacular simplicity of **Eq. 2.6** demonstrates that all ions with the same *m/z* ratio exhibit the same cyclotron frequency, ω_c and the independence on the velocity of the ions. The radius of the ion cyclotron motion demonstrated by **Figure 2.2** can also be calculated. Simply rearranging **Eq. 2.3** yields,

$$r = \frac{mv_{xy}}{qB_z} \quad \textbf{2.7}$$

The most probable xy-translational energy of an ion at ambient temperature, T, is

$$kT \approx \frac{m\langle v_{xy}^2 \rangle}{2} \quad \textbf{2.8}$$

Solving **Eq. 2.8** for v_{xy}, substituting into **Eq. 2.7**, and rearranging, yields the equation for the radius of thermal ion cyclotron motion.

$$r = \frac{\sqrt{2mkT}}{qB_z} \quad \textbf{2.9}$$

The result shown by **Eq. 2.9** demonstrates that at T = 25°C and $B_z = 4.7$ T a singly charged ion with *m/z* 100 has an orbiting radius of approximately 50.0 μm. For a comprehensive article containing the derivations shown above, in addition to equations describing the excitation and detection processes, the 1998 review article by Marshall is suggested.[54] With the knowledge of ion behaviour in the presence of a spatially uniform magnetic field, a brief description of how an FT-ICR MS is obtained follows.

2.2.2 Excitation and Detection in FT-ICR MS

In order to exploit the best properties of the superconducting magnetic field, the FT-ICR cell is placed in the bore of the magnet, where the magnetic field is the most homogeneous. The FT-ICR cell is where the ions are trapped, isolated and mass detected. A schematic and actual image of an FT-ICR cell are shown in **Figure 2.3** and **Figure 2.4**, respectively. The diameter of the FT-ICR cell shown in **Figure 2.4** is approximately 6 cm and it was shown earlier that the radius of the ion packet trapped at the centre of the cell is on the order of micrometres. In order to detect the ions, it is required that the ion orbit radius come within close proximity of the FT-ICR cell walls. The first purpose of the axial trapping plates is to prevent the drift of ions along the direction of the magnetic field, as well as to confine the ion packet at the centre of the cell. This is accomplished with a small potential of approximately 1 to 2 V. A secondary function of the trapping plates is to empty the cell of all ions following an experiment, a process that is called "quenching." The "quenching" process applies a disproportionate potential across the trapping plates, effectively pushing the ions out of the cell axially. The transmitter plates are used to apply a radio-frequency (RF) driven

electric field (approximately 1 V) onto the ions and increase their cyclotron radius. The ion cyclotron radius will only increase if the frequency of the RF signal is coherent with the characteristic cyclotron frequency (ω_c) of the ions.

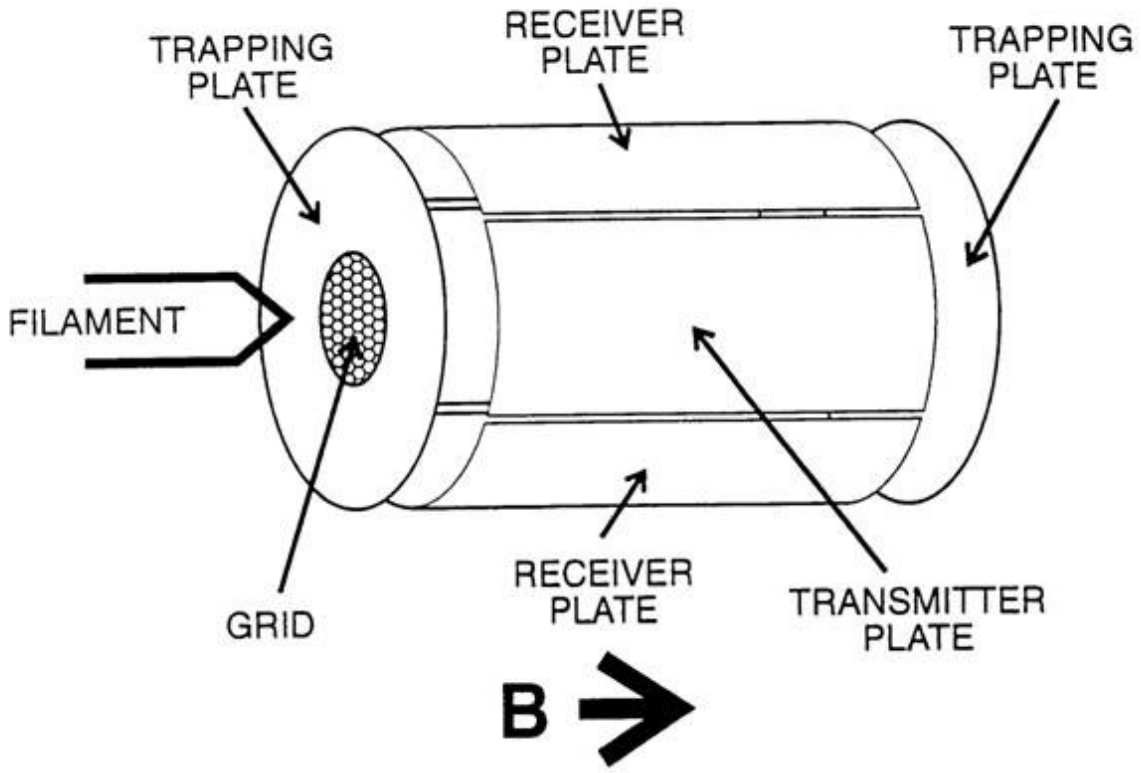

Figure 2.3: An FT-ICR cell demonstrating the pairs of receiving, transmitting and axial trapping plates constituting the cylindrical shape. A rhenium filament can be placed within close proximity of a gold grid found at the centre of trapping plates in order to permit Electron Ionization (EI).

The transmitter plates first serve to isolate individual types of ions by ejection of unwanted ions from the cell, and second, permit a way to increase the cyclotron radius of the ions to a

close proximity of the receiver plates such that a signal is generated for detection. As the ion packets orbit sufficiently close to the receiver plates, the charge of the ions (positive) will attract electrons to the surface of the plates generating an alternating "image current," collected as a function of time. Application of a Fourier transform to this time-domain signal generates a frequency-domain signal. Once the cyclotron frequency (ω_c) is calculated by the Fourier transform from the time domain signal, the *m/z* ratio is obtained from **Eq. 2.6**. A typical pulse sequence used for an FT-ICR experiment is shown in **Figure 2.5**.

One final and important feature of the FT-ICR is the very low pressure maintained within the cell region. The FT-ICR instrument used in the work presented here maintains a base pressure of 1.5 x 10^{-9} Torr, which amounts to one collision occurring approximately every 20 seconds. Due to the infrequency of collisions, the FT-ICR is perfectly suited for slow kinetics experiments. The author has personally experienced this, when he was able to detect ions which had been produced and trapped approximately one day earlier!

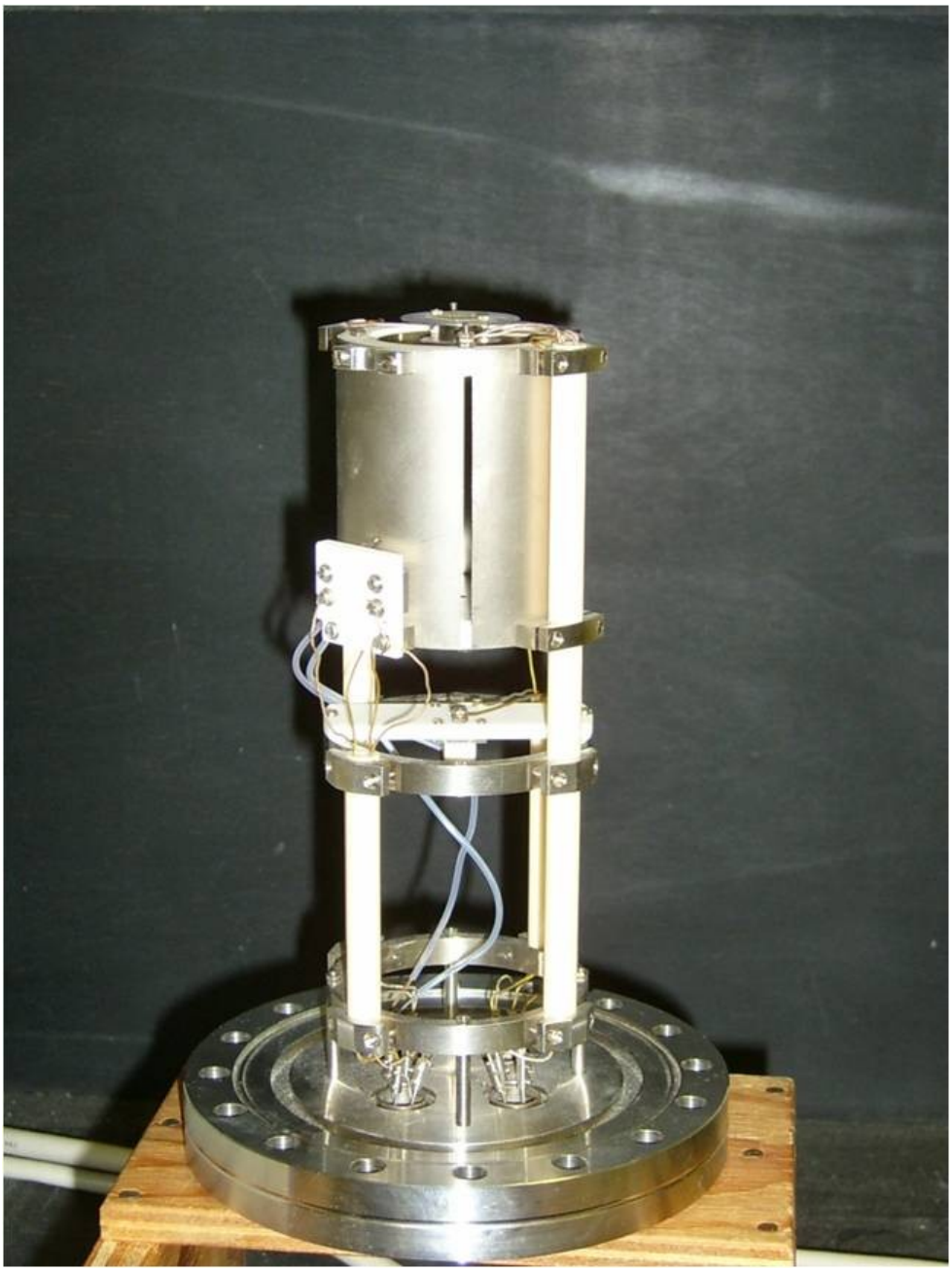

Figure 2.4: An FT-ICR cell showing the pairs of receiver, transmitter and axial trapping plates which constitute the cylindrical shape. The small plate mounted on top of the trapping plate has a platinum grid at the centre, allowing for injection of ions from an external ion source, and a similar assembly exists on the underside to permit EI.

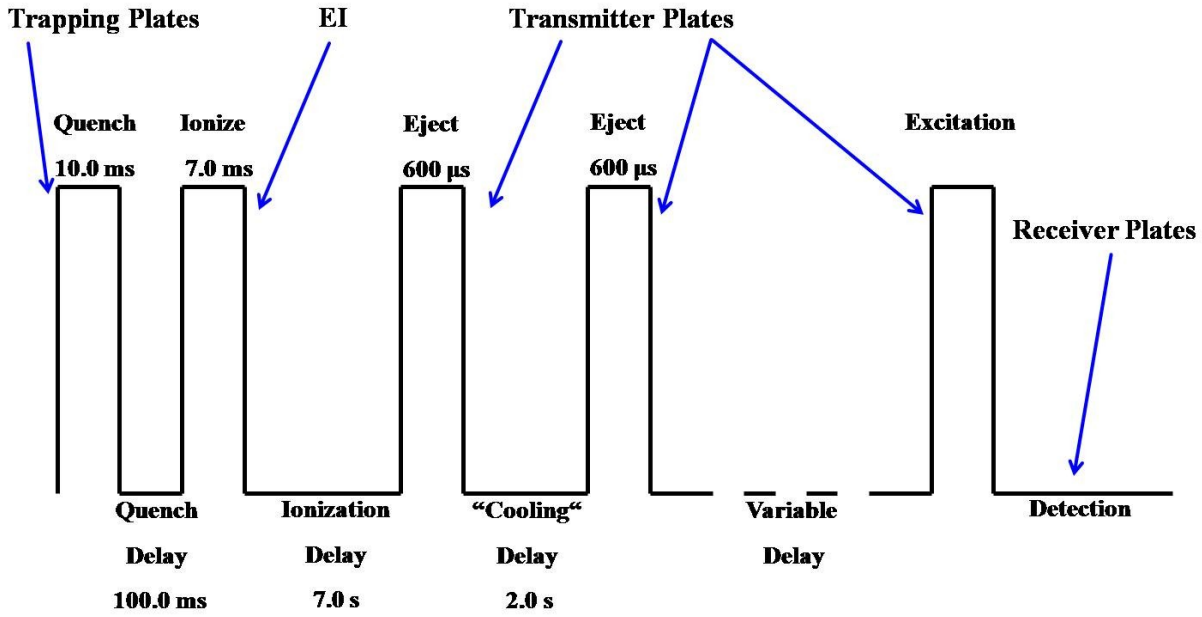

Figure 2.5: A typical pulse sequence performed in a FT-ICR MS experiment, demonstrating which plates are operating during each instance of the interval.

2.3 Quadrupole Ion Trap Mass Spectrometry

Like the FT-ICR MS previously described, the quadrupole ion trap (QIT) MS is, by definition of the name it possesses, an ion trap. The application of trapping ions in electric fields produced by a set of hyperbolic electrodes was first patented by Paul and Steinwedel in 1960.[55] In 1983, the method for measuring the *m/z* ratio of ions confined within a QIT was further developed by Stafford and coworkers and was known as the "mass-selective axial instability mode." It was this work that led to the commercialization of the QIT MS.

2.3.1 Theory of Quadrupole Ion Trap MS

The QIT consists of a set of three irregularly shaped electrodes shown in the "exploded" and "cut-away" images provided by **Figure 2.6**. All three electrodes are of hyperbolic geometry; the two saucer-shaped electrodes are referred to as the end-cap electrodes and the third electrode is called the ring electrode. The geometry for producing the optimum quadrupole electric field is given by $r_0^2 = 2z_0^2$, and the dimensions r_0 and z_0, are defined in the "cut-away" image (b) provided in **Figure 2.6**. The dimension, r_0, is the radius of the ring electrode and is commonly a value of 0.707 or 1.00 cm in the majority of commercial instruments.[56] The dimension, z_0, is the perpendicular distance from the centre of the ring electrode to the end-cap electrode.

The motion of an ion within a QIT is markedly different than the straight paths and arcs that an ion will take in a sector instrument, or the ion cyclotron motion found in an FT-ICR. An ion in the presence of a quadrupole field feels a strong restoring force, which effectively focuses it to the centre of the QIT cell assembly. This restoring force increases as the ion moves away from the centre of the cell. The correct expression for describing the effects of a quadrupole field on the trajectory of an ion was derived from the work of a mathematician who was investigating the regions of stability found on the surface of vibrating drum skins.

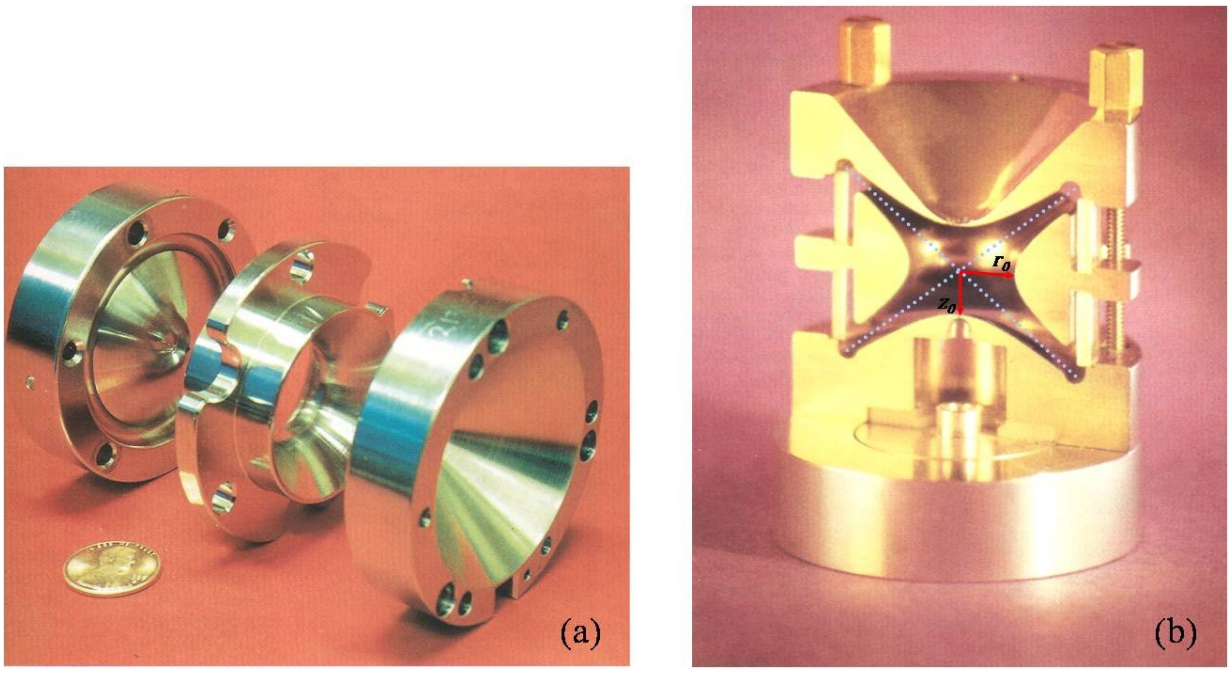

Figure 2.6: (a) An "exploded" view[56] of a QIT cell relative to a US Penny demonstrating the small size of the cell assembly. The end-cap electrodes are on either side of the ring electrode. (b) A "cut-away" view[56] of a QIT cell, showing the dimensions, r_0 and z_0. The light blue dashed lines show the theoretical asymptotes of the quadrupole fields generated.

The expression for describing this phenomenon is referred to, by the name of the inventor, as the Mathieu equation.[57] If it is applied to an ion in a quadrupole field, the canonical form of the Mathieu equation is

$$\frac{d^2u}{d\xi^2} + (a_u - 2q_u \cos 2\xi)u = 0 \qquad \textbf{2.9}$$

where u represents the displacement of the ion as a function of its x, y and z coordinates. The values of a_u and q_u are Mathieu's dimensionless parameters and many of the important

quantities for the QIT including frequencies, trap geometry and potentials will be expressed in terms of these parameters. The value of ξ is equal to $\Omega t/2$, where Ω is the angular frequency of the RF potential applied to the ring electrode. If $\xi = \Omega t/2$ it is easy to show that

$$\frac{d^2u}{dt^2} = \frac{\Omega^2}{4}\frac{d^2u}{d\xi^2} \qquad \textbf{2.10}$$

When **Eq. 2.10** is substituted into **Eq. 2.9**, multiplied by the mass, m and then rearranged, it yields

$$m\frac{d^2u}{dt^2} = \frac{-m\Omega^2}{4}(a_u - 2q_u \cos \Omega t)u \qquad \textbf{2.11}$$

The fields of a quadrupole device are uncoupled and thus can be treated separately, allowing for the force exerted on an ion by a quadrupole field in the x-direction to be expressed as

$$F_x = ma_x = m\frac{d^2x}{dt^2} = -e\frac{\partial \phi}{\partial x} \qquad \textbf{2.12}$$

There are similar expressions which can be obtained for F_y and F_z. The quadrupole potential is expressed as

$$\phi = \frac{\phi_0}{r_0^2 + 2z_0^2}(\lambda x^2 + \sigma y^2 + \gamma z^2) \qquad \textbf{2.13}$$

where the values, λ, σ and γ are weighting constants satisfying the Laplace condition of electric fields such that

$$\nabla^2\phi = \left(\frac{d^2}{dx^2} + \frac{d^2}{dy^2} + \frac{d^2}{dz^2}\right)\phi = 0 \qquad \textbf{2.14}$$

Therefore $\lambda + \sigma + \gamma = 0$ and for a QIT the values of λ, σ and γ turn out to be 1, 1 and -2, respectively. If the known values of λ, σ and γ are substituted back into **Eq. 2.13** then

$$\phi_{x,y,z} = \frac{\phi_0}{r_0^2 + 2z_0^2}(x^2 + y^2 - 2z^2) \qquad \textbf{2.15}$$

which is readily transformed to a cylindrical coordinate system ($x = r\cos\theta$, $y = r\sin\theta$ and $z = r$) to give

$$\phi_{r,z} = \frac{\phi_0}{r_0^2 + 2z_0^2}(r^2\cos^2\theta + r^2\sin^2\theta - 2z^2) \qquad \textbf{2.16}$$

From trigonometry, $\cos^2\theta + \sin^2\theta = 1$ so

$$\phi_{r,z} = \frac{\phi_0}{r_0^2 + 2z_0^2}(r^2 - 2z^2) \qquad \textbf{2.17}$$

The potential applied in the QIT is of the form,

$$\phi_0 = U + V\cos\Omega t \qquad \textbf{2.18}$$

with $\Omega = 2\pi f$, the angular frequency and f, the frequency in Hz . When **Eq. 2.18** is substituted into **Eq. 2.17**,

$$\phi_{r,z} = \frac{U + V\cos\Omega t}{r_0^2 + 2z_0^2}(r^2 - 2z^2) \qquad \textbf{2.19}$$

and differentiated with respect to r gives

$$\frac{d\phi_{r,z}}{dr} = \frac{2r}{r_0^2 + 2z_0^2}(U + V\cos\Omega t) \quad \textbf{2.20}$$

Substituting **Eq. 2.20** into **Eq. 2.12** yields

$$F_r = m\frac{dr^2}{dt^2} = \frac{-2e}{r_0^2 + 2z_0^2}(U + V\cos\Omega t)r \quad \textbf{2.21}$$

which is the expression for the force imposed on an ion in the r dimension. If **Eq. 2.11** and **Eq. 2.21** are compared directly, it is found that for a QIT,

$$a_r = \frac{8eU}{m(r_0^2 + 2z_0^2)\Omega^2} \quad \textbf{2.22}$$

and

$$q_r = \frac{-4eV}{m(r_0^2 + 2z_0^2)\Omega^2} \quad \textbf{2.23}$$

For the ion trap, $a_x = a_y = a_r$ and $q_x = q_y = q_r$. Similarly for the values of a_z and q_z, since $\gamma = -2$ then **Eq. 2.22** and **Eq. 2.23** can be expressed as

$$a_z = \frac{-16eU}{m(r_0^2 + 2z_0^2)\Omega^2} \quad \textbf{2.24}$$

and

$$q_z = \frac{8eV}{m(r_0^2 + 2z_0^2)\Omega^2} \quad \textbf{2.25}$$

For a typical commercial QIT, $U = 0$ so that $a_z = 0$. Thus the expression for q_z is a function of the *m/z* ratio (*m/e* for a singly charged ion), the ion trap dimensions r_0 and z_0, the intensity of the RF field, V, and the angular frequency of the RF field, Ω.

The equations, **Eq. 2.22** and **Eq. 2.23** can be used to form a stability diagram, which is obtained as a result of finding solutions to the Mathieu equation in cylindrical coordinates. An example of a stability diagram is shown in **Figure 2.6**. The trajectory of an ion confined in a QIT is "figure-eight" like and composed of a secular frequency component in both the z and r dimensions. The general form of the secular frequency is given by

$$\omega_{u,n} = \left(n + \frac{1}{2}\beta_u\right)\Omega, \quad 0 \leq n < \infty \tag{2.24}$$

and

$$\omega_{u,n} = -\left(n + \frac{1}{2}\beta_u\right)\Omega, \quad -\infty \leq n < 0 \tag{2.25}$$

where $n = 0$ for the fundamental of the secular frequency. The value of β_u is found by solving a substantial transcendental equation involving the values of β_u, a_u and q_u.

$$\beta_u^2 = a_u + \frac{q_u^2}{(\beta_u+2)^2 - a_u - \dfrac{q_u^2}{(\beta_u+4)^4 - a_u - \dfrac{q_u^2}{(\beta_u+6)^6 - a_u - \cdots}}} + \frac{q_u^2}{(\beta_u-2)^2 - a_u - \dfrac{q_u^2}{(\beta_u-4)^4 - a_u - \dfrac{q_u^2}{(\beta_u-6)^6 - a_u - \cdots}}} \tag{2.26}$$

When different values of iso-β_z and iso-β_r lines are plotted, it generates lines which form the stable region shown in the **Figure 2.6**. As the RF field, V, is increased and the value of $q_z = 0.908$ is exceeded by an ion, it will experience an unstable trajectory and then be ejected. As the value of V is increased, the QIT will eject ions in the order of lowest to highest mass.

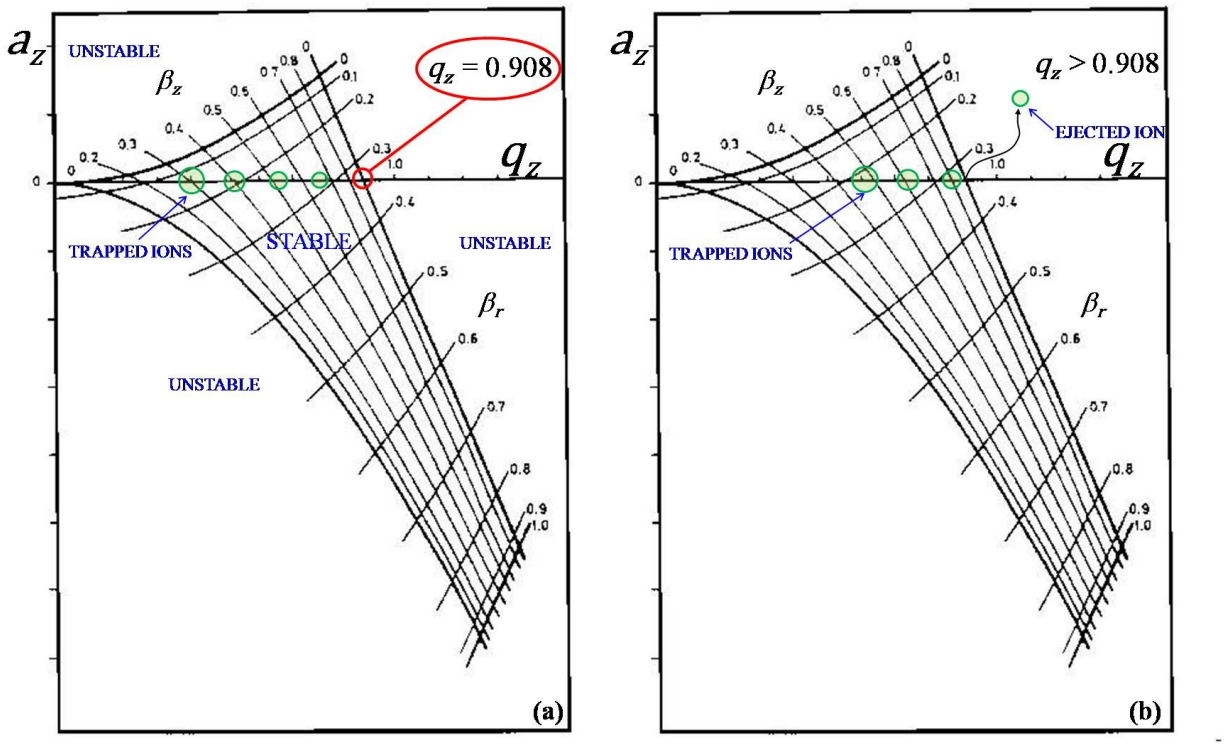

Figure 2.7: (a) The regions of stable and unstable ion trajectories within a QIT. Since $U = 0$, the ions remain along the q_z axis. (b) As the RF field V is increased from the original conditions in (a), the QIT systematically ejects ions from lowest to highest mass when the value of $\boldsymbol{q_z}$ for each ion exceeds 0.908.

2.3.2 Excitation and Detection in QIT MS

The QIT cell is maintained under a pressure of approximately 1 mTorr of He buffer gas, which serves to "cool" the ions and also focus them to the centre of the cell. The presence of the buffer gas greatly enhances the resolution of QIT MS.[56] Ions are introduced from an external ion source through a hole in one of the end-cap electrodes or produced directly by EI within the QIT cell. By applying a small RF potential (100 to 200 mV) across the end-cap electrode that is coherent with the secular frequency of the confined ions, $\omega_{z,0}$, they can be translationally excited along the z-axis and out of a hole located in one of the end-cap electrodes for detection. This can be accomplished at a q_z value lower than 0.908, which allows for the isolation of a single ionic species and is commonly referred to as applying a "tickle voltage." The "tickle voltage" is also used to induce strong collisions between the isolated ions and the buffer gas for the purpose of performing tandem mass spectrometry (MS^n) studies by CID.

2.4 High Pressure Mass Spectrometry (HPMS)

High Pressure Mass Spectrometry (HPMS) is a powerful technique for quantitatively determining the thermodynamic properties of IHBs in the gas phase. A description of this method is warranted because a new HPMS ion source is currently under development, permitting entry into chemical systems considered impossible to study with the existing instrumental configuration. The final chapter of this thesis will describe details of the new

ion source, and the exciting implications of its application in HPMS research at the University of Waterloo.

Ion-molecule reaction studies involving mass spectrometry using conventional low pressure (~ 10^{-4} Torr) ion sources have been performed since the 1950s.[58, 59] After World War II, radiation chemistry was considered an important area of research that originated from the development of nuclear weapons. The ionic species produced in the chemistry induced by ionizing radiation were detectable by mass spectrometry.[60] Studies using conventional low pressure ion sources were unable to explore gas phase ion-molecule equilibria by mass spectrometry for several reasons, such as thermalization of the ions, ion dwell-time following ionization, and, finally, ions possessing a non-Boltzmann distribution of energies due to the presence of electric fields. During a series of radiolysis experiments,[61-63] in which a polonium-210 α-particle source was used to ionize molecules contained in an ion source at near-atmospheric pressures, Kebarle serendipitously invented HPMS. The observation of a series of $H_3O^+(H_2O)_n$ cluster ions produced from a sample of "laboratory air" led to the realization that working at higher pressures had increased the dwell-time of ions and also provided a sufficient number of stabilizing collisions such that observable equilibrium was obtained. HPMS is one of the most reliable and widely used techniques for obtaining the thermodynamic quantities associated with IHB formation.[6]

2.4.1 VG 70-70 Double-Focusing Instrument Modified for HPMS

Discussion here will be based on the technical specifications of the HPMS instrument currently under modification in the McMahon laboratory, as it will provide much of the background information necessary for the topic presented in the final chapter of this thesis.

One of the three HPMS instruments found in the McMahon laboratory is based on a VG 70-70, double-focusing mass spectrometer modified to accommodate a home-built high pressure (5 to 20 Torr) ion source capable of generating ions in thermal and chemical equilibrium. This is achieved by forming ions under an electric field-free environment, and then allowing for numerous collisions ($\sim 10^6$ per second) between the ions and an inert bath gas which serves as both a "cooling" and CI agent. For studies involving IHB formation, the bath gas used is normally CH_4. A mixture of analyte and approximately 99% CH_4 are prepared in a calibrated 5.0 L, heated, stainless-steel reservoir, where the gas is then introduced into the ion source gas inlet. There are two small exits in the ion source consisting of 200 μm platinum apertures. One aperture is located at the top of the source, permitting entry of an electron beam, and the second is located at the front of the source, allowing for the effusion of ions into a high vacuum region ($\sim 10^{-7}$ Torr) where they are accelerated, mass selected and detected. The electron beam is accelerated to 2000 eV and focused into the ion source where it initiates a series of ion-molecule reactions involving CH_4 to yield "super acidic" species such as, CH_5^+ and $C_2H_5^+$. The proton affinities of CH_4 and C_2H_4 are always lower than that of the analyte molecule, and thus proton-transfer will occur from CH_5^+ or $C_2H_5^+$ to yield a protonated monomer of the analyte. The 2000 eV electron beam may seem

excessive; however it is required to have a high enough energy in order to penetrate deep into the ion source since the high pressure has a tendency to cause a low energy electron beam to build up charge at the entrance of the aperture. The electron beam is pulsed on for approximately 500 μs and then shut off to allow for the natural diffusion of ions to the walls of the ion source (5 to 50 ms). It is in this diffusion period where ion-molecule equilibrium is established, and in the study of IHB interactions (given by **Eq. 2.27)** it is typically the equilibrium formed between a protonated monomer, MH^+ and its proton-bound dimer (PBD), M_2H^+ that is of interest.

$$MH^+ + M \rightleftharpoons M_2H^+ \qquad \textbf{2.27}$$

During a single experiment, a series of 1000 to 10000 electron pulse events are made and summed, generating an ion intensity profile as a function of time. This is normally repeated ten times for one temperature, then reproduced for a range of ~ 100°C in ~ 10°C increments, in order to yield 100 data points.

The ion source body is constructed from non-magnetic stainless steel and heated with a band heater (up to ~ 400°C). The gas temperature is measured directly in the ion source reaction region with two chromel-aluminel k-type thermocouples accurate to ± 1.5°C. During the diffusion period, a small fraction of ions will exit the front aperture by effusion where they are accelerated, mass-selected and detected by a channeltron electron multiplier (CEM). The discriminated and amplified signal from the CEM is monitored by a multichannel scalar (MCS) and time-intensity profiles are generated. An example of a set of protonated monomer

and PBD time-intensity profiles is shown in **Figure 2.8** for protonated glycine and ammonia.[64]

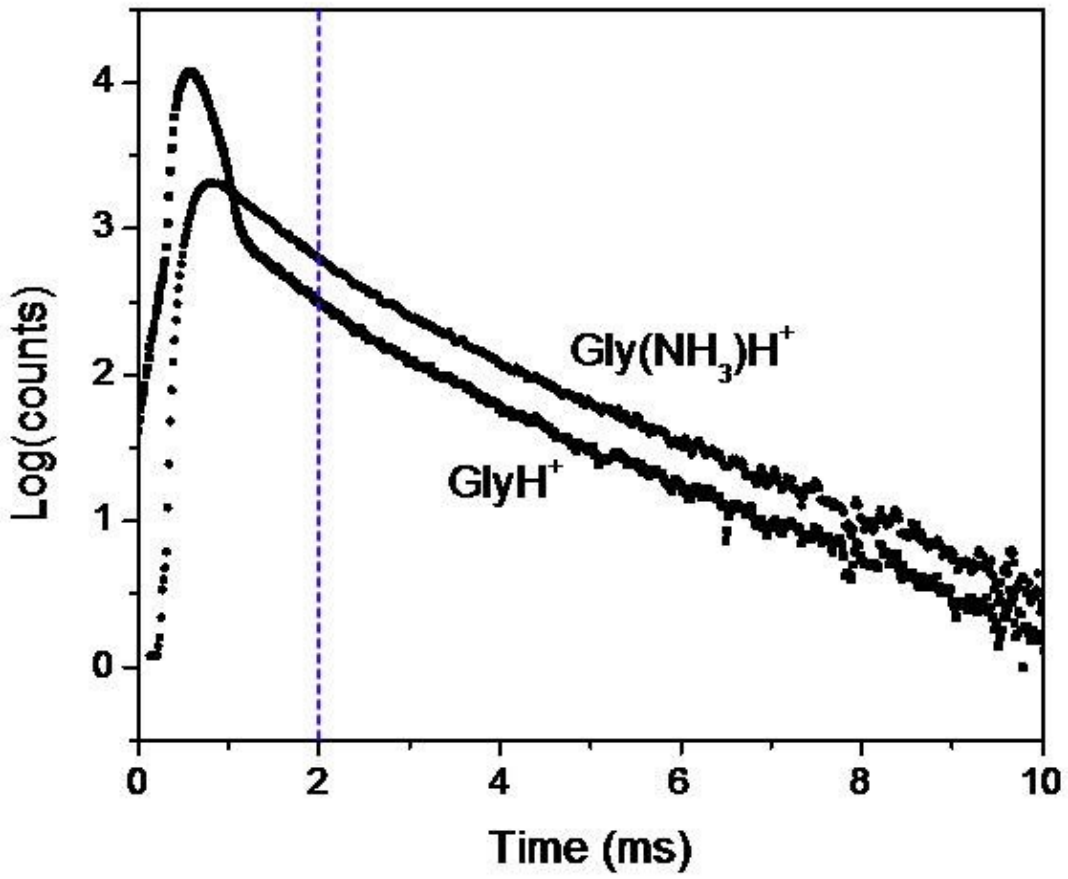

Figure 2.8: Variation of ion intensities with time for protonated glycine and its ammonia cluster, 0.66 Torr NH_3 in 2.54 L reservoir with total pressure of 1180 Torr. The temperature of the ion source is 430 K and pressure is 5 Torr.

Although the ions have significantly different masses, it is clear that in **Figure 2.8**, the diffusion profiles are parallel at longer times, which implies that the monomer and dimer are coupled through equilibrium (**Eq. 2.27**), effectively switching their chemical identity and resulting in an average diffusion time experienced only by ions under equilibrium conditions. At equilibrium, the rate of change of the number density of ions with respect to time is zero and because the number density is proportional to intensity, the monomer and dimer intensities can be normalized with respect to each other such that

$$I_{AH^+,normalized} = \frac{I_{AH^+}}{I_{AH^+} + I_{A_2H^+}} \quad \textbf{2.28}$$

and

$$I_{A_2H^+,normalized} = \frac{I_{A_2H^+}}{I_{AH^+} + I_{A_2H^+}} \quad \textbf{2.29}$$

to yield a normalized time-intensity profile. The region of time where the normalized intensities become parallel is where equilibrium is attained. The normalized version of the time-intensity profile displayed by **Figure 2.8** is shown in **Figure 2.9**.[64]

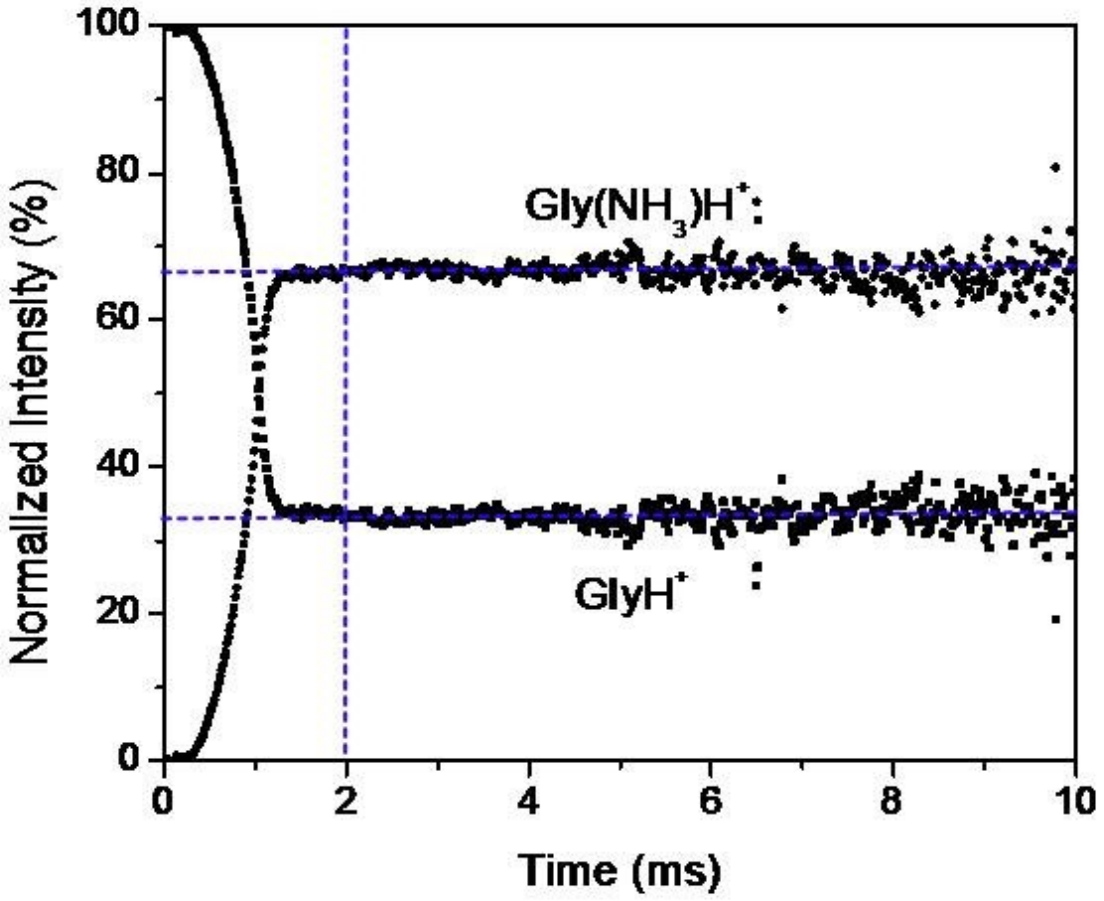

Figure 2.9: A normalized time-intensity profile obtained by an HPMS experiment for protonated glycine and its ammonia cluster. Equilibrium is obtained with certainty after ~ 2 ms, where the rate of change of intensity of each ion is equal to zero.

2.4.2 Theory of a Double-Focusing Sector HPMS

A detailed diagram of the instrument described in the last subchapter is provided by **Figure 2.10** and annotation of the numbered labels is found in **Table 2-1**. A brief description of how the VG 70-70 instrument serves as a mass spectrometer follows.

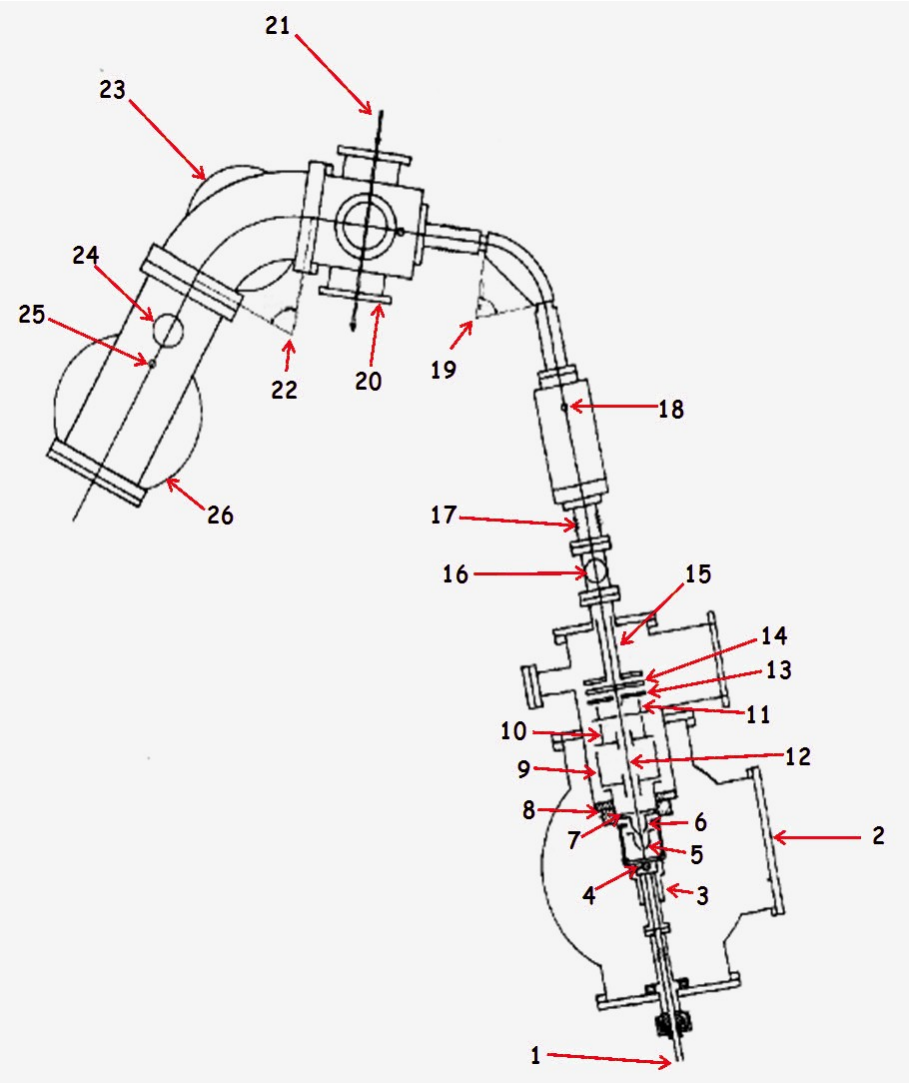

Figure 2.10: The VG 70-70, double-focusing mass spectrometer of reverse geometry, modified to accommodate a high pressure ion source.

Table 2-1: Annotation of the labels provided in Figure 2.7 describing the components of the modified VG 70-70 mass spectrometer.

Component Number	Description
1	Gas Inlet
2	Viewing Window and Diffusion Pump
3	Ion Source (~ 3000 V)
4	Electron Aperture (200 μm)
5	First Cone (~ 2800V)
6	Second Cone (~ 1700 V)
7	Top Hat (~ 1100 V)
8	Teflon Support and Sealing Plug
9	First Einzel Lens (~ 1700 V)
10	Second Einzel Lens (~ 200 V)
11	Third Einzel Lens (~ 1300 V)
12	Ion Flight Path
13	y-deflectors (~ 40 V)
14	z-deflectors (~ 6 V)
15	Tunnel (~ 600V)
16	Isolation Valve
17	Bellows
18	First Resolving Slit
19	Magnetic Sector (70° @ r = 12.7 cm)
20	Collision Cell Housing
21	Laser Beam (optional photodissociation)
22	Electrostatic Analyzer (70° @ r = 20.0 cm)
23	Diffusion Pump
24	Isolation Valve
25	Final Resolving Slit
26	Collector Housing and Diffusion Pump

The term, "double-focusing " refers to a mass spectrometer focusing both the momenta and kinetic energies of ions using a magnetic sector and electrostatic analyzer (ESA), respectively. The term, "reverse geometry, or BE" refers to the ordering of the sectors, such that in a reverse geometry instrument the magnetic sector precedes the ESA.

A schematic representation of the magnetic sector on the VG 70-70 is shown in **Figure 2.11**.

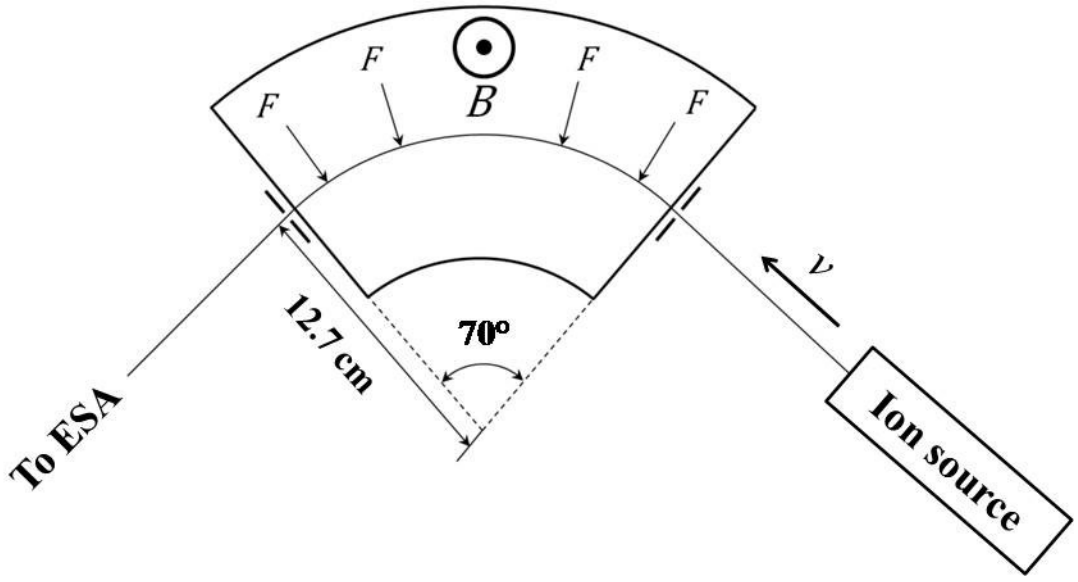

Figure 2.11: Schematic of the magnetic sector in the VG 70-70 HPMS. The magnetic field, B is coming out of the page toward the reader.

After exiting the ion source and acquiring the full acceleration potential, V, the kinetic energy of the ions is given by

$$E_k = \frac{1}{2}mv^2 = Vq \qquad \textbf{2.30}$$

where E_k is the kinetic energy, m is the mass of the ion and $q = Ze$, with Z as the number of charges and e as the proton charge constant. Substituting for q and rearranging for the velocity of the ions gives

$$v = \left(\frac{2VZe}{m}\right)^{1/2} \qquad \textbf{2.31}$$

It is intriguing to consider the high speed achieved by the ions following an acceleration of 3000 V. For example, a 100 amu ion will travel through the 2 m path of the mass spectrometer at a velocity of 76 km s^{-1} (~ mach 231), navigating the distance in 26 μs! In order to traverse the curved path through the magnetic sector, the centripetal force of the ions must balance the magnetic force applied by the magnetic field. The force experienced by an ion in the presence of electric and magnetic fields is given by the Lorentz force equation

$$\vec{F} = q(\vec{E} + \vec{v} \times \vec{B}) \qquad \textbf{2.32}$$

where $\vec{E}$ is the electric field strength; however, in this case, it is equal to zero since there is no electric field present, $\vec{v}$ is the ion velocity and $\vec{B}$ is the magnetic field strength. In the two dimensional case, **Eq. 2.32** reduces to

$$F_{mag} = qvB \qquad \textbf{2.33}$$

The centripetal force, F_c is given by

$$F_c = m\frac{v^2}{r} \quad \textbf{2.34}$$

where r, is the radius of the magnetic sector. For an ion to traverse the curved path and exit the magnetic sector, **Eq. 2.33** is set equal to **Eq. 2.34** and solved for v to give

$$v = \frac{rBZe}{m} \quad \textbf{2.35}$$

The equation for a magnetic sector relating the *m/z* ratio to the magnetic field strength, B and the acceleration potential, V is found by setting the velocities obtained by **Eq. 2.31** and **Eq. 2.35** equal and rearranging to yield

$$\frac{m}{z} = \frac{r^2B^2e}{2V} \quad \textbf{2.36}$$

It is shown by **Eq. 2.36** that the *m/z* ratio of the ion permitted through the magnetic sector can be changed by scanning the magnetic field strength or the acceleration potential. It is most common to scan the magnetic field by increasing or decreasing the current applied to the electromagnet.

The radial ESA is simply constructed of two parallel curved stainless steel plates, set to a potential difference of approximately 50 V in order to transmit ions accelerated to 3000 V for the VG 70-70 described here. The two dimensional version of the Lorentz equation for the force F_{elec} , exerted on an ion by an electric field with strength E, is

$$F_{elec} = qE \quad \textbf{2.37}$$

Analogously to the magnetic sector, in order for ions to negotiate the curved path of the radial ESA, **Eq. 2.37** is set equal to **Eq. 2.34** then

$$qE = m\frac{v^2}{r} \qquad \textbf{2.38}$$

If both sides of **Eq. 2.38** are multiplied by 1/2, the kinetic energy of the ions will fall out of the right side of the equation and the working form of the ESA equation is obtained as

$$E_k = \frac{rEq}{2} \qquad \textbf{2.39}$$

It is clear that there is no mass dependence in the radial ESA; however the kinetic energy of an ion can be scanned by varying the electric field strength between the plates, E. Kinetic energy filtering removes the spread in kinetic energy of the ions and increases the resolution of the instrument. In instruments of reverse geometry the ESA can be used by physical chemists to obtain metastable ion kinetic energy spectra (MIKES); however details of this type of experiment will not be discussed in this thesis.

2.4.3 Thermodynamic Quantities Obtained by HPMS

The general scheme for an association reaction between monomer A and its protonated counterpart AH^+ is

$$\mathrm{nA} + \mathrm{nAH}^+ \rightleftharpoons \mathrm{A}_2^1\mathrm{H}^+ + \mathrm{A}_2^2\mathrm{H}^+ + \cdots + \mathrm{A}_2^{\mathrm{n}}\mathrm{H}^+ \qquad \textbf{2.40}$$

where $A_2^n H^+$ is the n^{th} PBD of n possible isomers. The observed equilibrium constant, K_{obs} for the process shown by **Eq. 2.40** can be written as a product of the equilibrium constants used to describe each individual PBD formation such that

$$K_{obs} = K_1 K_2 \cdots K_n \quad \textbf{2.41}$$

Recall that

$$K = e^{-\frac{\Delta G^\circ_{rxn}}{RT}} \quad \textbf{2.42}$$

thus,

$$K_{obs} = \prod_{i=1}^{n} e^{-\frac{\Delta G_i^\circ}{RT}} \quad \textbf{2.43}$$

and taking the natural logarithm of both sides yields

$$\ln K_{obs} = -\frac{1}{RT} \sum_{i=1}^{n} \Delta G_i^\circ \quad \textbf{2.44}$$

Since

$$\Delta G_i^\circ = \Delta H_i^\circ - T\Delta S_i^\circ \quad \textbf{2.45}$$

then substituting **Eq. 2.45** into **Eq. 2.44** gives

$$\ln K_{obs} = -\frac{1}{RT}\sum_{i=1}^{n}\left(\Delta H_i^\circ - T\Delta S_i^\circ\right) \qquad \textbf{2.46}$$

$$\ln K_{obs} = -\frac{1}{RT}\sum_{i=1}^{n}\Delta H_i^\circ + \frac{1}{R}\sum_{i=1}^{n}\Delta S_i^\circ$$

The sums, $\sum_{i=1}^{n}\Delta H_i^\circ$ and $\sum_{i=1}^{n}\Delta S_i^\circ$, are the experimentally observed changes in enthalpy and entropy respectively, therefore

$$\ln K_{obs} = -\frac{\Delta H_{obs}^\circ}{RT} + \frac{\Delta S_{obs}^\circ}{R} \qquad \textbf{2.47}$$

Eq. 2.47 is the van't Hoff equation, and plotting $\ln K_{obs}$ as a function of 1/T will yield a straight line with $slope = -\Delta H_{obs}^\circ/R$ and $intercept = \Delta S_{obs}^\circ/R$. A series of van't Hoff plots corresponding to clustering reactions involving the sequential addition of ammonia to protonated glycine are given in **Figure 2.9**.[64]

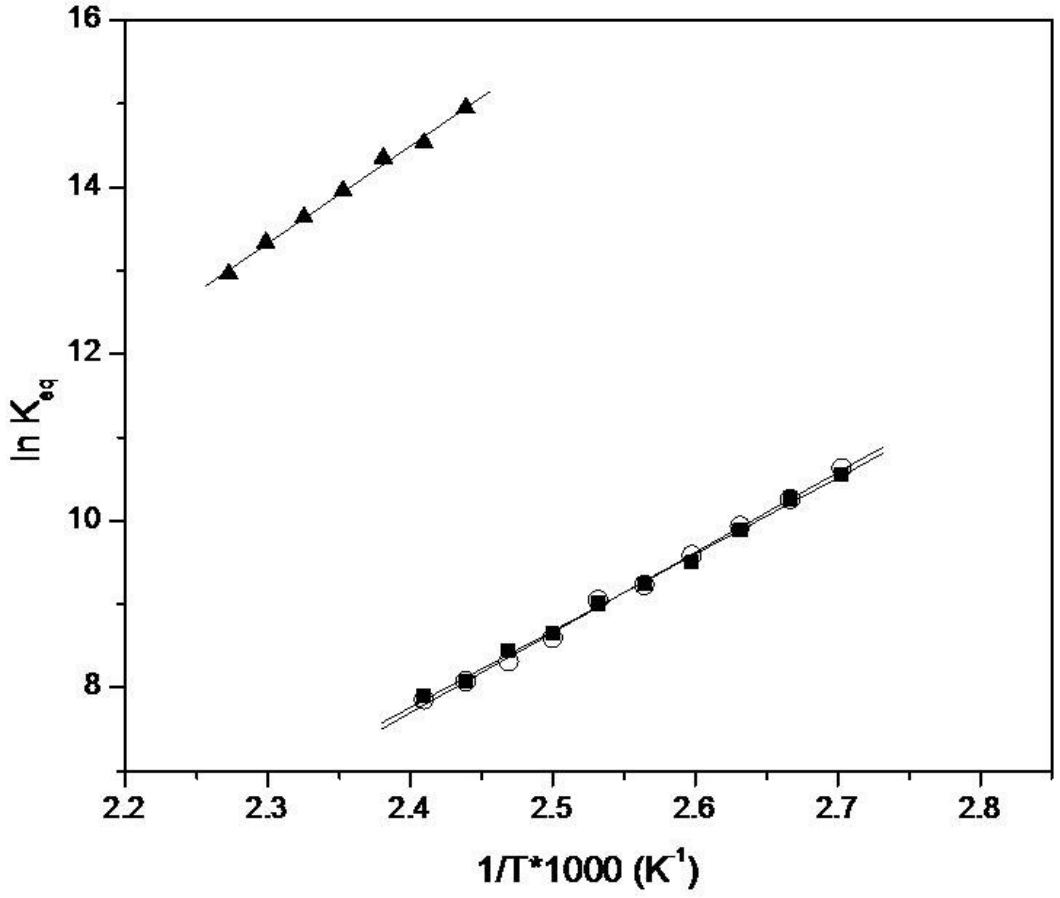

Figure 2.12: Van't Hoff plots for the association reactions: ▲ $GlyH^+ + NH_3 \leftrightarrows Gly(NH_3)H^+$; ■ $Gly(NH_3)H^+ + NH_3 \leftrightarrows Gly(NH_3)_2H^+$; ○ $(Gly)_2H^+ + NH_3 \leftrightarrows (Gly)_2(NH_3)H^+$

The temperature of the reaction is measured precisely by measuring the gas temperature within the reaction chamber, and $\ln K_{obs}$ is deduced from the intensities of the protonated monomer and PBD obtained by the HPMS experiments. A mass spectrometer cannot differentiate between the isomers of PBDs formed and therefore the measured

intensities of the protonated monomer and distribution of PBDs are I_{AH^+} and $I_{A_2H^+}^{obs} = \sum_{i=1}^{n} I_{A_2H^+}^{i}$, respectively. If the most basic scenario is considered, where only one isomer of the PBD (A_2H^+) exists then **Eq. 2.40** is

$$A + AH^+ \rightleftharpoons A_2H^+ \qquad \textbf{2.48}$$

It is not uncommon to have the PBD exist as one isomer if the monomer contains a single heteroatom. Several examples of PBDs that exist as only one isomer are those of H_2O, NH_3, CH_3CN, aliphatic ethers, cyclic ethers and symmetric ketones, however there are many more. The equilibrium constant for the reaction presented by **Eq. 2.40** is

$$K_{obs} = \frac{a_{A_2H^+}}{a_{AH^+}a_A} \qquad \textbf{2.49}$$

where $a_{A_2H^+}$, a_{AH^+} and a_A are the activities of the PBD, protonated monomer and neutral analyte respectively. The activity of a gas is $a_x = P_x/P^\circ$, where P_x is the partial pressure of the species, $P^\circ = 1\ bar$, and **Eq. 2.49** is expressed as

$$K_{obs} = \frac{P_{A_2H^+}P^\circ}{P_{AH^+}P_A} \qquad \textbf{2.50}$$

The partial pressures of the protonated monomer and dimer are directly proportional to their respective number densities as well as their intensities, forming a set of equalities

$$\frac{P_{A_2H^+}}{P_{AH^+}} = \frac{N_{A_2H^+}}{N_{AH^+}} = \frac{I_{A_2H^+}}{I_{AH^+}} \qquad \textbf{2.51}$$

Substituting the ratio of the partial pressures of the ions with the ratio of their intensities yields the working form of the equilibrium constant obtained by an HPMS experiment,

$$K_{obs} = \frac{I_{A_2H^+}P^\circ}{I_{AH^+}P_A} \tag{2.52}$$

The value of K_{obs} is used in **Eq. 2.47** to obtain the thermodynamic quantities, ΔH°_{rxn}, ΔS°_{rxn} and ΔG°_{rxn} for the association reaction given by **Eq. 2.48**.

For the case where multiple isomers of a PBD exist such that they are sufficiently close in Gibbs free energy (< 10 kJ mol^{-1}), a different approach must be taken. Referring back to **Eq. 2.40**, and using analogous reasoning in the derivation of **Eq. 2.53**, K_{obs} is

$$K_{obs} = \prod_{i=1}^{n} P_{A_2H^+{}_i} \left(\frac{P^\circ}{P_{AH^+}P_A}\right)^n \tag{2.53}$$

and then

$$K_{obs} = \prod_{i=1}^{n} \frac{P_{A_2H^+{}_i}}{P_{AH^+}} \left(\frac{P^\circ}{P_A}\right)^n \tag{2.54}$$

Taking the natural logarithm of both sides of **Eq. 2.54** yields

$$\ln K_{obs} = \ln \prod_{i=1}^{n} \frac{P_{A_2H^+{}_i}}{P_{AH^+}} + n \ln\left(\frac{P^\circ}{P_A}\right) \tag{2.55}$$

and using the result of **Eq. 2.51,** then expanding **Eq. 2.55** gives

$$\ln K_{obs} = \sum_{i=1}^{n} \ln \frac{I_{A_2H^+{}_i}}{I_{AH^+}} + n \ln\left(\frac{P^\circ}{P_A}\right) \tag{2.56}$$

The individual PBD intensity components $I_{A_2H^+{}_i}$ are not measured directly, however the observed intensity $I_{A_2H^+}^{obs} = \sum_{i=1}^{n} I_{A_2H^+{}_i}$ is and if a Boltzmann distribution of energies is assumed then

$$\frac{N_{A_2H^+{}_i}}{N_{A_2H^+}^{obs}} = \frac{I_{A_2H^+{}_i}}{I_{A_2H^+}^{obs}} = \frac{e^{-\frac{\Delta G_i^\circ}{RT}}}{e^{-\frac{\Delta G_{obs}^\circ}{RT}}} = e^{\frac{\Delta G_{obs}^\circ - \Delta G_i^\circ}{RT}} \qquad \textbf{2.57}$$

and the components of intensity can now be related to the measured intensity of the PBD by

$$I_{A_2H^+{}_i} = I_{A_2H^+}^{obs} e^{\frac{\Delta G_{obs}^\circ - \Delta G_i^\circ}{RT}} \qquad \textbf{2.58}$$

The important realization is that the values of ΔG_{obs}° and ΔG_i° must be obtained by electronic structure methods, since K_{obs} must already be known to find the experimental value of ΔG_{obs}°. Therefore, the calculated values of ΔG_{obs}° and ΔG_i° will now be referred to as $\Delta G_{obs,c}^\circ$ and $\Delta G_{i,c}^\circ$ and substitution of these new values into **Eq. 2.58**, followed by substitution into **Eq. 2.56** yields

$$\ln K_{obs} = \sum_{i=1}^{n} \ln\left[\left(\frac{I_{A_2H^+}^{obs}}{I_{AH^+}}\right) e^{\frac{\Delta G_{obs,c}^\circ - \Delta G_{i,c}^\circ}{RT}}\right] + n \ln\left(\frac{P^\circ}{P_A}\right) \qquad \textbf{2.59}$$

$$\ln K_{obs} = \sum_{i=1}^{n} \left[\ln\left(\frac{I_{A_2H^+}^{obs}}{I_{AH^+}}\right) + \frac{\Delta G_{obs,c}^\circ - \Delta G_{i,c}^\circ}{RT}\right] + n \ln\left(\frac{P^\circ}{P_A}\right) \qquad \textbf{2.60}$$

$$\ln K_{obs} = \sum_{i=1}^{n} \frac{\Delta G^{\circ}_{obs,c} - \Delta G^{\circ}_{i,c}}{RT} + n \ln\left(\frac{I^{obs}_{A_2H^+}}{I_{AH^+}}\right) + n \ln\left(\frac{P^{\circ}}{P_A}\right) \quad \textbf{2.61}$$

Recall that $\sum_{i=1}^{n} \Delta G^{\circ}_{i,c} = \Delta G^{\circ}_{obs,c}$. Substitution of this relationship into **Eq. 2.61** and rearranging yields the final form of an expression of the observed equilibrium constant where a mixture of PBD isomers of similar energy occurs.

$$\ln K_{obs} = n \ln\left(\frac{I^{obs}_{A_2H^+} P^{\circ}}{I_{AH^+} P_A}\right) + \frac{n-1}{RT} \sum_{i=1}^{n} \Delta G^{\circ}_{i,c} \quad \textbf{2.62}$$

It is easily shown under the condition where only one PBD isomer ($n = 1$) exists that **Eq. 2.52** naturally arises from **Eq. 2.62**. The accuracy of the correction applied by the second term in **Eq. 2.62** is first, heavily weighted on the ability to elucidate and calculate all n-possible minimum energy isomers within a range of Gibbs free energies of 0 to 10 kJ mol^{-1} and second, the reliability of calculations of Gibbs free energies based on the level of theory used.

Chapter 3
Computational Considerations

When coupled with a powerful laser source such as the FEL, the mass spectrometric methods described in the previous chapter can provide detailed information about the nature of IHB formation and other important structural features of gaseous ions, in the form of IRMPD spectrum. Although there is a wealth of information available within a mass-selected IRMPD spectra, it can be very difficult to interpret based solely on chemical intuition. The tools one can use to greatly simplify the characterization of IRMPD spectra come in the form of electronic structure theory calculations. With the extraordinary advancement of computing power over the last several decades, very detailed and accurate calculations of the energetic and spectroscopic properties of gaseous ions and molecules can be obtained. These calculations come in the form of several types *ab initio* and density functional theory (DFT) methods which may be coupled with a seemingly endless choice of basis sets used to model the wave functions of molecular systems. A description of the specific calculation methods and basis sets that were used in the work presented in this thesis will be given. All electronic structure theory calculations were obtained using the *GAUSSIAN 03*[65] software, and visualization of structure, vibrational frequencies, charge distribution and the three-dimensional "construction" of molecular species was provided by *GAUSSVIEW 4.1.2*.[65]

3.1 Quantum Mechanics

3.1.1 The Schrödinger Equation

The objective of predicting the electronic properties of ions and molecules is facilitated by solving either the time-dependent or -independent Schrödinger equation. For calculation of the properties pertaining to the work presented in this thesis, the time-independent Schrödinger equation is required, however it can be obtained directly from the time-dependent Schrödinger equation.[66] The time-dependent Schrödinger equation is given by

$$\hat{H}\boldsymbol{\Psi}(\vec{\mathbf{r}},\mathrm{t}) = -\frac{\hbar}{i}\frac{\partial\boldsymbol{\Psi}(\vec{\mathbf{r}},\mathrm{t})}{\partial\mathrm{t}} \qquad \textbf{3.1}$$

where $\boldsymbol{\Psi}(\vec{\mathbf{r}},\mathrm{t})$ is the molecular wave function that gives the specific quantum state of a molecule as a function of the coordinates, $\vec{\mathbf{r}}$, of all particles in the system at any point in time, t. The symbol, $\hat{H}$, is the Hamiltonian operator for the system and has the form,

$$\hat{H} = \sum_{\mathrm{i}}^{\text{particles}} \frac{\hbar^2}{2\mathrm{m_i}}\nabla_\mathrm{i}^2 + \mathrm{V}(\vec{\mathbf{r}}) \qquad \textbf{3.2}$$

where $\mathrm{m_i}$ is the mass of particle i and $\hbar$ is Planck's constant divided by 2π. The first term in **Eq. 3.2** accounts for the kinetic energy of the electrons and nuclei, and the symbol, ∇_i^2 is the Laplacian operator, commonly referred to as "Del-squared," given by

$$\nabla_\mathrm{i}^2 = \frac{\partial^2}{\partial\mathrm{x_i^2}} + \frac{\partial^2}{\partial\mathrm{y_i^2}} + \frac{\partial^2}{\partial\mathrm{z_i^2}} \qquad \textbf{3.3}$$

$V(\vec{\mathbf{r}})$ is the potential energy arising from the nuclear-nuclear, nuclear-electron and electron-electron interactions and is given by

$$V(\vec{\mathbf{r}}) = \frac{1}{4\pi\epsilon_0}\left[-\sum_{j}^{electrons}\sum_{k}^{nuclei}\left(\frac{Z_k e^2}{\Delta r_{jk}}\right) + \sum_{j}^{electrons}\sum_{l<j}^{electrons}\left(\frac{e^2}{\Delta r_{jl}}\right) + \sum_{k}^{nuclei}\sum_{m<k}^{nuclei}\left(\frac{Z_k Z_m e^2}{\Delta R_{km}}\right)\right] \quad \textbf{3.4}$$

In **Eq. 3.4**, the first term represents the electron-nuclear attraction, the second and third terms are the electron-electron and nuclear-nuclear repulsions, respectively. The value ϵ_0, is the permittivity of a vacuum, e is the proton charge constant, Z_k (or Z_m) is the atomic number of nucleus k (or m), Δr_{jk} is the displacement between electron j and nucleus k, Δr_{jl} is the displacement between electron j and electron l, and finally, ΔR_{km} is the displacement between nucleus k and nucleus m.

In order to obtain the time-independent Schrödinger equation, it must be assumed that the wave function, $\boldsymbol{\Psi}(\vec{\mathbf{r}}, t)$ can be written as a product of spatial and temporal functions such that

$$\boldsymbol{\Psi}(\vec{\mathbf{r}}, t) = \boldsymbol{\Psi}(\vec{\mathbf{r}}) \cdot f(t) \quad \textbf{3.5}$$

If **Eq. 3.5** is operated on by ∇_i^2 and then separately by $\frac{\partial}{\partial t}$ it yields the two relationships

$$\nabla_i^2 \boldsymbol{\Psi}(\vec{\mathbf{r}}, t) = f(t) \cdot \nabla_i^2 \boldsymbol{\Psi}(\vec{\mathbf{r}}) \quad \textbf{3.6}$$

and

$$\frac{\partial \boldsymbol{\Psi}(\vec{\mathbf{r}}, t)}{\partial t} = \boldsymbol{\Psi}(\vec{\mathbf{r}}) \cdot \frac{\partial f(t)}{\partial t} \quad \textbf{3.7}$$

Substituting **Eq. 3.6** and **Eq. 3.7** into **Eq. 3.1**, then separating the variables yields

$$\frac{1}{\boldsymbol{\Psi}(\vec{\mathbf{r}})} \cdot \left[\sum_{\mathrm{i}}^{\text{particles}} \frac{\hbar^2}{2\mathrm{m_i}} \nabla_{\mathrm{i}}^2 \right] \boldsymbol{\Psi}(\vec{\mathbf{r}}) + \mathrm{V}(\vec{\mathbf{r}}) = -\frac{\hbar}{i} \frac{1}{\mathrm{f(t)}} \cdot \frac{\partial\, \mathrm{f(t)}}{\partial \mathrm{t}} \qquad \textbf{3.8}$$

Since the left side of **Eq. 3.8** is independent of time and the right side is independent of position, the overall function must be equal to a constant in order for the equality to hold true.[66] Let the right side of **Eq. 3.8** be equal to E, then

$$\frac{\partial\, \mathrm{f(t)}}{\mathrm{f(t)}} = -\frac{iE}{\hbar} \mathrm{dt} \qquad \textbf{3.9}$$

and integrating **Eq. 3.9** with respect to t gives

$$\ln \mathrm{f(t)} = -\frac{iE\mathrm{t}}{\hbar} + \mathrm{C} \qquad \textbf{3.10}$$

where C is an arbitrary constant of integration. Therefore

$$\mathrm{f(t)} = \mathrm{e}^{\mathrm{C}} \mathrm{e}^{-iE\mathrm{t}/\hbar} = \mathrm{A}\mathrm{e}^{-iE\mathrm{t}/\hbar} \qquad \textbf{3.11}$$

Since A is a constant, it can be included as a factor in $\boldsymbol{\Psi}(\vec{\mathbf{r}})$ that multiplies $\mathrm{f(t)}$ in **Eq. 3.1** and is omitted from **Eq. 3.11** to give the final form of $\mathrm{f(t)}$ as

$$\mathrm{f(t)} = \mathrm{e}^{-iE\mathrm{t}/\hbar} \qquad \textbf{3.12}$$

Finally, if the left side of **Eq. 3.8** is set equal to E, the total energy of the molecule, the time-independent Schrödinger equation is obtained.

$$\left[\sum_{\mathrm{i}}^{\text{particles}} \frac{\hbar^2}{2\mathrm{m_i}} \nabla_{\mathrm{i}}^2 + \mathrm{V}(\vec{\mathbf{r}}) \right] \boldsymbol{\Psi}(\vec{\mathbf{r}}) = E\boldsymbol{\Psi}(\vec{\mathbf{r}}) \qquad \textbf{3.13}$$

$$\hat{H}\boldsymbol{\Psi}(\vec{\mathbf{r}}) = E\boldsymbol{\Psi}(\vec{\mathbf{r}}) \quad \textbf{3.14}$$

3.1.2 The Born-Oppenheimer Approximation

The Born-Oppenheimer approximation is the first of several approximations that are required to perform electronic structure calculations based on simplified solutions to the time-independent Schrödinger equation. The mass of a nucleus is many orders of magnitude larger that of an electron; therefore the Born-Oppenheimer approximation states that the motion of electrons are sufficiently fast such that the nuclei are stationary on the time scale of electronic motion. In this circumstance, the electron distribution is dependent on only the position of the nuclei and not their velocities. It is useful to show the effect of this approximation on the form of the molecular Hamiltonian, as the result is critically important for the calculation of the vibrational spectra of polyatomic molecules.[67] The full molecular Hamiltonian can be expressed in terms of kinetic ($\hat{T}$) and potential (V) energy operators for the nuclei and electrons of the system.

$$\hat{H} = \hat{T}^e(\vec{\boldsymbol{r}}) + \hat{T}^n(\vec{\boldsymbol{R}}) + V^{ne}(\vec{\boldsymbol{R}},\vec{\boldsymbol{r}}) + V^n(\vec{\boldsymbol{R}}) + V^e(\vec{\boldsymbol{r}}) \quad \textbf{3.15}$$

Because the velocities of the nuclei are assumed to be zero relative to the velocities of the electron motion, the nuclear kinetic energy term, $\hat{T}^n(\vec{\boldsymbol{R}})$, is removed from **Eq. 3.15** and the electronic Hamiltonian is simply

$$\hat{H}^e = \hat{T}^e(\vec{\boldsymbol{r}}) + V^{ne}(\vec{\boldsymbol{R}},\vec{\boldsymbol{r}}) + V^n(\vec{\boldsymbol{R}}) + V^e(\vec{\boldsymbol{r}}) \quad \textbf{3.16}$$

The electronic Hamiltonian is then applied to the wave function of electronic motion about a fixed-field of nuclei,

$$\hat{H}^{e}\boldsymbol{\Psi}^{\mathbf{e}}\left(\vec{\boldsymbol{R}},\vec{\boldsymbol{r}}\right) = E_{eff}\left(\vec{\boldsymbol{R}}\right)\boldsymbol{\Psi}^{\mathbf{e}}\left(\vec{\boldsymbol{R}},\vec{\boldsymbol{r}}\right) \qquad \textbf{3.17}$$

where, $E_{eff}\left(\vec{\boldsymbol{R}}\right)$ is the effective nuclear potential, dependent only on the coordinates of the nuclei. The significant result of the Born-Oppenheimer approximation is that $E_{eff}\left(\vec{\boldsymbol{R}}\right)$ is used as the effective potential for the nuclear Hamiltonian (**Eq. 3.18)**, which is applied to the nuclear wave functions responsible for vibrational, rotational and translational states of the molecule. In order to compute the vibrational spectrum of a polyatomic molecule, the solutions of the nuclear Hamiltonian (**Eq. 3.18**) must be obtained.

$$\hat{H}^{n} = \hat{T}^{n}\left(\vec{\boldsymbol{R}}\right) + E_{eff}\left(\vec{\boldsymbol{R}}\right) \qquad \textbf{3.18}$$

3.1.3 The Wave function

The choice of wave function, $\boldsymbol{\Psi}(\vec{\boldsymbol{r}})$ is another factor which greatly determines the accuracy of an electronic structure calculation. There are fundamental requirements of $\boldsymbol{\Psi}(\vec{\boldsymbol{r}})$ in order for the function to be an appropriate solution of the Schrödinger equation. The first requirement for $\boldsymbol{\Psi}(\vec{\boldsymbol{r}})$ is that it be normalized such that the probability be unity over all space.

$$\int_{-\infty}^{+\infty} \boldsymbol{\Psi}(\vec{\boldsymbol{r}})^{\mathbf{2}}\, \mathrm{d}\vec{\boldsymbol{r}} = 1 \qquad \textbf{3.19}$$

A second requirement is the antisymmetry of $\boldsymbol{\Psi}(\vec{\boldsymbol{r}})$ under the exchange of two identical fermions, and due to the classification of electrons as fermions, this is a necessity. The mathematical definition of antisymmetry as applied to $\boldsymbol{\Psi}(\vec{\boldsymbol{r}})$ is

$$\boldsymbol{\Psi}\left(\vec{\boldsymbol{r}}_{1,\ldots}\vec{\boldsymbol{r}}_{a,\ldots}\vec{\boldsymbol{r}}_{b,\ldots}\vec{\boldsymbol{r}}_{N}\right) = -\boldsymbol{\Psi}\left(\vec{\boldsymbol{r}}_{1,\ldots}\vec{\boldsymbol{r}}_{b,\ldots}\vec{\boldsymbol{r}}_{a,\ldots}\vec{\boldsymbol{r}}_{N}\right) \qquad \textbf{3.20}$$

Careful consideration is required for how $\boldsymbol{\Psi}(\vec{\boldsymbol{r}})$ is formed, since it must conform with the criteria described above. A typical way to yield a "well-behaved" wave function is to construct it in the form of a Slater determinant, as shown by **Eq. 3.21**.[67] The closed shell Hartree Fock wave function for a N electron system constructed of N/2 molecular orbitals, is given by

$$\boldsymbol{\Psi}(\vec{\mathbf{r}}) = \frac{1}{\sqrt{\mathrm{N!}}}\begin{vmatrix} \phi_1(\vec{r}_1)\alpha(1) & \phi_1(\vec{r}_1)\beta(1) & \phi_2(\vec{r}_1)\alpha(1) & \phi_2(\vec{r}_1)\beta(1) & \cdots & \phi_{\frac{\mathrm{N}}{2}}(\vec{r}_1)\alpha(1) & \phi_{\frac{\mathrm{N}}{2}}(\vec{r}_1)\beta(1) \\ \phi_1(\vec{r}_2)\alpha(2) & \phi_1(\vec{r}_2)\beta(2) & \phi_2(\vec{r}_2)\alpha(2) & \phi_2(\vec{r}_2)\beta(2) & \cdots & \phi_{\frac{\mathrm{N}}{2}}(\vec{r}_2)\alpha(2) & \phi_{\frac{\mathrm{N}}{2}}(\vec{r}_2)\beta(2) \\ \vdots & \vdots & \vdots & \vdots & \ddots & \vdots & \vdots \\ \phi_1(\vec{r}_a)\alpha(\mathrm{a}) & \phi_1(\vec{r}_a)\beta(\mathrm{a}) & \phi_2(\vec{r}_a)\alpha(\mathrm{a}) & \phi_2(\vec{r}_a)\beta(\mathrm{a}) & \cdots & \phi_{\frac{\mathrm{N}}{2}}(\vec{r}_a)\alpha(\mathrm{a}) & \phi_{\frac{\mathrm{N}}{2}}(\vec{r}_a)\beta(\mathrm{a}) \\ \phi_1(\vec{r}_b)\alpha(\mathrm{b}) & \phi_1(\vec{r}_b)\beta(\mathrm{b}) & \phi_2(\vec{r}_b)\alpha(\mathrm{b}) & \phi_2(\vec{r}_b)\beta(\mathrm{b}) & \cdots & \phi_{\frac{\mathrm{N}}{2}}(\vec{r}_b)\alpha(\mathrm{b}) & \phi_{\frac{\mathrm{N}}{2}}(\vec{r}_b)\beta(\mathrm{b}) \\ \vdots & \vdots & \vdots & \vdots & \ddots & \vdots & \vdots \\ \phi_1(\vec{r}_N)\alpha(\mathrm{N}) & \phi_1(\vec{r}_N)\beta(\mathrm{N}) & \phi_2(\vec{r}_N)\alpha(\mathrm{N}) & \phi_2(\vec{r}_N)\beta(\mathrm{N}) & \cdots & \phi_{\frac{\mathrm{N}}{2}}(\vec{r}_N)\alpha(\mathrm{N}) & \phi_{\frac{\mathrm{N}}{2}}(\vec{r}_N)\beta(\mathrm{N}) \end{vmatrix} \qquad \textbf{3.21}$$

where, $\phi_1(\vec{r}_N)\alpha(\mathrm{N})$ and $\phi_1(\vec{r}_N)\beta(\mathrm{N})$ are an example of the pairs of molecular spin-orbitals of the N$^{\mathrm{th}}$ electron which comprise the matrix elements of the determinantal wave function, $\boldsymbol{\Psi}(\vec{\mathbf{r}})$. The spin-orbitals are orthonormal due to the fact that

$$\int \phi_{\mathrm{a}}^{*}\phi_{\mathrm{a}}\, \mathrm{d}\vec{\boldsymbol{r}} = 1 \qquad \textbf{3.22}$$

and

$$\int \phi_a^* \phi_b \, d\vec{\boldsymbol{r}} = 0 \qquad \textbf{3.23}$$

The purpose of including both α- and β-type spin-orbitals is to account for an electron existing as either spin up $(+1/2)$ or spin down $(-1/2)$ within the orbital. For spin $+1/2$, $\alpha(\mathrm{N}) = 1$ and $\beta(\mathrm{N}) = 0$, and for spin $-1/2$, $\alpha(\mathrm{N}) = 0$ and $\beta(\mathrm{N}) = 1$. Finally, the constant, $\frac{1}{\sqrt{\mathrm{N}!}}$ ensures that $\boldsymbol{\Psi}(\vec{\mathbf{r}})$ is normalized under the condition provided by **Eq. 3.19**.

3.1.4 Basis Sets

The molecular spin-orbitals, which comprise the matrix elements of the determinantal wave function, $\boldsymbol{\Psi}(\vec{\boldsymbol{r}})$ have the form, $\phi(\vec{r})\alpha$ or $\phi(\vec{r})\beta$. When performing electronic structure calculations, the spatial component of the spin-orbital, $\phi(\vec{r})$ is expressed as a linear combination of atomic orbitals (LCAO) shown by **Eq. 3.24**.

$$\phi(\vec{r}) = \sum_{i=1}^{N} a_i \varphi_i \qquad \textbf{3.24}$$

The set of N mathematical functions which approximate the atomic orbitals used to construct $\phi(\vec{r})$ is called the basis set and the functions are referred to as basis functions. In Hartree Fock (HF) theory, the lowest energy approximation attainable is called the "Hartree-Fock limit,"[68] however this requires that $\phi(\vec{r})$ be expressed as a linear combination of an infinite sum of basis functions. In practice, this is obviously an impossible feat, however, the existence of hundreds of predefined basis sets of various size and accuracy can permit a very good approximation to the electronic energy of a molecule. A mathematically efficient way

to construct the basis functions used to form the wave function, is to express them as a normalized Gaussian type orbitals (GTO)[68] in atom-centred Cartesian coordinates of the general form

$$\varphi(x,y,z,i,j,k) = \left(\frac{2\alpha}{\pi}\right)^{3/4} \left[\frac{(8\alpha)^{i+j+k} i!\, j!\, k!}{(2i)!\,(2j)!\,(2k)!}\right]^{1/2} x^i y^j z^k e^{-\alpha(x^2+y^2+z^2)} \qquad \textbf{3.25}$$

where α is an exponent governing the width of the GTO, and i, j and k are non-negative integers that determine the shape (angular momentum function) of the atomic orbital. The number of ways to form the sum of i, j and k will dictate the number of angular momentum functions produced. For example, there is one way to form the sum of all three integers as equal to zero, yielding an s-type GTO of spherical symmetry, as should be expected. There are three ways to produce a value of one by the summation of the integers, and thus, three axially symmetric p-type functions are generated as p_x, p_y and p_z. For d-type orbitals, there are six different ways to combine the summation of the integers to be equal to a value of two, and thus the six Cartesian d-type orbitals, d_{xy}, d_{xz}, d_{yz}, d_{x^2}, d_{y^2} and d_{z^2}. The canonical d-type orbitals, d_{xy}, d_{xz}, d_{yz}, $d_{3z^2-r^2}$ and $d_{x^2-y^2}$, are readily formed by linear combinations of the Cartesian d-type GTOs.[68]

3.2 Electronic Structure Calculations

The previous section gave a very brief background, in selected topics of quantum mechanics, in order to demonstrate the approximations made to solve a simplified form of the time-independent Schrödinger equation. The discussion will now centre on the specific

types of procedures used in the electronic structure calculations performed, as well as the justification of the choices of methodologies and basis sets.

One of the primary applications of electronic structure calculations to the work presented in this thesis is for the calculation of vibrational spectra. Because many of the arguments presented later will be based on the definition of spectral features obtained in a mass-selected IRMPD spectrum, it is useful to have the ability to produce a theoretically obtained IR spectrum of an ion in the gaseous state. The second use of electronic structure calculations is to provide accurate energies of the (sometimes many) constituent isomers that arise as a result of ion-molecule interactions. For example, the mass-selected IRMPD spectrum of protonated caffeine will be presented, and in considering only protonated isomers, there are eight possible isomers of varying energies obtained. A mass spectrometer will isolate all isomers of the same *m/z* ratio, resulting in the complication of the IRMPD spectrum obtained due to the combined spectral characteristics of each isomer appearing in the spectrum. This situation can arise when the difference in Gibbs free energy between the isomers at 298 K, ΔG°_{298} is approximately 10 kJ mol^{-1} or less. At a ΔG°_{298} of 12 kJ mol^{-1}, if a Boltzmann distribution of Gibbs free energies is considered, then the lower energy isomer is favoured by more than 100:1. The Boltzmann distribution describing a unimolecular isomerism between two isomers, A and B, is simply equal to the equilibrium constant for the reaction given by **Eq. 3.26**.

$$A_{(g)} \rightleftharpoons B_{(g)} \qquad \textbf{3.26}$$

If $\Delta G^{\circ}_{298} < 0$, for the forward reaction, then under ideal conditions, the equilibrium constant, K_P is

$$K_P = \frac{P_B}{P_A} = e^{-\frac{\Delta G^{\circ}_{298}}{RT}} \quad \textbf{3.27}$$

where P_B and P_A are the partial pressures of the molecules. Since the ratio of partial pressures (P_B/P_A) is equal to the ratio of the number density (N_B/N_A) of molecules, K_P is directly equal to the Boltzmann equation given by **Eq. 3.28**.

$$\frac{N_B}{N_A} = e^{-\frac{G^{\circ}_{298,B} - G^{\circ}_{298,A}}{RT}} = e^{-\frac{\Delta G^{\circ}_{298}}{RT}} = K_P \quad \textbf{3.28}$$

A Boltzmann distribution of the Gibbs free energy of isomers is normally valid, unless a pair of isomers is separated by a small energy barrier allowing for interconversion by unimolecular isomerism, which is more appropriately described by a kinetic, rather than thermodynamic argument. Another process which causes deviation from a Boltzmann distribution of isomers is the catalysis of isomer interconversion by a secondary ion-molecule interaction. If a Boltzmann distribution of energies exists for a mixture of isomers experimentally, the calculated spectra of the mixed isomers are readily combined based on their relative abundances as determined by **Eq. 3.28**.

3.2.1 Methods: Definitions and Applications

It is necessary to make two decisions prior to performing an electronic structure calculation. First, is the choice of the method used to perform the calculation, referred to as a

"model chemistry,"[67] and second, the type of basis set used to construct the molecular wave function. The methods used in this work consisted exclusively of the *ab initio* method, Møller-Plesset second order perturbation (MP2)[69-71] theory, and the hybrid density functional theory (DFT) method, B3LYP.[72-74] The formulation of the methods introduced above is rigorous, however a brief description of the pertinent equations is given, beginning with a discussion about HF-theory, as it is used as a starting point for MP2 calculations and as a component of B3LYP theory.

3.2.1.1 Hartree Fock Theory

In HF-theory, the molecular orbitals (MOs) used to make up the wave function, $\boldsymbol{\Psi}(\vec{\boldsymbol{r}})$, are individually determined as eigenfunctions of a set of i one-electron operators[68] called the Fock operators given by

$$\widehat{f}_i = -\frac{1}{2}\nabla_{\mathrm{i}}^2 - \sum_{k}^{nuclei} \frac{Z_k}{r_{ik}} + V_i^{HF}\{j\} \qquad \textbf{3.29}$$

The third term $V_i^{HF}\{j\}$ is equal to $2J_i - K_i$, where J_i and K_i are operators used to form the coulomb and exchange integral, J_{ij} and K_{ij}, respectively. The coulomb integral arises due to the repulsion experienced between the pairs of electrons in ϕ_{i} and ϕ_{j}. The exchange integral does not have a classically physical analogue; however it arises due to the choice of a Slater determinantal wave function, and is a consequence of the Pauli principle. The coulomb and exchange integrals[75] are

$$J_{ij} = \iint \phi_i(\vec{r}_1)^* \phi_i(\vec{r}_1) r_{12}^{-1} \phi_j(\vec{r}_2)^* \phi_j(\vec{r}_2)\, d\vec{r}_1 d\vec{r}_2 \quad \textbf{3.30}$$

$$J_{ij} = \iint |\phi_i(\vec{r}_1)|^2 r_{12}^{-1} |\phi_j(\vec{r}_2)|^2 \, d\vec{r}_1 d\vec{r}_2$$

and

$$K_{ij} = \iint \phi_i^*(\vec{r}_1)\, \phi_j(\vec{r}_1) r_{12}^{-1} \phi_j^*(\vec{r}_2) \phi_i(\vec{r}_2) d\vec{r}_1 d\vec{r}_2 \quad \textbf{3.31}$$

The Fock matrix elements are

$$F_{ij} = \left\langle i \left| -\frac{1}{2}\nabla^2 \right| j \right\rangle - \sum_k^{nuclei} Z_k \left\langle i \left| \frac{1}{r_k} \right| j \right\rangle + \sum_{lm} P_{lm} \left[(ij|lm) - \frac{1}{2}(il|jm) \right] \quad \textbf{3.32}$$

where

$$\left\langle i \left| -\frac{1}{2}\nabla^2 \right| j \right\rangle = \int \phi_i^*(\vec{r}_1) \left(-\frac{1}{2}\nabla^2 \phi_j(\vec{r}_1) \right) d\vec{r}_1 \quad \textbf{3.33}$$

and

$$\left\langle i \left| \frac{1}{r_k} \right| j \right\rangle = \int \phi_i^*(\vec{r}_1) \left(\frac{1}{r_k} \phi_j(\vec{r}_1) \right) d\vec{r}_1 \quad \textbf{3.34}$$

The terms $(ij|lm)$ and $(il|jm)$ are a shorthand representation of the coulomb and exchange integrals shown by **Eq. 3.30** and **Eq. 3.31** respectively. The element P_{lm} belongs to the density matrix which establishes the weighting of the individual basis functions in the wave function and has the form

$$P_{lm} = 2 \sum_{i}^{occupied} a_{li} a_{mi} \qquad \textbf{3.35}$$

The factor of two in front of the summation appears as a result of only considering restricted Hartree Fock (RHF) theory, where singlet wave functions are composed of doubly occupied molecular orbitals. The HF-energy is determined by solving a secular equation of N basis functions, in order to find the N roots of E, and has the form

$$\begin{vmatrix} F_{11} - ES_{11} & \cdots & F_{1N} - ES_{1N} \\ \vdots & \ddots & \vdots \\ F_{N1} - ES_{N1} & \cdots & F_{NN} - ES_{NN} \end{vmatrix} = 0 \qquad \textbf{3.36}$$

where S_{11} is an example of a overlap matrix element given by

$$S_{11} = \int \phi_1^*(\vec{\boldsymbol{r}}_1)\phi_1(\vec{\boldsymbol{r}}_1)\, \mathrm{d}\vec{\boldsymbol{r}}_1 \qquad \textbf{3.37}$$

The procedure HF-theory uses to calculate the orbital energies is called the self-consistent field (SCF) method, and is an iterative process. Since the MO-coefficients used to construct the density matrix $\boldsymbol{P}$, are required to initialize the calculation, they are initially estimated and a iteration procedure is employed until the specified convergence criteria is met. A convenient way to describe the HF-SCF optimization procedure is in the form of a flow chart, which is shown in **Figure 3.1**.

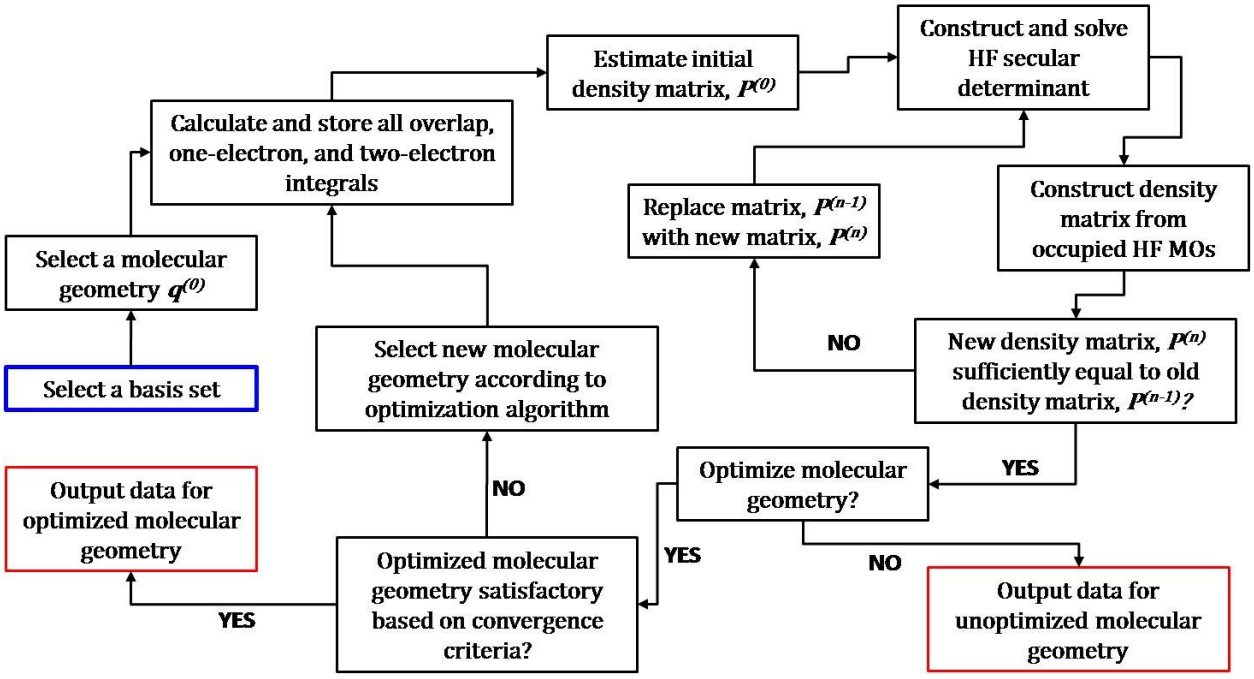

Figure 3.1: The HF-SCF procedure, beginning at the blue box labeled, "Select a basis set." The red box labeled, "Output data for optimized molecular geometry", is the result of a geometry optimization and energy calculation. The red box labeled, "Output data for unoptimized molecular geometry", is the result of an energy calculation only and is referred to as a "single point calculation".[68]

One of the serious shortcomings of the HF-SCF method is the lack of inclusion of electron correlation effects. HF-theory uses the fundamental assumption that an electron experiences the average field of all other electrons and does not include the individual electron-electron interactions (dynamic correlation). Thus, where correlation effects are

important, it will fail to produce chemically accurate energies. The "HF-limit" was defined earlier and it is common to refer to the correlation energy neglected by HF theory as

$$E_{correlation} = E_{exact} - E_{HF} \quad \textbf{3.38}$$

where E_{exact} is the exact electronic energy of the molecular system and E_{HF} is the energy obtained at the HF-limit. It is especially important to consider the long-range correlation and dispersion interactions in hydrogen-bound systems.[76] This is more relevant still, if the system involves aromatic and or conjugated species such as many of the protonated and IHB species presented in this thesis, where the ions are characterized by both factors. The MP2 and B3LYP methods used in the work presented here both include some amount of electron correlation, and will always provide a more accurate electronic energy than HF-theory, albeit the fortuitous cancellation of errors may sometimes favour HF-theory.

3.2.1.2 B3LYP Method

3.2.1.2.1 Optimization of Molecular Structure

In 1965, Kohn and Sham[77] cleverly considered the overall ground-state density of a fictitious system ("uniform electron gas") of non-interacting electrons as a starting point for a real system with the same density, $\rho(\vec{r})$, where electrons do interact. If the densities are the same, then the position and atomic numbers of the fictitious system match that of the real system. The formulation of the operators used in Kohn-Sham (KS) theory is strikingly similar to that of HF-theory, as is the SCF method used to solve the equations and therefore the following discussion will focus on the energy functional corresponding to DFT, and more

specifically for the DFT method, B3LYP. The general form of the DFT energy functional is comprised of several terms dependent on the electron density, $\rho(\vec{r})$, some of which are rather complex functions, and since derivation of them is beyond the scope of this thesis, only a brief mention of each term is provided.[†] The general form of the DFT energy functional is

$$E[\rho(\vec{r})] = T_{ni\ elec}[\rho(\vec{r})] + V_{nuc-ele}[\rho(\vec{r})] + V_{elec-elec}[\rho(\vec{r})] + \Delta T[\rho(\vec{r})] + \Delta V_{elec-elec}[\rho(\vec{r})] \qquad \textbf{3.39}$$

where the terms on the right side of **Eq. 3.39** are, $T_{ni\ elec}[\rho(\vec{r})]$, the kinetic energy of the non-interacting electrons, $V_{nuc-ele}[\rho(\vec{r})]$, the electron-nuclear attraction, $V_{elec-elec}[\rho(\vec{r})]$, the electron-electron repulsion, $\Delta T[\rho(\vec{r})]$, the correction to the kinetic energy for interacting electrons, and, $\Delta V_{elec-elec}[\rho(\vec{r})]$, the quantum mechanical correction to the electron-electron repulsion.

The B3LYP method has become the most popular DFT method to date.[68] It proves to serve more efficiently and accurately in some applications relative to other popular *ab initio* methods, for example, in the ability of B3LYP to reproduce vibrational spectra more reliably than the MP2 method coupled with comparable sized basis sets.[68] In this thesis, all of the vibrational spectra have been produced from the calculated frequencies of ions optimized with the B3LYP method, since in the author's experience, it has generally proved to be much more efficient and accurate at reproducing experimental spectra than that of the MP2 method. However, all single point electronic energies (**Figure 3.1**) presented here used the MP2 method, as it is better at predicting the energies for systems containing hydrogen-bonds, long range and weak dispersive interactions.[76] The B3LYP energy functional has the form

[†] For the exact form of the B3LYP energy density functional, please refer to references 57-59.

$$E_{xc}^{B3LYP} = (1-a)E_x^{LSDA} + aE_x^{HF} + b\Delta E_x^B + (1-c)E_c^{LSDA} + cE_c^{LYP} \quad \textbf{3.40}$$

where E_x^{LSDA} and E_c^{LSDA} are the local spin density functionals related to exchange and correlation, respectively, E_x^{HF} is the HF exchange (**Eq. 3.31**) functional, ΔE_x^B is the Becke 88 generalized gradient approximation (GGA) correlation functional,[73] and E_c^{LYP} is the GGA correlation function al of Lee, Yang and Parr.[74] The three parameters a, b and c are optimized for the B3PW91 method; however they are also used in the B3LYP method and have values of 0.20, 0.72 and 0.81, respectively.

The SCF procedure for solving of the KS MOs is very similar to that of HF theory; however the subtle differences are demonstrated in the flow chart shown in **Figure 3.2**

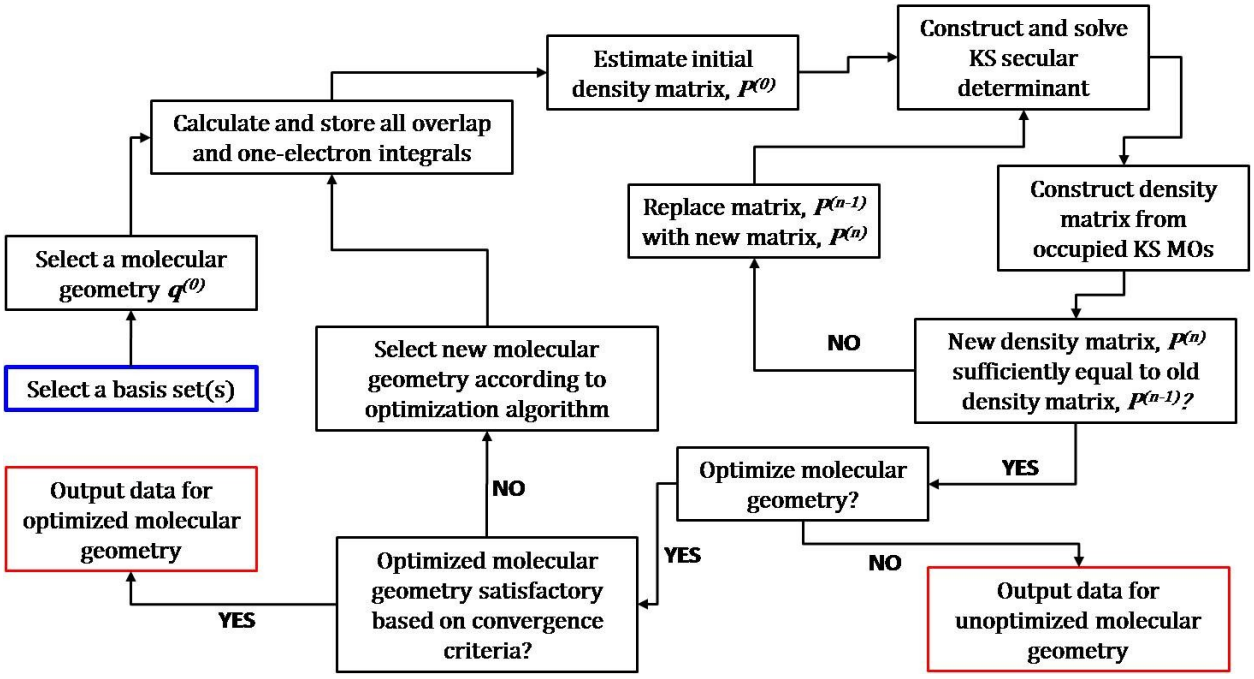

Figure 3.2: A flow chart demonstrating the KS-SCF procedure, beginning at the blue box labeled, "Select basis set(s)." The red box labeled, "Output data for optimized molecular geometry", is the result of a geometry optimization and energy calculation. The red box labeled, "Output data for unoptimized molecular geometry", is the result of an energy calculation only and is referred to as a "single point calculation".[68]

3.2.1.2.2 Vibrational Frequencies

In chapter 5, all structures included in the study of caffeine and theophylline have been optimized using density functional theory (DFT), employing the B3LYP exchange-correlation functional and the 6-311+G(d,p) basis set. B3LYP is known to be a relatively reliable and economical computational method and is extensively employed in the

investigation of small and medium size molecules.[14, 21, 78-81] All harmonic frequencies obtained at this level of theory have been scaled by 0.9679.[82] This is performed in order to compensate for errors arising from the use of a harmonic oscillator approximation in calculating the frequencies, as well as long range electron correlation effects and basis set incompleteness.[83]

The simple harmonic oscillator-approximated Schrödinger equation, in mass-weighted displacement coordinates, $q_{3N-2} = \sqrt{m_N}\Delta x_N$, $q_{3N-1} = \sqrt{m_N}\Delta y_N$ and $q_{3N} = \sqrt{m_N}\Delta z_N$ is

$$\left[-\frac{1}{2}\sum_{i}^{3N}\frac{\partial^2}{\partial q_i^2} + \frac{1}{2!}\sum_{ij}^{3N}\left(\frac{\partial^2 V}{\partial q_i \partial q_j}\right)_{eq} q_i q_j + \cdots\right]\Xi(\mathbf{q}) = E\Xi(\mathbf{q}) \qquad \textbf{3.41}$$

where the first term is the kinetic energy of nuclear motion, the second term is the potential energy function resulting from a Taylor expansion about the equilibrium displacement and $\Xi(\mathbf{q})$ is the nuclear wave function. The value $\left(\partial^2 V/\partial q_i \partial q_j\right)_{eq} = f_{ij}$ is the harmonic force constant and the matrix composed of such elements is called the Hessian (**F**).

A simplified description of how *GAUSSIAN* calculates the harmonic vibrational frequencies will be given. The **F** matrix is diagonalized, producing a set of 3N eigenvectors and eigenvalues. The eigenvectors are the normal modes of nuclear motion, **Q**, which are temporarily discarded, then recalculated once the translational and rotational modes are recognized and separated out. The six normal modes (five for a linear molecule) corresponding to translations and rotations are recognized as the frequencies with values that are essentially zero and removed. The 3N lowest roots of the eigenvalues are the fundamental

frequencies of the molecule and are then converted to cm^{-1} and produced as an output file. After the vibrational frequencies are obtained, it is important to check for the existence of "imaginary" frequencies which are reported as one or more negative frequency value(s). If there are zero imaginary frequencies, then the structure is a minimum on the potential energy surface (PES). If there is one imaginary frequency, then a first-order saddle point has been obtained, also known as a critical configuration or transition state structure. If there are more than one imaginary frequencies present, then the calculated structure has no chemical significance. In this work all structures have been verified as minima by frequency analysis.

It is well established that the harmonic fundamental frequencies determined by *ab* initio and DFT SCF methods over-estimate experimental fundamental frequencies for typical, covalently bound molecules by 8 to 12%. The reasons for such deviations include: 1. basis set incompleteness, 2. electron correlation effects, and 3. anharmonicity.[83] Continuing the expansion of **Eq. 3.41**, an anharmonically-corrected Schrödinger equation of the form

$$\left[-\frac{1}{2}\sum_{i}^{3N}\frac{\partial^2}{\partial q_i^2}+\frac{1}{2!}\sum_{ij}^{3N}\left(\frac{\partial^2 V}{\partial q_i \partial q_j}\right)_{eq} q_i q_j + \frac{1}{3!}\sum_{ij}^{3N}\left(\frac{\partial^3 V}{\partial q_i \partial q_j \partial q_k}\right)_{eq} q_i q_j q_k + \frac{1}{4!}\sum_{ij}^{3N}\left(\frac{\partial^4 V}{\partial q_i \partial q_j \partial q_k \partial q_{lj}}\right)_{eq} q_i q_j q_k q_l + \cdots\right]\Xi(\mathbf{q}) = E\Xi(\mathbf{q}) \qquad \textbf{3.42}$$

is obtained, where the third and fourth order partial derivatives are the anharmonic force constants. It is the calculation of these higher order partial derivatives that cause evaluation of anharmonic frequencies to be substantially more costly than harmonic frequencies. In many cases, the cubic and quartic potentials are treated as a perturbation to the harmonic

oscillator potential.[83] For example, the largest molecule in this thesis, consisting of 13 heavy atoms, required approximately 18 days to obtain the anharmonic frequencies. The same molecule, using the exact same computer hardware and level of theory, required only 45 minutes to produce the harmonic frequencies. Anharmonic frequencies[65, 83, 84], have been obtained at the B3LYP/6-311+G(d,p) level of theory for several of the species considered, however not comprehensively since the calculation of anharmonic frequencies (at the current computing capacity) is very costly and impractical for ions exceeding approximately 15 non-hydrogen atoms. Due to the natural anharmonicity of real vibrations it is always instructive to calculate anharmonic frequencies. It is especially useful here since the quartic potential the anharmonic calculation incorporates is more flexible at describing the shallow and sometimes flattened potential energy wells associated with IHBs. In the work presented in this thesis, it will be shown that the use of calculated anharmonic frequencies greatly improves the fit between the mass-selected IRMPD spectra and the results of theory in all cases. Although the anharmonic calculation is useful for reproducing the frequency range of 1000 to 2000 cm^{-1}, it is important to note that in species containing many low energy vibrations, anharmonic calculations can grossly overestimate the values of such frequencies. This is also true for more rigorous anharmonic treatments such as the vibrational self-consistent field (VSCF) method.[85] The harmonic approximation also calculates low energy vibrations in error, due to treatment of hindered internal rotations as vibrations; however this effect is less significant. The consequence of producing inaccurate low energy vibrations (< 100 cm^{-1}) is that the strong inverse dependence of the vibrational entropy on the values of

the frequencies results in the calculation of unrealistic thermodynamic values. All thermodynamic quantities presented here will be based on the calculated harmonic S°_{298}, H°_{298} and G°_{298} values.

3.2.1.2.3 Thermodynamic Quantities

Once the optimization and frequency analysis of a molecule is performed, the three principal moments of inertia and fundamental vibrational frequencies are obtained. These microscopic values can be used to obtain the macroscopic thermodynamic quantities of S°_{T}, H°_{T} and G°_{T}. This is accomplished using the equations provided by the results of statistical thermodynamics.[86] An overview of how these thermodynamic quantities are obtained will now proceed. If enthalpy is considered first, at temperature, T, then

$$H^{\circ}_{T} = U_{T} + P^{\circ}V \qquad \textbf{3.43}$$

where U°_{T} is the internal energy of the molecule and $P^{\circ}V$ is the pressure-volume work associated with increasing or decreasing the moles of gas in a chemical reaction (with $P^{\circ} = 1\ bar$). Recall that $P^{\circ}V = nRT$ and thus, $H^{\circ}_{T} = U_{T} + nRT$. For one mole of molecules, the expression is further expanded as,

$$U_{T} = E_{trans} + E_{rot} + E_{vib} + E_{elec} \qquad \textbf{3.44}$$

and each of the four terms involving the translational, rotational, vibrational and electronic energy contributions are expanded to give,

$$\frac{U_T}{RT} = \frac{3}{2} + \frac{3}{2} + \sum_{i=1}^{3N-6} \left(\frac{\Theta_{vi}}{2T} + \frac{\Theta_{vi}/T}{e^{\Theta_{vi}/T} - 1} \right) - \frac{D_e}{RT} \qquad \textbf{3.45}$$

The vibrational temperature is defined as $\Theta_{vi} = h\nu_i/k_B$, where ν_i is the i^{th} vibrational frequency, h is Planck`s constant and k_B is the Boltzmann constant. The quantity $-D_e$ is the energy of the ground electronic state, and is the only term in **Eq. 3.45** effected by performing a single point energy calculation, which will be discussed in the next sub-chapter. By observing **Eq. 3.45** it is clear that only the quantities ν_i and $-D_e$, obtained by the optimization and frequency calculations, are required to calculate H_T°. The absolute entropy, S_T°, for one mole of molecules is

$$S_T^\circ = S_{trans} + S_{rot} + S_{vib} + S_{elec} \qquad \textbf{3.46}$$

and each of the four terms involving the translational, rotational, vibrational and electronic entropy contributions are expanded to give,

$$\frac{S_T^\circ}{RT} = ln\left[\frac{2\pi M k_B T}{h^2}\right]^{3/2} \frac{Ve^{5/2}}{N_A} + ln\frac{\pi^{1/2}e^{3/2}}{\sigma}\left(\frac{T^3}{\Theta_A\Theta_B\Theta_C}\right)^{1/2} \qquad \textbf{3.47}$$

$$+ \left[\sum_{i=1}^{3N-6} \frac{\Theta_{vi}/T}{e^{\Theta_{vi}/T} - 1} - ln\left(1 - e^{-\Theta_{vi}/T}\right)\right] - ln\omega_{e1}$$

The rotational temperature is defined as, $\Theta_i = h^2/8\pi^2 I_i k_B$, where I_i is one of the three principal moments of inertia of a symmetric top (where $i = A$, B or C), M is the mass, V is the volume of the system, N_A is Avogadro`s constant, σ is the symmetry number of the molecule and ω_{e1} is the degeneracy of the ground electronic state. The degeneracy of the

ground electronic state is normally equal to one and thus, $S_{elec} = 0$. Observation of **Eq. 3.47** shows that only the quantities v_i , I_i and ω_{e1} obtained by the optimization and frequency calculations, are required to calculate S_T°. With H_T° and S_T° calculated, G_T° easily follows since

$$G_T^\circ = H_T^\circ - TS_T^\circ \quad \textbf{3.48}$$

Therefore, if the general form of an ion-molecule association reaction is considered,

$$\mathrm{A_{(g)} + BH^+{}_{(g)} \rightleftharpoons (AB)H^+{}_{(g)}} \quad \textbf{3.49}$$

then the change in enthalpy for the reaction (298 K) shown by **Eq. 3.49** is

$$\Delta H_{rxn,298}^\circ = H_{(AB)H^+,298}^\circ - \left[H_{A,298}^\circ + H_{BH^+,298}^\circ\right] \quad \textbf{3.50}$$

$$\Delta H_{rxn,298}^\circ = \left(U_{(AB)H^+,298}^\circ + RT\right) - \left[\left(U_{A,298}^\circ + RT\right) + \left(U_{BH^+,298}^\circ + RT\right)\right]$$

$$\Delta H_{rxn,298}^\circ = \Delta U_{rxn,298}^\circ - RT$$

The change in entropy (298 K) for the reaction shown by **Eq. 3.49** is simply

$$\Delta S_{rxn,298}^\circ = S_{(AB)H^+,298}^\circ - \left[S_{A,298}^\circ + S_{BH^+,298}^\circ\right] \quad \textbf{3.51}$$

and finally, the change in Gibbs free energy (298 K) is

$$\Delta G_{rxn,298}^\circ = \Delta H_{rxn,298}^\circ - T\Delta S_{rxn,298}^\circ \quad \textbf{3.52}$$

3.2.1.2.4 Choice of Basis Sets for Optimization and Frequency Calculations

The majority of B3LYP optimizations and frequency calculations have been performed using the 6-311+G(d,p) basis set[87], as it was optimized with methods that include electron

correlation. The reasonable size of this basis set made it well suited for the optimization of all of the largest molecules presented in this thesis. An explanation of the notation and the basis set functions is as follows: the 6-311+G(d,p) basis set is a triple-zeta, split-valence basis set, meaning that the valence orbitals of the electrons are separated into three regions defined by a specific number of sp-type orbitals describing the inner, central and outer regions of the valence electron orbitals. Each orbital has a "zeta" exponent responsible for governing its size, and hence where the term, "triple-zeta" is derived. The "6" represents that six s-type Gaussian functions are used to describe the heavy atom core electron orbitals. The "-" defines the basis set as split-valence, and the "311" represents that three, one and one sp-type functions are used to define the inner, central and outer regions of heavy atom valence electron orbitals, respectively. The "+" corresponds to the placement of one set of diffuse sp-type functions on heavy atoms, adding flexibility to the orbital size and more appropriately describing long-range interactions, such as hydrogen-bonding. The "(d,p)" represents placement of one set of d-type polarization functions on heavy atoms and one set of p-type functions on hydrogen atoms. The addition of polarization functions can be thought of as a form of "hybridization", since it allows for an increase in the spatial flexibility of forming MOs by adding contributions from higher order angular momentum functions. Calculation of the system energy determines the weighting of such contributions to the overall wave function. For hydrogen atoms, there are a set of three core s-type and two valence s-type functions, in addition to the set of p-type polarization functions.

3.2.1.3 MP2 Method

3.2.1.3.1 Single Point Energies

Once a molecular structure is optimized, a frequency calculation should follow in order to check for the existence of imaginary frequencies. If there are no imaginary frequencies, the electronic energy, $E_{elec} = -D_e$ (**Eq. 3.44**) can be recalculated at a higher level of theory using the equilibrium geometry provided by the optimization, and is referred to as a single point calculation. This is shown within the box stating, "output data for unoptimized molecular geometry", in the flow charts provided by **Figures 3.1** and **3.2**. A single point calculation is based on the energy of electron motion about a fixed field of nuclei and is less resource demanding than an optimization or frequency calculation, therefore higher level methods incorporating electron correlation effects and larger basis sets can be prescribed. The majority of single point energies presented in this thesis have been calculated with an *ab initio* method incorporating electron correlation effects, specifically the MP2 method.[69-71] The MP2 method[88] begins by considering a small perturbation to the HF Hamiltonian,

$$\hat{H} = \hat{H}_0 + \lambda\hat{V} \qquad \textbf{3.53}$$

where $\hat{H}_0$ is the HF Hamiltonian and $\hat{V}$ is a small perturbation scaled by a dimensionless parameter, λ. If an expansion is made to the exact HF-wave function, Ψ_0 and energy, $E^{(0)}$ then

$$E = E^{(0)} + \lambda E^{(1)} + \lambda^2 E^{(2)} + \lambda^3 E^{(3)} + \cdots \qquad \textbf{3.54}$$

and

$$\Psi = \Psi_0 + \lambda\Psi^{(1)} + \lambda^2\Psi^{(2)} + \lambda^3\Psi^{(3)} + \cdots \quad \textbf{3.55}$$

Substitution of **Eq. 3.54** and **Eq. 3.55** into the Schrödinger equation and gathering the terms in λ^n gives

$$\hat{H}_0\Psi_0 = E^{(0)}\Psi_0 \quad \textbf{3.56}$$

$$\hat{H}_0\Psi^{(1)} + \hat{V}\Psi_0 = E^{(0)}\Psi^{(1)} + E^{(1)}\Psi^{(1)} \quad \textbf{3.57}$$

$$\hat{H}_0\Psi^{(2)} + \hat{V}\Psi^{(1)} = E^{(0)}\Psi^{(2)} + E^{(1)}\Psi^{(1)} + E^{(2)}\Psi_0 \quad \textbf{3.58}$$

$$\vdots$$

By multiplying **Eq. 3.56** through **Eq. 3.58** from the left side by Ψ_0 and integrating over all space, the expression for the nth-order MPn energy is obtained such that,

$$E^{(0)} = \int \cdots \int \Psi_0\hat{H}_0\Psi_0 \, d\tau_1 d\tau_1 \cdots d\tau_n \quad \textbf{3.59}$$

$$E^{(1)} = \int \cdots \int \Psi_0\hat{V}\Psi_0 \, d\tau_1 d\tau_1 \cdots d\tau_n \quad \textbf{3.60}$$

$$E^{(2)} = \int \cdots \int \Psi_0 \hat{H}_0 \Psi^{(1)} \, d\tau_1 d\tau_1 \cdots d\tau_n \qquad \textbf{3.61}$$

$$\vdots$$

It is important to realize that the sum of the MP0 and MP1 energies is the HF-energy

$$E^{HF} = E^{(0)} + E^{(1)} = \int \cdots \int \Psi_0 \left(\hat{H}_0 + \hat{V}\right) \Psi^{(1)} \, d\tau_1 d\tau_1 \cdots d\tau_n \qquad \textbf{3.62}$$

The MP2-energy is obtained by adding the value of the correction, $E^{(2)}$ to the HF-energy, giving the working form of $E^{(2)}$ as

$$E^{(2)} = \sum_{a<b}^{occupied} \sum \sum_{r<s}^{virtual} \sum \frac{[(ab|rs) - (as|br)]^2}{(\epsilon_a + \epsilon_b + \epsilon_r + \epsilon_s)} \qquad \textbf{3.63}$$

with

$$(ab|rs) = \iint \phi_a{}^*(\vec{\boldsymbol{r}}_1)\, \phi_r(\vec{\boldsymbol{r}}_1) r_{12}^{-1} \phi_b{}^*(\vec{\boldsymbol{r}}_2) \phi_s(\vec{\boldsymbol{r}}_2) \mathrm{d}\vec{\boldsymbol{r}}_1 \mathrm{d}\vec{\boldsymbol{r}}_2 \qquad \textbf{3.64}$$

Inclusion of the virtual (unoccupied) orbitals, r and s permits excitations to be considered which are neglected by HF-theory. The integral $(ab|rs)$ is obtained from a transformation of the coulomb integral, $(ij|lm)$, shown in the discussion of HF-theory and is

$$(ab|rs) = \sum_{i}^{spin-orbitals} \sum_{j} \sum_{l} \sum_{m} c_{ia} c_{jb} c_{lr} c_{ms} (ij|lm) \qquad \textbf{3.65}$$

As stated earlier, the MP2 energy is expressed as

$$E^{MP2} = E^{(0)} + E^{(1)} + E^{(2)} = E^{HF} + E^{(2)} \quad \textbf{3.66}$$

The MP2 approximation will always yield a more accurate ground state electronic energy, $E^{MP2} = E_{elec} = -D_e$ than HF-theory, due to the inclusion of electron correlation effects.

3.2.1.3.2 Choice of Basis Sets for Single Point Energy Calculations

The Pople-style basis sets 6-311+G(d,p)[87] and 6-311+G(2d,2p)[87] have been used in conjunction with the MP2 method to provide single point calculations for several of the systems described in this thesis. The definition of the notation for these basis sets has been provided earlier. In the work[20] presented in chapter 4, the MP2(full)/6-31G(d)[89] level of theory was used to optimize the structures of all ions and a brief explanation of the history behind this choice follows.

The study presented in the next chapter was performed at a time when so-called "compound method" techniques were a popular choice for providing accurate energies for small molecular systems. One example of such techniques is the G3(MP2) method[90] by Curtiss and coworkers, which performs systematic corrections to the electronic energy using high levels of theory (i.e. QCISD(T)/6-31G(d)) and with very large basis sets (i.e. MP2/6-311++G(3d2f,2df,2p)). In G3(MP2) theory, single point energy corrections are applied to a structure optimized at the MP2(full)/6-31G(d) level of theory, where "(full)" refers to inclusion of the correlation of core electrons. The author was interested in providing a G3(MP2)-defined potential energy surface (PES), to aid in deducing the mechanism associated with a complex series of bimolecular ion-molecule reactions.[20] To reduce the cost of performing G3(MP2) calculations, all structures were pre-optimized at the

MP2(full)/6-31G(d) level of theory, as they would have received in the G3(MP2) procedure. However, many of the larger systems in the study were found to be too costly for G3(MP2) calculations, and as an alternative, the MP2(full)/6-311+(d,p) level of theory was used to perform single point calculations. Due to the complex nature of the PESs obtained at the MP2(full)/6-31G(d) level of theory, the structures were not optimized using an alternative method, and the optimized structures proved more than adequate as a foundation for high-accuracy single point calculations. It should be stated however, that all of the calculated vibrational spectra shown in chapter 4, have been obtained using the B3LYP/6-31+G(d,p) level of theory due to its ability to reproduce mass-selected IRMPD spectra more efficiently and accurately than MP2.[68]

A large portion of this thesis will incorporate the use of single point calculations at the MP2/aug-cc-pVXZ level of theory, where aug-cc-pVXZ is the nomenclature of the family of correlation consistent, polarized valence, X-zeta basis sets, augmented with diffuse functions on all atoms,[76, 91-94] where "X" is equal to T or Q for triple and quadruple-zeta basis sets, respectively. The basis sets described here exist from the double to sextuple-zeta level of quality. The two versions of this basis set used in many of the studies presented in chapters 4 and 5 are aug-cc-pVTZ and aug-cc-pVQZ and a brief description of the characteristics of these basis sets is now provided. The aug-cc-pVTZ basis set places three sets of s-type, two sets of p-type and one set of d-type functions on hydrogen atoms, as well as, four sets of s-type, three sets of p-type, two sets of d-type functions and one set of f-type functions on all of the heavy atoms from Boron to Neon. The "aug" prefix adds an additional set of diffuse

functions to each of the polarizations listed above, for both light and heavy atoms. The aug-cc-pVQZ basis set places four sets of s-type, three sets of p-type, two sets of d-type and one set of f-type functions on hydrogen atoms, as well as, five sets of s-type, four sets of p-type, three sets of d-type functions, two sets of f-type and one set of g-type functions on all of the heavy atoms from Boron to Neon. This basis set is also augmented with diffuse functions on all atoms. The large degree of spatial flexibility provided by correlation consistent basis sets due to the inclusion of several sets of higher order angular momentum functions, as well as their optimization for use with correlated methods such as MP2, permits for the calculation of single point energies of a high degree of accuracy.

One final consideration to make before proceeding to the chapters involving experimental work, is regarding the notation used for electronic structure calculations. For example, MP2/aug-cc-pVTZ//B3LYP/6-311+G(d,p) represents that a single point energy calculation was provided using the MP2 method with the aug-cc-pVTZ basis set, and optimization and frequency calculation was provided using the B3LYP method and 6-311+(d,p) basis set.

3.3 RRKM Calculations

In the circumstance where ion-molecule reactions occur in a low pressure environment (10^{-9} to 10^{-11} Torr) the products formed will not experience a significant number of stabilizing collisions within their reactive lifetime. Ineffective stabilization of a product ion or molecule, will cause it to have an excess of internal energy sufficiently high to cross a transition state barrier resulting in unimolecular dissociation or isomerism. If an ion

possesses a sufficient amount of excess internal energy, it may also be able to proceed through more than one transition state, with each different reaction channel yielding a unique product distribution. The relative product distribution between each reaction channel is found by comparing the values obtained for a set of energy-dependent rate constants, $k(E)$, where each is proportional to the rate at which an energized ion passes through each possible transition state. Consider the mechanism for the following unimolecular process leading to the dissociation, or isomerism of energized molecule A^*

$$A^* \xrightarrow{k(E)} A^\dagger \longrightarrow \text{products} \qquad \textbf{3.67}$$

where $A^\dagger$ is the transition state and $k(E)$ is the microcanonical transition state theory rate constant which is a function of the energy content (E) of A^*.

Values of $k(E)$ are obtained from **Eq. 3.68**, a simplified result of RRKM theory,[32-36] employing the use of microscopic quantities for A^* and $A^\dagger$ obtained through electronic structure calculations such as the zero point vibrational energies, vibrational frequencies and moments of inertia. The derivation of RRKM theory is beyond the scope of this thesis; however the important features of the theory, as applied to the study presented in chapter 4, will be described.

$$k(E) = \frac{1}{h}\frac{G(E^\dagger)}{\rho(E_v)} \qquad \textbf{3.68}$$

The values $G(E^\dagger)$ and $\rho(E_v)$ are the sum and density of all active quantum states of $A^\dagger$ and A^* in an energy range of 0 to $E^\dagger$ and 0 to E_v, respectively. In this context the term, "active"

refers to vibrational states of the harmonic oscillator coupled through an IVR-type process allowing for the randomization of energy through vibrational modes. External rotations are treated as adiabatic transitions. In order to describe the sum of states, $G(\varepsilon)$, an example will be given. Consider a hypothetical system consisting of the two vibrational modes, $v_1 = 1\ \mathrm{cm}^{-1}$ and $v_2 = 5\ \mathrm{cm}^{-1}$. The sum of states is the sum of all possible energy configurations of the oscillators from 0 to the total energy, ε. For a total energy $\varepsilon = 7\ \mathrm{cm}^{-1}$, then $G(7) = 11$. This is best illustrated by **Table 3-1**.

Table 3-1: The sum of states $G(7) = 11$ is found by adding up all of the unique energy configurations involving the oscillators $v_1 = 1\ \mathrm{cm}^{-1}$ and $v_2 = 5\ \mathrm{cm}^{-1}$ in the energy range of 0 to 7 cm^{-1}.

Mode	**ε / cm^{-1}**	**0**	**1**	**2**	**3**	**4**	**5**	**6**	**7**
	number of quanta								
$\boldsymbol{v_1}$		0	1	2	3	4	5	6	7
$\boldsymbol{v_2}$		0	0	0	0	0	0	0	0
$\boldsymbol{v_1}$							0	1	2
$\boldsymbol{v_2}$							1	1	1

The value of $G(\varepsilon)$ becomes large very rapidly with ε, for example, for $v_1 = 1\ \mathrm{cm}^{-1}$ and $v_2 = 5\ \mathrm{cm}^{-1}$, $G(100) \approx 10^3$, $G(1000) \approx 10^5$ and $G(10000) \approx 10^7$. The density of states, $\rho(\varepsilon)$ also increases rapidly with ε and is related to $G(\varepsilon)$ by

$$\rho(\varepsilon) = \frac{dG(\varepsilon)}{d\varepsilon} \qquad \textbf{3.69}$$

Although there are very good approximations for calculating $G(\varepsilon)$ and $\rho(\varepsilon)$,[95] the most accurate method is by a direct count of the state configurations. This was shown for a trivial case in **Table 3-1**; however, it is obvious that calculation of $G(\varepsilon)$ and $\rho(\varepsilon)$ must be completed by a computer algorithm due to the magnitudes of real values being on the order of 10^{10} to 10^{25}. Such an algorithm was developed by Beyer and Swinehart and is useful for calculating the number of ways to make change from 0 to \$1.00 using pennies, nickels, dimes, etc.., but more importantly here, for calculating the values of $G(\varepsilon)$ and $\rho(\varepsilon)$ exactly.[96] The Beyer-Swinehart algorithm was used in conjunction with the visual mathematics software Mathcad 14.0, in order to calculate values of $k(E)$ for the work presented the next chapter. The annotated Mathcad 14.0 worksheets are included in Appendix A.

In **Eq. 3.68**, the energy values $E^{\dagger}$ and E_v are

$$E^{\dagger} = E - E_0 - E_r^{\dagger} \qquad \textbf{3.70}$$

and

$$E_v = E - E_r \qquad \textbf{3.71}$$

A schematic representation is very useful for interpretation of **Eq. 3.70** and **Eq. 3.71** and is provided by **Figure 3.3**.

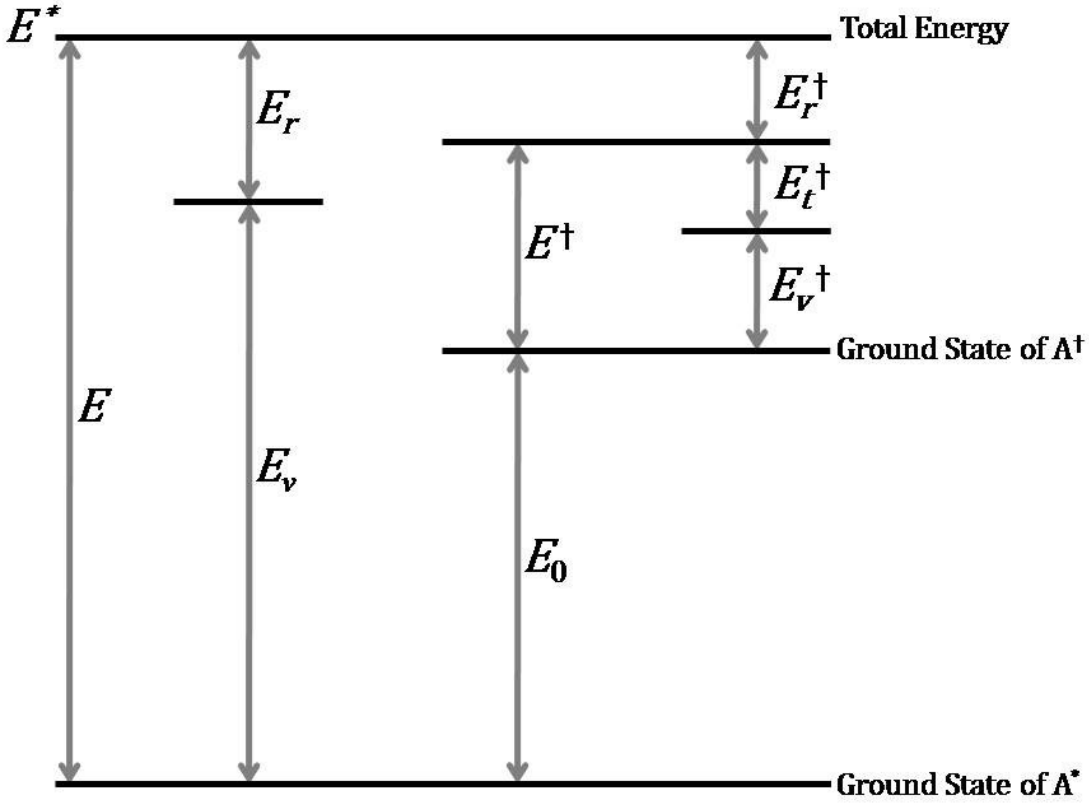

Figure 3.3: Schematic representation of energy levels associated with RRKM theory.[97] The values of E, E_v, and E_r are the total, vibrational and rotational energies of A*, respectively. The values of $E^\dagger$, $E_v^\dagger$, $E_t^\dagger$ and $E_r^\dagger$ are the total, vibrational, translational and rotational energies of A†, respectively. E_0 is the difference in energy between the ground states of A† and A*.

Chapter 4

A Mechanism for the Formation of the Proton-Bound Dimer of Water by Sequential Bimolecular Reactions Involving 1,1,3,3-Tetrafluorodimethyl Ether

4.1 Introduction

There has been a considerable effort in probing the gas phase structure of the PBD of water as well as other symmetric and asymmetric protonated dimers of small molecules using mass-selected IRMPD spectroscopy.[7, 98-100] This has been accomplished by mating either an FT-ICR MS[7, 99, 100] or QIT MS to a tunable, infrared light source of high intensity, such as a FEL. In an FT-ICR cell, the pressure is typically between 10^{-10} to 10^{-8} Torr and under these low pressure conditions, it is difficult to produce weakly bound cluster ions, such as the PBD of water (**Eq. 4.1**) *via* direct ion-molecule association reactions, since there are very few collisions available during the lifetime of the collision complex to remove sufficient internal energy to stabilize the complex.

$$H_2O + H_3O^+ \longrightarrow H_5O_2^+ \qquad \textbf{4.1}$$

Some years ago, Clair and McMahon devised an elegant technique for the efficient production of $H_5O_2^+$ within the low pressure confines of the FT-ICR cell.[101] This method involved the addition of 1,1,3,3-tetrafluorodimethyl ether (TFDE) in the presence of water vapour directly into the FT-ICR cell. $H_5O_2^+$ is the dominant ionic species rapidly formed as the terminal ion-molecule reaction product. Electron impact (70 eV) on TFDE results almost

exclusively in the formation of difluoromethyl cation at m/z 51, the result of cleavage of the C—O bond in the TFDE radical cation. This electrophilic species reacts quickly with TFDE by fluoride abstraction and elimination of fluoroform to yield an ion of *m/z* 99 which does not react further with TFDE (**Eq. 4.2**).

$$CF_2H^+ + (CF_2H)_2O \longrightarrow C_2F_3H_2O^+ + CF_3H \qquad \textbf{4.2}$$

Addition of water to the ICR cell in which *m/z* 99 was the dominant ion resulted in facile formation of $H_5O_2^+$. A mechanism for the formation of $H_5O_2^+$ was proposed in the work of Clair and McMahon[101] in which it was suggested that *m/z* 99 undergoes S_N2 attack by water to form protonated difluoromethanol and formyl fluoride. Protonated difluoromethanol and water were then suggested to form a nascent PBD which eliminates difluorocarbene to generate $H_5O_2^+$ (**Scheme 1**).[101]

A second mechanism was proposed in which it was presumed that *m/z* 99 had the structure of a PBD between difluorocarbene and formyl fluoride. Water then displaces formyl fluoride, producing a PBD of water and difluorocarbene which then undergoes displacement of difluorocarbene by a second water molecule to yield $H_5O_2^+$ (**Scheme 2**).[101] This second mechanism was proposed to account for the rapid production of $H_5O_2^+$, since it involves a series of exchange reactions where H_2O acts as a stronger base that can displace both formyl fluoride and difluorocarbene. These reactions involving H_2O to form PBDs are then presumed to each occur at or near the collision rate.[102]

Scheme 1

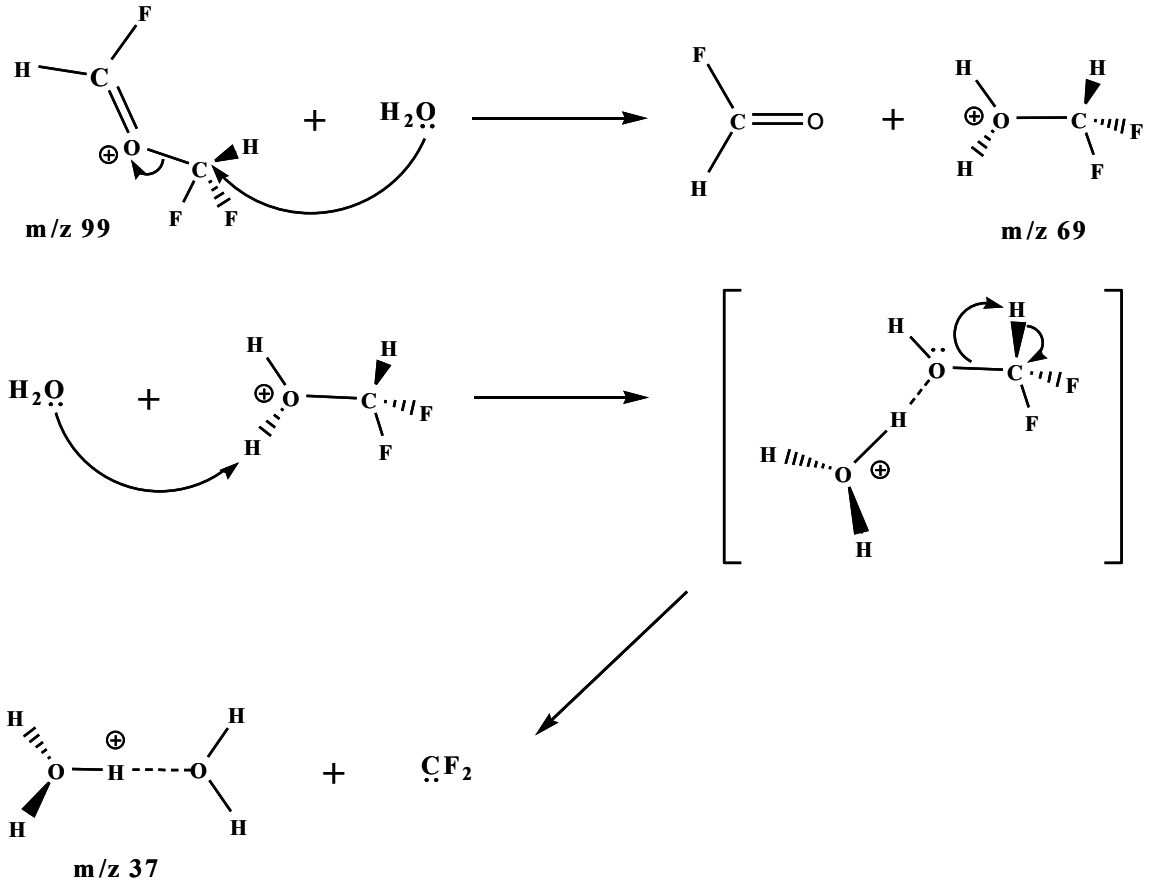

A third mechanism was also proposed which was not initiated by the *m/z* 99 ion, but rather a hydronium ion reacting with TFDE to produce the PBD of formyl fluoride and water with elimination of fluoroform. A second water molecule then displaces formyl fluoride to form $H_5O_2^+$ (**Scheme 3**).[101]

Scheme 2

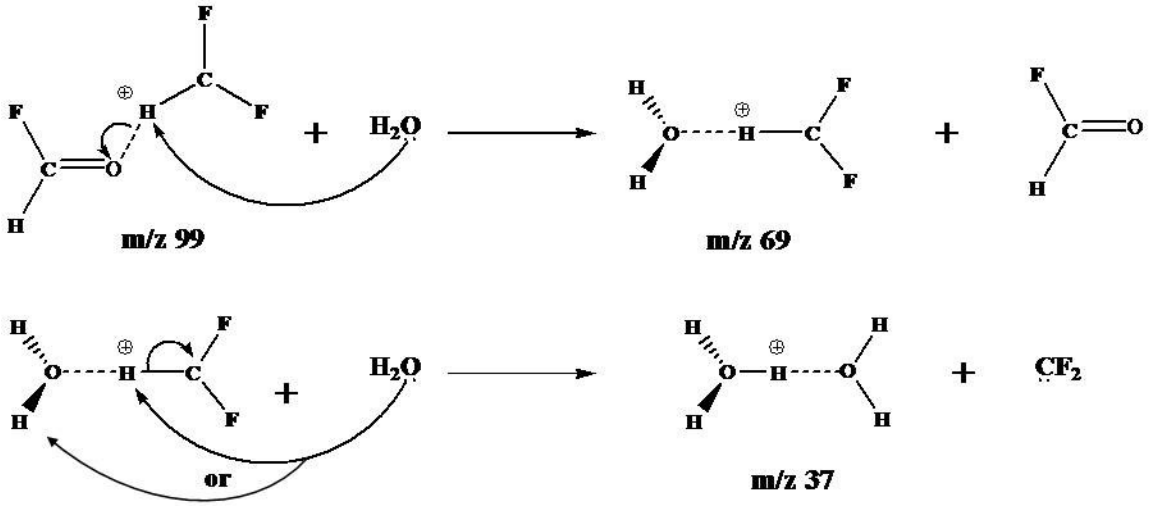

Scheme 3

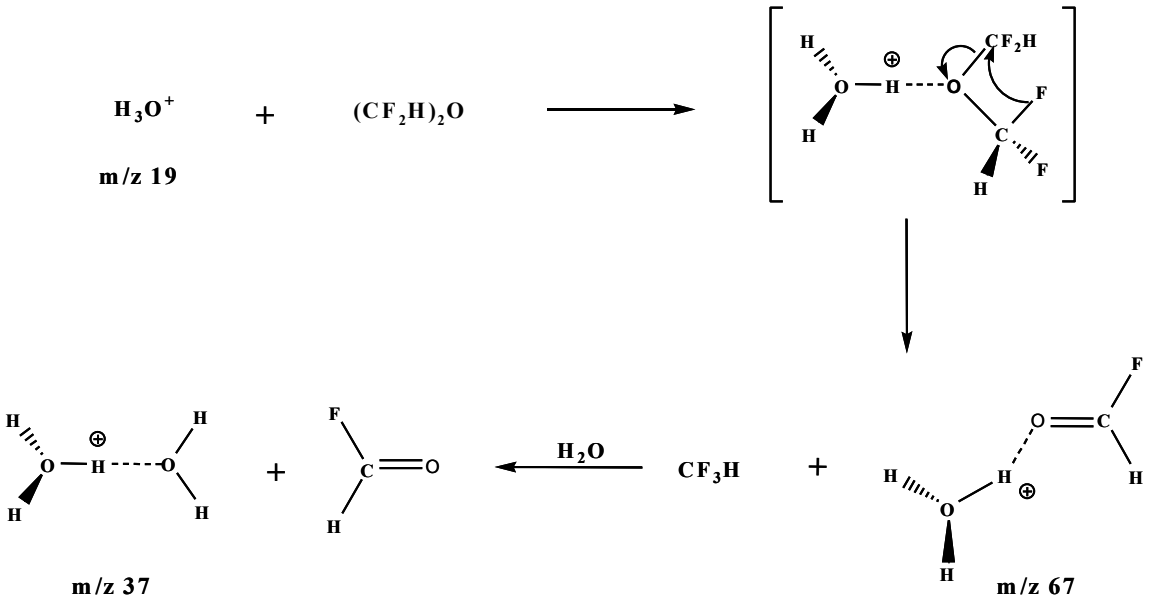

The schemes proposed by Clair and McMahon were based on evolution of ion intensities as a function of reaction time obtained using conventional trapped-ion cyclotron resonance experiments. At the time of that work, the limited capabilities of the instrumentation did not allow for ion ejection to permit single-species ion isolation to be performed. The consequence of this inability to isolate a single ion of interest was that all possible ion-molecule reaction sequences occurred simultaneously. Therefore several mechanistic arguments could be made in order to describe the observed time-intensity profiles. A further aid that was not readily available at that time was that of electronic structure calculations and high performance computing capabilities.

The present study incorporates the use of FT-ICR kinetics experiments, mass-selected IRMPD spectroscopy, electronic structure and RRKM calculations to better understand the novel ion-chemistry leading to bimolecular production of PBDs.

The application of the method using TFDE to efficiently generate $H_5O_2^+$ has been extrapolated to yield several examples of homogeneous and heterogeneous PBDs formed within an FT-ICR apparatus designed specifically for IRMPD spectroscopy, with the objective of structural characterization.[7, 99, 100]

4.2 Experimental

4.2.1 FT-ICR MS: Kinetic Studies

Experiments involving kinetic measurements have been performed using a Spectrospin CMS 47 FT-ICR MS, equipped with a 4.7 T, 150 mm horizontal bore superconducting magnet.

Kinetics of bimolecular ion-molecule reactions are readily amenable to investigation with an FT-ICR experiment (**Eq. 4.3**).

$$A^+ + B \xrightarrow{k_2} C^+ + D \qquad \textbf{4.3}$$

The partial pressure of the neutral reactant molecule is carefully maintained constant *via* a molecular leak valve. If the number density of the neutral (N_B) is held constant, then **Eq. 4.3** may be expressed as a pseudo-first order kinetic process with $k_{obs} = k_2 N_B$ (**Eq. 4.4**) , where N_B is the number density of neutral reactant molecules, B.

$$A^+ \xrightarrow{k_{obs}} C^+ + D \qquad \textbf{4.4}$$

If the ion A^+ reacts *via* a pseudo-first order kinetic process, then the differential equation for the instantaneous rate of change of the concentration of A^+ with respect to time is given by **Eq. 4.5** as

$$-\frac{d[A^+]}{dt} = k_{obs}[A^+] \qquad \textbf{4.5}$$

Eq. 4.5 can then be integrated to yield **Eq. 4.6**.

$$\ln[A^+] = -k_{obs}\,t \qquad \textbf{4.6}$$

In this study, the quantity $[A^+]$ is the normalized ion intensity of A^+. A plot of $\ln[A^+]$ versus t will yield a straight line with negative slope equal to the observed pseudo-first order rate constant (k_{obs} / s^{-1}). The bimolecular rate constant (k_2 / cm^3 $molecule^{-1}$ s^{-1}) associated with **Eq. 4.3** can then also be obtained as shown by **Eq. 4.7**.

$$k_2 = \frac{k_{obs}}{N_B} \qquad \textbf{4.7}$$

The pressure of water reported here has been corrected for the sensitivity of the calibrated ionization gauge.

4.2.2 Mass-Selected IRMPD Spectroscopy: Structural Elucidation

All IRMPD experiments were conducted at the Centre Laser Infrarouge d'Orsay (CLIO),[103-106] which houses a FEL to which a Mobile Ion Cyclotron Resonance Analyzer (MICRA)[107] has been mated. IRMPD efficiency spectra are obtained by observing IRMPD of an ion of interest and all photoproducts of IRMPD as a function of radiation wavelength. The FEL wavelength was stepped in increments of ~ 5 cm^{-1} and the laser bandwidth is 0.3-0.5 % of the spectral wavelength. Ions were irradiated for 2 seconds. The laser wavelength and bandwidth are monitored *via* a monochromator associated with a spiricon multichannel detector. The ions were prepared directly within the ICR cell by electron-impact on 1,1,3,3-tetrafluorodimethyl ether which was pulsed into the cell and then allowed to react with water vapour which was also subsequently pulsed into the ICR cell.

4.3 Theoretical Calculations

4.3.1 Electronic Structure Calculations

Geometry optimization of all reactant and product species have been performed at the MP2(full)/6-31G(d) level of theory. In order to obtain the enthalpies and thermal corrections required to calculate Gibbs free energy changes of reaction, harmonic frequencies have been determined at the same level of theory and scaled by 0.9427.[67] Only minimum energy structures have been used in calculations of thermochemical parameters. All optimized structures possessed no imaginary frequencies. For transition state structures, only one imaginary frequency associated with the mode connecting reactant and product species was present. The accuracy of the electronic energy calculation was further improved for all species by performing single-point calculations at the MP2/aug-cc-pVTZ level of theory, followed by the MP2/aug-cc-pVQZ level of theory to ensure basis set convergence. Basis set convergence is assumed if the difference in calculated Gibbs free energy changes varied by less than ± 2 kJ mol^{-1}, between use of the aug-cc-pVQZ and aug-cc-pVTZ basis sets. All potential energy surfaces (PES) are presented in terms of relative ΔG°_{298} at the MP2/aug-cc-pVQZ// MP2(full)/6-31G(d) level of theory. In order to provide very accurately calculated PA values required for this work, several small molecules have their PAs calculated at the CCSD(T)//UMP2(full)/aug-cc-pVTZ level of theory. The coupled-cluster method[108], which includes direct single, double and perturbatively calculated triple excitations (CCSD(T)), is arguably one of the most accurate[68] of practical electron correlation methods; however, the

cost rises extraordinarily with the number of atoms included and its current application is feasible (with aug-cc-pVTZ) for molecules consisting of approximately six to ten atoms.

To compare with experiment, infrared spectra have been calculated using the B3LYP/6-31+G(d,p) level of theory. Density functional theory has been found to give very good agreement with gas phase IRMPD in the past.[7, 99, 100] The harmonic frequencies provided by the B3LYP/6-31+G(d,p) calculation were not scaled. All calculations have been performed using the *GAUSSIAN 03* software package.[65]

4.3.2 RRKM Calculations

Due to the low pressure environment maintained in the FT-ICR, the products of ion-molecule reactions will not undergo sufficient stabilizing conditions within their reactive lifetime, resulting in the ions having an excess of internal energy prior to participation in secondary ion-molecule reactions. The RRKM rate constant, $k(E)$ (Eq. 3.68) has been calculated for each of three competing reaction channels using the Beyer-Swinehart Algorithm,[96] yielding exact values of $G(E^{\dagger})$ and $\rho(E_v)$. Vibrational frequencies, rotational constants and ground state energies for the reacting ion and all transition state species have been obtained at the MP2/aug-cc-pVQZ//MP2(full)/6-31G(d) level of theory. All calculations of $k(E)$ have been performed using Mathcad 14.0, with the worksheets provided in Appendix A. The relative size of each $k(E)$ is compared in order to determine the contribution of each reaction channel at elevated internal energies.

4.4 Results and Discussion

The ability to trap and isolate single ions of interest allows for a partial kinetic evaluation of the mechanisms proposed by Clair and McMahon.[101] A comparison of **Scheme 1** and **Scheme 2** reveals that the difference between the two mechanisms is the assumed structure of the ion of *m/z* 99 as well as that of the intermediate ion of *m/z* 69. In **Scheme 1** it is proposed that *m/z* 99 has the structure of a difluoromethylated formyl fluoride ion, while **Scheme 2** proposes that this species is a PBD of formyl fluoride and singlet difluorocarbene. Similarly, **Scheme 1** suggests that *m/z* 69 has the structure of protonated difluoromethanol, while **Scheme 2** implicates a PBD of water and difluorocarbene. In accordance with pseudo-first order kinetics, under a constant partial pressure of water, the sequences shown in **Schemes 1** and **2** should exhibit first-order decay of *m/z* 99. The time-intensity profile for isolated *m/z* 99 in the presence of water and TFDE at a partial pressure of water of 9.6×10^{-9} mbar is shown in **Figure 4.1**. In addition to *m/z* 69, several other product ions are observed and a selection of these ions is shown clearly in **Figure 4.2**.

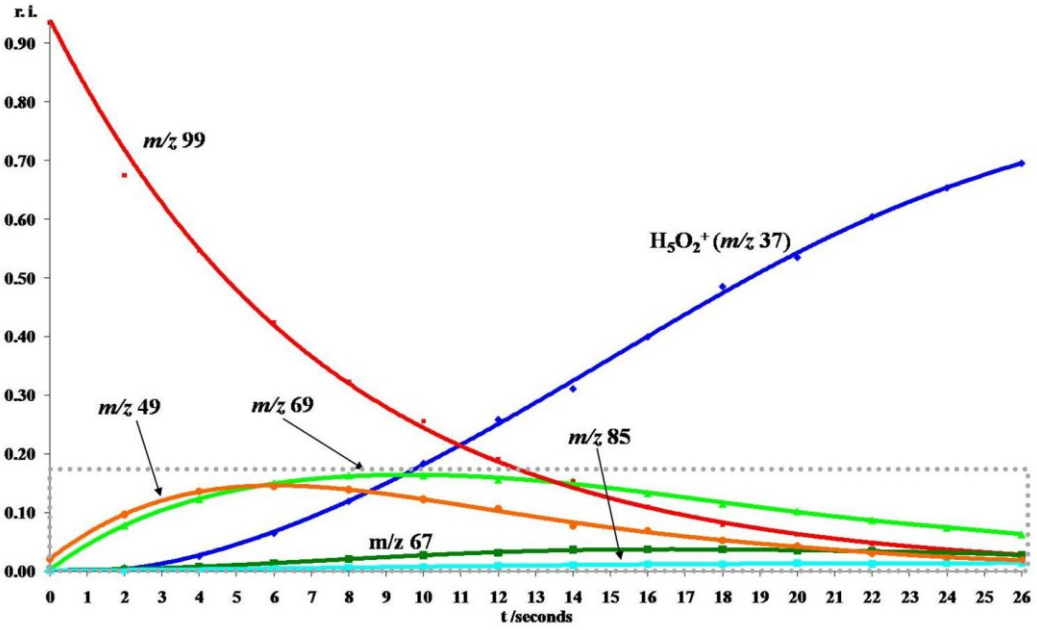

Figure 4.1: Relative intensity (r.i.) vs. time profile produced by reaction of the ion with *m/z* 99 with water at partial pressure of 9.6 x 10^{-9} mbar.

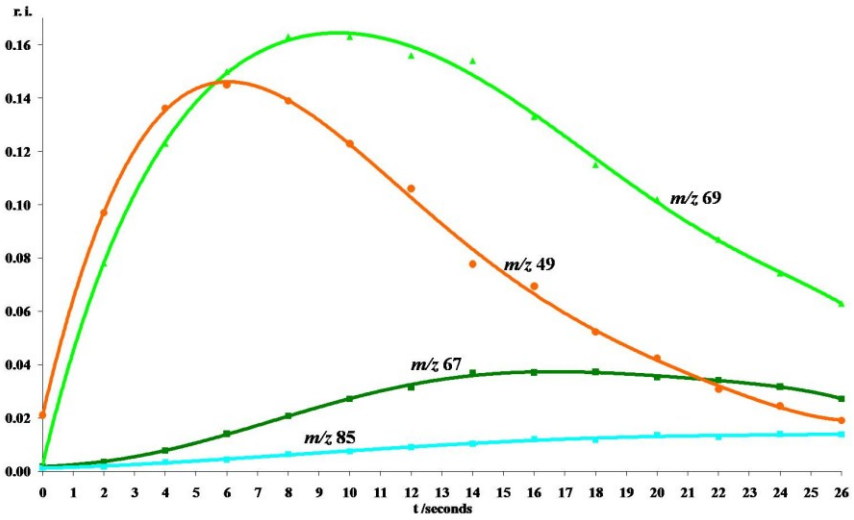

Figure 4.2: Relative intensity (r.i.) vs. time profile for a selection of the low-intensity ions presented in the boxed region of Figure 4.1.

The pseudo-first order rate constant (k_{obs}) for the disappearance of *m/z* 99 is found to be 1.35 (±0.01) x 10^{-1} s^{-1} at a partial pressure of H_2O of 9.6 x 10^{-9} mbar (**Figure 4.3**), leading to a bimolecular rate constant for the reaction of *m/z* 99 with water of 6.0 (± 1.4) x 10^{-10} cm^3 $molecule^{-1}$ s^{-1} which corresponds to approximately 22 percent of the ion-molecule collision rate.[102]

The structural identity of *m/z* 99 ($C_2F_3H_2O^+$) was interrogated using mass-selected IRMPD spectroscopy and density functional theory calculations (**Figure 4.4**).

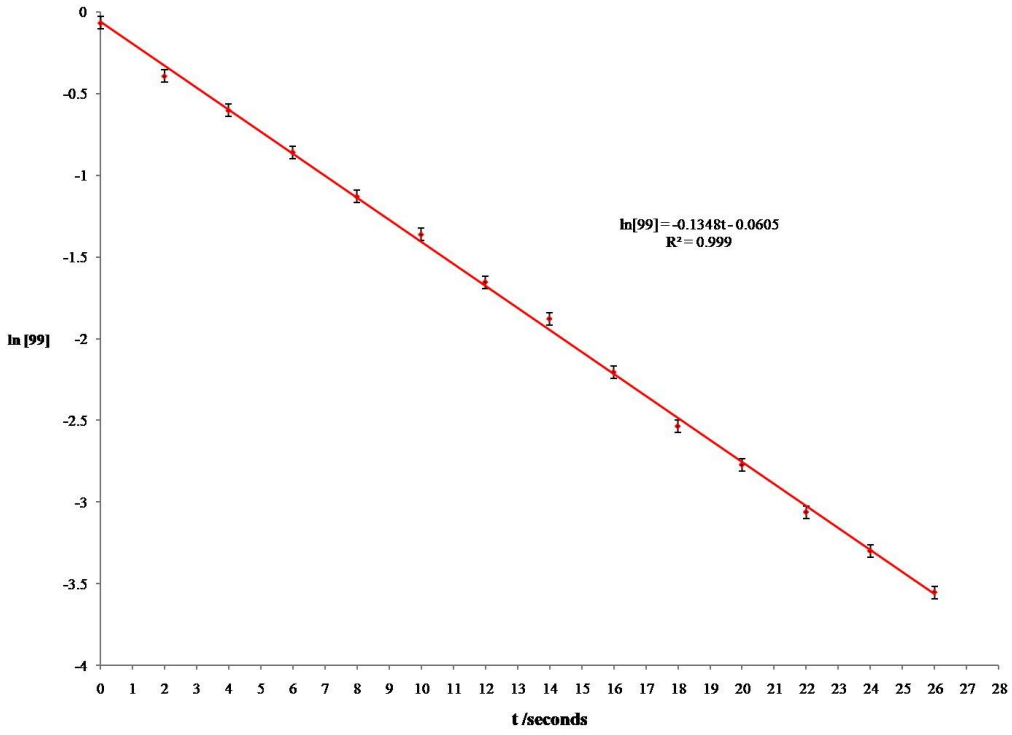

Figure 4.3: Plot of the natural logarithm of the relative intensity versus time for the ion with *m/z* 99 demonstrating pseudo-first order kinetic behaviour under a constant partial pressure of water.

IRMPD of *m/z* 99 revealed two dissociation pathways, loss of CF_3H and CO, which yields ions at *m/z* 29 and 71, respectively. The relative intensities of the two fragments slightly favoured *m/z* 29, protonated carbon monoxide, over *m/z* 71, presumably protonated fluoroform. Both fragments most probably result from an initial intramolecular transfer of fluoride to the CF_2H moiety resulting in either loss of fluoroform (producing *m/z* 29) accompanied by near thermoneutral proton-transfer from HCO^+ to CF_3H such that the neutral loss is CO (producing *m/z* 71). According to NIST, the proton affinity (PA) of CF_3H is higher than that of CO by approximately 30 kJ mol^{-1}, which would suggest that the more abundant fragment ion should be *m/z* 71. The PA of CF_3H as reported by NIST is the same PA as that of CF_2H_2 of 620 kJ mol^{-1}, which raises considerable concern for the uncertainty of this reported value. The uncertainty of this value warranted high-level calculations at the CCSD(T)//UMP2(full)/aug-ccpVTZ level of theory and the PA of CF_3H and CF_2H_2 are found to be 571 kJ mol^{-1} and 580 kJ mol^{-1}, respectively. The preceding PA values are markedly different from the PA values of 620 kJ mol^{-1} reported by NIST. The calculated PA for CO is found to be 594 kJ mol^{-1} at the same level of theory, which is in good agreement with the value reported by NIST of 590 kJ mol^{-1}. The high level CCSD(T)//UMP2(full)/aug-cc-pVTZ calculations are thus consistent with observation of the dominant fragmentation of *m/z* 99 to yield protonated CO (HCO^+) at *m/z* 29 rather than protonated CF_3H at *m/z* 71. This demonstrates that caution should be taken with the NIST PA value reported for both CF_3H

and CF_2H_2. The vibrational band assignments for the most probable isomer of *m/z* 99 (**Ia**) are shown in **Table 4-1**.

The vibrational spectrum for ion *m/z* 99, species **Ia**, obtained by the electronic structure calculations is consistent with the IRMPD experiment. In addition, the calculations show that the difluoromethylated formyl fluoride (**Ia**) isomer is favoured by 40.5 kJ mol^{-1} over the PBD of difluorocarbene and formyl fluoride (**II**), with a very small energy barrier of 3.50 kJ mol^{-1} separating the two (**Figure 4.5**). The difluoromethylated formyl fluoride isomer at *m/z* 99 **Ia** will henceforth be referred to as isomer **I**.

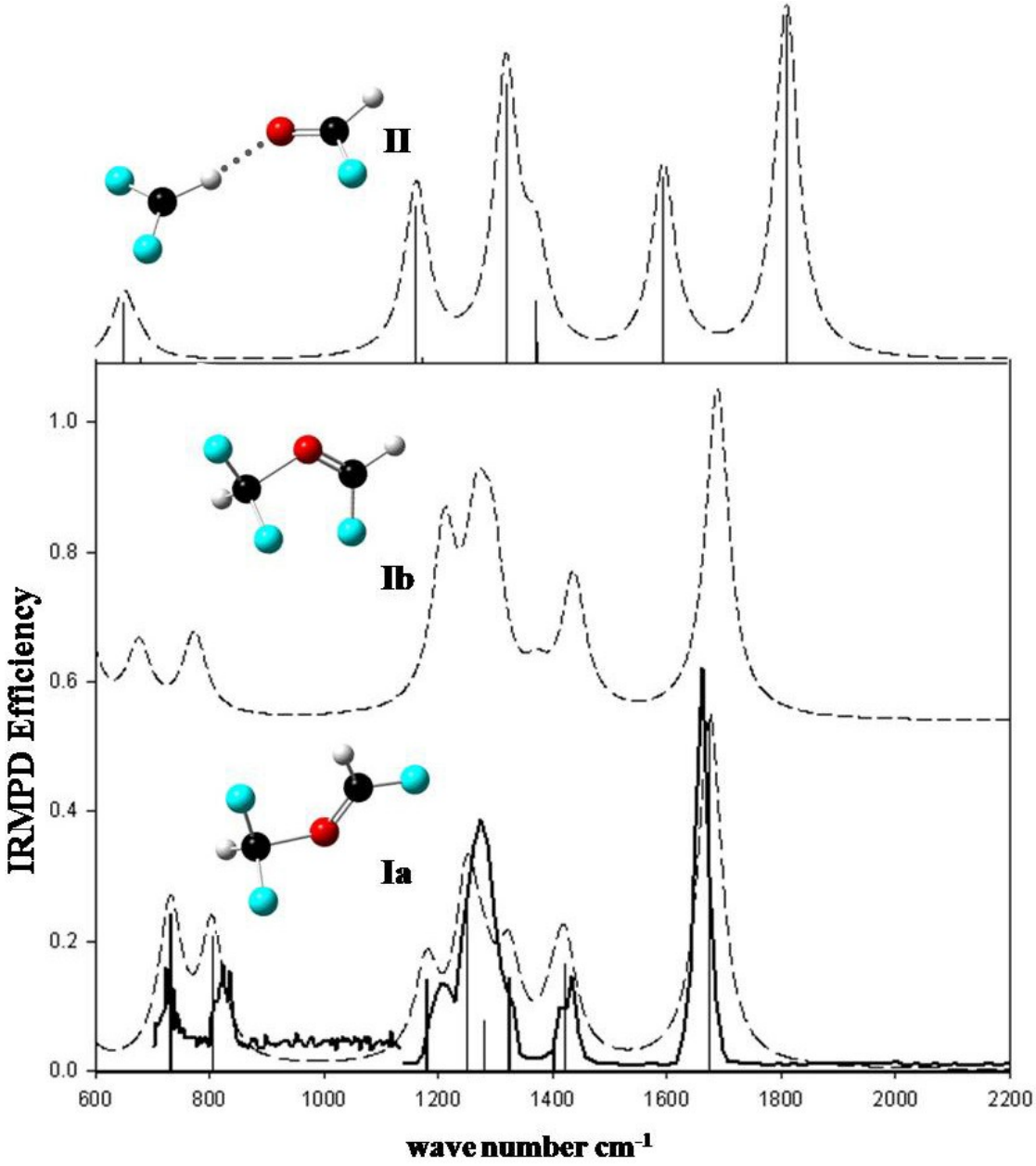

Figure 4.4: The IRMPD spectrum for the ion with *m/z* 99 is shown in solid black line and a B3LYP/6-31+G** calculated spectrum is shown in dashed black line for each of the species, **Ia**, **Ib** and **II**. The ions **Ia** and **Ib** are two stable difluoromethylated formyl fluoride isomers. The rotomer Ia is favoured in Gibbs free energy by 1.50 kJ mol^{-1} relative to Ib. The PBD of difluorocarbene and formyl fluoride is species II.

Table 4-1: Band assignments and comparison of predicted band positions for the IRMPD spectrum of isomer Ia of *m/z* 99, FHC=O-CF_2H^+. The harmonic frequencies of Ia have been calculated at the B3LYP/6-31+G** level of theory The frequencies are assigned in units of wavenumbers (cm^{-1}).

Vibrational Mode	IRMPD	Ia
* **C-O stretch**	725	732
* **F-C=O bend**	824	805
* **C-F stretch**	1206	1180
* **C-F stretch**	1275	1251
* **O-C-H bend**		1280
* **H-C-F bend**		1324
* **H-C=O bend**	1434	1402
* **H-C-F bend (on CF_2H moiety)**		1434
* **C=O stretch**	1663	1675

The preceding evidence thus implies that the dominant structure of the ion with *m/z* 99 is difluoromethylated formyl fluoride (**I**). The ion is formed efficiently by reaction of difluoromethyl cation, the dominant fragment ion obtained by electron impact on TFDE, with TFDE to yield *m/z* 99 and fluoroform. Electronic structure calculations show this reaction (**Eq. 4.2**) to be exergonic by 128 kJ mol^{-1} (298 K).

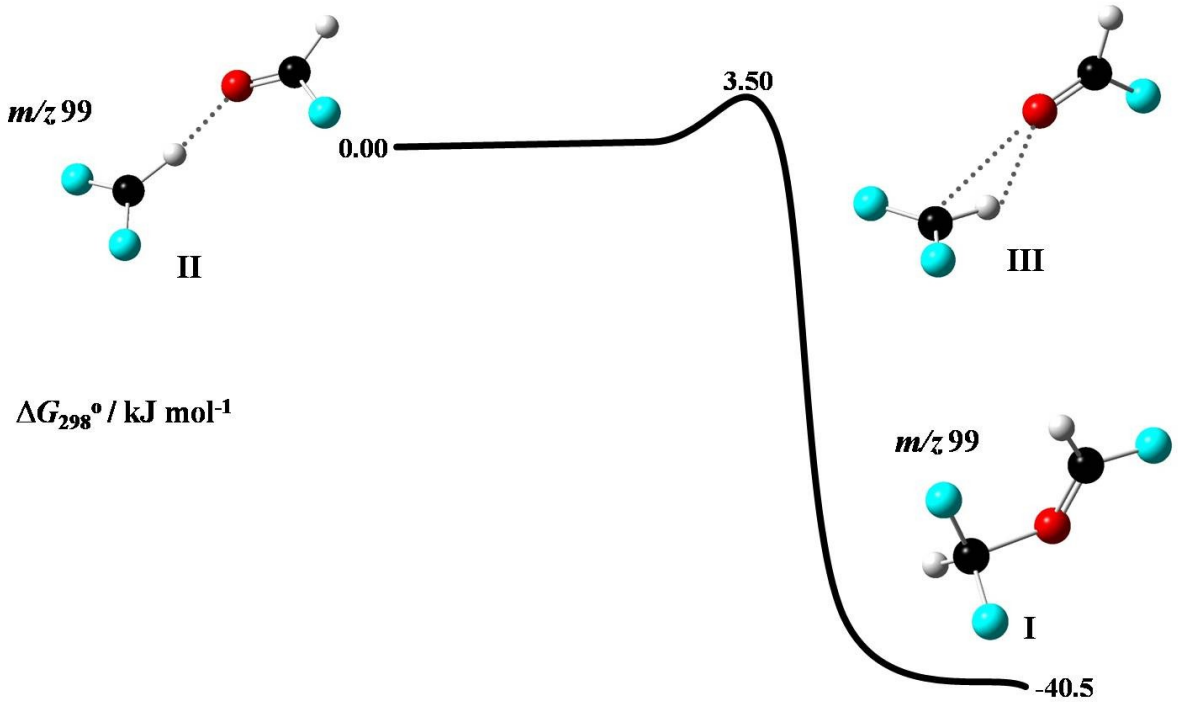

Figure 4.5: Relative ΔG°_{298} profile for the unimolecular isomerization of difluoromethylated formyl fluoride at *m/z* 99 (**I**) to the PBD of difluorocarbene and formyl fluoride at *m/z* 99 (**II**) through a transition state (**III**). Values are calculated at the MP2/aug-cc-pVQZ//MP2(full)/6-31G(d) level of theory.

Assuming the starting structure for *m/z* 99 to be species **Ia**, as shown in **Figure 4.4**, it is then of interest to ascertain the most probable channel for the formation of $H_5O_2^+$. In **Scheme 1** the S_N2 displacement of formyl fluoride from *m/z* 99 *via* attack of water is calculated to be exergonic by 39.0 kJ mol^{-1} (298 K) and is shown in **Figure 4.6**. The bimolecular rate constant (k_2) for this reaction between water and *m/z* 99 of 6.0 (± 1.4) x 10^{-10} cm^3 $molecule^{-1}$ s^{-1} is a significant fraction of the collision rate constant, implying an absence of any

substantial barrier to reaction. This is in contrast to the smaller gas phase bimolecular rate constants (300 K) measured for symmetric chloride[109] and bromide[110] gas phase nucleophilic displacement reactions with rate constants at 3.5 (± 1.8) x 10^{-14} cm^3 $molecule^{-1}$ s^{-1} and 2.4 (± 0.6) x 10^{-11} cm^3 $molecule^{-1}$ s^{-1}, respectively. The symmetric exchange reactions above are described generally by **Eq. 4.8**

$$X_a^- + CH_3X_b \rightarrow X_aCH_3 + X_b^- \qquad \textbf{4.8}$$

and resemble the S_N2 reactions observed for positive ions such as the displacement of H_2O in the reaction of protonated methanol with methanol (**Eq. 4.9**). The rate constant obtained for the reaction described by **Eq. 4.9** was found by McMahon and Beauchamp[111] to be 1.05 x 10^{-10} cm^3 $molecule^{-1}$ s^{-1}. This was later verified by Fridgen and coworkers[112] who obtained a value of 1.04 (± 0.02) x 10^{-10} cm^3 $molecule^{-1}$ s^{-1}. The rate constant determined in this work of 6.0 (± 1.4) x 10^{-10} cm^3 $molecule^{-1}$ s^{-1} is of the same order of magnitude as the rate constants obtained in the above studies[111, 112] involving a positive ion as the electrophilic substrate.

$$CH_3OH_2^+ + CH_3OH \rightarrow (CH_3)_2OH^+ + H_2O \qquad \textbf{4.9}$$

Since the reaction of *m/z* 99 with water does not occur at the collision rate, this provides further evidence that a displacement-type process involving proton transfer such as the one proposed in **Scheme 2** is not likely. A reaction of this type would be expected to occur very close to or at the collision rate. The change in Gibbs free energy at 298 K for an S_N2 type mechanism proposed in the first step of **Scheme 1** is shown in **Figure 4.6**.

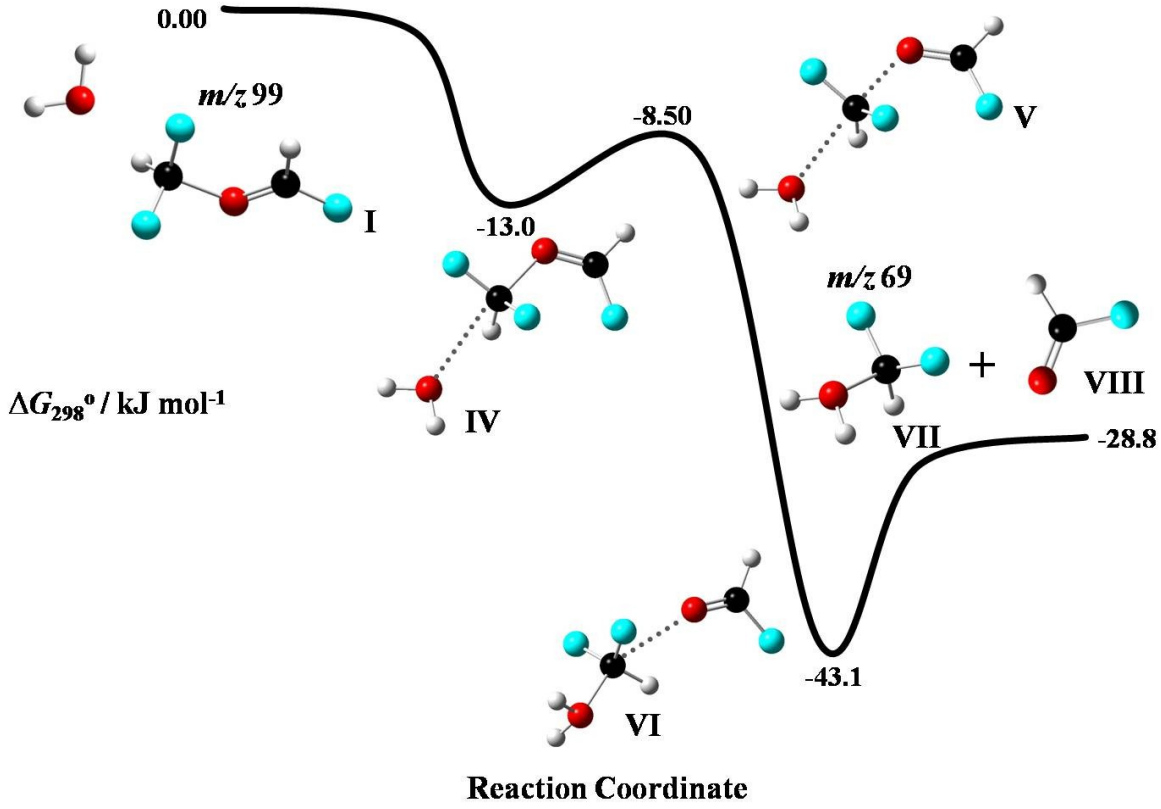

Figure 4.6: Relative ΔG°_{298} profile for the nucleophilic attack of water on difluoromethylated formyl fluoride with *m/z* 99 (**I**) to yield protonated difluoromethanol with *m/z* 69 (**VII**) and formyl fluoride (**VIII**). Values are calculated at the MP2/aug-cc-pVQZ//MP2(full)/6-31G(d) level of theory.

The energetic pathway leading to formation of ions with *m/z* 49 and 69, whose time-intensity profiles are shown in **Figure 4.2**, is presented in **Figure 4.6**. The ions with *m/z* 49 and 69 are the protonated forms of formyl fluoride and difluoromethanol, respectively. The product ion is shown in **Figure 4.6** exclusively as protonated difluoromethanol at *m/z* 69 (**VII**). It is feasible that protonated formyl fluoride with *m/z* 49 could be formed by simple

proton transfer from the dissociating complex (**VI**). The difference in PA calculated at the CCSD(T)//UMP2(full)/aug-ccpVTZ level of theory is only 1.0 kJ mol^{-1} in favour of the protonation of difluoromethanol over formyl fluoride. The PA values calculated for difluoromethanol and formyl fluoride are 664 and 663 kJ mol^{-1}, respectively. It is thus reasonable to suggest that the proton will be statistically distributed between the two molecule entities. Also it is possible that protonated difluoromethanol formed with an excess of internal energy might undergo unimolecular loss of HF to yield protonated formyl fluoride and thus result in a non-statistical distribution.

The possibility of unimolecular isomerism between protonated difluoromethanol (**VII**) and the PBD of difluorocarbene and water (**IX**) was examined using electronic structure calculations. The PBD of difluorocarbene and water (**IX**) was presented in **Scheme 2**. Protonated difluoromethanol (**VII**) is favoured over the PBD of difluorocarbene and water (**IX**) by 51.6 kJ mol^{-1} at 298 K (**Figure 4.7**). There is also a large barrier to isomerization from protonated difluoromethanol (**VII**) to the PBD of difluorocarbene and water (**IX**) of 62.8 kJ mol^{-1} at 298 K (**Figure 4.7**). The protonated alcohol (**VII**) is both thermodynamically and kinetically favoured over the PBD (**IX**).

It was an unproductive effort to probe the structure of *m/z* 69 by IRMPD spectroscopy. This was due to protonated difluoromethanol at *m/z* 69 (**VII**) reacting rapidly with water resulting in an inadequate amount of isolation time for the ion to be irradiated by the laser.

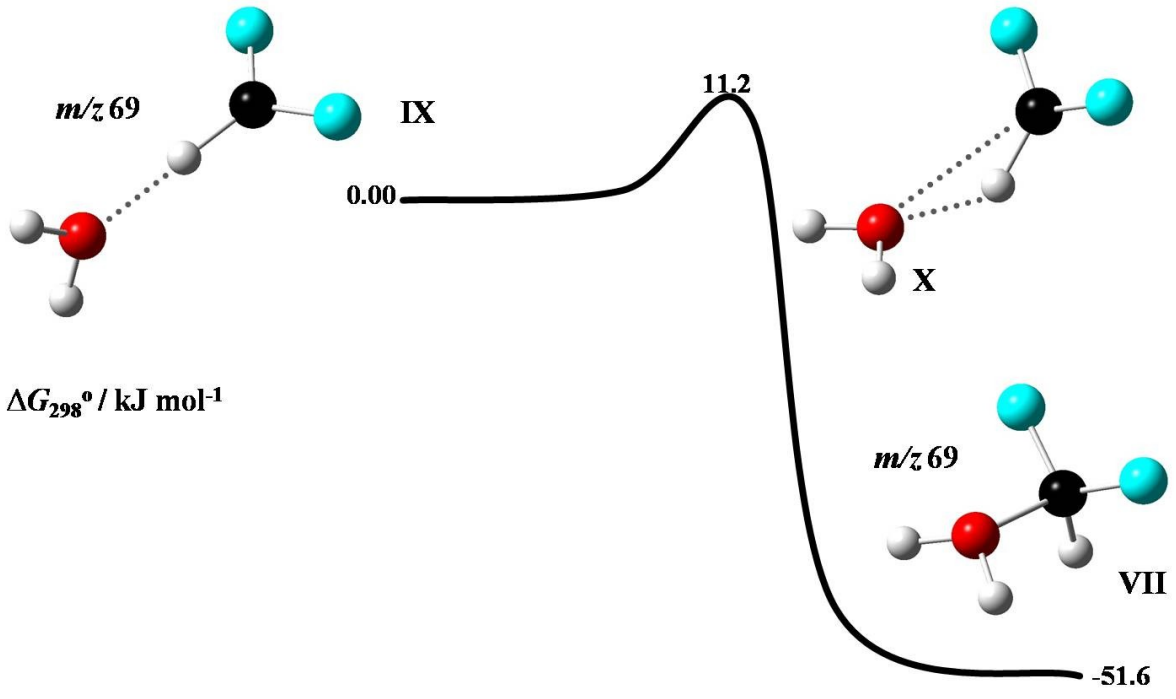

Figure 4.7: Relative ΔG°_{298} profile for the unimolecular isomerization of protonated difluoromethanol at *m/z* 69 (**VII**) to the PBD of difluorocarbene and water at *m/z* 69 (**IX**) through a transition state (**X**). Values are calculated at the MP2/aug-cc-pVQZ//MP2(full)/6-31G(d) level of theory.

It was rationalized that a species analogous in structure to *m/z* 69, however less reactive, could be formed by reacting difluoromethylated formyl fluoride at *m/z* 99 (**I**) with dimethyl ether rather than water. This alternative reaction was performed and an oxonium ion with *m/z* 97 (**B**) was isolated and examined by IRMPD spectroscopy (**Figure 4.8**). By replacing the once acidic hydrogen atoms found attached to the oxygen in protonated difluoromethanol (**VII**), with methyl groups, the reactivity with water of the oxonium ion at *m/z* 97 (**B**) is

reduced relative to protonated difluoromethanol at *m/z* 69 (**VII**) . This reduced reactivity allowed the oxonium ion at *m/z* 97 (**B**) to be isolated readily for IRMPD analysis.

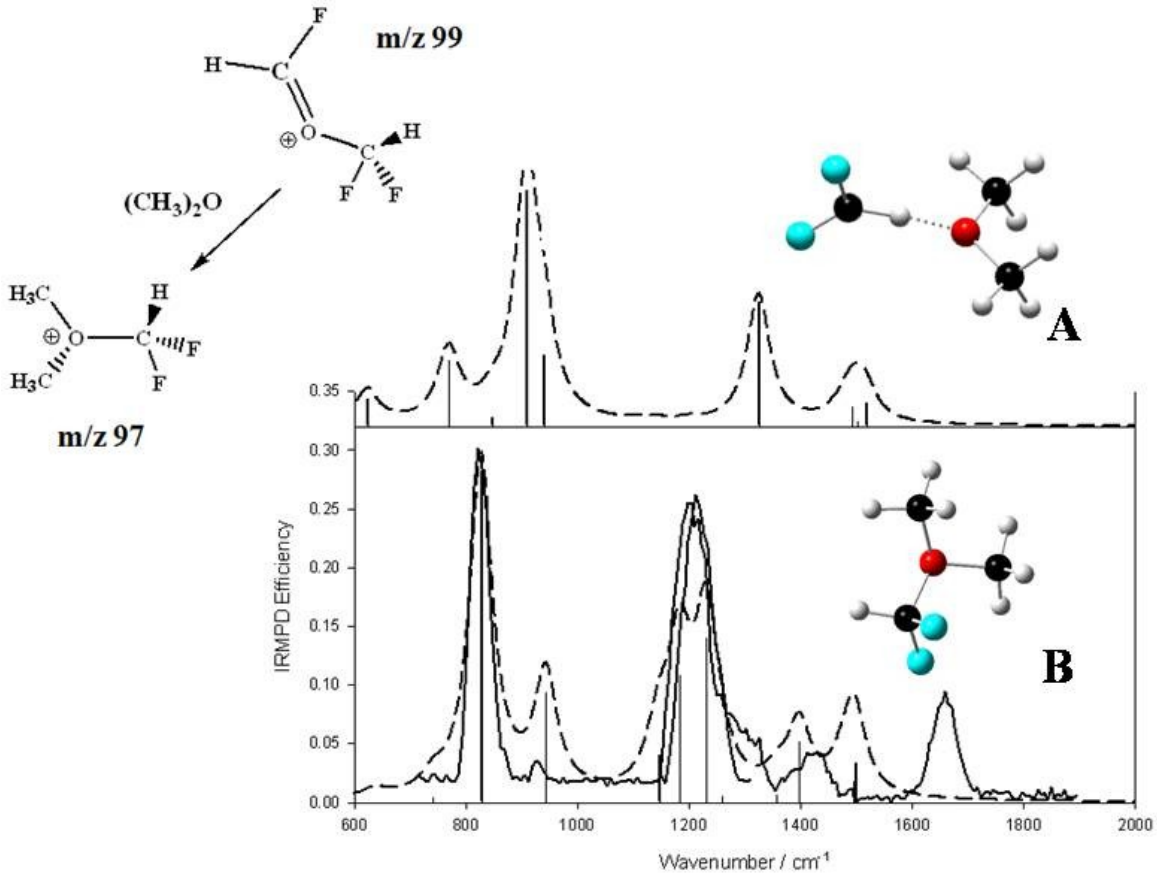

Figure 4.8: The IRMPD spectrum for the ion with *m/z* 97 (solid) and the B3LYP/6-31G* calculated spectra (dashed) for the PBD of difluorocarbene and dimethyl ether (**A**) and a oxonium ion that can be described as difluoromethylated dimethyl ether (**B**).

The vibrational band assignments for difluoromethylated dimethyl ether at *m/z* 97 (**B**) are given in **Table 4-2**.

Table 4-2: Band assignments and comparison of predicted band positions for the IRMPD spectrum of species of *m/z* 97, $HF_2CO(CH_3)_2^+$ (**B**). The harmonic frequencies of **B** have been calculated at the B3LYP/6-31+G** level of theory The frequencies are assigned in units of wavenumbers (cm^{-1}).

Vibrational Mode	IRMPD	B
*** C-O stretch**	822	828
*** C-O stretch**	926	944
*** symm. C-F stretch**	1213	1148
*** C-F stretch**		1184
*** C-F stretch**		1233
*** H-C-F bend (?)**	1418	1398
*** symm. CH_3 def. (?)**	1434	1500

IRMPD of difluoromethylated dimethyl ether at *m/z* 97 resulted in ionic products with *m/z* of 63 and 47, the latter being the slightly more dominant fragment. These ions are presumably methylated formyl fluoride (*m/z* 63) and protonated dimethyl ether (*m/z* 47) formed by loss of CH_3F and CF_2, respectively. The latter fragmentation might have indicated a PBD of difluorocarbene and dimethyl ether at *m/z* 97 (**A**). A comparison of the experimental infrared spectrum with the predicted spectra for the PBD of difluorocarbene

and dimethyl ether at *m/z* 97 (**A**) and difluoromethylated dimethyl ether at *m/z* 97 (**B**) reveals that the PBD of difluorocarbene and dimethyl ether (**A**) is not a good candidate structure. The ion at *m/z* 47 is thus likely the result of proton transfer from the CF_2H to $(CH_3)_2O$ moiety in the exit channel complex initiated by F_2HC-O bond cleavage as shown by **Scheme 4**.

Scheme 4

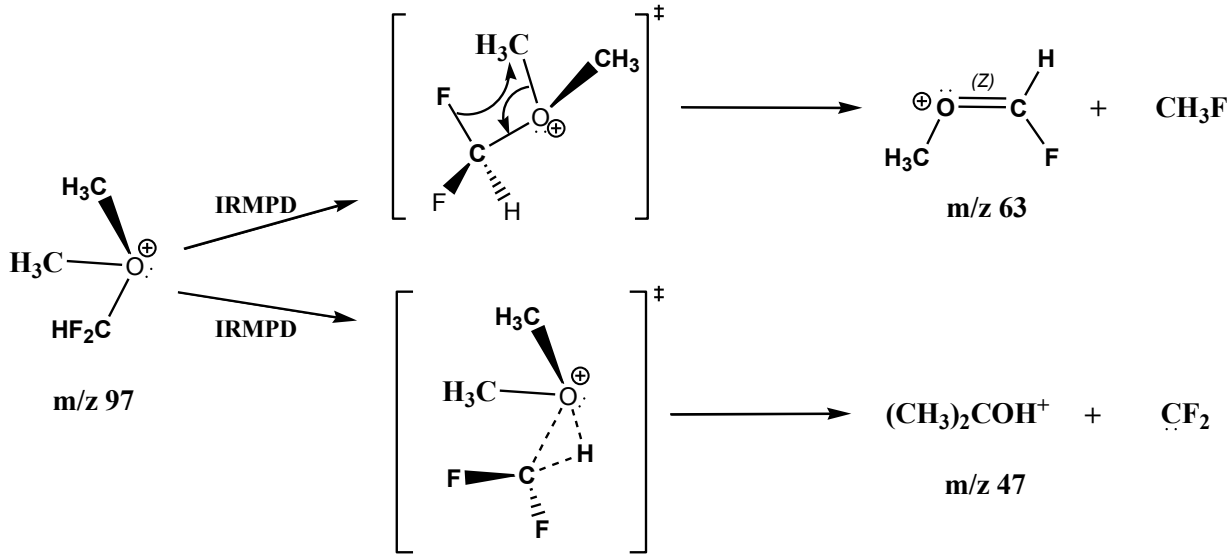

From a comparison of the experimental and predicted spectra, it is likely that the structure is the oxonium ion, difluoromethylated dimethyl ether, at *m/z* 97 **(B)**. However, there is some disagreement between the experimental and predicted spectra, especially in the 1500-1700 cm^{-1} region. The symmetric CH_3 deformation is predicted to occur at ~1500 cm^{-1}which is typical for this mode. The observed position for this band could be either that at 1418 cm^{-1}, or at higher energy, 1660 cm^{-1}. If the experimental band is not 1660 cm^{-1}, then it is difficult to account for it as there are not any other bands predicted to occur at higher energy other than the C-H stretches.

The spectra presented in **Figure 4.8** show that the identity of the ion with *m/z* 97 is more likely the difluoromethylated dimethyl ether (**B**) isomer rather than the PBD of difluorocarbene and dimethyl ether (**A**). If formation of difluoromethylated dimethyl ether at *m/z* 97 (**B**) is analogous to the formation of protonated difluoromethanol at *m/z* 69 (**VII**), this then further justifies assignment of protonated difluoromethanol at *m/z* 69 (**VII**) as the reactive isomer involved in the mechanism considered here.

The first step shown by **Scheme 1** proposed by Clair and McMahon is supported experimentally and computationally. This is based on the evidence that there is an S_N2 attack of water on the difluoromethylated formyl fluoride ion at *m/z* 99 (**I**) with a bimolecular rate coefficient of 6.0 (± 1.4) x 10^{-10} cm^3 $molecule^{-1}$ s^{-1}. The magnitude of the rate coefficient is consistent with an S_N2 process involving a positive ion as the electrophilic substrate.[109, 110] This reaction forms protonated difluoromethanol at *m/z* 69 predominantly, but will also yield protonated formyl fluoride at *m/z* 49 (**Figure 4.2**). This is further evidence that the S_N2 process proposed for the first step of **Scheme 1** by Clair and McMahon is a dominant reaction channel.

IRMPD spectroscopy has been used to directly identify the ion with *m/z* 99 as difluoromethylated formyl fluoride (**I**) and has been used to find the structure of the ion with *m/z* 69 as protonated difluoromethanol (**VII**). Identification of the structure of the ion with *m/z* 69 as protonated difluoromethanol (**VII**) was accomplished indirectly by isolation of an ion with *m/z* 97 formed analogously to protonated difluoromethanol (**VII**) by reacting

dimethyl ether instead of water with difluoromethylated formyl fluoride (**I**). This species was an oxonium ion of difluoromethylated dimethyl ether at *m/z* 97 (**B**).

Electronic structure calculations at the MP2/aug-cc-pVQZ//MP2(full)/6-31G(d) level of theory show the S_N2 process presented in **Scheme 1** to be exergonically favoured at room temperature by 28.8 kJ mol^{-1} (**Figure 4.6**).

The second step proposed in **Scheme 1** is formation of $H_5O_2^+$ at *m/z* 37 (**XIV**) and difluorocarbene from the reaction of protonated difluoromethanol at *m/z* 69 (**VII**) with water (**Figure 4.9**). This process is endergonic at 298 K by 59.6 kJ mol^{-1} (**Figure 4.9**), thus rendering this process most unlikely at room temperature. The barrier to decomposition is also relatively high and is 41.5 kJ mol^{-1} above the reactant species. The loss of difluorocarbene from ionic species has been previously observed in compounds containing trifluoromethyl groups,[113-115] and thus it seems reasonable to assume also that it may be possible to lose difluorocarbene in compounds containing difluoromethyl groups. Since the loss of difluorocarbene from the water and protonated difluoromethanol complex (**XI**) is a high energy channel, it then suggests that a more energetically favorable channel is facilitating the rapid production of $H_5O_2^+$. A feasible explanation for the elementary step leading to the formation of $H_5O_2^+$ is found by considering the two ions at *m/z* 67 and 85 shown in **Figure 4.2**.

A possible source of the ion with *m/z* 67 is from the spontaneous decomposition of the complex formed by the reaction of water and protonated difluoromethanol (**XI**). This occurs by loss of hydrogen fluoride (HF) through a 1,4-elimination transition state (**XVII**) that is

exergonic by 64.0 kJ mol^{-1} (298 K). The elimination of HF yields a PBD of water and formyl fluoride at *m/z* 67 (**XV**) (**Figure 4.9**). It is not uncommon for ionic fluorine containing species to lose HF and this process has been investigated previously both experimentally and computationally.[113, 116, 117] Following the configuration of the six member ring-like transition state (**XVII**), a ring-opened intermediate (**XIX**) is produced that can readily lose HF and yield the PBD of water and formyl fluoride at *m/z* 67 (**XV**). The formation of the ring-opened intermediate (**XIX**) is exergonic by 153 kJ mol^{-1} (298 K). The production of HF and the PBD of water and formyl fluoride at *m/z* 67 (**XV**) is exergonic by 144 kJ mol^{-1} (298 K).

A secondary channel to produce HF and the PBD of water and formyl fluoride at *m/z* 67 (**XV**) was also considered. This secondary channel assumed a four member ring-like transition state (**XVI**) structure which proceeds through a 1,2-elimination of HF as opposed to the 1,4-elimination of HF proposed above. The 1,2-elimination was found to possess an endergonic barrier to decomposition of 41.9 kJ mol^{-1} (298 K) and it is thus not a kinetically accessible channel. The transition species (**XVI**) exhibits ring-strain and this will cause it to be high in energy.

RRKM rate constants associated with **XI** crossing through the barriers of transition states **XII**, **XVII**, and **XVI** have been calculated at the maximum possible value (260 kJ mol^{-1}) of excess internal energy above the **XI** ground state. The RRKM rate constants for **XI** passing through transition states **XII**, **XVII**, and **XVI** are 3.75×10^{10} s^{-1}, 1.62×10^{12} s^{-1} and 2.26×10^{9} s^{-1}, respectively. In the unlikely event that the excess internal energy of **XI**

achieves a value of 260 kJ mol^{-1}, it will proceed through **XVII** 43 times faster than **XII** and 719 times faster than **XVI**, and thus **XI** is most likely to progress through the channel with transition state **XVII**. All of the Mathcad 14.0 worksheets used to calculate the RRKM rate constants shown above are provided in Appendix A.

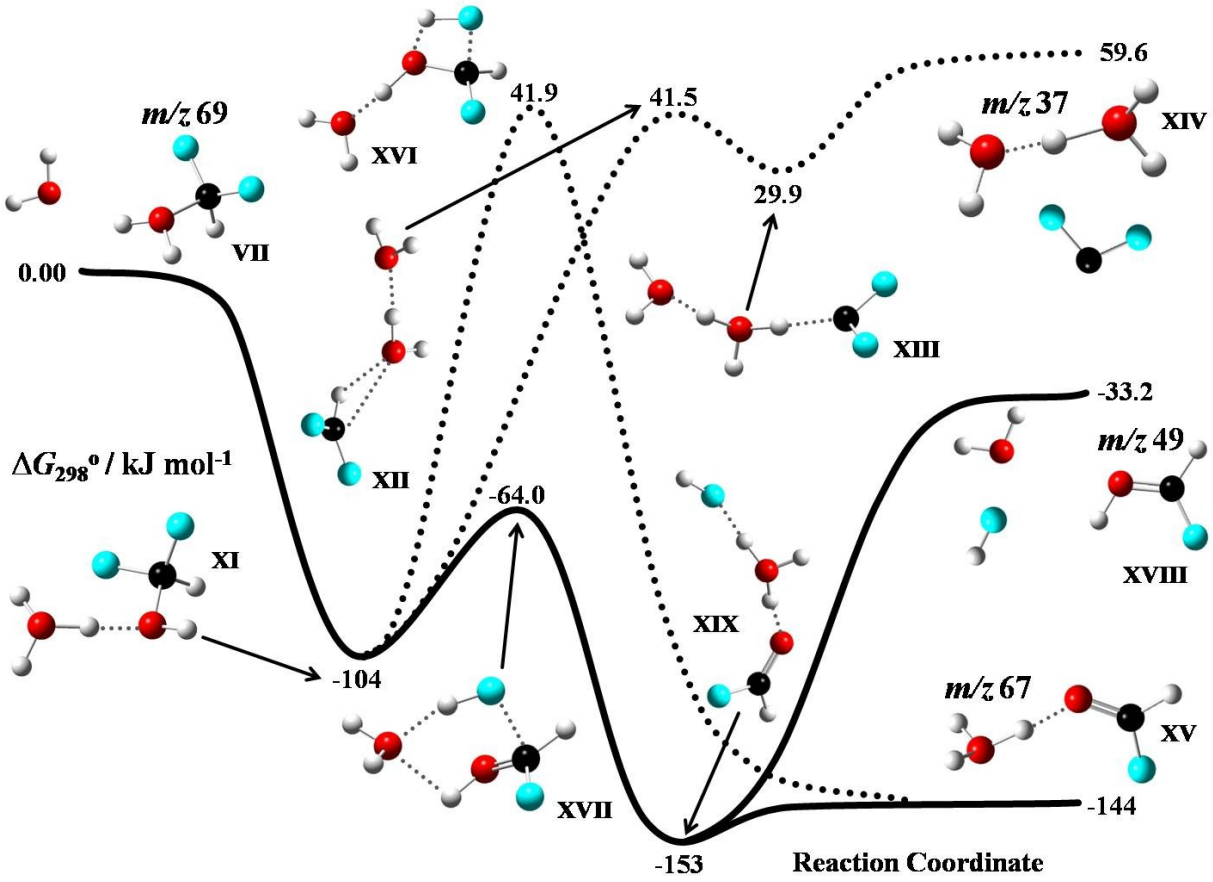

Figure 4.9: Relative ΔG°_{298} profile for the association of protonated difluoromethanol at *m/z* 69 (**VII**) with water to yield the PBD of water and formyl fluoride at *m/z* 67 (**XV**) (solid black). Reaction processes that are endergonic relative to the reactants are shown in dashed black. Values are calculated at the MP2/aug-cc-pVQZ//MP2(full)/6-31G(d) level of theory.

Following the production of the PBD of water and formyl fluoride at *m/z* 67 (**XV**), a third water molecule may then associate with this ion to yield an ion at *m/z* 85 (**XX**) (**Figure 4.10**). This step is exergonic by 64.7 kJ mol^{-1} (298 K). The ion at *m/z* 85 (**XX**) can then decompose to produce $H_5O_2^+$ at *m/z* 37 (**XIV**) and formyl fluoride (**VIII**). The formation of $H_5O_2^+$ at *m/z* 37 (**XIV**) by the displacement of formyl fluoride (**VIII**) by water from the ion at *m/z* 85 (**XX**) is exergonic by 33.3 kJ mol^{-1} (**Figure 4.10**).

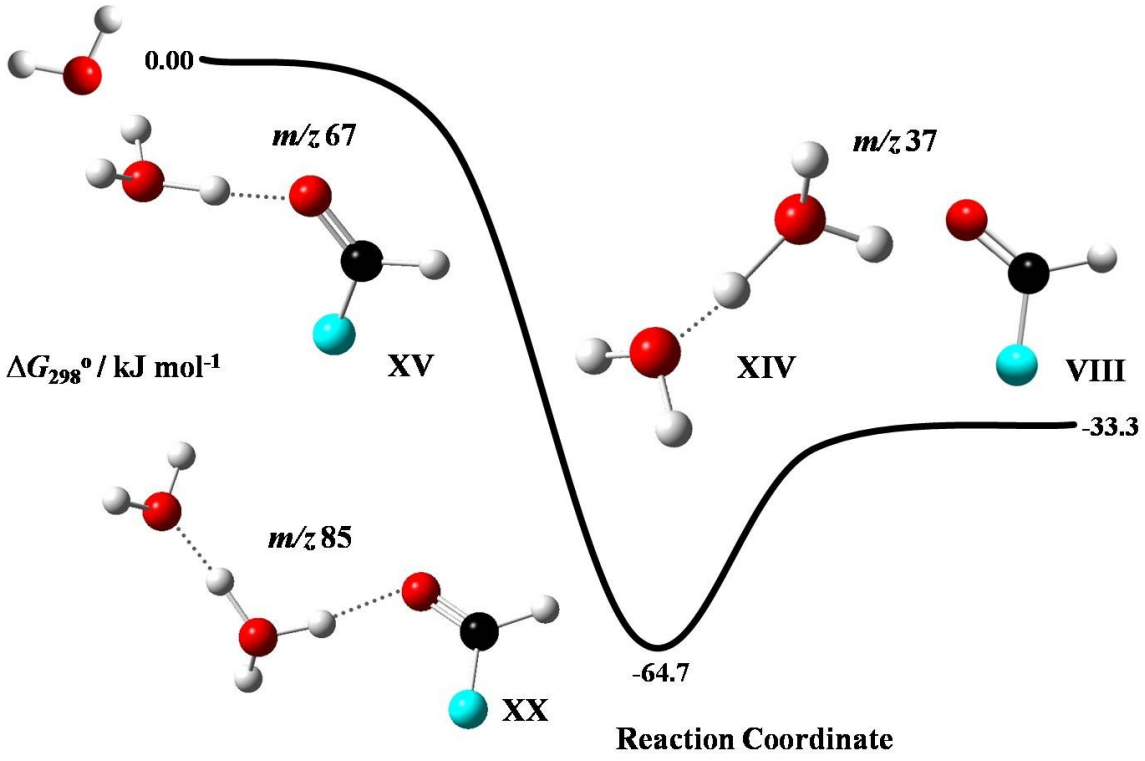

Figure 4.10: Relative ΔG°_{298} profile for the decomposition of the ion with *m/z* 85 (**XX**) into $H_5O_2^+$ at *m/z* 37 (**XIV**) and formyl fluoride (**VIII**). Values are calculated at the MP2/aug-cc-pVQZ//MP2(full)/6-31G(d) level of theory.

It is interesting to note that a species at *m/z* 85 is visible as a small constituent in the evolution of ion intensities shown in **Figures 4.1** and **4.2**. This collisionaly stabilized entity provides further support of the mechanism proposed.

4.5 Concluding Remarks

An efficient bimolecular process involving 1,1,3,3-tetrafluorodimethyl ether and water has been examined with Fourier transform ion cyclotron resonance (FT-ICR) mass spectrometry, mass-selected infrared multiple photon dissociation (IRMPD) spectroscopy and electronic structure theory calculations.

The process involves the rapid production of the PBD of water at *m/z* 37 ($H_5O_2^+$) (**XIV**). The dominant reaction channel occurs *via* the nucleophilic attack of water on difluoromethylated formyl fluoride at *m/z* 99 (**I**) to produce protonated difluoromethanol at *m/z* 69 (**VII**) and formyl fluoride (**VIII**). The bimolecular rate constant (k_2) for nucleophilic attack of water on difluoromethylated formyl fluoride at *m/z* 99 (**I**) was found to be 6.0 (± 1.4) x 10^{-10} cm^3 $molecule^{-1}$ s^{-1}. The rate of nucleophilic attack is of the same order of magnitude as previously measured systems involving positive ions as an electrophilic substrate.

Association of a second water molecule with protonated difluoromethanol at *m/z* 69 (**VII**) leads to decomposition *via* the 1,4-elimination of hydrogen fluoride (**XVII**) to form the PBD of water and formyl fluoride at *m/z* 67 (**XV**). This is strongly supported by the result of RRKM calculations which show the reaction of **XI** to proceed through transition state, **XVII** 43 and 719 times faster than through transition states **XII** and **XVI**, respectively. Finally, the

displacement of formyl fluoride occurs by the association of a third water molecule with the PBD of water and formyl fluoride at *m/z* 67 to yield $H_5O_2^+$ at *m/z* 37 (**XIV**) (**Scheme 5**).

Scheme 5

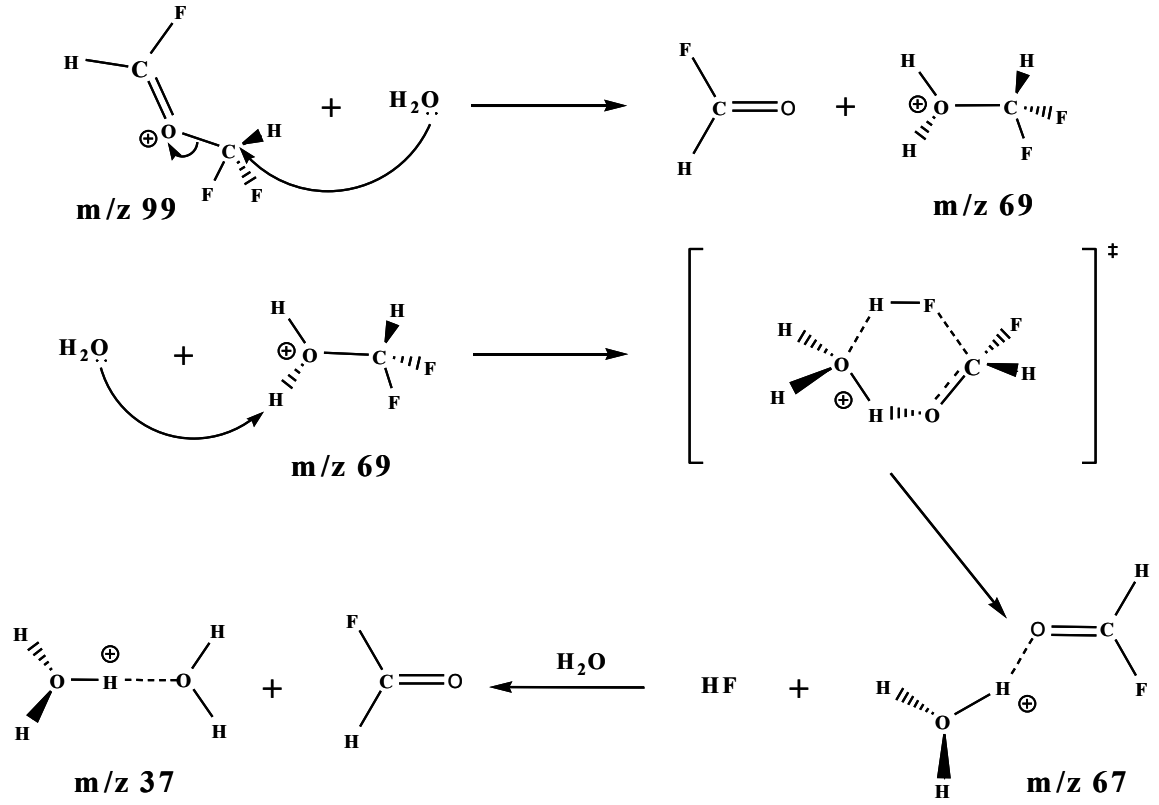

IRMPD spectroscopy and density functional theory calculations have been used to determine the most probable structure of the ions observed at *m/z* 99 and *m/z* 69. The ions with *m/z* 99 and 69 are difluoromethylated formyl fluoride (**I**) and protonated difluoromethanol (**VII**), respectively.

Electronic structure calculations at the MP2/aug-cc-pVQZ//MP2(full)6-31G(d) level of theory show that the exergonicity of the sequential reaction steps as proposed by **Scheme 5**

facilitate the abundant formation of $H_5O_2^+$ (**XIV**). For the system described here, it was found that single point energy calculations would have been adequate at the MP2/aug-cc-pVTZ level of theory, since the mean absolute deviation (MAD) between single point energies calculated at the MP2/aug-cc-pVTZ and MP2/aug-cc-pVQZ levels of theory was only 0.6 kJ mol^{-1}, demonstrating basis set convergence.

Chapter 5

Structural Characterization of Gaseous Ions Involving Caffeine and Theophylline Resolved by Mass-Selected IRMPD and Electronic Structure Calculations

5.1 General Introduction

The methylxanthines make up a large class of purine-based molecules with two of the most noteworthy being caffeine and theophylline.

Caffeine is the most widely consumed psychoactive stimulant in the world[118] and consumption of caffeine has been shown to influence a variety of physiological functions on the cellular level.[119-122] Studies have shown the reduction in pharmacological activity of several aromatic anticancer drugs due to their chemical interactions with caffeine and its derivatives.[123-127]

Theophylline has properties that make it useful as a bronchodilator in the treatment of asthma.[128-130] Despite theophylline being pharmaceutically available, little is known about its mechanism of action. Theophylline medications are very popular in North America; however many physicians remain uncertain with regards to its prescription, due to the occurrence of side effects in its users. Although there are possible side effects, it still remains an important medication in the treatment of acute severe asthma.

Caffeine and theophylline both possess four nitrogen atoms and two oxygen atoms, making them very rich candidates for the study of IHB interactions. Caffeine has three methyl groups attached to three ring nitrogen atoms, (**Figure 5.1)** whereas theophylline has two methyl groups and one hydrogen atom attached to three ring nitrogen atoms (**Figure 5.2**). In caffeine, one of the carbonyl oxygen atoms, O(6), is in close proximity to a methyl moiety attached to N(7), whereas in theophylline the carbonyl oxygen atom, O(6), is in close proximity to a hydrogen atom attached to N(7). It is proposed that such subtle structural differences could result in significant changes in IHB schemes. To observe such differences, the gas phase structures of the protonated (MH^+), proton-bound homodimers (M_2H^+), proton-bound ammonia heterodimers ($M(NH_3)H^+$) and sodium-cation bound homodimers (M_2Na^+) of the gaseous ions (M = caffeine or theophylline) for caffeine and theophylline have been studied using mass-selected IRMPD and electronic structure methods. Although sodium cation-bound dimers (SCBDs) are not categorized as IHB systems, the prevalence of sodium in nature and within the body of those who consume caffeine or theophylline, warrant this topic as a valid complement to the proton-based chemistry presented.

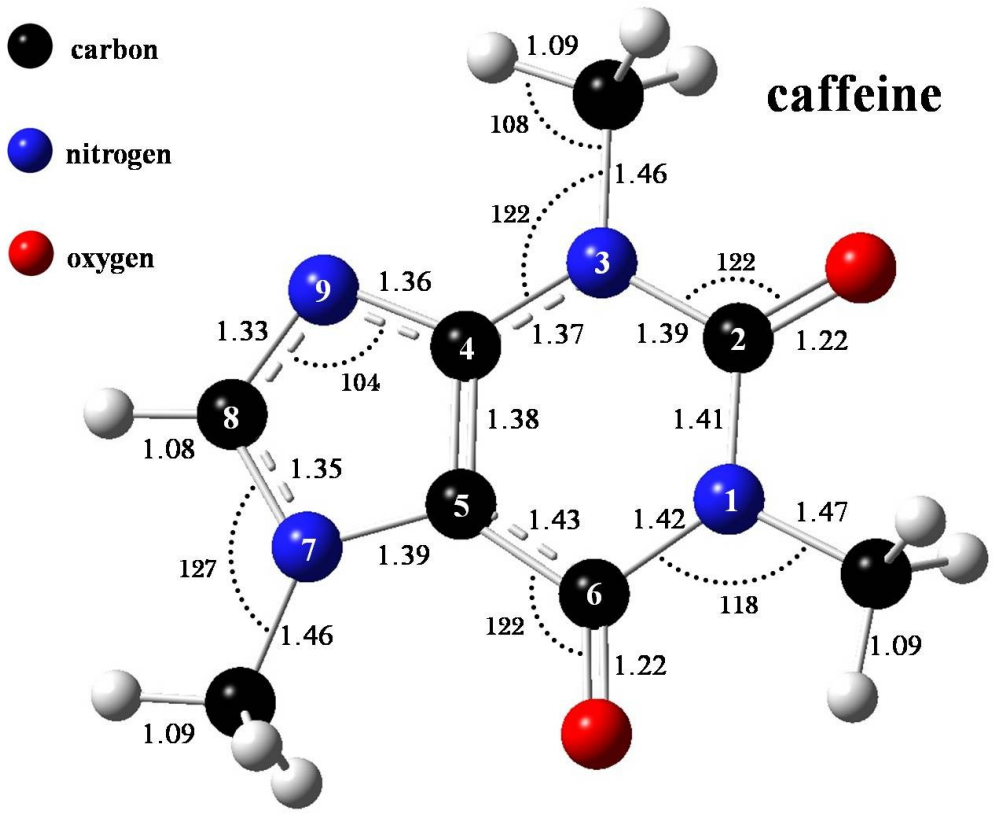

Figure 5.1: Calculated structure of caffeine, with bond lengths in angstroms and angles in degrees. Optimized at the B3LYP/6-311+G(d,p) level of theory.

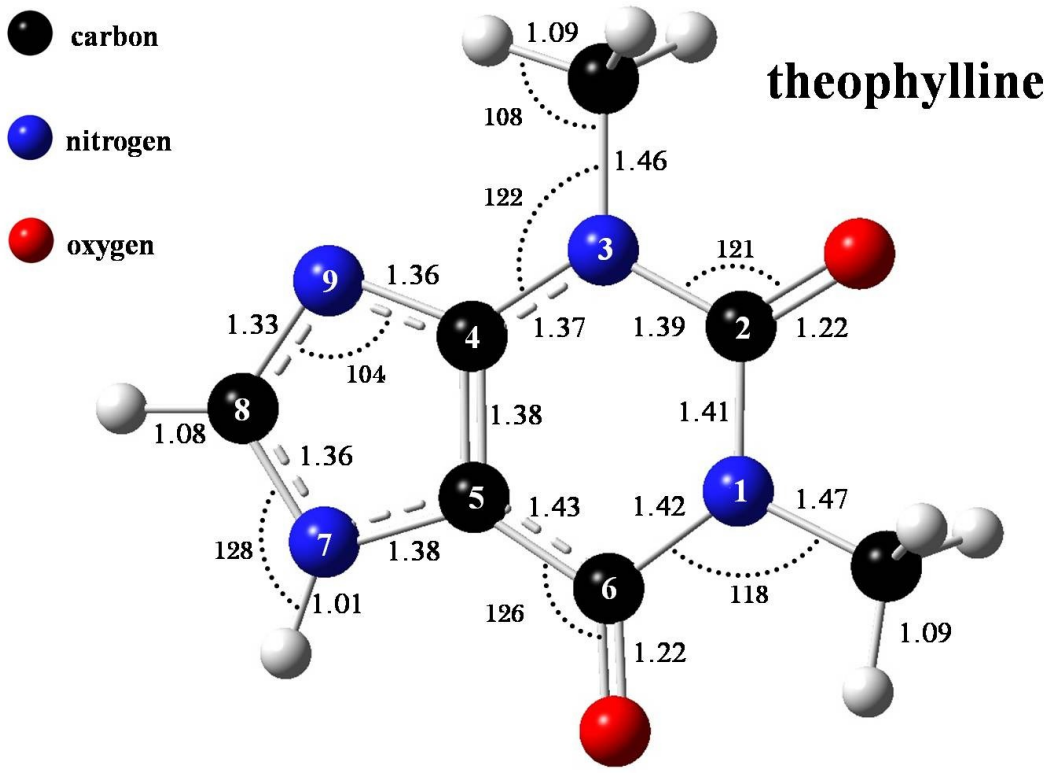

Figure 5.2: Calculated structure of theophylline with bond lengths in angstroms and angles in degrees. Optimized at the B3LYP/6-311+G(d,p) level of theory.

5.1.1 Experimental

The mass-selected IRMPD experiments have been performed using the infrared free electron laser (FEL) at the Centre de Laser Infrarouge d'Orsay (CLIO) facility in Orsay, France. The FEL beam is guided into to a Bruker Esquire 3000+ ion trap mass spectrometer, equipped with electrospray ionization. This experimental arrangement has previously been described in detail.[14, 103, 131] The FEL beam is produced by emission from a 10-50 MeV electron beam. The emission photon wavelength can be tuned, through the mid-infrared

range, by adjusting the physical gap between a set of periodic undulator magnets. The undulator is housed within a 4.8 m long optical cavity. The laser beam is accumulated in the optical cavity and outcoupling is permitted through a 1-3 mm hole in one of two protected silver mirrors, each with a diameter of 38 mm.

The present work used an electron energy of 48 MeV and the infrared output was scanned continuously over a range of 1000 cm^{-1} to 2000 cm^{-1}. The FEL output consists of a set of 8 μs macropulses, with a repetition rate of 25 Hz. Each macropulse is composed of approximately 500 micropulses, with a width of a few picoseconds per pulse. For an average IR power of 500 mW, the subsequent micropulse and macropulse energies are about 40 μJ and 20 mJ, respectively.

Solutions for studies involving the MH^+, M_2H^+ and $M(NH_3)H^+$ ions of caffeine and theophylline were prepared by combining a 2:1 mixture of ammonium chloride and the selected methylxanthine, respectively, at concentrations of ~ 10^{-4} M. Solutions for studies involving M_2Na^+ ions were prepared analogously to those reported above, but with sodium chloride as opposed to ammonium chloride. The solvent system consisted of a 1:1 mixture of acetonitrile and water. Ions were provided from the solution using electrospray ionization. The desired ionic species was then isolated and confined within the ion trap mass spectrometer. The FEL beam was focused and introduced into the center of the ion trap of the mass spectrometer. Consequence mass spectra were recorded following laser irradiation and an accumulation of ten spectra were obtained for each wavelength. IRMPD spectra were

acquired by scanning the wavelength in steps of ~4 cm^{-1}. The intensities of the spectra reported here are expressed as the IRMPD efficiency, as defined by **Eq. 1.3.**

5.1.2 Electronic Structure Calculations

Electronic structure calculations have been performed using the *GAUSSIAN* 03 software package.[65] All structures involving caffeine and theophylline have been optimized using density functional theory, employing the B3LYP exchange-correlation functional and the 6-311+G(d,p) basis set. Harmonic frequencies obtained at this level of theory have been scaled by 0.9679.[82] This was performed in order to compensate for errors arising from the use of a harmonic oscillator approximation in calculating the frequencies, as well as, long range electron correlation effects. Anharmonic frequencies[65, 84] have also been obtained at the same level of theory for many of the species considered here. Visualization of nuclear motion corresponding to calculated vibrational modes is provided by *GAUSSVIEW 4.1*[65] and is used to aid in the assignment of frequencies to IRMPD spectra.

In order to obtain more accurate interaction energies, single point electronic energies have been calculated using a MP2/aug-cc-pVTZ protocol. The triple zeta, aug-cc-pVTZ basis set, augmented with diffuse functions on heavy atoms and hydrogen has been described as an excellent compromise between cost and accuracy for medium sized systems.[76] The double zeta, aug-cc-pVDZ basis set, although less costly, is known to be inadequate for obtaining electronic energies near the level of chemical accuracy.[76] Electronic energies obtained using the MP2 method for systems involving long range interactions, such as hydrogen bonding, have been found to be calculated very reliably when combined with a sufficiently large

correlation consistent basis set.[76] It was found that use of aug-cc-pVTZ was too costly for the PBD systems, therefore all PBD single point calculations have been performed at the MP2/6-311+G(2d,2p)[87] level of theory. In order to produce more accurate energies for the SCBD systems, single point calculations have been specified at the MP2(full)/aug-cc-pCVTZ level of theory for sodium and all heavy atoms involved in interactions with sodium cation, with the remaining heavy atoms and hydrogen atoms specified at the MP2(full)/6-311+G(2d,2p) level of theory. It has been suggested that calculations involving sodium cation should include core-core and core-valence electron correlation.[132, 133] The aug-cc-pCVTZ basis set[134, 135] has been optimized for use with methods that include core-core and core-valence correlation such as MP2(full).

All optimized structures have been verified as minima by performing frequency calculations, in order to provide a guarantee that no imaginary frequencies were present. The calculation of all critical configurations (transition states) have been verified by frequency calculations, in order to ensure that there was only one imaginary frequency present, indicating a first-order saddle point.

5.2 Structural Elucidation of Protonated Caffeine, Protonated Theophylline and the Proton-Bound Dimer of Theophylline and Ammonia

5.2.1 Introduction

It would seem natural to commit all discussion of the IRMPD spectra for the protonated forms of caffeine and theophylline to an individual section before considering the

more complex spectra obtained for the PBDs and SCBDs; however since only the $M(NH_3)H^+$ PBD of theophylline was observable by mass-selected IRMPD, the uniqueness of the situation warrants its own discussion. It will be shown that the mass-selected IRMPD spectra of protonated caffeine and protonated theophylline are useful in aiding in the interpretation of why theophylline was exclusively observed to form a PBD with ammonia under the conditions provided by the experiment.

5.2.2 Protonated Caffeine

Caffeine (**I**) possesses several lone pair electron donation sites, including four nitrogen and two oxygen atoms (**Figure 5.3**). These sites readily facilitate formation of IHB interactions. To aid in determining the most energetically favourable site of IHB formation, it is instructive to find the most probable site of protonation. This is important, since all positive IHB forming reactions involve an initial protonation of one of the association partners. In symmetric association reactions, such as the scheme shown by **Eq. 5.1**, one does not have to consider a difference in proton affinity (PA) and gas basicity (GB) between the monomers.

$$M + MH^+ \rightarrow M_2H^+ \qquad \textbf{5.1}$$

The PA is defined as the negative of the enthalpy change for the exothermic reaction,

$$M + H^+ \rightarrow MH^+ \qquad \textbf{5.2}$$

and therefore a more positive PA implies that a molecule is more likely to be protonated. The GB is defined as the negative of the Gibbs free energy change of the reaction

shown by **Eq. 5.2**, and thus incorporates the contribution made by entropy and temperature upon protonation. All values of Gibbs free energy reported here are calculated at 298 K.

In the case of asymmetric association reactions, such as the scheme shown by **Eq. 5.3**, one should consider the difference in PA and GB between the monomer species (M and N). The species which exhibits the larger PA (or GB) between the pair of monomers is typically preferentially protonated initially, where PA(N) > PA(M) in **Eq. 5.3**.

$$M + NH^+ \rightarrow (MN)H^+ \qquad \textbf{5.3}$$

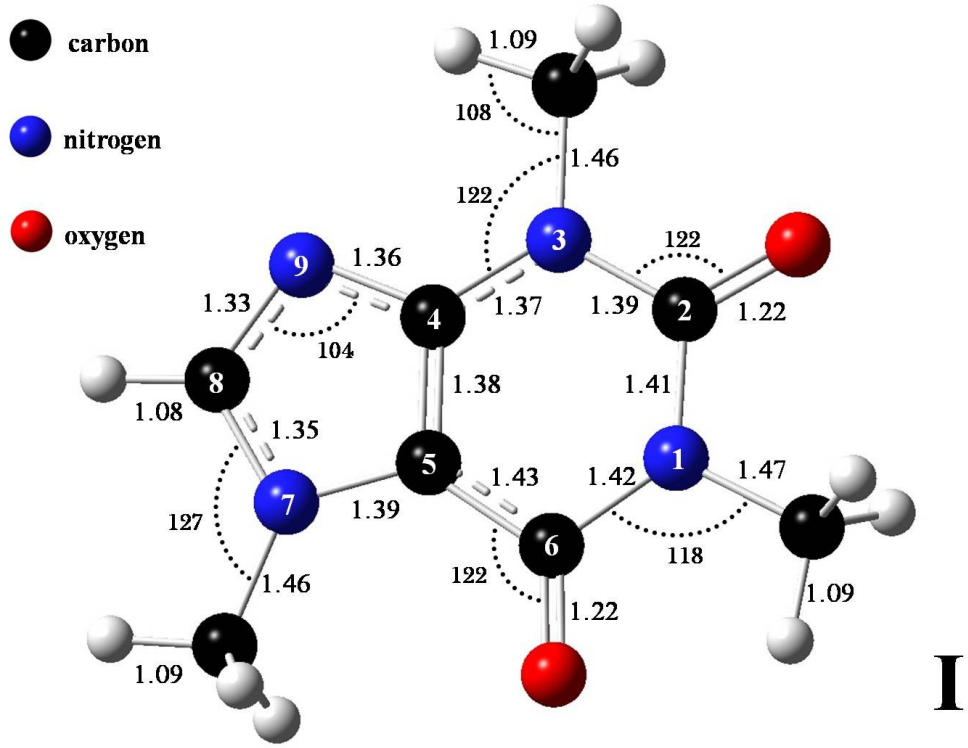

I

Figure 5.3: Calculated structure of caffeine (**I**), with bond lengths in angstroms and angles in degrees. Optimized at the B3LYP/6-311+G(d,p) level of theory.

5.2.2.1 Electronic Structure: Proton Affinities and Gas Basicities of Caffeine

All Lewis basic sites within caffeine were considered and electronic structure calculations have been employed to provide a summary of the absolute and relative PAs and GBs for the proposed protonated isomers (**Figure 5.4**). These values are summarized in **Table 5-1**, where PA and GB are the absolute values and ΔPA and ΔGB are the relative values. The relative energy values are defined with respect to the lowest energy isomer (**II**), where the isomer with the lowest ΔPA and ΔGB is preferentially protonated.

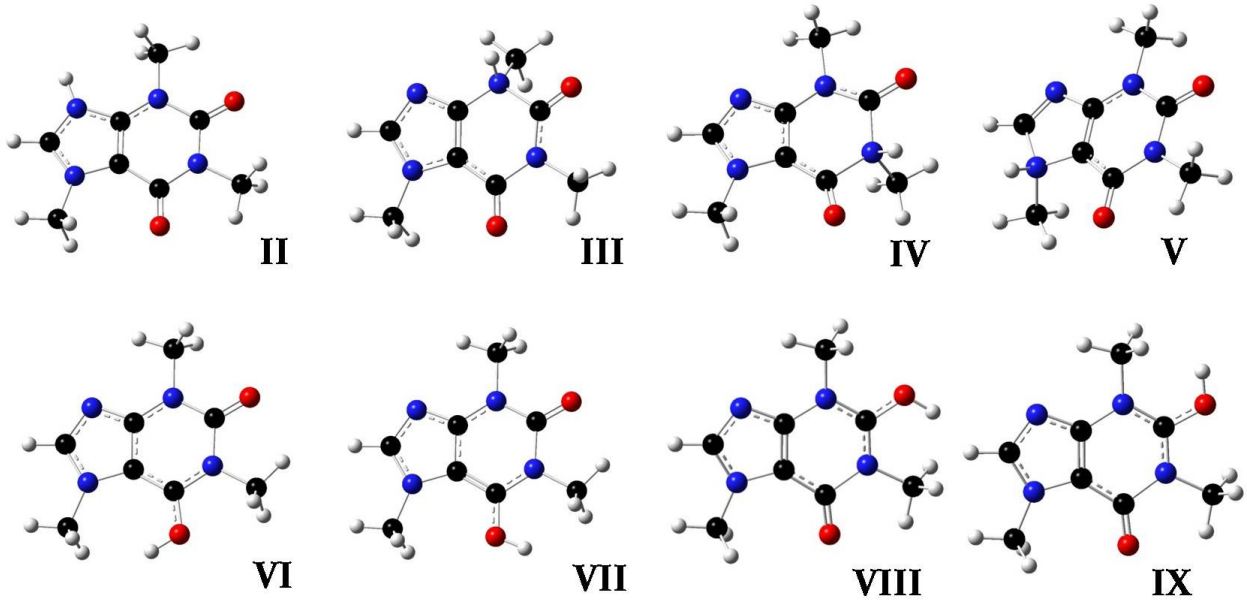

Figure 5.4: Calculated structures of the isomers of protonated caffeine. Optimized at the B3LYP/6-311+G(d,p) level of theory.

Table 5-1: Calculated proton affinities and gas basicities of the possible protonated isomers of caffeine. Energies have been calculated at the MP2/aug-cc-pVTZ//B3LYP/6-311+G(d,p) level of theory (kJ mol^{-1}).

Species	PA	ΔPA	GB (298 K)	ΔGB (298 K)
II	902	0	871	0
III	804	98	772	99
IV	811	91	779	92
V	738	164	703	168
VI	870	32	838	33
VII	877	25	844	27
VIII	885	17	852	19
IX	883	19	850	21

The data summarized in **Table 5-1** show that the dominant site of protonation is expected to occur at the N(9) position in caffeine (**II**). A detailed calculated structure of **II** is given in **Figure 5.5**. The second most favourable site of protonation is expected to be at the C(2) oxygen, as shown in isomer **VIII**. However, based on the ΔGB between the two isomers, **II** is expected to be statistically favoured by a factor of approximately 2000:1 over the formation of **VIII** in the gas phase (298 K). Electronic structure calculations thus reveal that the most probable isomer of protonated caffeine is **II**. The mass-selected IRMPD spectrum of isolated, protonated caffeine was obtained and in conjunction with the results of

electronic structure calculations, it is possible to experimentally determine the structural identity.

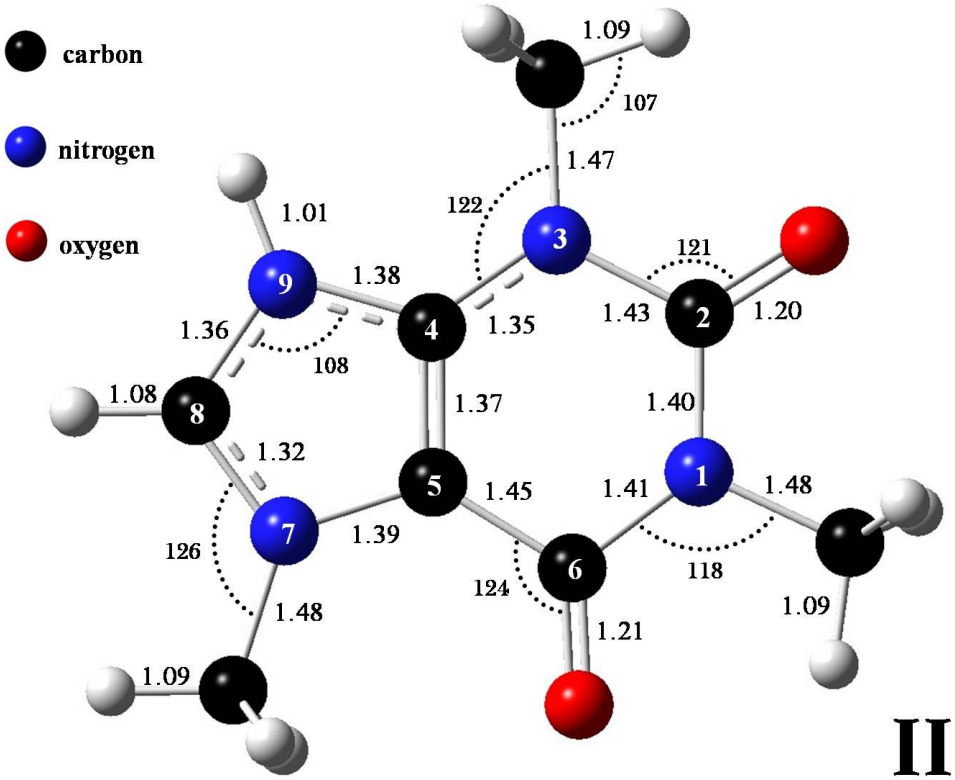

Figure 5.5: Calculated structure of protonated caffeine (II), with bond lengths in angstroms and angles in degrees. Optimized at the B3LYP/6-311+G(d,p) level of theory.

5.2.2.2 Mass-Selected IRMPD: Protonated Caffeine

The gas phase, infrared consequence spectrum of protonated caffeine was obtained and is shown in **Figure 5.6**. The IRMPD spectrum reveals peaks at only the strongest absorbing modes for protonated caffeine. This was not unexpected since breaking bonds within a

covalent species requires significantly more energy than doing so for an electrostatically bound species. Following the FEL irradiation of isolated, protonated caffeine (*m/z* 195), a single product ion with *m/z* 138 was observed. Two forms of the product ion with *m/z* 138 have been proposed (**Figure 5.7**) and the mechanism for dissociation of protonated caffeine is best described as a retro-hetero-Diels-Alder process. Fragmentation of this nature has been observed for protonated caffeine previously in experiments involving rapid desorption electrospray ionization (DESI) and collision induced dissociation (CID) performed by Scrivens *et al.*[136] The first mechanism proposed for production of the ion with *m/z* 138, was the formation of a β-lactam containing ion (**X**), in addition to loss of methyl isocyanate (**XII**). This process was very high in energy, with the change in Gibbs free energy calculated at approximately 323 kJ mol^{-1}. An alternate and substantially more favourable channel exists, which does not involve forming the ring strained β-lactam, but rather a ketene ion (**XI**), in addition to the loss of **XII**. This process was more favourable, with the Gibbs free energy change calculated at approximately 252 kJ mol^{-1}. Although the latter process was lower in energy than the first mechanism proposed, 252 kJ mol^{-1} is still an appreciable thermodynamic barrier to overcome. The change in Gibbs free energy of activation for dissociation may be considered to be a lower limit, since a critical transition state configuration for such a process was not calculated; however the value must be higher than 252 kJ mol^{-1}. Therefore, it requires an absorption in excess of 252 kJ mol^{-1} of FEL photons by the molecule, in order to achieve dissociation within the time scale of irradiation (600 ms). Thus, IRMPD was facilitated by only the strongest IR-absorbing normal modes within protonated caffeine. The

loss of neutral methyl isocyanate from protonated caffeine revealed that protonation did not occur at the C(2) oxygen, since there was no peak observed at *m/z* 58, corresponding to the loss of protonated methyl isocyanate.

The assignment of the IRMPD frequencies was extremely useful in determining the structure of the protonated form of **I**. Peak assignments for the IRMPD spectrum of protonated caffeine (**Figure 5.6**) are shown in **Table 5-2**. Referring to **Figure 5.6**, it was evident that the IRMPD spectrum of protonated caffeine is best represented by the calculated spectrum of isomer **II**. Protonation of either of the two carbonyl oxygen atoms in caffeine would have resulted in an increase in the length of the oxygen carbon bond, an increase in single bond character and a decrease in the bond energy. For example, the oxygen-carbon bond of the free carbonyl located at C(6) in isomer **VIII** has a length of 1.20 Å, while the protonated carbonyl at C(2) has an oxygen-carbon bond length of 1.32 Å. The effect of a weakened bond would then be demonstrated by a large red-shift in the frequency of the free carbonyl stretch. Such a shift, would be evident in the IRMPD spectrum of protonated caffeine and was not observed. The IRMPD spectrum showed the symmetric and asymmetric stretching modes of the free C(2) and C(6) carbonyls, occurring at 1757 and 1723 cm^{-1}, respectively. Protonation of either carbonyl would have shifted the frequency closer to 1600 cm^{-1} and was calculated to occur at 1593 cm^{-1} for isomer **VIII**. Another strong absorption peak would have appeared around 1650 cm^{-1}, corresponding to the proton bend of a protonated carbonyl, however, this was also absent in the IRMPD spectrum.

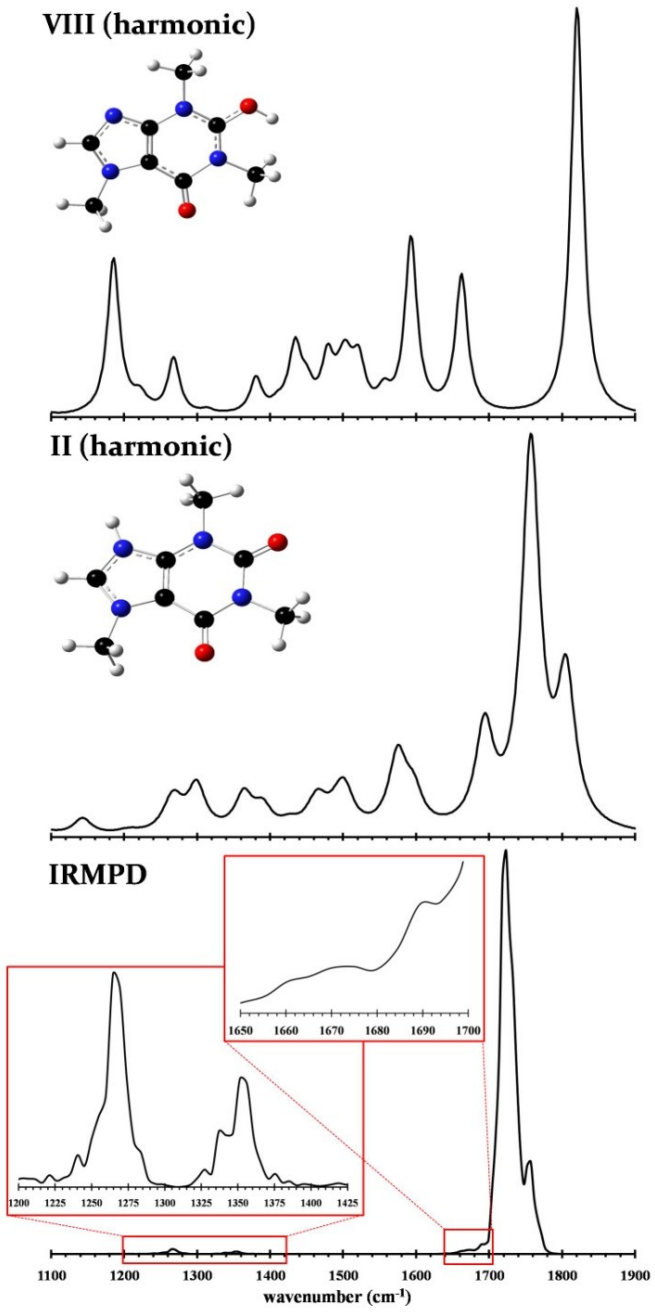

Figure 5.6: IRMPD spectrum of protonated caffeine (bottom) and the spectra of two of the lowest energy isomers determined by calculation at the B3LYP/6-311+G(d,p) level of theory. Harmonic frequencies have been scaled by 0.9679. Intensities for the experimental and calculated spectra are in relative units of IRMPD efficiency and km mol^{-1}, respectively.

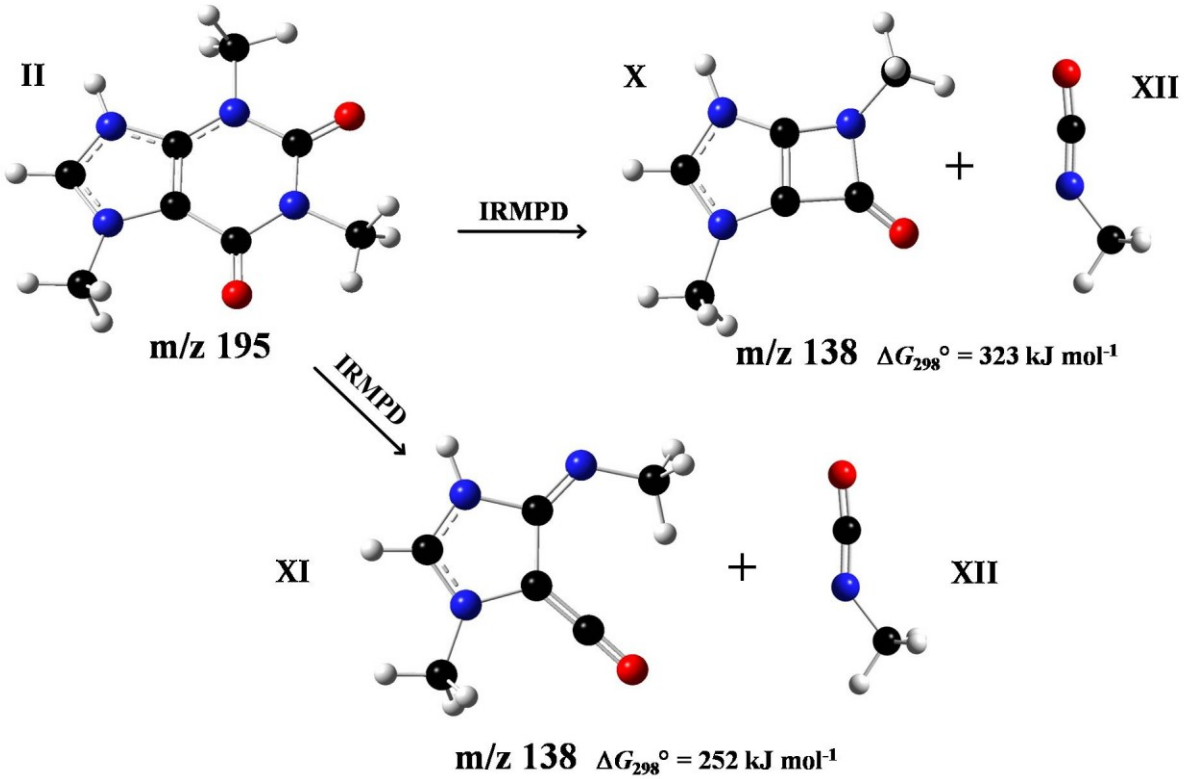

Figure 5.7: Proposed fragmentation scheme of **II** following IRMPD. Energies have been obtained at the MP2/aug-cc-pVTZ//B3LYP/6-311+G(d,p) level of theory.

If protonation were to occur at N(9), then several N(9)-H proton wag and combination modes would be expected. Such proton wag and combination modes were found to exist at 1675, 1351 and 1264 cm^{-1}, in the IRMPD spectrum of protonated caffeine.

Table 5-2: Infrared peak assignments associated with the IRMPD and calculated spectra of protonated caffeine presented in **Figure 5.6**. The frequencies are assigned in units of wavenumbers (cm^{-1}).

Vibrational Mode	IRMPD	II (harmonic)	VIII (harmonic)
*** 2 x C=O stretch (symm.)**	1757	1805	----
*** 2 x C=O stretch (asymm.)**	1723	1757	1821
***C(2)=O-H^+ bend**	----	----	1662
*** C(2)=O-H^+ stretch**	----	----	1593
*** N(9)-H^+ wag + C(4)=C(5) stretch**	1675	1694	----
*** N(9)-H^+ wag + C(5)=N(7) stretch**	1351	1390	----
*** N(9)-H^+ + C(8)-H wag(s)**	1264	1299	----

The evidence provided by the IRMPD spectrum of protonated caffeine, coupled with the results of electronic structure calculations strongly supports that the principal site of protonation as occurring at N(9) in caffeine. Although the calculated, harmonic frequencies obtained for **II** were in better agreement with the IRMPD spectrum, relative to **VIII**, anharmonic frequencies were also calculated for **II**, in order to determine if a better reproduction of the IRMPD spectrum would be obtained. The anharmonic spectrum of **II** is shown in **Figure 5.8**.

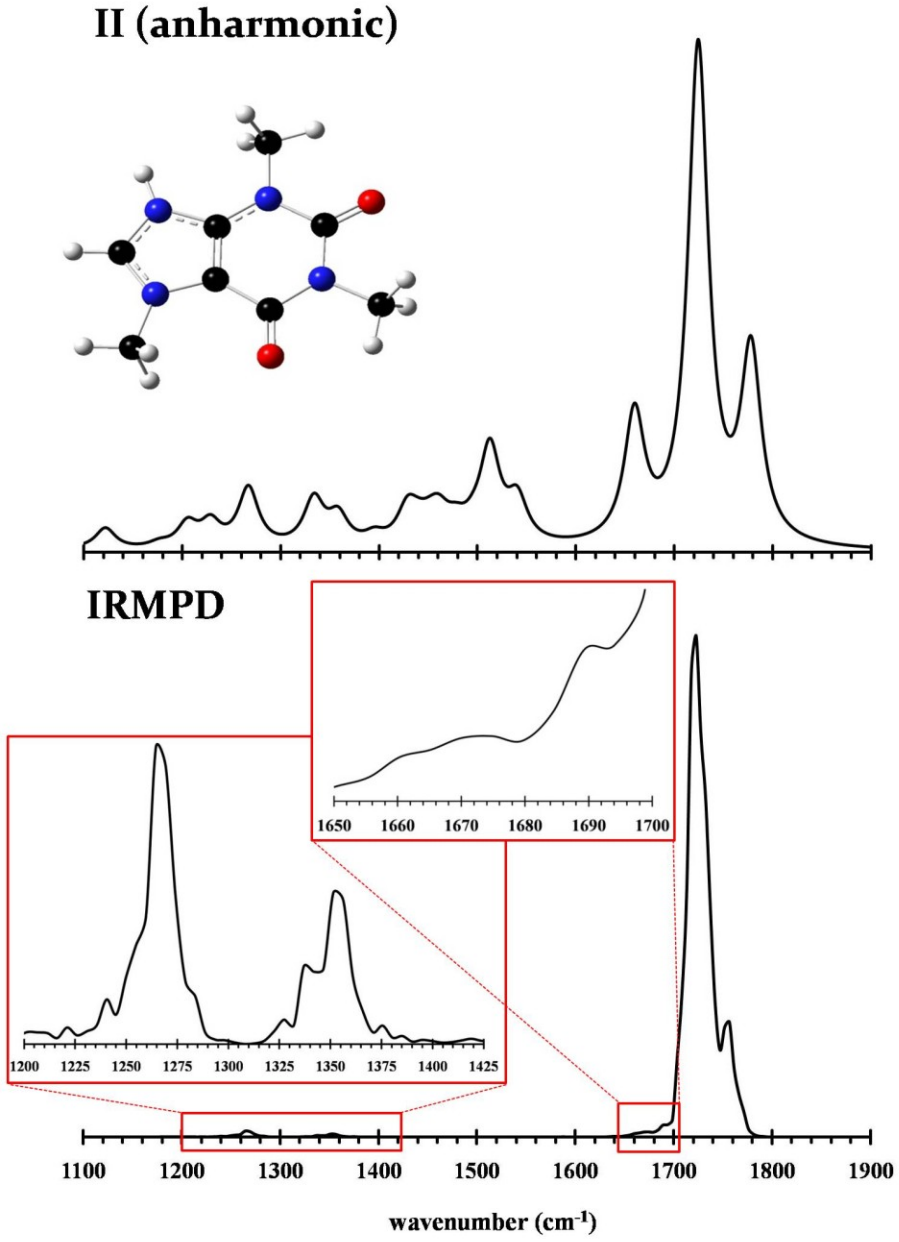

Figure 5.8: IRMPD spectrum of protonated caffeine (bottom) and the calculated anharmonic spectra of isomer **II**, determined by calculation at the B3LYP/6-311+G(d,p) level of theory. Intensities for the experimental and calculated spectra are in relative units of IRMPD efficiency and km mol^{-1}, respectively.

Table 5-3: Infrared peak assignments associated with the IRMPD, anharmonic and harmonic calculated spectrum of protonated caffeine (**II**), presented in **Figure 5.8**. The mean absolute deviation (MAD) of calculated frequencies from the obtained IRMPD values are shown. All values are assigned in units of wavenumbers (cm^{-1}).

Vibrational Mode	IRMPD	II (anharmonic)	II (harmonic)
*** 2 x C=O stretch (symm.)**	1757	1778	1805
*** 2 x C=O stretch (asymm.)**	1723	1724	1757
*** N(9)-H^+ wag+ C(4)=C(5) stretch**	1675	1659	1694
*** N(9)-H^+ wag + C(5)=N(7) stretch**	1351	1357	1390
*** N(9)-H^+ + C(8)-H wag(s)**	1264	1267	1299
MAD from IRMPD	0	9	36

There was a notable improvement in the match between the IRMPD spectrum and calculated anharmonic spectrum over that of the calculated harmonic spectrum of **II**. The mean absolute deviation (MAD) of the calculated harmonic frequencies from the IRMPD obtained frequencies, for **II,** was 36 cm^{-1}. The MAD of the calculated anharmonic frequencies relative to the IRMPD frequencies for **II** was only 9 cm^{-1}. The structure of the protonated isomer of caffeine is thus concluded to be represented by isomer **II**.

5.2.3 The Proton-Bound Dimer of Ammonia and Caffeine

One of the main goals of this work was to examine the IHB interactions between ammonia and protonated caffeine. Ammonia is chosen as a prototypical molecule for studying ionic interactions with the biologically relevant species caffeine and theophylline,

since the R-NH_3^+ functionality is abundant in proteins and peptides. It was found however that isolation of a usable intensity of such ions, for the purpose of FEL irradiation, was impossible under the experimental conditions. Unlike protonated caffeine (**II)**, where the covalently bound structure is extremely robust, the proton-bound dimer (PBD) of ammonia and caffeine is formed *via* much weaker electrostatic IHB interactions. These weakly bound IHB interactions may then have facilitated premature dissociation of the parent ion, due to collisions with the helium buffer gas contained within the ion trap. In order to produce a useful IRMPD spectrum, the parent ion must principally dissociate as a result of being irradiated by the FEL. Another factor leading to difficulty in obtaining the IRMPD spectrum of the PBD of ammonia and caffeine was due to laser intensity. The definition of the IRMPD efficiency (**Eq. 1.1**), demands that a fraction of the parent ion population remain following induced dissociation. If the value of the parent ion intensity approaches zero, then the value of P_{frag} approaches infinity, resulting in signal saturation. Because the laser intensity caused complete dissociation of the parent ion, then one solution attempted was the attenuation of the FEL beam. Attenuation of the laser intensity results in the deposition of fewer photons into the molecule within the irradiation time. Although several attenuation levels of the beam (2X, 4X, 6X and 8X) were attempted, the PBD of ammonia and caffeine was found to be too fragile to isolate. As shown below, protonated theophylline was able to form a more stable PBD with ammonia, which allowed for the production of an IRMPD spectrum. Before it was understood why PBD formation was possible for theophylline and not for caffeine, it was considered to be useful to examine the calculated binding energies for the proposed isomers

of the PBD of caffeine and ammonia. Optimized structures for each of the calculated isomers are presented in **Figure 5.9**. The standard change in enthalpy and Gibbs free energy of binding for each isomer is shown in **Table 5-4**. The calculated Gibbs free energy of binding for all of the proposed PBDs of caffeine and ammonia were found to be quite low when compared to other IHB species that have been successfully studied previously by IRMPD mass spectrometry. For example, Fridgen *et al.* characterized the IRMPD spectra of several homo and hetero PBDs with well defined IHB strengths.[99] Binding energies the IHBs were obtained using high pressure mass spectrometric (HPMS) methods.[137-140] Two of the PBDs studied included dimethyl ether and tetrahydrofuran, with the average literature values, of the change in Gibbs free energy of binding, of 92.8[137, 140] and 91.8[138, 139] kJ mol^{-1}, respectively. The most strongly bound PBD of ammonia and caffeine (**XVI**) possessed a calculated Gibbs free energy of binding of only 68.2 kJ mol^{-1}, which is significantly weaker than the IHBs found in the proton-bound ether systems described above.

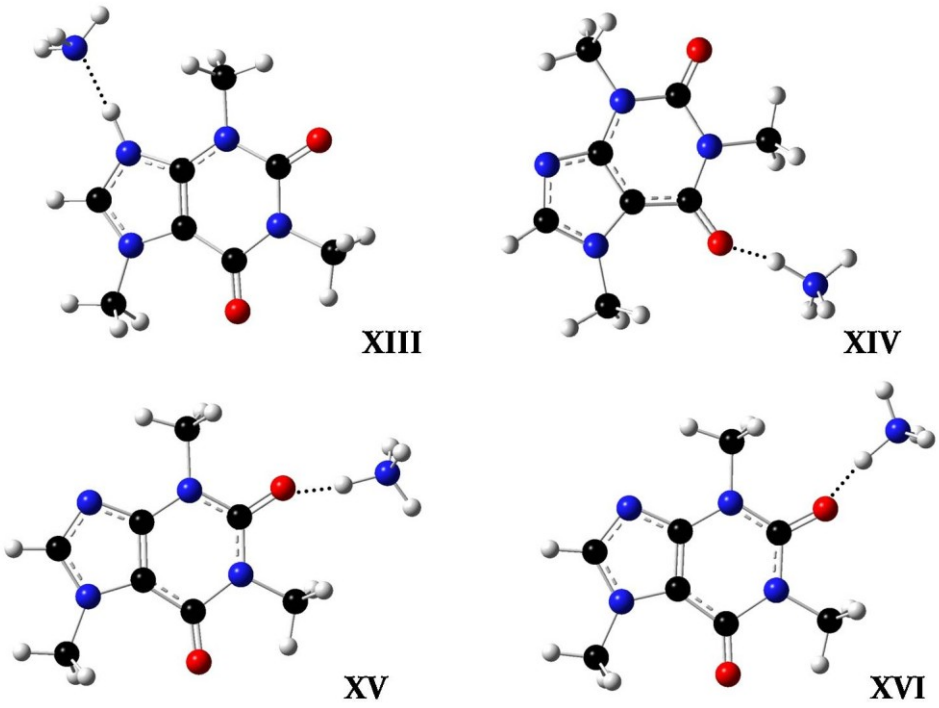

Figure 5.9: Calculated structures of the isomers of the PBD of ammonia and caffeine. Optimized at the B3LYP/6-311+G(d,p) level of theory.

Table 5-4: Calculated energies of the isomers produced by association of ammonia with protonated caffeine. Energies have been obtained at the MP2/aug-cc-pVTZ//B3LYP/6-311+G(d,p) level of theory. Energies are reported in kJ mol^{-1}.

Species	ΔH°_{rxn}	ΔG°_{298}
XIII	-80.5	-44.3
XIV	-98.5	-60.9
XV	-100.7	-66.0
XVI	-100.8	-68.2

5.2.4 Protonated Theophylline

Similarly to caffeine (**I**), theophylline (**XVII**) possesses several lone pair electron donation sites, including four nitrogen and two oxygen atoms (**Figure 5.10**). The difference between the structure of **I** and **XVII** is the substitution of the CH_3 moiety in **I** with hydrogen at the N(7) position in **XVII**. The location of hydrogen at the N(7) position, places it within close proximity of the C(6) oxygen. This structural arrangement was found to have interesting consequences in terms of both the appearance of the protonated spectrum of **XVII** and the ability to obtain a spectrum involving PBD formation with ammonia. As was provided for **I** previously, energetic arguments follow for the initial site of protonation of **XVII**.

5.2.4.1 Electronic Structure: Proton Affinities and Gas Basicities of Theophylline

All possible Lewis basic sites within **XVII** were considered and electronic structure calculations were employed to provide a summary of the absolute and relative PAs and GBs for the proposed protonated isomers of theophylline (**Figure 5.11**). These values are summarized in **Table 5-5**, where PA and GB are absolute values and ΔPA and ΔGB are relative values. The relative energy values are defined with respect to the lowest energy isomer (**XVIII**). The data summarized in **Table 5-5** shows that the site of protonation was expected to occur at the N(9) position in theophylline (**XVIII**). The detailed structure of **XVIII** is given in **Figure 5.12**. The second most likely site of protonation was expected at the C(2) oxygen, as shown in isomer **XXIII**.

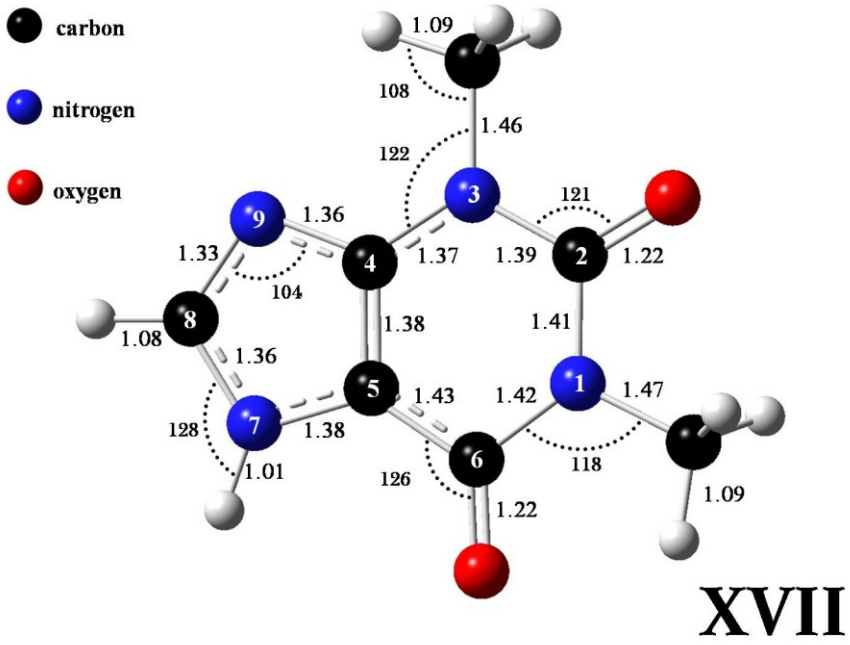

Figure 5.10: Calculated structure of theophylline (**XVII**), with bond lengths in angstroms and angles in degrees. Optimized at the B3LYP/6-311+G(d,p) level of theory.

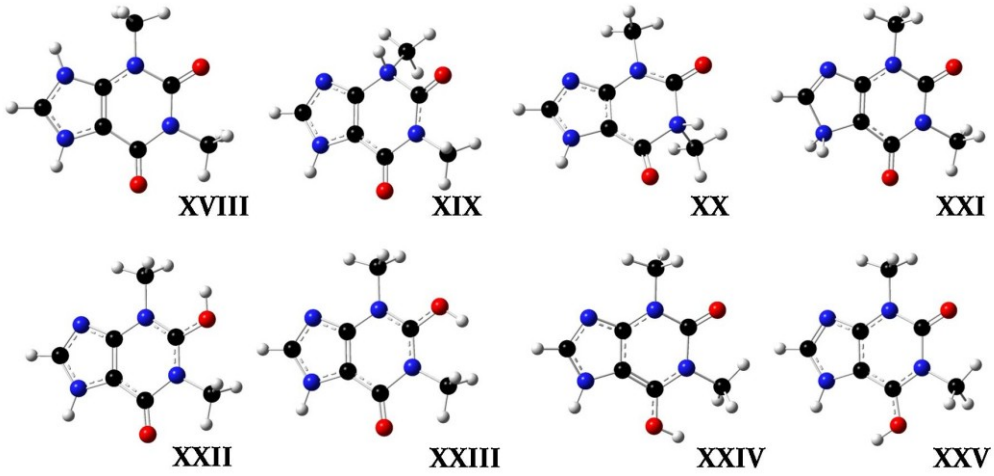

Figure 5.11: Calculated structures of the isomers of protonated theophylline. Optimized at the B3LYP/6-311+G(d,p) level of theory.

However, based on the ΔGB between the two isomers, **XVIII** would be statistically favoured by approximately 50:1 over formation of **XXIII** in the gas phase. Electronic structure calculations have suggested that the most probable isomer of protonated theophylline exists as **XVIII**. The IRMPD spectrum of isolated, protonated theophylline was obtained and was found to reveal a surprisingly more complicated spectrum when compared to the IRMPD spectrum which was obtained for protonated caffeine (**II**).

Table 5-5: Calculated proton affinities (PA) and gas basicities (GB) of the possible protonated isomers of theophylline (**XVII**). Energies have been calculated at the MP2/aug-cc-pVTZ//B3LYP/6-311+G(d,p) level of theory (kJ mol^{-1}).

Species	PA	ΔPA	GB (298 K)	ΔGB (298 K)
XVIII	882	0	851	0
XIX	799	83	768	83
XX	792	90	761	90
XXI	711	171	680	171
XXII	873	9	841	10
XXIII	875	7	842	9
XXIV	869	13	837	14
XXV	861	21	831	20

5.2.4.2 Mass-Selected IRMPD: Protonated Theophylline : Part One

The gas phase, infrared consequence spectrum of protonated theophylline is given in **Figure 5.14**. Like protonated caffeine (**II**), protonated theophylline is a covalently bound species and the IRMPD spectrum reveals peaks at only the strongest absorbing modes. Following the FEL irradiation of isolated, protonated theophylline (*m/z* 181), a single product ion with *m/z* 124 was observed. As with protonated caffeine, two forms of the product ion with *m/z* 124 were proposed (**Figure 5.13**) and the mechanism for dissociation of protonated theophylline can best be described as a retro-hetero-Diels-Alder process.[136] The formation of a β-lactam containing ion (**XXVI**), in addition to loss of methyl isocyanate (**XII**), is very costly in energy, with the change in Gibbs free energy calculated at approximately 320 kJ mol^{-1}. The more favourable dissociation channel formed a ketene ion (**XXVII**), in addition to the loss of **XII**, with a change in Gibbs free energy of 233 kJ mol^{-1}.

In contrast to the IRMPD spectrum of **II**, the spectrum of protonated theophylline contained a strong peak centred at 1632 cm^{-1}. The normal modes which were most likely responsible for such contributions are first, the stretch of a protonated carbonyl carbon-oxygen bond (approximately 1600 cm^{-1}) and second, the proton bending mode (approximately 1650 cm^{-1}) of a protonated carbonyl oxygen.

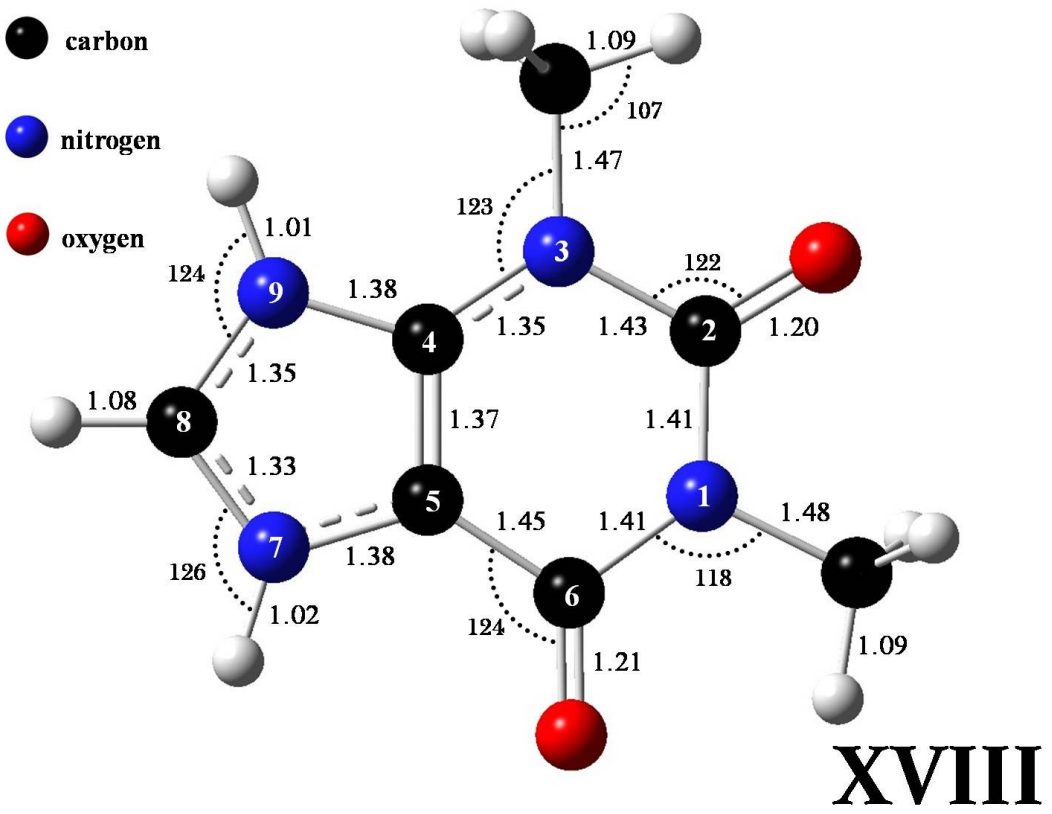

Figure 5.12: Calculated structure of protonated theophylline (**XVIII**), with bond lengths in angstroms and angles in degrees. Optimized at the B3LYP/6-311+G(d,p) level of theory.

Such spectral signatures would suggest the presence of a carbonyl protonated isomer. It could be argued that since the ΔGB between the first two most favourable sites of protonation in **XVII** was substantially smaller than that of in **I**, that a mixture of protonated isomers could have resulted, even though statistically this should not have been the case. The protonation of **I** at N(9) was favoured over protonation of the C(2) oxygen by 2000:1, whereas in **XVII**, protonation of N(9) was favoured over protonation of the C(2) oxygen by

50:1. The ratio 50:1 would amount to 98% of protonation occurring at N(9), however the spectrum would indicate that there was a much larger presence of a carbonyl protonated isomer. The IRMPD spectrum of protonated theophylline, along with the calculated harmonic spectra of the two most probable isomers, is shown in **Figure 5.14**.

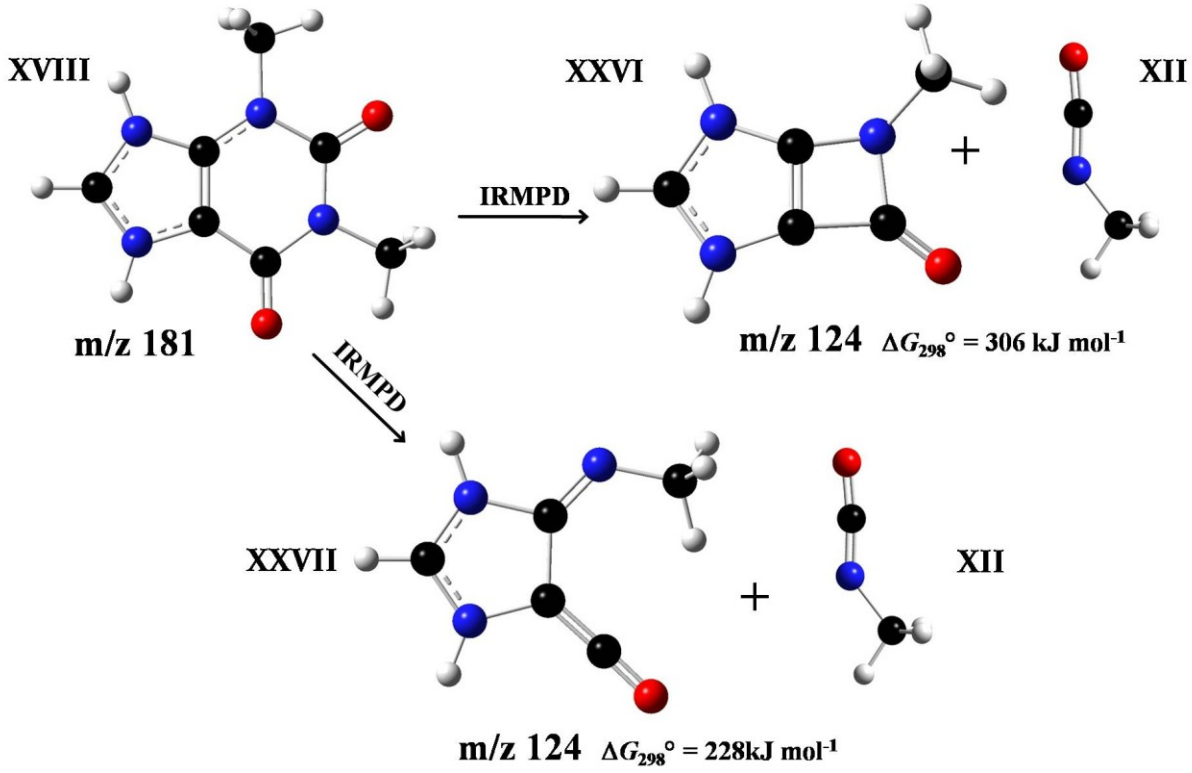

Figure 5.13: Proposed fragmentation scheme of **XVIII** upon IRMPD. Energies have been obtained at the MP2/aug-cc-pVTZ//B3LYP/6-311+G(d,p) level of theory.

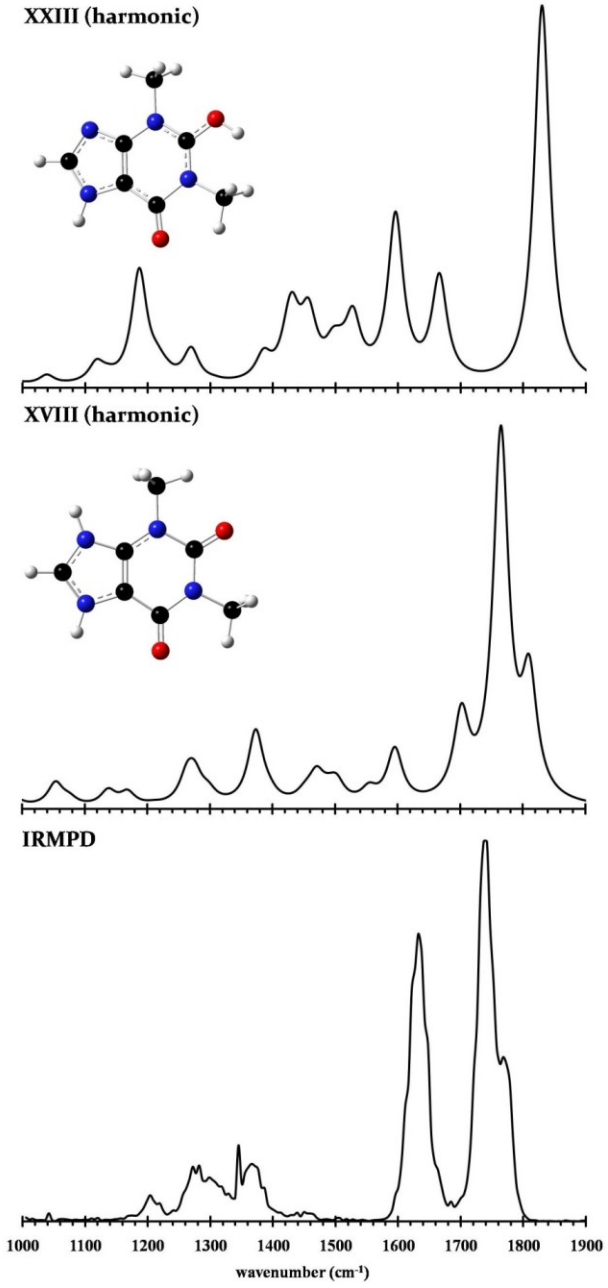

Figure 5.14: IRMPD spectrum of protonated theophylline (bottom) and the spectra of two of the lowest energy isomers determined by calculation at the B3LYP/6-311+G(d,p) level of theory. Harmonic frequencies have been scaled by 0.9679. Intensities for the experimental and calculated spectra are in relative units of IRMPD efficiency and km mol^{-1}, respectively.

Table 5-6: Infrared peak assignments associated with the IRMPD and calculated spectra for protonated theophylline, presented in **Figure 5.14**. The frequencies are assigned in units of wavenumbers (cm^{-1}).

Vibrational Mode	IRMPD	XVIII (harmonic)	XXIII (harmonic)
*** 2 x C=O stretch (symm.)**	1768	1810	----
*** 2 x C=O stretch (asymm.)**	1738	1765	1830
*** C(2)=O-H$^+$ bend + ring deformation**	1632	----	1666
*** C(2)=O-H$^+$ stretch**	----	----	1596
*** N(9)-H wag**	1345	1373	----

It was clear that neither of the calculated harmonic spectra shown in **Figure 5.14** were an especially good match of the IRMPD spectrum obtained for protonated theophylline. Although the isomers, **XVIII** and **XXIII** represent the first and second most probable protonated forms of theophylline, respectively, there is a reasonable explanation for the appearance of the IRMPD spectrum obtained. The combination of the spectra arises from the serendipitous result of preparing the theophylline solutions with the intended purpose of observing the PBD of theophylline and ammonia. The solutions were prepared with ammonium chloride and theophylline in a mole ratio of approximately 2:1, respectively. The excess of ammonium chloride was provided to ensure an environment where protonated, PBD and ammoniated species would all have existed in abundance. This was found to work very well, since the ion trap mass spectrometer was able to isolate any of such species from

the single solution sample. It can be proposed that the formation of the PBD between theophylline and ammonia had catalyzed the formation of a mixture of protonated theophylline isomers. To better understand such a phenomenon, the IRMPD spectrum of the PBD of theophylline and ammonia is presented and then, the IRMPD spectrum of protonated theophylline revisited.

5.2.5 Mass-Selected IRMPD: The Proton-Bound Dimer of Theophylline and Ammonia

The fragility of the weak IHB formed between ammonia and protonated caffeine leads to the inability to isolate the PBD for the purpose of IRMPD. This was rationalized by the correspondingly low binding energy of the IHB formed in all of the proposed isomers of the PBD between ammonia and caffeine (**Table 5-4**). Similarly, PBDs of theophylline and ammonia can be proposed (**Figure 5.15**) and their structures and energies (**Table 5-7**) calculated. The isomers, **XXVIII**, **XXX**, **XXXI** and **XXXII**, like the PBDs of caffeine and ammonia, exhibited relatively low IHB energies, which would imply that none of these species should be isolable in the ion trap mass spectrometer. There is however one form of the PBD of theophylline and ammonia which is found to be highly stabilized relative to all of the other isomers. The isomer, **XXIX** was unique in that it contained a double IHB between ammonium and theophylline. This results in a calculated Gibbs free energy change of binding for **XXIX** 22.5 kJ mol^{-1} lower than that of the second most likely isomer, **XXXI**. The statistical ratio of forming **XXIX** to **XXXI** would then be approximately 7000:1, respectively, in favour of **XXIX**.

The most probable mechanism for describing the formation of **XXIX**, must begin with the assumption that the protonated form of theophylline exists as, **XVIII**. Upon protonation at N(9) in **XVII**, the hydrogen atom located at N(7) is made partially positive due to resonance about N(7), C(8) and N(9). This results in an increase of the N(7) hydrogen atom acidity and, consequently, an increase in the ability to act as a hydrogen bond donor. After protonation of **XVII**, the length of the N(7) and N(9) N-H bonds in **XVIII** are 1.02 and 1.01 Å, respectively, making them nearly equal (**Figure 5.12**). The Mulliken charge distributions for both **XVII** and **XVIII** have been calculated at the B3LYP/6-311+G(d,p) level of theory and are shown in **Figure 5.16**. In **XVIII**, the partial positive charges found on the N(7) and N(9) hydrogen atoms are 0.384 and 0.376, respectively. In **XVII**, the partial positive charge on the N(7) hydrogen atom is originally 0.326, which reveals an increase in the partial charge on the N(7) hydrogen atom of +0.058 units upon protonation at N(9) in **XVII**. The next step involves the addition of ammonia to **XVIII** to form **XXIX**. Although the solution that was prepared began with the specific addition of ammonium chloride and theophylline, it is important to recognize that ammonium ion would always be in equilibrium with ammonia. The abundance of free ammonia in a solution of ammonium, independent of theophylline, is very low. Because the PA and GB of theophylline exceed those of ammonia, theophylline can be expected to remove a proton from ammonium to yield free ammonia. As the free ammonia became bound to protonated theophylline, in solution the production of more ammonia and the clustering reaction would have increased. No literature values for the PA and GB of theophylline were found. The calculated PA and GB of theophylline, to

produce isomer **XVIII**, are 881 and 852 kJ mol^{-1}, respectively. The literature values of PA and GB, for ammonia[141] are 854 and 819 kJ mol^{-1}, respectively. The calculated PA and GB of ammonia were determined to be 849 and 818 kJ mol^{-1}, respectively, for both the MP2/aug-cc-pVTZ//B3LYP/6-311+G(d,p) and MP2/aug-cc-pVQZ//B3LYP/6-311+G(d,p) levels of theory, demonstrating basis set convergence at the MP2/aug-cc-pVTZ//B3LYP/6-311+G(d,p) level of theory and excellent agreement with the values reported in the literature.

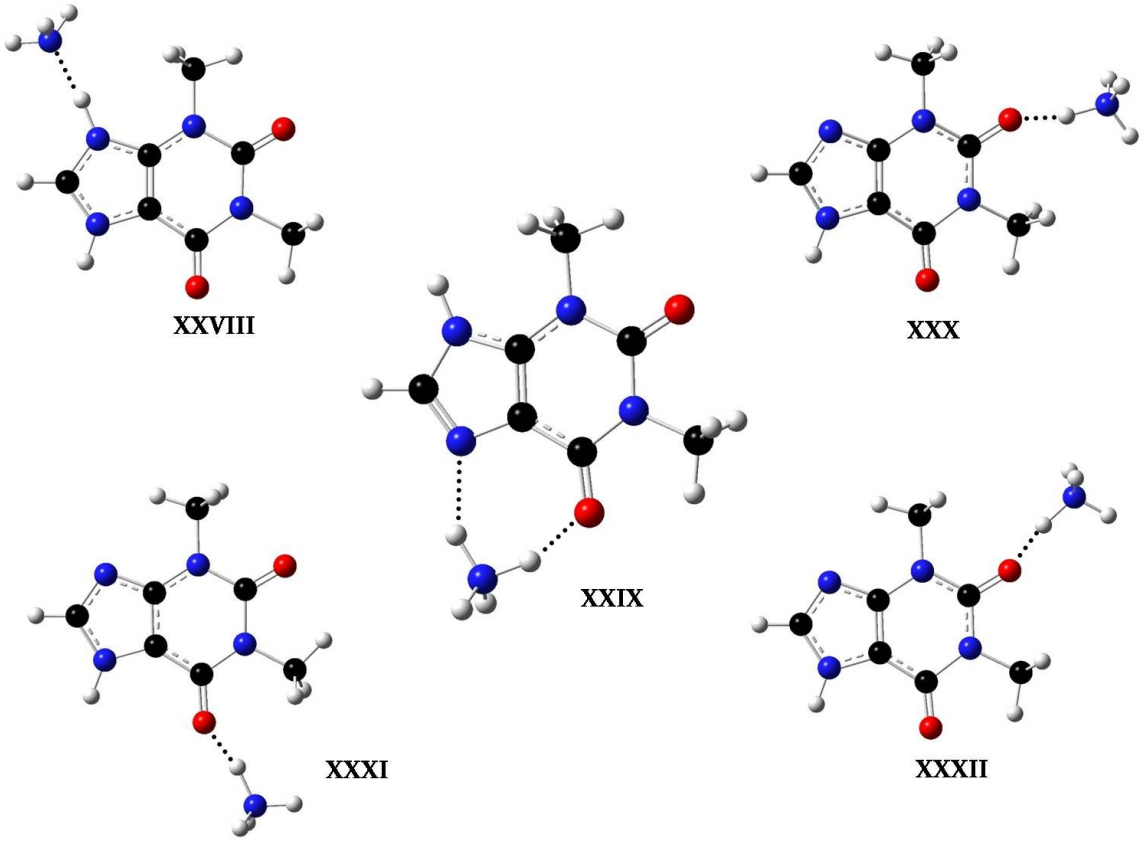

Figure 5.15: Calculated structures of the isomers of ammoniated theophylline. Optimized at the B3LYP/6-311+G(d,p) level of theory.

Table 5-7: Calculated energies of the isomers produced by association of ammonia with protonated theophylline. Energies have been obtained at the MP2/aug-cc-pVTZ//B3LYP/6-311+G(d,p) level of theory. Energies are reported in kJ mol^{-1}.

Species	ΔH°_{rxn}	ΔG°_{298}
XXVIII	-98.6	-64.5
XXIX	-142	-101
XXX	-112	-78.1
XXXI	-97.8	-66.4
XXXII	-105	-70.9

The IRMPD spectrum of ammoniated theophylline is shown in **Figure 5.17**, along with the calculated spectra of the two most favourable isomers, **XXIX** and **XXX**. An important feature found in the spectrum, was the abundance of peaks generated across the entire frequency range. This contrasts markedly with the spectra of protonated caffeine and theophylline. The IRMPD of ammoniated theophylline, which exists as a weakly-bound, electrostatic complex, requires the absorption of far fewer photons than the covalently-bound, protonated ions. If the binding energy of the ion is too high, then spectral information would be lost due to lack of fragmentation. Specifically, this should have occurred when the vibrational modes of low absorption intensity failed to absorb a number of quanta sufficient to reach the dissociation threshold of the ion. This is demonstrated by the IRMPD spectra of both protonated caffeine and theophylline. When the binding energy is too low, then the parent ion dissociates prematurely, as was the case for the PBD of ammonia and caffeine.

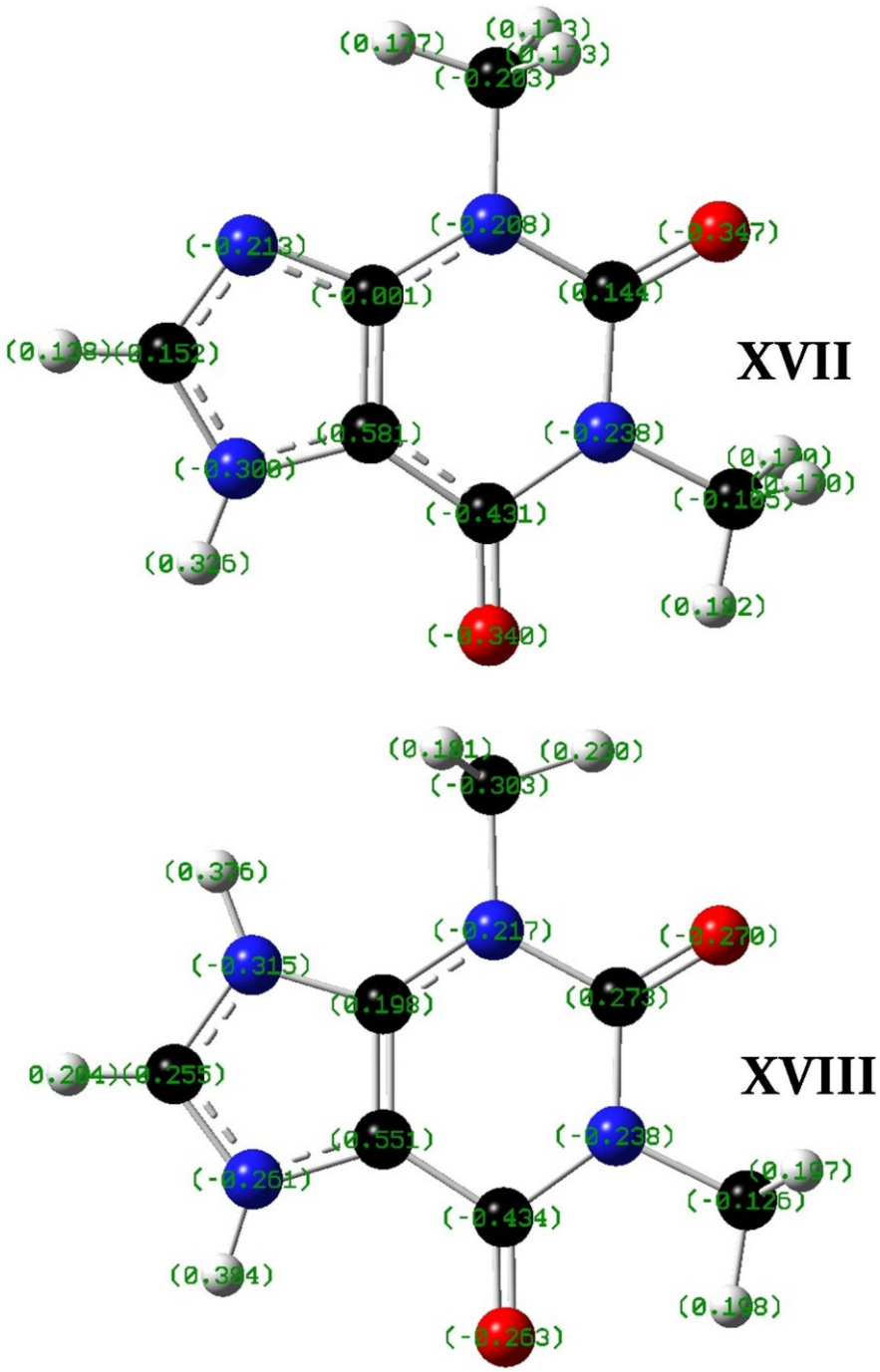

Figure 5.16: Mulliken charge distributions for both **XVII** and **XVIII** calculated at the B3LYP/6-311+G(d,p) level of theory.

The IRMPD spectrum of ammoniated theophylline has several large and well defined peaks (**Figure 5.17**). In the IRMPD spectrum of ammoniated theophylline, the observed oxygen-carbon stretching modes corresponding to the C(2) and C(6) carbonyls occur at 1757 and 1591 cm^{-1}, respectively. The red-shift of the C(6) carbonyl stretching frequency is characteristic of the presence of a protonated carbonyl oxygen. The peak centred at 1646 cm^{-1} is the combination of a NH_4 asymmetric bend, N(9)-H wag and C(4)=C(5) stretch. The dominant peak in the spectrum centred at 1646 cm^{-1} is indicative of a pure NH_4 asymmetric bend. The calculated harmonic spectra of the two most favourable isomers of ammoniated theophylline, **XXIX** and **XXX**, are shown along with the IRMPD spectrum in **Figure 5.17**. Qualitatively, the calculated harmonic spectrum of isomer **XXIX** would appear to represent better the observed IRMPD spectrum, compared to that of the calculated harmonic spectrum of isomer **XXX**. An important feature missing in the calculated spectrum of isomer **XXX** was the identifying, asymmetric ammonium, N-H bend, centred at 1646 cm^{-1}, in the IRMPD spectrum of ammoniated theophylline. A summary of the proposed normal modes for the IRMPD and calculated harmonic spectra of ammoniated theophylline is given in **Table 5-8**.

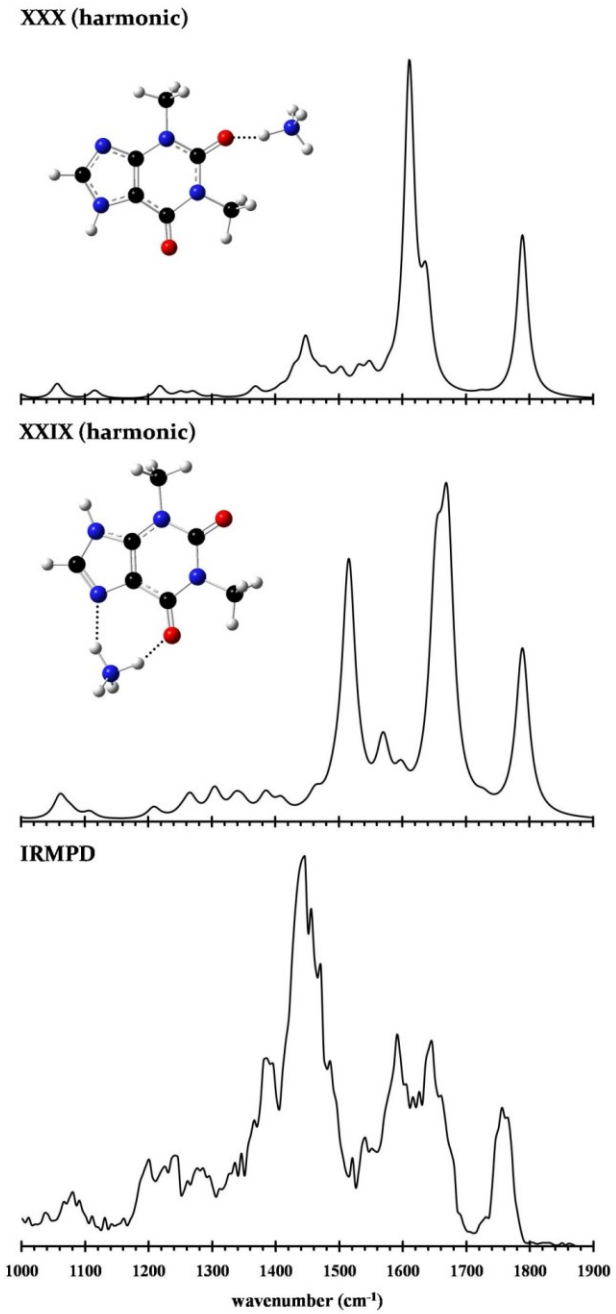

Figure 5.17: IRMPD spectrum of ammoniated theophylline (bottom) and the spectra of two of the lowest energy isomers determined by calculation at the B3LYP/6-311+G(d,p) level of theory. Harmonic frequencies have been scaled by 0.9679. Intensities for the experimental and calculated spectra are in relative units of IRMPD efficiency and km mol^{-1}, respectively.

Table 5-8: Infrared peak assignments associated with the IRMPD and calculated spectra for ammoniated theophylline, presented in **Figure 5.17**. The frequencies are assigned in units of wavenumbers (cm^{-1}).

Vibrational Mode	IRMPD	XIXX (harmonic)	XXX (harmonic)
*** C(2)=O stretch**	1757	1789	----
*** C(2)=O-H^+ stretch**	----	----	1611
*** N(7)-H wag + C(4)=C(5) stretch**	----	----	1637
*** C(6)=O stretch**	----	----	1789
*** C(6)=O stretch + NH_4 asymm. stretch**	1646	1671	----
*** C(6)=O-H^+ bend + NH_4 asymm. stretch**	1591	1653	----
*** NH_4 asymm. bend**	1446	1515	1593

Although the calculated harmonic spectrum of **XXIX** matched many of the bands observed in the IRMPD spectrum of ammoniated theophylline, the calculation of anharmonic frequencies for **XXIX** was performed in order to further improve the consistency of the calculated spectrum with that of experiment. The anharmonic spectrum of **XXIX** is shown with the IRMPD spectrum of theophylline in **Figure 5.18**. A summary of the IRMPD, anharmonic and harmonic frequencies for species **XXIX** are given in **Table 5-9**. As was demonstrated previously for protonated caffeine (**II**), there was a distinct improvement in the match between the IRMPD spectrum and calculated anharmonic spectrum over that of the calculated harmonic spectrum of **XXIX**. The MAD of the calculated harmonic frequencies

from the IRMPD obtained frequencies, for **XXIX,** is 47 cm^{-1}. The MAD of the calculated anharmonic frequencies relative to the IRMPD frequencies for **XXIX** is only 16 cm^{-1}. Many of the IRMPD obtained frequencies found in the 1000 to 1900 cm^{-1} range are red-shifted of calculated harmonic frequencies, due to the anharmonic nature of real molecular vibrations.

The modes involving the carbonyl stretch and NH_4 bending, located at 1646 and 1591 cm^{-1} in the IRMPD spectrum, are both higher in frequency than those predicted by the anharmonic calculation at 1622 and 1578 cm^{-1}, respectively. This would suggest that the anharmonic frequency procedure may overcompensate for the anharmonic nature of modes involving the vibrational motion of several coupled nuclei.

Based on energetic considerations, and the IRMPD and calculated spectra of **XXIX**, it is thus reasonable to conclude that the most probable structure of ammoniated theophylline is **XXIX**. A detailed structure of **XXIX** is shown in **Figure 5.19**. Confirmation of the structure of **XXIX**, allows for an explanation of the anomalous detail observed in the IRMPD spectrum of protonated theophylline.

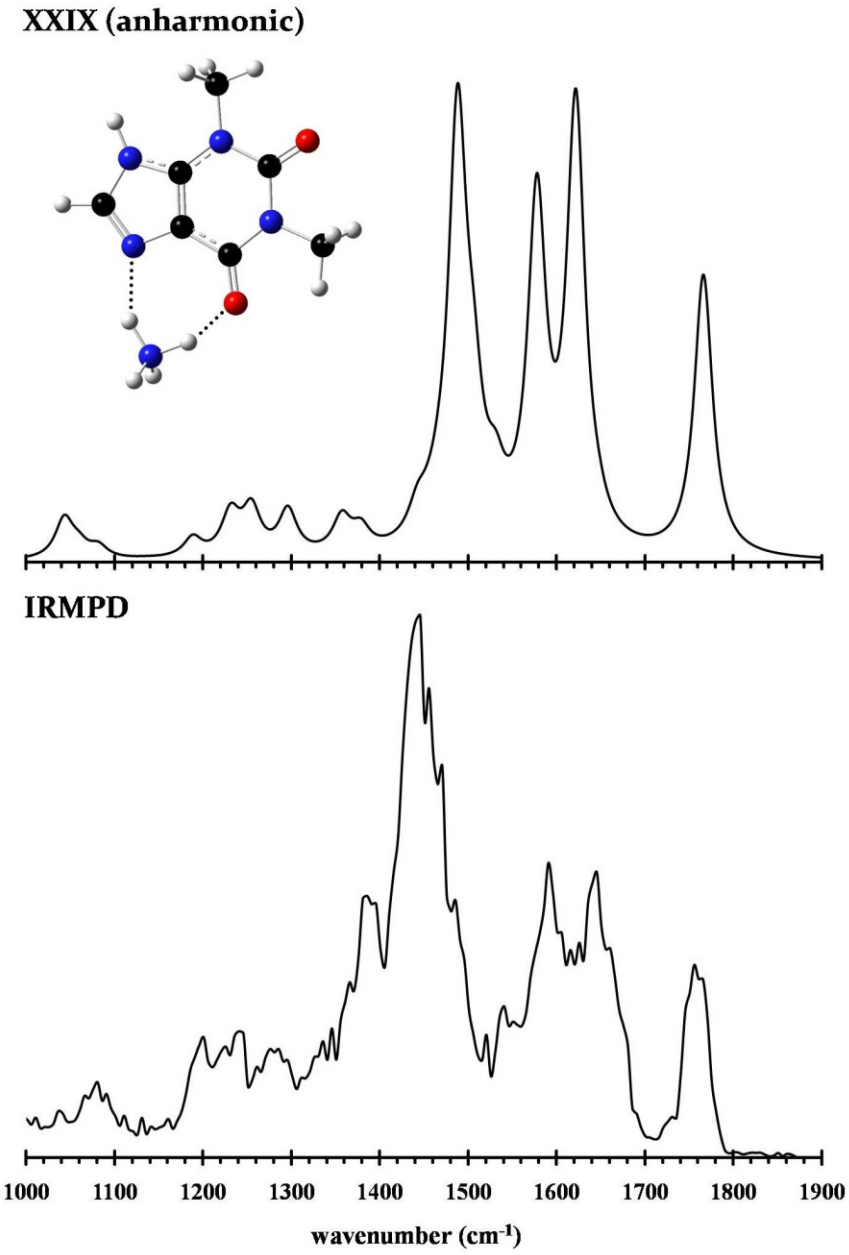

Figure 5.18: IRMPD spectrum of ammoniated theophylline (bottom) and the calculated anharmonic spectrum of isomer **XXIX**, determined by calculation at the B3LYP/6-311+G(d,p) level of theory. Intensities for the experimental and calculated spectra are in relative units of IRMPD efficiency and km mol^{-1}, respectively.

Table 5-9: Infrared peak assignments associated with the IRMPD and calculated spectra for ammoniated theophylline, presented in **Figure 5.18**. The mean absolute deviation (MAD) of calculated frequencies from obtained IRMPD values are shown. All values are assigned in units of wavenumbers (cm^{-1}).

Normal Mode Identity	IRMPD	XXIX (anharmonic)	XXIX (harmonic)
*** C(2)=O stretch**	1757	1766	1789
*** C(6)=O stretch + NH_4 asymmetric stretch**	1646	1622	1671
*** C(6)=O-H^+ bend + NH_4 asymmetric stretch**	1591	1578	1653
*** NH_4 asymmetric bend**	1446	1465	1515
MAD from IRMPD	0	16	47

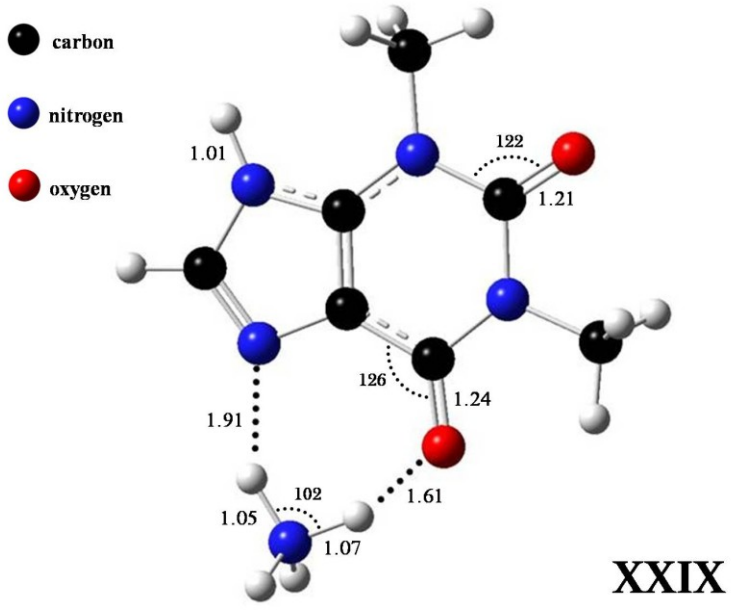

Figure 5.19: Calculated structure of ammoniated theophylline (**XXIX**), with bond lengths in angstroms and angles in degrees. Optimized at the B3LYP/6-311+G(d,p) level of theory.

5.2.5.1 Mass-Selected IRMPD: Protonated Theophylline: Part Two

The IRMPD spectrum of protonated theophylline (**Figure 5.14**) demonstrates that neither of the suggested products of direct protonation of theophylline, **XVIII** and **XXIII,** were ideal matches for the IRMPD spectrum obtained. Because the solutions of protonated theophylline were prepared in the same manner as those to produce the ammoniated theophylline ion (**XXIX**), it can be proposed that another isomer of protonated theophylline exists as a product of proton-transport catalysis (PTC). There are several detailed studies by Terlouw and coworkers that demonstrate the isomerism of gaseous ionic clusters, involving the phenomenon of PTC.[142-144] The IRMPD spectrum of protonated theophylline (**Figure 5.14**) implies the presence of a carbonyl protonated isomer. The series of protonated theophylline isomers, shown in **Figure 5.11**, could only occur as a result of direct protonation. The IRMPD spectrum of protonated theophylline shows a mixture of two isomers: The first isomer is **XVIII** while the second isomer is proposed to be the result of proton-transport catalysis by ammonia as presented in **Figure 5.20** to yield **XXXIII**.

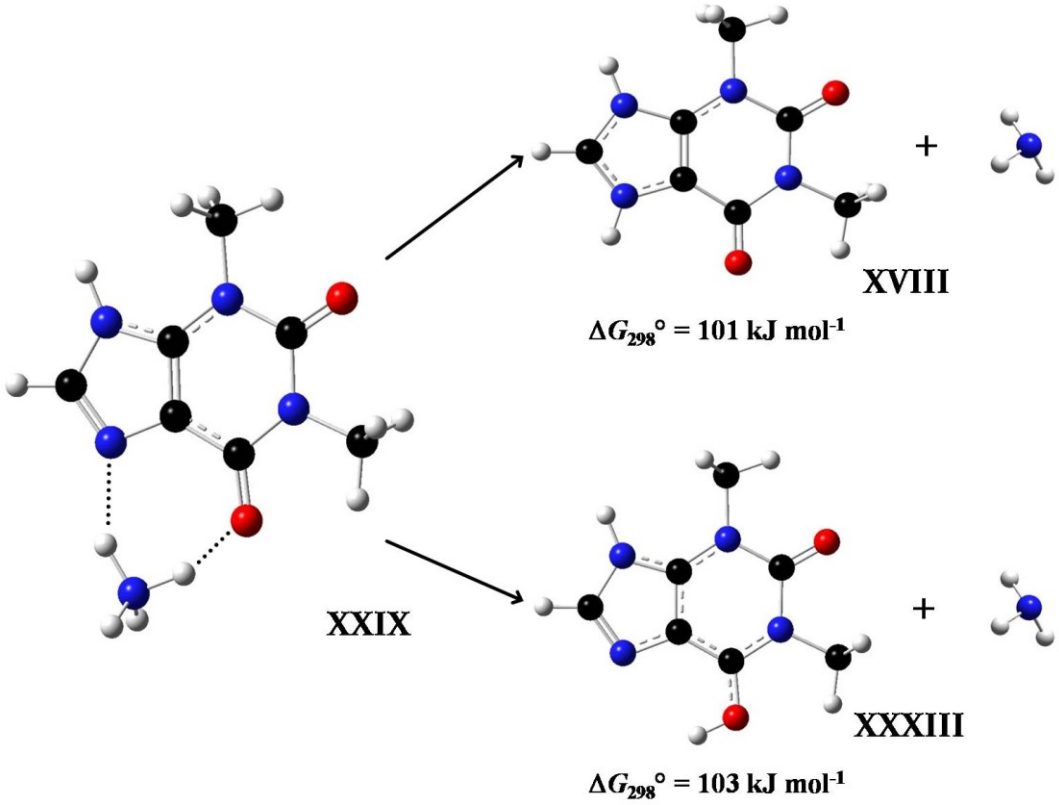

Figure 5.20: Proposed dissociation scheme of **XXIX** to afford a mixture of the protonated isomers of theophylline, **XVIII** and **XXXIII**. Energies have been obtained at the MP2/aug-cc-pVTZ//B3LYP/6-311+G(d,p) level of theory.

Figure 5.20 shows that the calculated $\Delta\Delta G_{298}°$ of the production of isomers **XVIII** and **XXXIII** from **XXIX** is only 2.00 kJ mol^{-1} in favour of **XVIII**. This would indicate why there would be a mixture of the two protonated theophylline isomers in the IRMPD spectrum obtained (**Figure 5.14**). Due to the close proximity of N(7) and O(6), in protonated theophylline, the intramolecular proton transfer between N(7) and O(6) was considered and a critical configuration (**XXXIV)** for such a process was found by use of electronic structure

calculations (**Figure 5.21**). The Gibbs free energy changes of activation ($\Delta G_{298}^{\dagger\circ}$ **)** for the unimolecular isomerism of **XVIII** into **XXXIII** are 105 and 103 kJ mol^{-1} for the forward and reverse process, respectively. These calculated barrier values are considerable and would make such an intramolecular process thermally inaccessible. However, the production of isomer **XXXIII** *via* PTC of **XVIII** by ammonia to yield **XXIX** is possible, and consequently **XXIX** could dissociate to produce both **XVIII** and **XXXIII**.

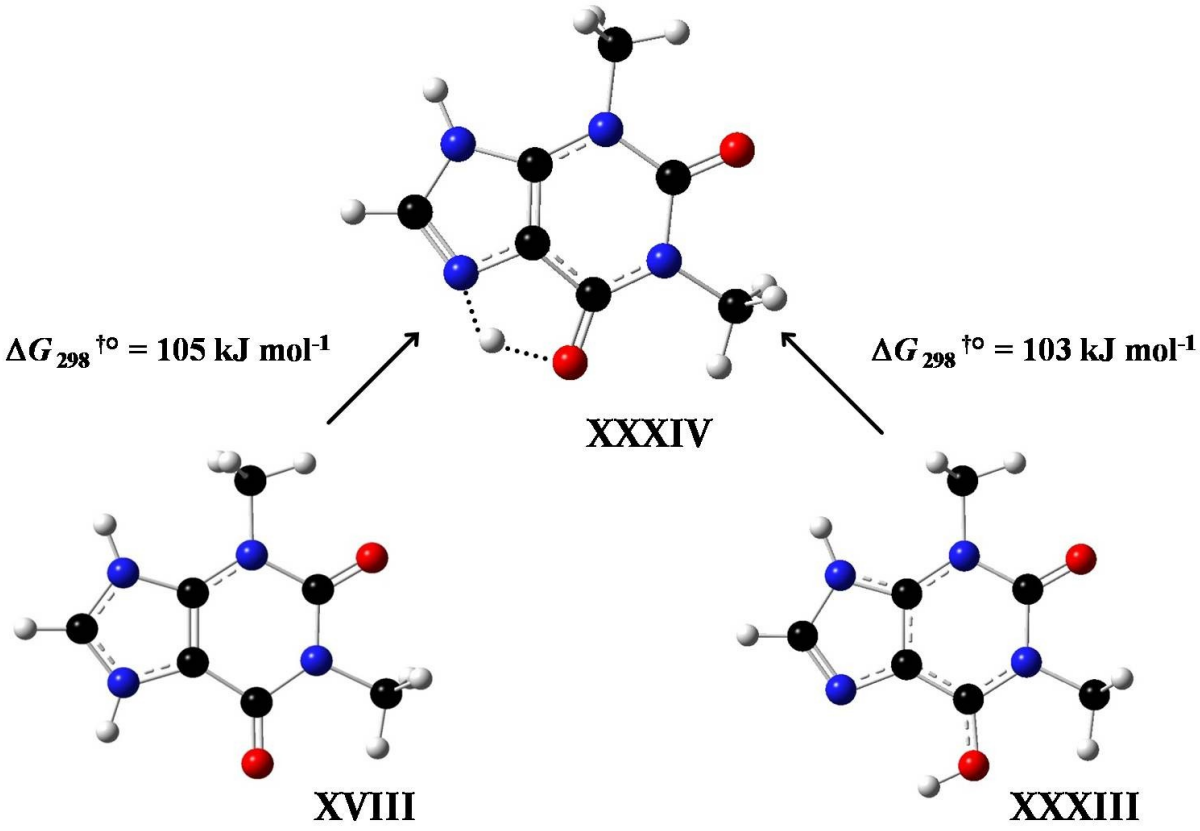

Figure 5.21: Calculated structure of critical configuration (**XXXIV**), representing the intramolecular proton transfer connecting the isomers, **XVIII** and **XXXIII**. Energies have been obtained at the MP2/aug-cc-pVTZ//B3LYP/6-311+G(d,p) level of theory.

Due to the very small difference in the calculated energy between the formation of **XVIII** and **XXXIII** from **XXIX**, it was assumed that a mixture of the two isomers exists in a approximate 1:1 ratio in the IRMPD spectrum of protonated theophylline. To further improve the fit of the calculated spectrum of each isomer to that of the IRMPD spectrum, anharmonic frequencies were calculated for both isomers and the anharmonic spectrum of each isomer is shown in comparison to with the IRMPD spectrum obtained (**Figure 5.22**). After mixing the intensities of the calculated anharmonic spectra of the two protonated theophylline isomers in a ratio of 1:1, a combined spectrum was produced and is shown in **Figure 5.23**.

Referring to the peak assignments shown in **Table 5-10**, it is clear that the calculation of anharmonic frequencies significantly improves the fit of the IRMPD spectrum, compared those calculated using harmonic frequencies. For protonated theophylline, **XVIII** had a MAD relative to the IRMPD obtained frequencies of 43 and 9 cm^{-1}, for the harmonic and anharmonic calculated frequencies, respectively. Isomer **XXXIII** has a MAD from the IRMPD obtained frequencies of 33 and 13 cm^{-1}, for the harmonic and anharmonic calculated frequencies, respectively.

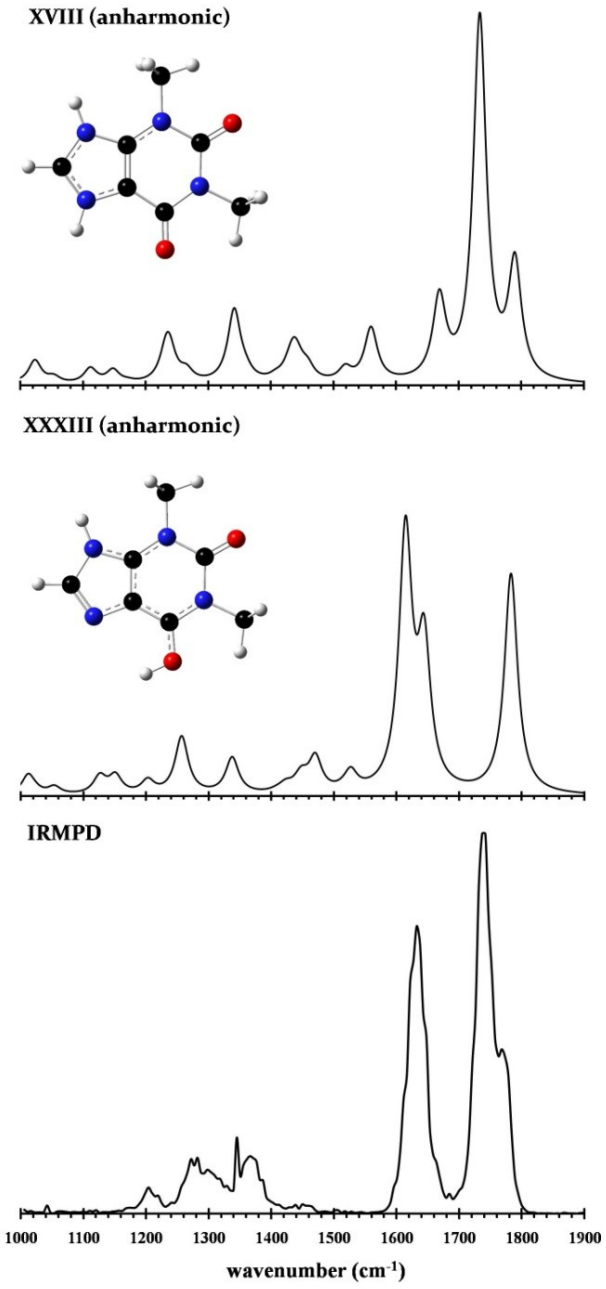

Figure 5.22: IRMPD spectrum of protonated theophylline (bottom) and the spectra of the two isomers, **XVIII** and **XXXIII** determined by anharmonic calculation at the B3LYP/6-311+G(d,p) level of theory. Intensities for the experimental and calculated spectra are in relative units of IRMPD efficiency and km mol^{-1}, respectively.

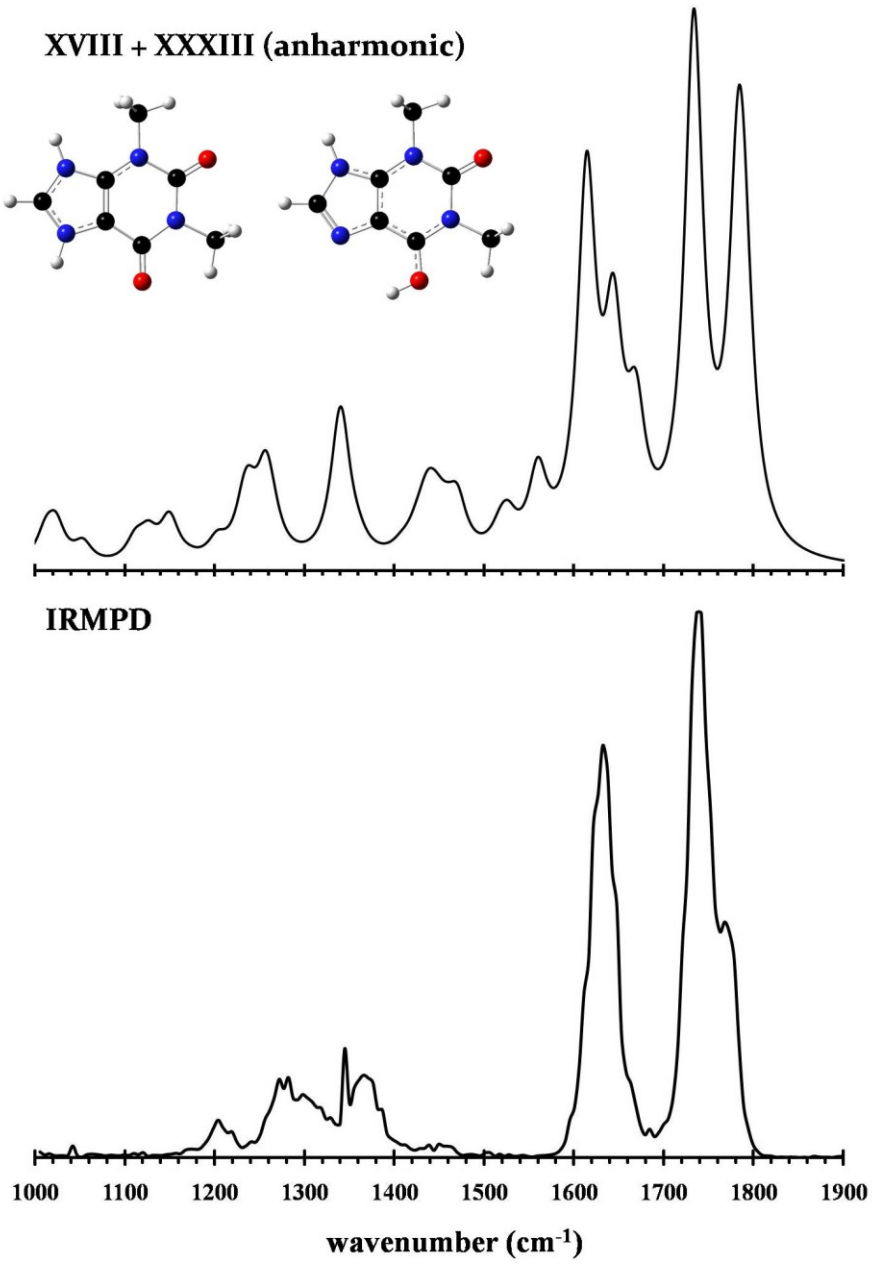

Figure 5.23: IRMPD spectrum of protonated theophylline (bottom) and the 1:1 combined spectrum of the two isomers **XVIII** and **XXXIII** determined by anharmonic calculation at the B3LYP/6-311+G(d,p) level of theory. Intensities for the experimental and calculated spectra are in relative units of IRMPD efficiency and km mol^{-1}, respectively.

Table 5-10: Infrared peak assignments associated with the IRMPD and calculated spectra for protonated theophylline, shown in **Figure 5.23**.The mean absolute deviation (MAD) of calculated frequencies from obtained IRMPD values are shown. All values are assigned in units of wavenumbers (cm^{-1}).

Vibrational Mode		**XVIII**		**XXXIII**	
	IRMPD	**Anharmonic**	**Harmonic**	**Anharmonic**	**Harmonic**
*** C(2)=O stretch**	1767	1789	1810	1783	1815
*** C(6)=O stretch**	1737	1733	1765	----	----
*** N(9)-H^+ wag + C(4)=C(5) stretch**	1663	1669	1702	----	----
*** C(6)=<u>O-H^+</u> bend**	1648	----	----	1644	1685
*** <u>C(6)=O</u>-H^+ + C(4)=C(5) stretch(es)**	1632	----	----	1614	1650
*** N(9)-H + C(8)-H (both isomers) + N(7)-H wag(s) (XVIII only)**	1345	1341	1373	1337	1370
C(6)=<u>O-H^+</u> bend+ C(8)-H wag	1272	----	----	1257	1307
MAD from IRMPD	0	9	43	13	33

5.2.6 Concluding Remarks

The IRMPD spectra of protonated caffeine (**II**), protonated theophylline (**XVIII**) and ammoniated theophylline (**XXIX**) have been obtained and characterized with the aid of calculated spectra and energies provided by electronic structure calculations, at the MP2/aug-cc-pVTZ//B3LYP/6-311+G(d,p) level of theory.

The IRMPD spectrum of protonated caffeine reveals that each of the two carbonyl oxygen atoms located at C(2) and C(6) are unprotonated and that protonation has occurred at the N(9) site (**II**). The MAD of the assigned calculated harmonic and anharmonic frequencies from the IRMPD obtained frequencies was 36 and 9 cm^{-1}, respectively.

The IRMPD spectrum of protonated theophylline is complicated by the presence of two isomers. Although, the most favourable form of protonated theophylline exists with the proton located at the N(9) position (**XVIII**), the presence of ammonia in the electrospray solution initiated PTC to afford the C(6) oxygen, carbonyl-protonated isomer, **XXXIII**. For **XVIII**, the MAD of the assigned calculated harmonic and anharmonic frequencies from the IRMPD obtained frequencies is 43 and 9 cm^{-1}, respectively. For **XXXIII**, the MAD of the assigned calculated harmonic and anharmonic frequencies from the IRMPD obtained frequencies is 33 and 13 cm^{-1}, respectively. There is only a 2.0 kJ mol^{-1} difference in energy, in favour of forming **XVIII**, resulting from the dissociation of **XXIX**. The protonated theophylline isomer, **XXXIII** could only be formed as a product of PTC and not by direct protonation. It is also found that a critical configuration (**XXXIV**) corresponding to the intramolecular proton-transfer of **XVIII** to form **XXXIII** is not thermally accessible under the experimental conditions. In order to verify that the existence of **XXXIII** as a product of PTC, a possible future experiment will entail use of a solution that is prepared with trimethyl ammonium chloride in the place of ammonium chloride. Based on the structure of **XXIX**, it is reasonable to assume that formation of an analogous isomer in the presence of trimethyl

ammonium chloride would be impossible, due to the substitution of the labile, ammonia hydrogen atoms with unreactive methyl moieties.

The IRMPD spectrum of the PBD of theophylline and ammonia is found to be very detailed relative to the spectra of protonated caffeine and theophylline. This is due to the ease with which the cluster dissociates under irradiation by the FEL. The IRMPD spectrum reveals that the PBD contains a bidentate IHB between ammonia and the N(7) and C(6) carbonyl oxygen in theophylline (**XXIX**). For **XXXIII**, the MAD of the assigned calculated harmonic and anharmonic frequencies from the IRMPD obtained frequencies is 47 and 16 cm^{-1}, respectively.

It can be concluded that the use of anharmonic calculated frequencies at the B3LYP/6-311+G(d,p) level of theory significantly improves the match between the results of theory and the IRMPD spectra obtained in all cases for the spectral range of 1000 to 1900 cm^{-1}, with an average MAD of the assigned calculated harmonic and anharmonic frequencies from the IRMPD obtained frequencies of 40 and 12 cm^{-1}, respectively.

5.3 The Proton-Bound Dimers of Caffeine and Theophylline

5.3.1 Electronic Structure: The Proton-Bound Dimer of Caffeine

The caffeine molecule is relatively small and inflexible; however the existence of two carbonyl oxygen atoms (O(2) and O(6)) as well as one basic nitrogen atom (N(9)) permits the possibility of several configurations of IHB between caffeine and its protonated analogue. All possible stable structures of the PBD of caffeine have been considered and are given by

Figure 5.24 through **Figure 5.26**. The calculated changes in enthalpies, entropies, Gibbs free energies and relative change in Gibbs free energies at 298 K for the formation of PBDs (**Eq. 5.1**) are given in **Table 5-11**. There are three classes of IHB interactions arising from the twelve possible isomers of the PBD of caffeine including, $O-H^+\cdots O$, $N-H^+\cdots O$ and $N-H^+\cdots N$. The $O-H^+\cdots O$ PBDs are characterized by the shortest average distance between heteroatoms of 2.47 Å, followed by 2.66 Å for $N-H^+\cdots O$ and 2.74 Å for $N-H^+\cdots N$. All of the PBDs possess asymmetric IHBs where the proton is located at a minimum favouring one side of the bond consistent with a symmetric double well potential for $O-H^+\cdots O$ and $N-H^+\cdots N$ and an asymmetric double well potential for $N-H^+\cdots O$, favouring the N-side of the bond.

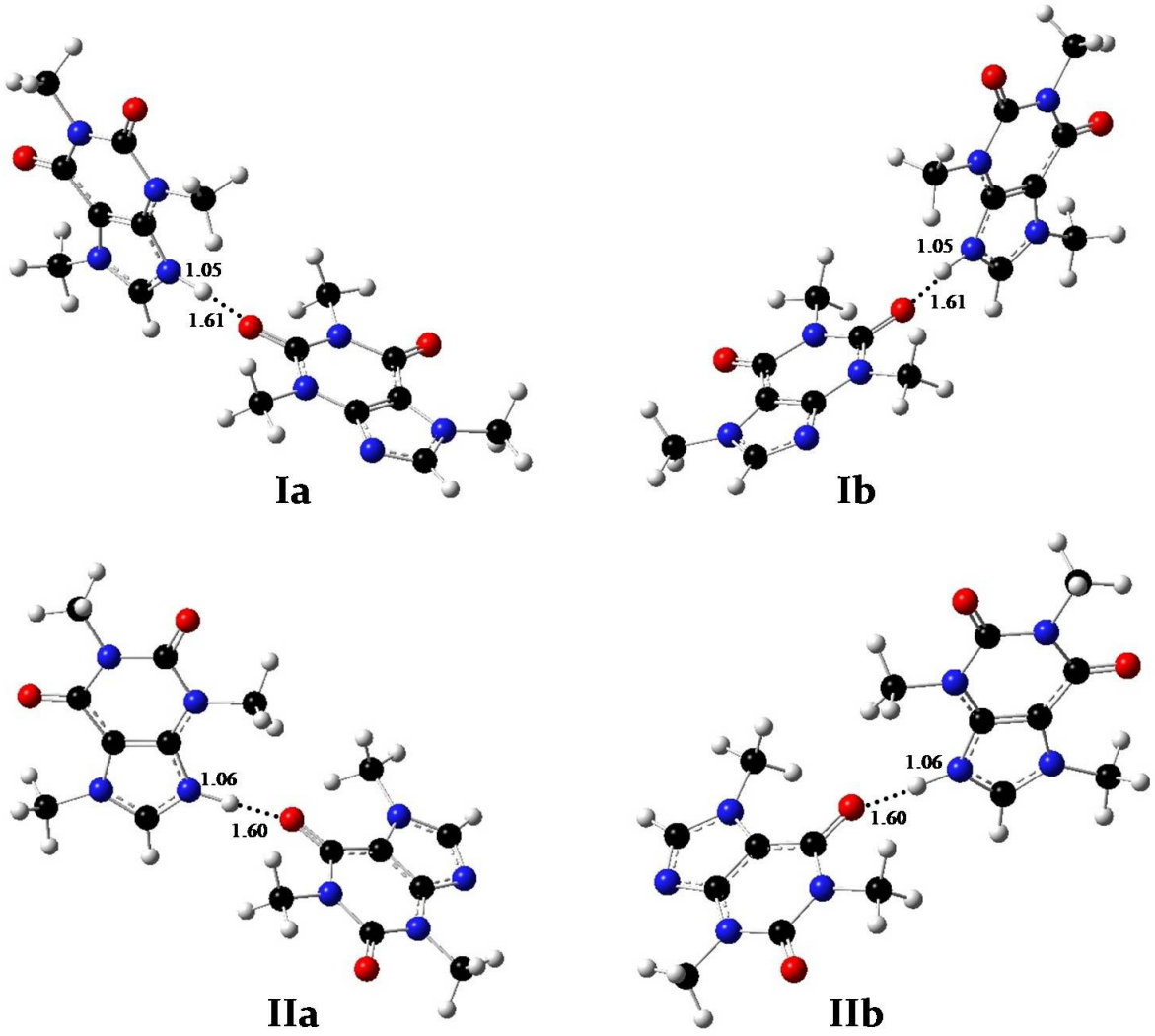

Figure 5.24: Calculated structures of possible isomers of the PBD of caffeine. Optimized at the B3LYP/6-311+G(d,p) level of theory.

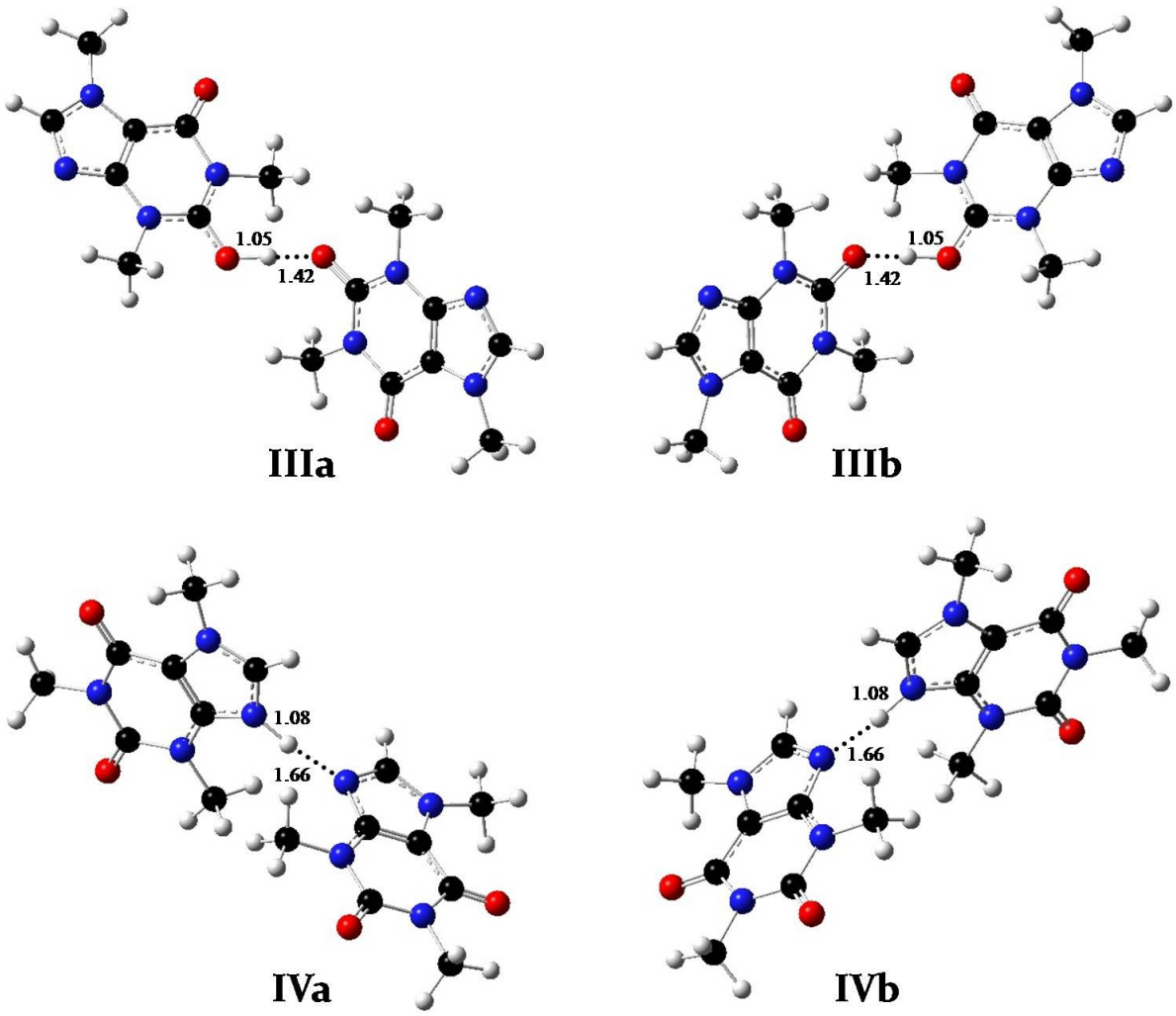

Figure 5.25: Calculated structures of possible isomers of the PBD of caffeine. Optimized at the B3LYP/6-311+G(d,p) level of theory.

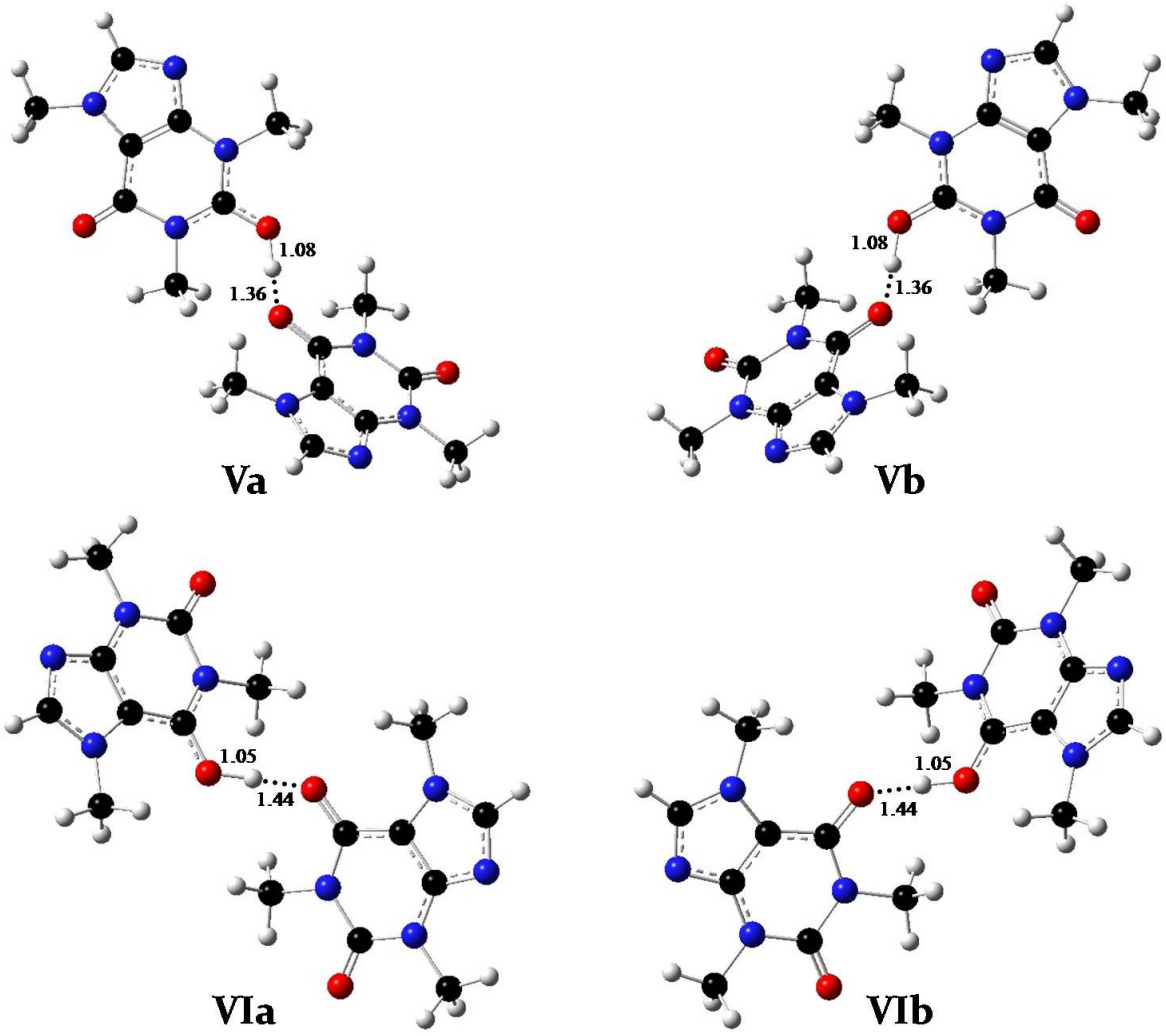

Figure 5.26: Calculated structures of possible isomers of the PBD of caffeine. Optimized at the B3LYP/6-311+G(d,p) level of theory.

Table 5-11: Calculated energies of PBD isomers formed by caffeine associating with protonated caffeine. Energies have been obtained at the MP2/6-311+G(2d,2p)//B3LYP/6-311+G(d,p) level of theory. Energies are reported in kJ mol^{-1}. The quantity $\Delta\Delta G^{\circ}_{298}$, is calculated with respect to the lowest energy isomer, **IIIa**.

Species	ΔH°_{rxn}	ΔS°_{rxn}	ΔG°_{298}	$\Delta\Delta G^{\circ}_{298}$
Ia	-107	-130	-67.8	1.4
Ib	-106	-133	-66.7	2.5
IIa	-96.0	-138	-55.0	14.2
IIb	-97.0	-137	-56.2	13.0
IIIa	-113	-146	-69.2	0.0
IIIb	-113	-151	-67.8	1.4
IVa	-97.0	-136	-56.4	12.7
IVb	-97.0	-145	-53.6	15.6
Va	-103	-151	-58.4	10.8
Vb	-104	-147	-60.1	9.0
VIa	-101	-144	-58.2	11.0
VIb	-101	-142	-58.6	10.6

The range of calculated Gibbs free energy changes for the twelve proposed isomers of the PBD of caffeine is narrow, with a 15.6 kJ mol^{-1} difference in energy between the lowest and highest energy isomers. The four isomers **Ia**, **Ib**, **IIIa** and **IIIb** are separated by only 2.5

kJ mol^{-1} in Gibbs free energy, therefore interpretation of the IRMPD spectrum of the PBD of caffeine must proceed with careful attention. This is due to the possibility of the spectral characteristics of all four isomers arising in the IRMPD spectrum. One factor which moderately reduces the complexity of the system is the structural relationship between each pair of isomers **a** and **b**. For example, if rotation is permitted about the IHB between the monomer units in the PBD, then isomer **Ia** is equivalent to **Ib** and the two isomers exist as rotamers. However, if the rotation is hindered, such that each isomer is locked in the **a** or **b** conformation, then the relationship between **a** and **b** is that of enantiomers, since they are non-superimposable mirror images and of equivalent energy. If either type of relationship exists between the isomers **a** and **b,** the vibrational modes of each species will be effectively identical. Electronic structure calculations show that rotation about the IHB from the most stable geometry into the most eclipsed configuration for the PBD of caffeine containing the longest IHB (**IVa/b**) results in a rise in electronic energy of 1577 $kJmol^{-1}$. The large increase in electronic energy can be regarded as an infinitely large rotational barrier under the experimental conditions and thus it is reasonable to assume that the twelve isomers described above can be treated as six pairs of enantiomers. For example, the MAD between the 141 calculated vibrational modes for **IIIa** and **IIIb** is found to be only 1 cm^{-1} resulting in identical spectral signatures for each isomer. In order to qualitatively interpret the IRMPD spectrum of the PBD of caffeine, the calculated spectrum will first include the averaged intensities of the pair of lowest energy isomers, **IIIa** and **IIIb**, followed by spectra that will include the averaged intensities of the next lowest energy isomers in addition to **IIIa** and **IIIb**. Because

the range of energies of the six pairs of isomers is narrow, it is difficult to estimate how much closer in energy the PBDs are in solution relative to the range of calculated values representative of gaseous thermodynamic quantities given in **Table 5-11**.

5.3.2 Mass-Selected IRMPD: The Proton-Bound Dimer of Caffeine

The mass-selected IRMPD spectrum of the PBD of caffeine has been obtained and is given in **Figure 5.27** along with a calculated spectrum including contributions from the lowest energy isomer pair, **IIIa** and **IIIb**. In order to investigate the contribution of all isomers within a 10 kJ mol^{-1} range of Gibbs free energies, **Figures 5.28** and **5.29** give spectra where the intensities of **Ia** and **Ib**, followed by **Va** and **Vb,** are sequentially summed in with **IIIa** and **IIIb**, respectively. Mass-selected IRMPD of the isolated PBD of caffeine with *m/z* 389 afforded protonated caffeine with *m/z* 195 as an exclusive product ion. As found with the PBD of theophylline and ammonia described previously, the weak IHB bond in the PBD of caffeine results in dissociation occurring for even the lowest intensity absorptions generating an IRMPD spectrum spanning the entire observable frequency range.

By inspection, it would seem necessary to include at least the first four set of isomers (**Figure 5.28**) in order to have the calculated spectrum begin to resemble the IRMPD spectrum of the PBD of caffeine. It is not valid to compare the intensities between the calculated and IRMPD spectrum; therefore assignment of the relative peak positions is the sole means of matching calculated and experimentally obtained vibrational frequencies.

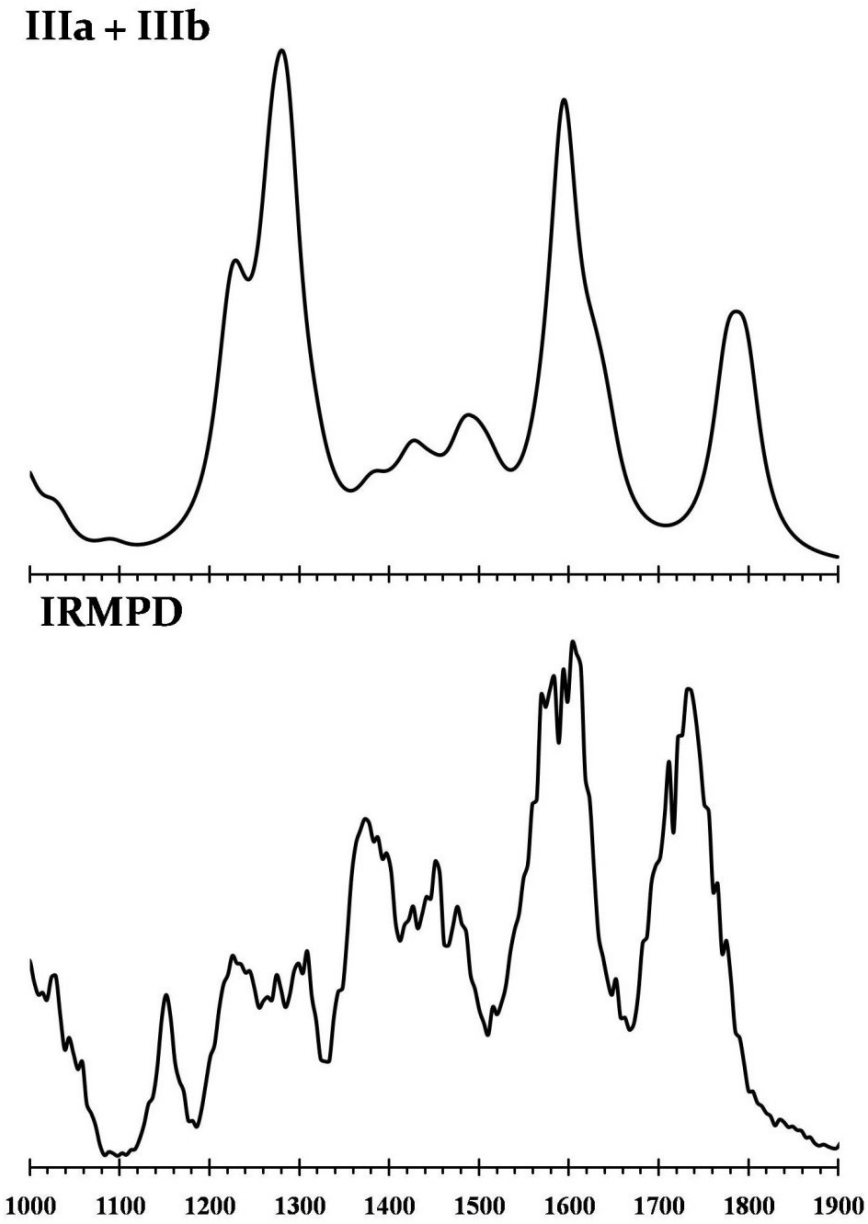

Figure 5.27: IRMPD spectrum of the PBD of caffeine (bottom) and the 1:1 combined spectrum of the two isomers **IIIa** and **IIIb** determined by calculation at the B3LYP/6-311+G(d,p) level of theory. Harmonic frequencies have been scaled by 0.9679. Intensities for the experimental and calculated spectra are in relative units of IRMPD efficiency and km mol^{-1}, respectively.

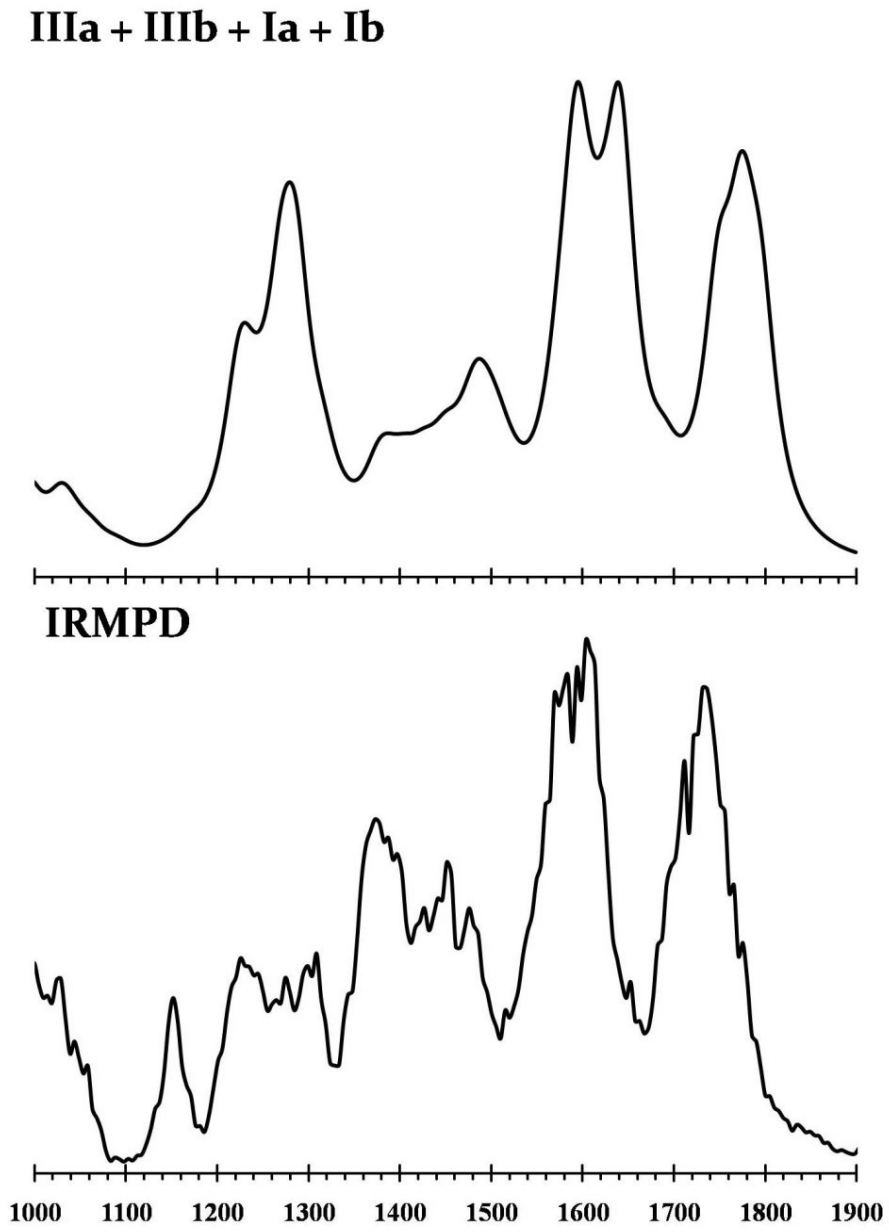

Figure 5.28: IRMPD spectrum of the PBD of caffeine (bottom) and the equally weighted combined spectrum of the four isomers **IIIa**, **IIIb**, **Ia** and **Ib** determined by calculation at the B3LYP/6-311+G(d,p) level of theory. Harmonic frequencies have been scaled by 0.9679. Intensities for the experimental and calculated spectra are in relative units of IRMPD efficiency and km mol^{-1}, respectively.

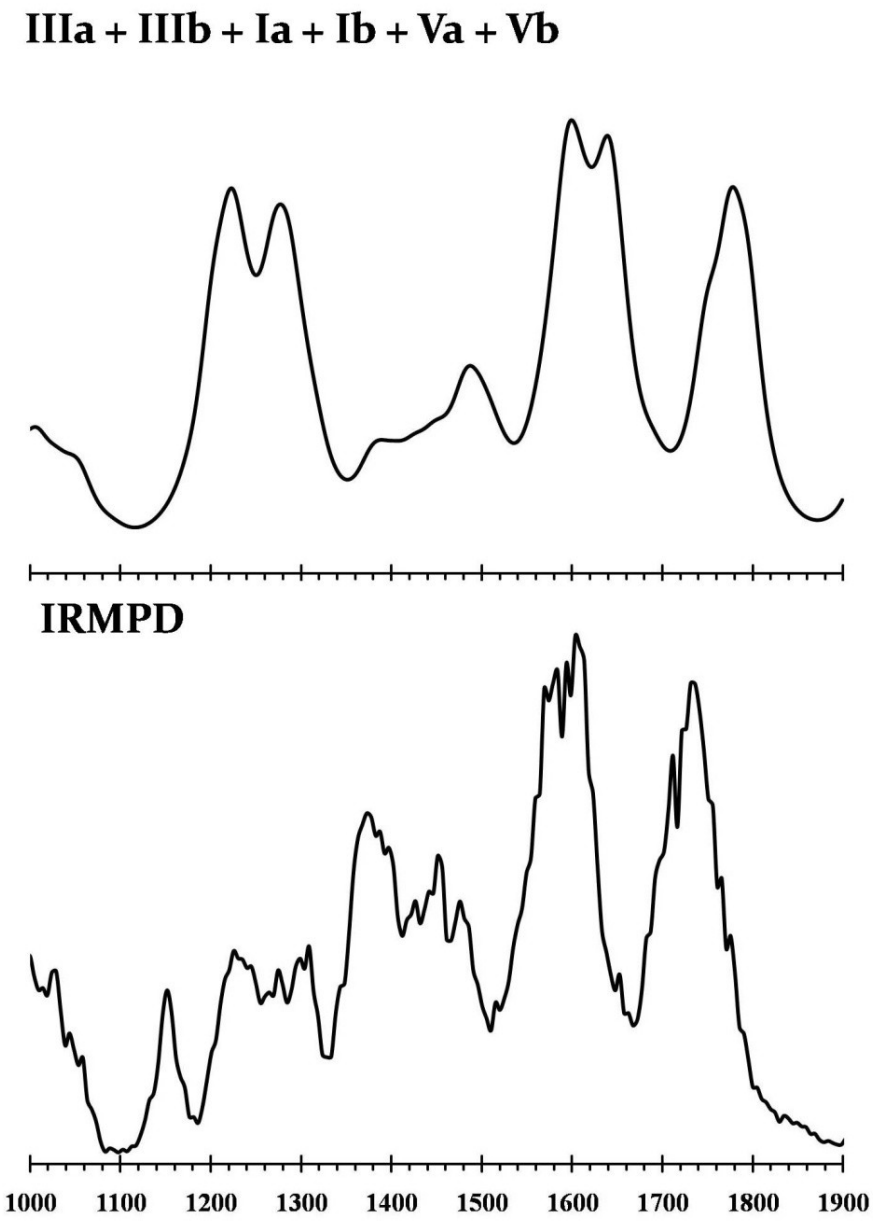

Figure 5.29: IRMPD spectrum of the PBD of caffeine (bottom) and the equally weighted combined spectrum of the six isomers **IIIa**, **IIIb**, **Ia**, **Ib**, **Va** and **Vb** determined by calculation at the B3LYP/6-311+G(d,p) level of theory. Harmonic frequencies have been scaled by 0.9679. Intensities for the experimental and calculated spectra are in relative units of IRMPD efficiency and km mol^{-1}, respectively.

Peak assignments for the IRMPD spectrum and calculated spectrum based on incorporation of three pairs of isomers (**IIIa/b**, **Ia/b** and **Va/b**) within a 10 kJ mol^{-1} range (**Figure 5.29**) is given in **Table 5-12**, with the frequencies of each pair of **a** and **b** isomers averaged. The complexity of interpreting the IRMPD spectrum of the PBD of caffeine cannot be understated, thus a level of ambiguity unfortunately exists within the assignment of vibrational modes. The MAD between IRMPD and calculated frequencies is not reported here due to the possibility of uncertainty in peak assignments leading to a deceptive measure of accuracy of the B3LYP/6-311+G(d,p) level of theory at reproducing IRMPD frequencies.

The calculated vibrational frequencies have been assigned to the IRMPD bands in **Table 5-12** and show that the contributions from each pair of the six isomers are consistent with regions of significant spectral activity in the IRMPD spectrum of the PBD of caffeine. It can be concluded that the lowest energy isomer pair, **IIIa/b** is not the only contributor to the IRMPD spectrum of the PBD of caffeine due to the presence of the free C=O stretching modes at 1731, 1751 and 1785 cm^{-1} in the IRMPD spectrum. The vibrational modes located at 1731 and 1751 cm^{-1} are consistent with the free C=O stretches found in the IRMPD spectrum of protonated caffeine at 1723 and 1757 cm^{-1}, respectively. The presence of three free C=O stretching modes indicates that an isomer involving the formation of a $N-H^{+}\cdots O$ IHB is present (**Ia/b**), since three chemically distinct free carbonyls may only exist under such conditions.

Table 5-12: Infrared peak assignments associated with the IRMPD and calculated spectra for the PBD of caffeine presented in **Figure 5.29**. The frequencies are assigned in units of wavenumbers (cm^{-1}). The subscript of 1 or 2 on a carbonyl carbon indicates which monomer group the mode is associated with, where 1 refers to the monomer bound more closely to the proton.

Vibrational Mode	IRMPD	IIIa/b	Ia/b	Va/b
* C_2(2)=O stretch	1751	----	----	1778
* C_1(6)=O stretch	1785	1797	1793	1794
* C_2(6)=O stretch	1731	1776	1772	----
* C_1(2)=O-H^+ bend(s)	1225	1225	----	1223
	1274	1285	----	----
	1308	----	----	1303
	1594	1595	----	----
	1603	----	----	1606
* C_2(2)=O-H^+ stretch	1652	----	1641	----
* C_2(6)=O-H^+ stretch	1623	----	----	1654

5.3.3 Electronic Structure: The Proton-Bound Dimer of Theophylline

Similarly to caffeine, the theophylline molecule is relatively small and inflexible, however the existence of two carbonyl oxygen atoms (O(2) and O(6)) as well as one basic nitrogen atom (N(9)) permits the possibility of several configurations of IHB between theophylline and its protonated analogue. Possible stable structures of the PBD of theophylline have been considered and are given by **Figure 5.30** through **Figure 5.32**. The calculated change in enthalpies, entropies, Gibbs free energies and relative changes in Gibbs free energies at 298 K for the formation of PBDs (**Eq. 5.1**) are given in **Table 5-12**. Similarly to caffeine, there are three classes of IHB interactions arising from twelve possible isomers of the PBD of theophylline with the $O-H^+\cdots O$ PBDs characterized by the shortest average distance between heteroatoms of 2.46 Å, followed by 2.65 Å for $N-H^+\cdots O$ and 2.74 Å for $N-H^+\cdots N$.

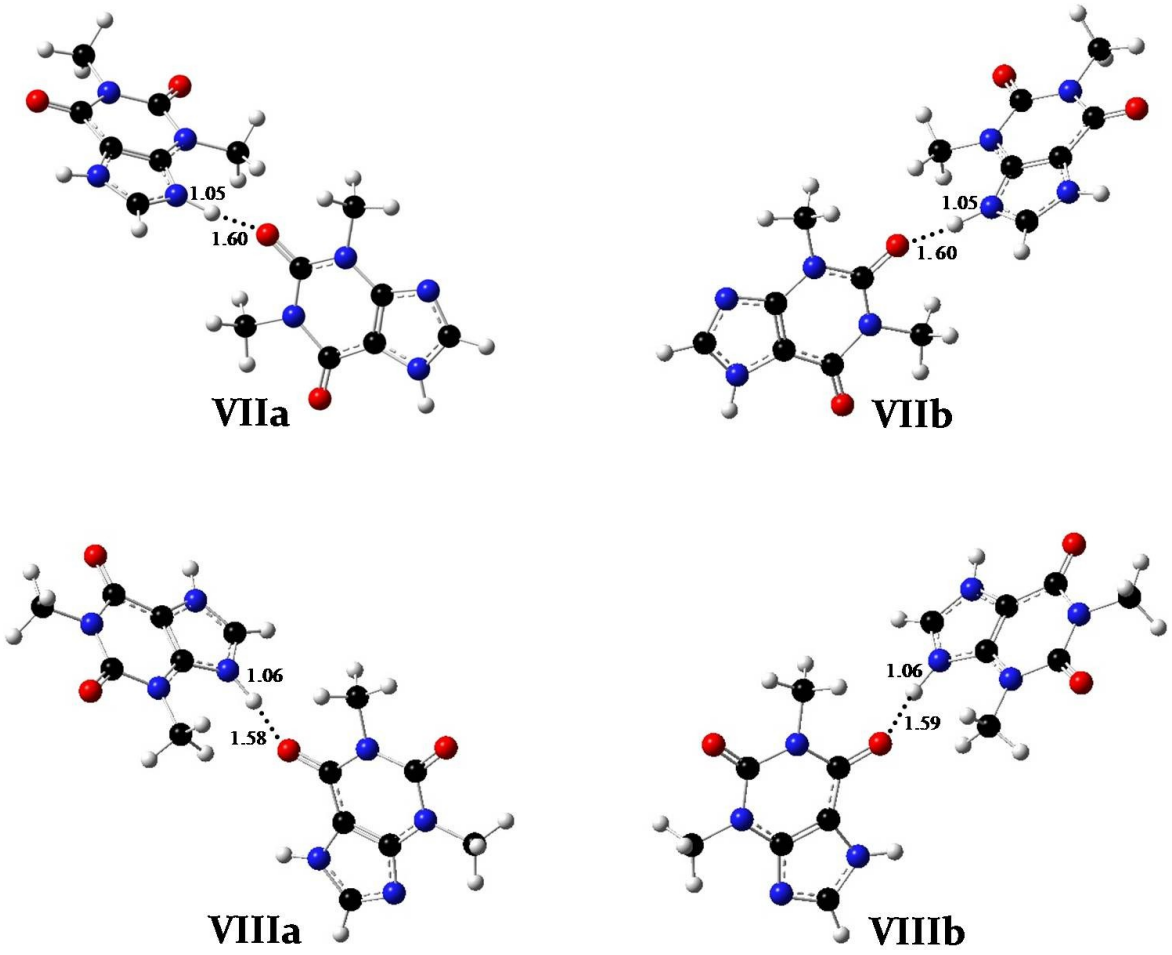

Figure 5.30: Calculated structures of possible isomers of the PBD of theophylline. Optimized at the B3LYP/6-311+G(d,p) level of theory.

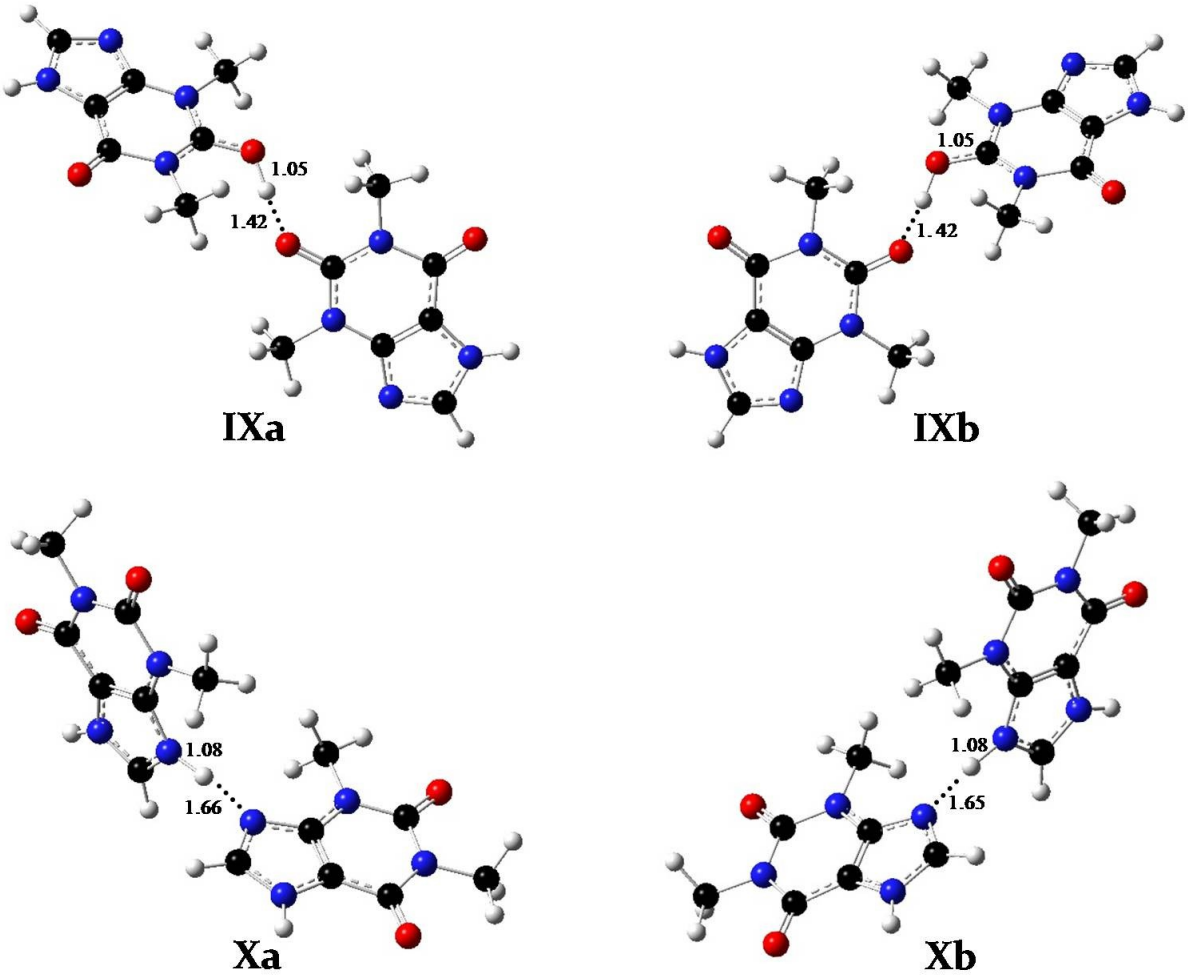

Figure 5.31: Calculated structures of possible isomers of the PBD of theophylline. Optimized at the B3LYP/6-311+G(d,p) level of theory.

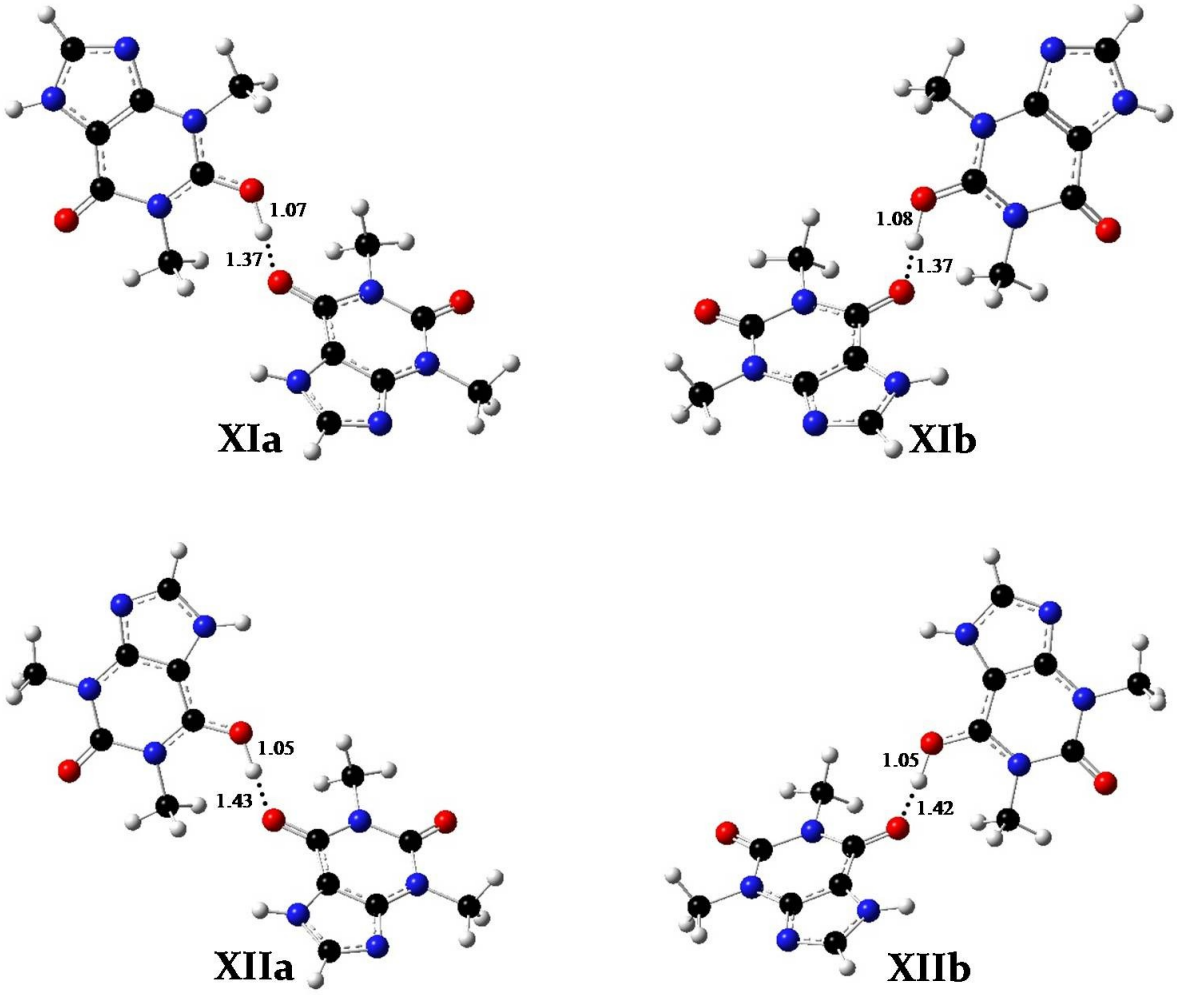

Figure 5.32: Calculated structures of possible isomers of the PBD of theophylline. Optimized at the B3LYP/6-311+G(d,p) level of theory.

A unique isomer (**XIIIA**) of the PBD of theophylline can also be proposed that exhibits no similarities with the PBDs of caffeine described previously. This isomer is calculated to be the most stable PBD with a 9.75 kJ mol^{-1} difference in Gibbs free energy separating it from the most stable pair of enantiomers, **IXa/b** and a 26.9 kJ mol^{-1} difference from the least

stable pair of enantiomers, **Xa/b**. The possibility of forming **XIIIA** is directly the result of theophylline possessing a hydrogen in the N(7) position, compared to a methyl moiety found in caffeine. It is also this structural distinction from caffeine that is responsible for bidentate IHB formation in the PBD of ammonia and theophylline (**XXIX**) described previously. The isomer **XIIIA** exhibits some structural similarities to those found in **XXIX**; however the IHB in **XIIIA** is formed between the N(7) hydrogen (proton) on the first monomer and the C(6) carbonyl oxygen of the second monomer, and *vice versa* (**Figure 5.33**).

Superficially, inspection of the structure of **XIIIA** leads to the perception of high molecular symmetry since both monomer units lie in a horizontal reflection plane with the ion appearing to possess an inversion centre. The inversion symmetry is broken due to the presence of a single hydrogen atom at N(9) in monomer **1** and not in the **2**, and also the asymmetry exhibited by the $N-H^{+}\cdots O$ bonds, thus **XIIIA** belongs to the low symmetry point group of C_s. Due to bidentate IHB formation in the proposed structure of **XIIIA**, the adaption of a planar configuration exhibits striking similarities to the base-pairing observed between nucleobases (adenine, thymine, guanine and cytosine). The calculated changes in enthalpy, entropy, Gibbs free energy and relative change in Gibbs free energy at 298 K for the formation of **XIIIA** (**Eq. 5.1**) are given in **Table 5-13** along with all other proposed isomers of the PBD of theophylline.

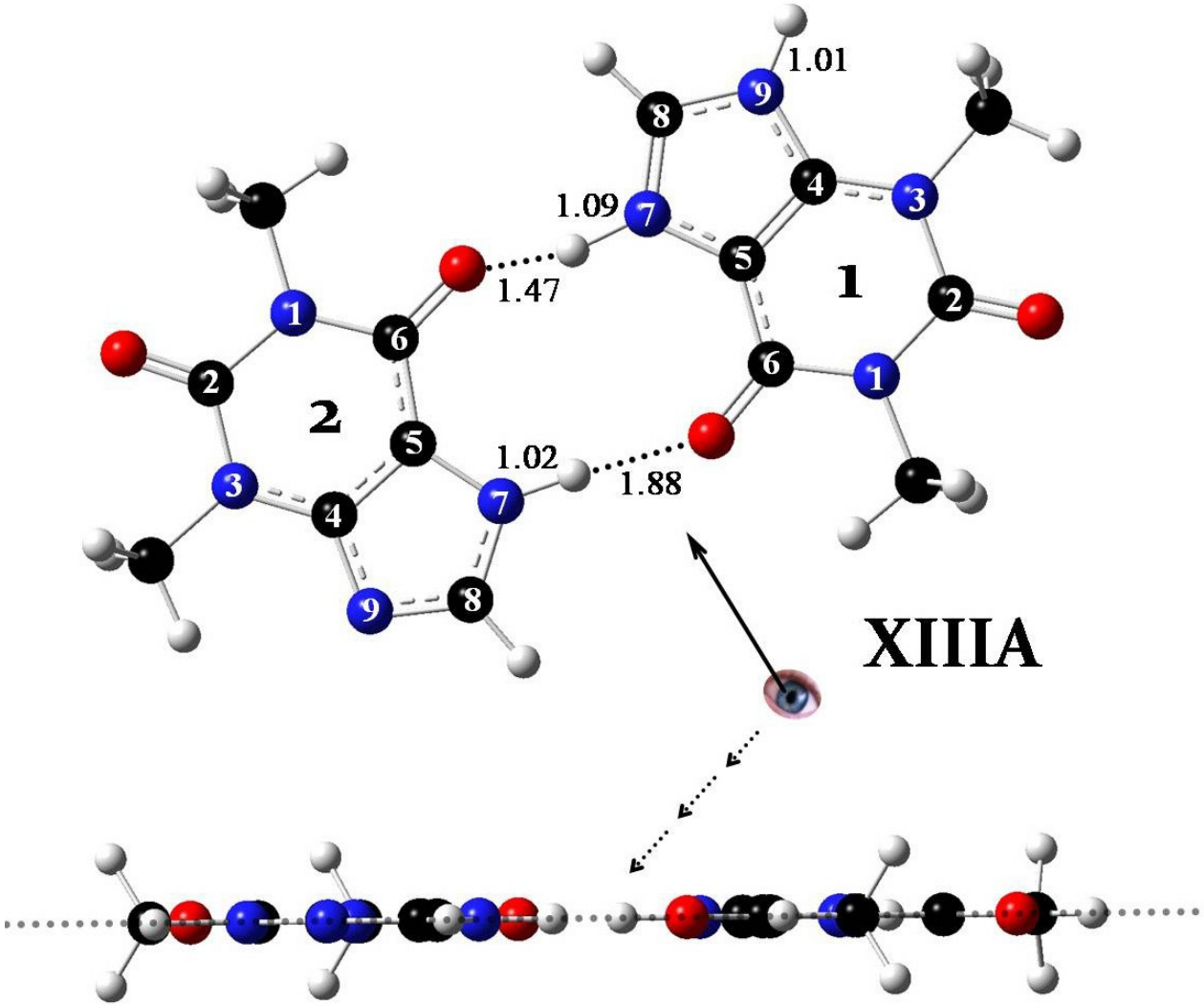

Figure 5.33: Calculated structure of isomer **XIIIA** of the PBD of theophylline. Optimized at the B3LYP/6-311+G(d,p) level of theory. Each theophylline monomer is labeled **1** and **2**. The original site of protonation occurs at N(9) in monomer **1**. The bottom of the diagram shows the PBD oriented in such a way to observe the single reflection plane possessed by the ion

The existence of **XIIIA** (**Figure 5.33**) is most probably initiated once the hydrogen atom located at N(7) of monomer **1** becomes labile upon initial protonation of theophylline at N(9). This is also proposed for the initial circumstances that drive stable formation of the PBD of theophylline and ammonia (**XXIX**). It was previously shown (**Figure 5.16**) that in protonated theophylline (**XVIII**) the partial positive charges found on the N(7) and N(9) hydrogen atoms are 0.384 and 0.376, respectively, indicating that N(7) is the most likely site of proton transfer. In theophylline (**XVII**), the partial positive charge on the N(7) hydrogen atom is originally 0.326, which shows an increase in the partial charge on the N(7) hydrogen atom of +0.058 units upon protonation at N(9) in **XVII**. The Mulliken charge distribution for **XIIIA** has been calculated at the B3LYP/6-311+G(d,p) level of theory and is given in **Figure 5.34**. The proton with a partial positive charge of 0.659 located between N(7) and O(6) in monomers one and two, respectively, originally existed as a hydrogen at N(7) in theophylline (**XVII**) with partial positive charge of 0.326, demonstrating a considerable change of +0.333 units. In **XIIIA** the hydrogen located at N(9) has a partial positive charge of 0.377, nearly identical to the value of the equivalent hydrogen atom found in protonated theophylline (**XVIII**). Calculations predict that the proton located at N(7) carries the most partial positive charge in **XVII**, **XXIX** and **XIIIA**, with the location of the proton being facilitating the formation of a bidentate IHB in **XXIX** and **XIIIA**.

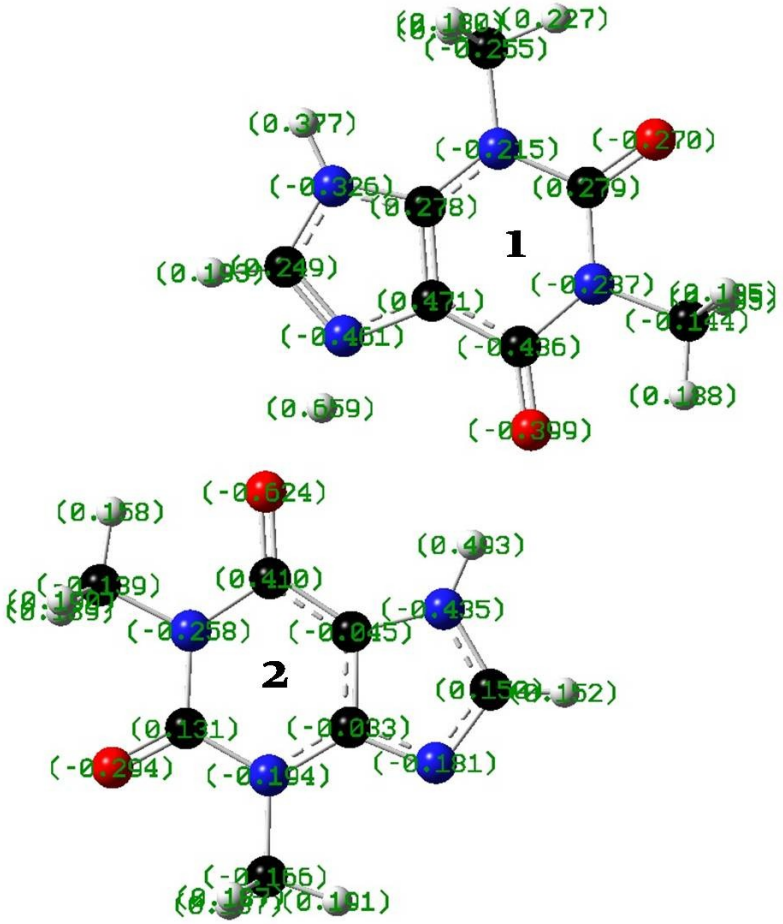

Figure 5.34: Mulliken charge distribution for **XIIIA** calculated at the B3LYP/6-311+G(d,p) level of theory.

Table 5-13: Calculated energies of PBD isomers formed by theophylline associating with protonated theophylline. Energies have been obtained at the MP2/6-311+G(2d,2p)//B3LYP/6-311+G(d,p) level of theory. Energies are reported in kJ mol^{-1}. The quantity $\Delta\Delta G^{\circ}_{298}$, is calculated with respect to the lowest energy isomer, **XIIIA**.

Species	ΔH°_{rxn}	ΔS°_{rxn}	ΔG°_{298}	$\Delta\Delta G^{\circ}_{298}$
VIIa	-107	-136	-66.4	10.8
VIIb	-107	-130	-67.8	9.4
VIIIa	-99.4	-133	-59.6	17.5
VIIIb	-98.9	-133	-59.2	17.9
IXa	-111	-141	-68.3	8.8
IXb	-111	-147	-66.7	10.5
Xa	-91.7	-136	-51.0	26.1
Xb	-91.7	-141	-49.5	27.6
XIa	-104	-146	-60.1	17.1
XIb	-104	-141	-61.9	15.3
XIIa	-102	-137	-61.6	15.5
XIIb	-102	-135	-62.1	15.1
XIIIA	-122	-150	-77.2	0.0

5.3.4 Mass-Selected IRMPD: The Proton-Bound Dimer of Theophylline

The mass-selected IRMPD spectrum of the PBD of theophylline is shown in **Figure 5.35** along with a calculated spectrum for the lowest energy isomer **XIIIA**. In order to investigate the contribution of all isomers within a 10 kJ mol^{-1} range of Gibbs free energies, **Figure 5.36** gives a calculated spectrum with intensities from **IXa** and **IXb** with **XIIIA** combined in a 1:1:1 ratio. Statistically **XIIIA** should dominate the formation of **IXa/b** by 58:1 however, IRMPD intensities are not quantitative, and intensities calculated here are also treated qualitatively due to the lack of using a very complete basis set including electron correlation.[68] Although the B3LYP/6-311+G(d,p) level of theory is shown to produce frequencies adequately in this work, it fails to meet the criteria required to produce quantitative intensities. Providing the 1:1:1 combined spectrum in **Figure 5.36** is to ensure that the contributions of the calculated intensities of **IXa/b** are visible relative to intensity contributions from **XIIIA**. Values of both IRMPD and calculated intensities have not been displayed in the spectra presented here in order to prevent the use of qualitative data in justifying structural features.

The Mass-selected IRMPD of the isolated PBD of theophylline with *m/z* 361 afforded protonated theophylline with *m/z* 181 as the exclusive product ion. As found with the PBD of theophylline and ammonia and the PBD of caffeine, the weak IHB bond in the PBD of theophylline results in dissociation occurring for even the lowest intensity absorptions, producing a well structured IRMPD spectrum spanning the entire observable frequency range.

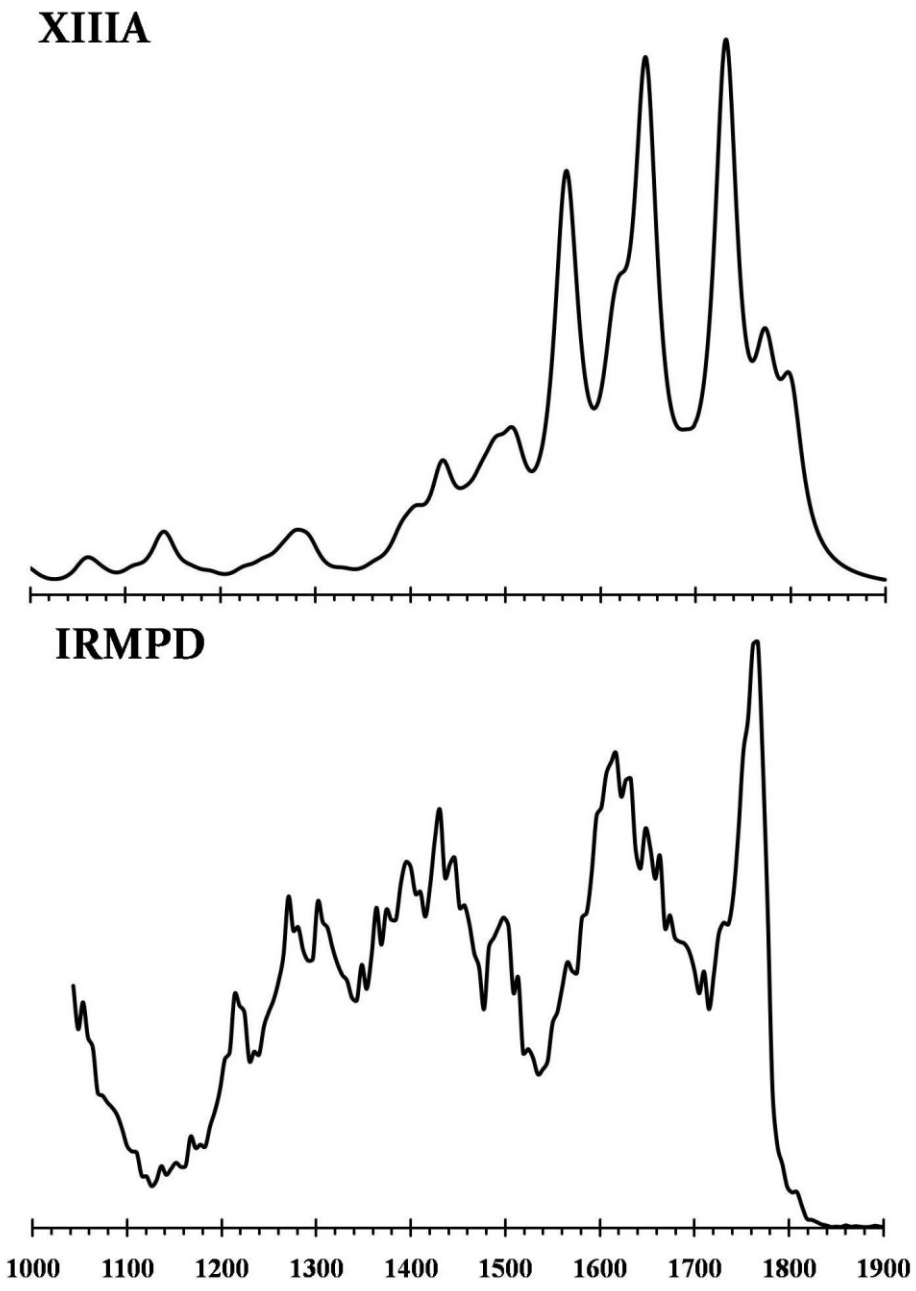

Figure 5.35: IRMPD spectrum of the PBD of theophylline (bottom) and the spectrum of the isomer **XIIIA** determined by calculation at the B3LYP/6-311+G(d,p) level of theory. Harmonic frequencies have been scaled by 0.9679. Intensities for the experimental and calculated spectra are in relative units of IRMPD efficiency and km mol^{-1}, respectively.

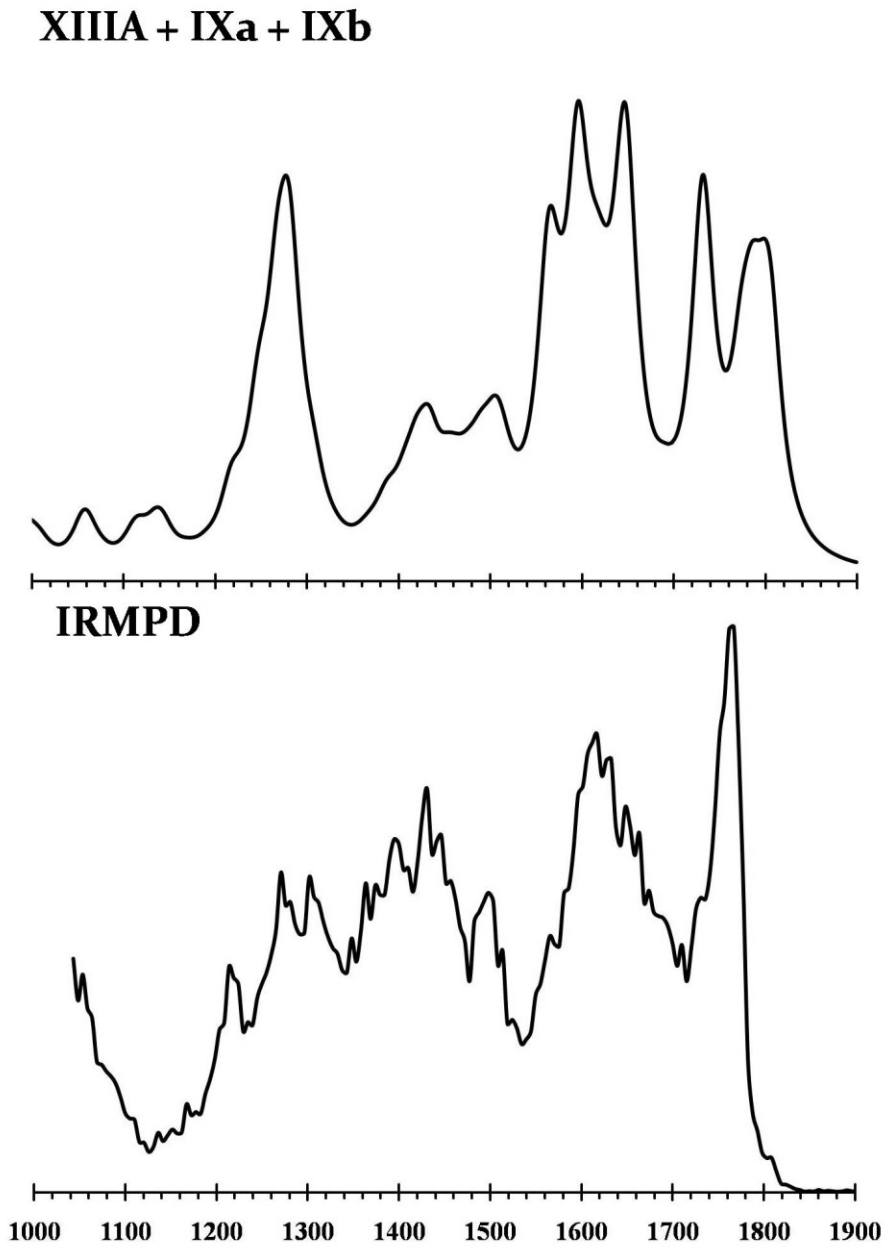

Figure 5.36: IRMPD spectrum of the PBD of theophylline (bottom) and the spectrum of **XIIIA** averaged with contributions from **IXa** and **IXb** determined by calculation at the B3LYP/6-311+G(d,p) level of theory. Harmonic frequencies have been scaled by 0.9679. Intensities for the experimental and calculated spectra are in relative units of IRMPD efficiency and km mol^{-1}, respectively.

Table 5-14: Infrared peak assignments associated with the IRMPD and calculated spectra for the PBD of theophylline presented in **Figure 5.36**. The frequencies are assigned in units of wavenumbers (cm^{-1}). The subscript of 1 or 2 on a carbonyl indicates which monomer group the mode is associated with, where 1 refers to the monomer bound more closely to the proton.

Vibrational Mode	IRMPD	XIIIA	IXa/b
* $C_1(2)$=O stretch	1803	1800	1748
* $C_2(2)$=O stretch	1762	1773	----
* $C_1(6)$=O stretch	1731	1732	1806
* $C_2(6)$=O stretch	1762	----	1785
* $C_2(6)$=O-H^+ stretch	1623	----	----
* $C_2(2)$=O-H^+ stretch + $C_2(2)$=O-H bend	1652	----	1641
* $C_2(2)$=O-H^+ stretch + proton stretch	1565	1563	----
* $C_1(2)$=O-H^+ bend	1270	----	1280
* $C_2(6)$=O-H^+ bend	1653	1647	----
* N(7)-H bend + methyl bends	1498	1492	----

Electronic structure calculations would predict **XIIIA** to be the dominant isomer among the thirteen proposed confirmations of the PBD of theophylline. The spectrum of **XIIIA** given in **Figure 5.35** would indicate that many of the calculated peaks correspond well in the carbonyl region of the IRMPD spectrum from 1600 to 1803 cm^{-1}. Similar to the

PBD of caffeine, the accuracy of the vibrational assignments must be treated with a level of ambiguity due to the complexity of the spectrum. One important factor to consider about the nature of **XIIIA** is the high likelihood of anharmonicity in the IHB interaction region. It was found previously for the PBD of theophylline and ammonia (**XXIX**) that several of the protonated carbonyl modes involved in interactions with ammonia are significantly red-shifted in the IRMPD spectrum. For example, the IRMPD spectrum of **XXIX** has two peaks located at 1446 and 1591 cm^{-1} which are calculated to occur at 1515 and 1653 cm^{-1}, respectively for the harmonic values and 1446 and 1578 cm^{-1} for the anharmonic values. There is a large amount of spectral activity in the frequency range of 1400 to 1600 cm^{-1} for the IRMPD spectrum of the PBD of theophylline, suggesting that the calculation of anharmonic frequencies of **XIIIA** could be very useful. Calculation of anharmonic frequencies has been attempted for **XIIIA**, however after 21 days of running on a 3 GHz, four processor workstation, equipped with 32 GB of memory and a high-speed serial attached hard drive, a power outage terminated the calculation. One drawback mentioned previously is the exceptional cost of running the anharmonic frequency calculations for systems of considerable molecular size. The anharmonic frequency calculations for protonated caffeine (**II**) and theophylline (**XVIII**) required ten days, and those for **XXIX** required 18 days. It is estimated that with currently available computing resources, it would require at least one month or more to calculate the anharmonic frequencies of **XIIIA**.

It is instructive to use the frequencies obtained from the IRMPD of protonated theophylline in order to assign free carbonyl stretching frequencies in the IRMPD spectrum

of the PBD of theophylline. For example, the free carbonyl stretching frequencies located at 1731 and 1762 cm^{-1} in the IRMPD spectrum of the PBD of theophylline are found at 1737 and 1767 cm^{-1}, respectively, in the spectrum of protonated theophylline (**Figure 5.8**). Frequencies for protonated carbonyl stretching and proton bending modes have been assigned at 1623 and 1652 cm^{-1} in the IRMPD spectrum of the PBD of theophylline and exist at 1632 and 1648 cm^{-1} in the spectrum of protonated theophylline (**Figure 5.8**).

The combined spectrum is provided in **Figure 5.36** including the intensities from the isomer pair **IXa/b** combined with the intensities from **XIIIA** in the ratio of 1:1 since the average relative Gibbs free energy change was less than 10 kJ mol^{-1}. There is also one vibrational mode calculated for **IXa/b** at 1280 cm^{-1} corresponding to a prominent C(2)=$\underline{O\text{-}H^{+}}$ bend that cannot be attributed to **XIIIA** and is possibly responsible for the peak found at 1270 cm^{-1} in the IRMPD spectrum.

5.3.5 Concluding Remarks

It was originally proposed that substitution of the N(7) methyl moiety in caffeine with the hydrogen atom found in theophylline could lead to significant differences in IHB schemes in the respective PBDs. This has been demonstrated previously by exclusive formation of the PBD of theophylline and ammonia due to the presence of a strong bidentate IHB facilitated by the existence of a hydrogen located at N(7) in theophylline.

In general, the six pairs of enantiomers that constitute the possible configurations of the PBDs of caffeine and theophylline are similar in structural characteristics and energies with a 15.6 and 18.2 kJ mol^{-1} range in relative Gibbs free energies between each set of enantiomers

respectively. The most stable pair of enantiomers out of six possible configurations for both caffeine and theophylline arise by IHB formation between the C(2)=O carbonyl groups of each monomer with the Gibbs free energies of binding calculated as -69.2 and -68.3 kJ mol^{-1}, respectively. However the larger spread in energies between the enantiomers of theophylline in conjunction with the existence of the unique bidentate IHB containing species **XIIIA** (9.75 kJ mol^{-1} lower in relative Gibbs free energy than the enantiomer pair **IXa/b**) gives an IRMPD spectrum for the PBD of theophylline principally based on vibrational intensities from **XIIIA**. A C(2)=O-H bend is observed at 1270 cm^{-1} in the IRMPD spectrum that does not correspond to any vibrational mode calculated for **XIIIA** which may arise as a result of the presence of the enantiomer pair **IXa/b**.

The IRMPD spectrum of the PBD of caffeine is complicated by the existence of at least two pairs of the entantiomers **IIIa/b** and **Ia/b**, with the strong likelihood of vibrational intensities of **Va/b** also being present. Verification of a pair of enantiomeric PBDs (**Ia/b**) containing a $N-H^{+}\cdots O$ IHB is observed in the IRMPD spectrum of the PBD of caffeine due to the presence of three free carbonyl stretching modes located at 1731, 1751 and 1785 cm^{-1}.

5.4 The Sodium Cation-Bound Dimers of Caffeine and Theophylline

There have been several experimental and computational studies recently involving sodium cation interactions with biologically relevant molecules. For example, Balaj and coworkers have reported IRMPD spectra of the di- and tripeptides of glycine and alanine involved in interactions with sodium cation.[145] This work shows both spectroscopically and

computationally that the most favourable structure of the triglycine-Na^+ cluster ion involves a tridentate interaction between the three amide carbonyl oxygen atoms and the sodium cation.

Kapota and coworkers have examined the IRMPD spectra of ions formed by interactions of sodium cation with glycine and proline, in order to determine if such interactions would lead to "charge solvated" or "salt bridged" structures.[146] This work shows both spectroscopically and computationally that glycine-Na^+ is likely to favour a charge solvated structural configuration, while proline-Na^+ favours a salt bridged structural configuration.

Work also continues in the realm of exploring sodium cation affinities. Wang and coworkers studied sodium cation affinities in systems involving interactions of sodium cation with cytosine and methyl cytosine derivatives using kinetic methods and electronic structure calculations.[147]

Although the structural information provided by studying IHB interactions in the PBDs of caffeine and theophylline is very useful, the labile nature of the proton involved in the IHB can lead to complications in the form of the existence of several isomers, as well as the anharmonicity associated with vibrational modes involving proton motion. There is a possibility that the sodium cation-bound homodimers of caffeine and theophylline may give a less complicated IRMPD spectra than their analogous PBDs. For example, there are no C=O-Na^+ bending modes; however the C=O-H^+ bending mode is a feature present in the IRMPD spectrum of the PBDs described previously. Another difference exists between the C=O-Na^+ and C=O-H^+ stretching modes, where in the case of Na^+, the Na^+ nucleus is not coupled with

the stretch of the carbonyl and remains stationary, effectively behaving as an "electrostatic-anchor" between the two caffeine moieties. The smaller proton involved in all C=O-H^+ stretching modes is strongly coupled to the carbonyl oxygen atom, moving in phase with the stretching of the carbonyl with which it is more closely interacting. The differences described above will likely result in a less complicated IRMPD spectrum for a sodium cation-bound dimer (SCBD) relative to its analogous PBD spectrum. The SCBD systems do not possess the level of anharmonicity associated with IHBs and this is beneficial with regard to how well calculated harmonic frequencies match the IRMPD obtained frequencies. It is proposed that study of the interactions between caffeine and theophylline with Na^+ may contribute to the explanation of why complication arises in the PBD spectra, as well as furthering the understanding of the functionality of these molecules in forming gaseous ionic clusters.

5.4.1 Electronic Structure: The Sodium Cation-Bound Dimer of Caffeine

Analogous to calculation of the PA of the Lewis basic sites in caffeine, the sodium cation affinity (SCA) is instructive for locating the most probable site of sodium cation interaction. The SCA is defined as the negative value of the enthalpy change for the reaction

$$M + Na^+ \rightarrow M \cdots Na^+ \qquad \textbf{5.4}$$

Three stable sites of sodium cation interaction in caffeine are located at N(9) and the C(2) and C(6) carbonyl oxygen atoms. It is found that sodium cation forms fewer stable interactions with caffeine than is found for the protonation of caffeine, demonstrating that sodium cation exhibits more selectivity in where it will bind. The three SCA values of the

sites N(9), O(2) and O(6) along with the associated changes in entropies and Gibbs free energies (**Eq. 5.4**) are given in **Table 5-15**.

Table 5-15: Calculated sodium cation affinities (SCA) and thermodynamic quantities associated with the interaction of sodium cation with caffeine (**Eq. 5.4**). Energies for the interacting sites have been calculated at the MP2(full)/aug-cc-pCVTZ//B3LYP/6-311+G(d,p) level of theory on N(9), O(2) and O(6) in both monomer moieties, and also on Na. Energies for all remaining atoms have been calculated at the MP2(full)/6-311+(2d,2p)//B3LYP/6-311+G(d,p) level of theory. All energies are reported in kJ mol^{-1}.

Site of Sodium Cation Interaction	**SCA**	ΔS°_{rxn}	ΔG°_{298}	$\Delta\Delta G^{\circ}_{298}$
N(9)	125	-108	-92.8	34.6
O(2)	159	-105	-128	0.0
O(6)	142	-104	-111	16.4

With three sites of sodium cation interaction available in caffeine, it is possible to form six possible isomers of the SCBD of caffeine and the calculated structures are given in **Figure 5.37**. Thermodynamic quantities for the proposed isomers of the SCBD of caffeine are given in **Table 5-16**.

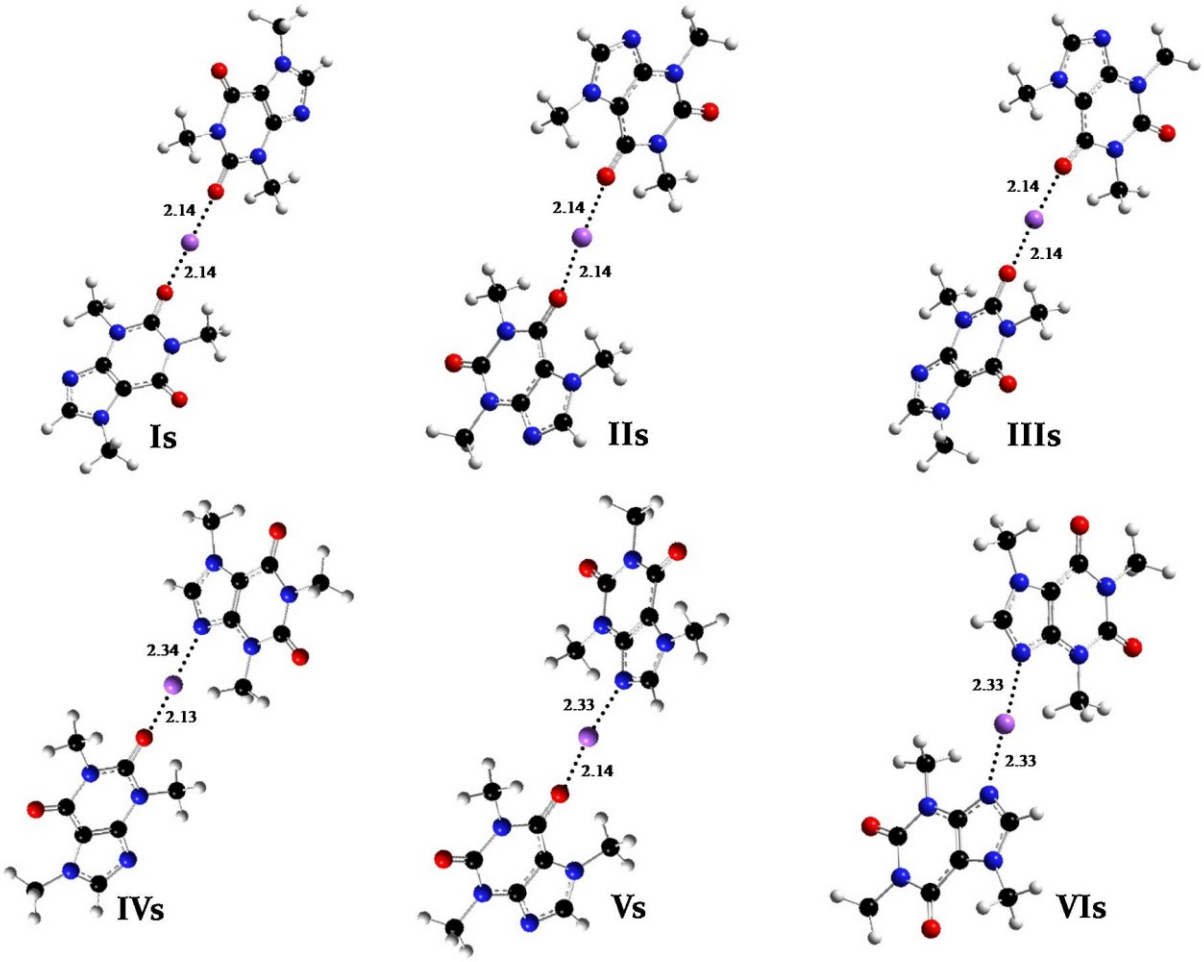

Figure 5.37: Calculated structures of possible isomers of the SCBD of caffeine. Optimized at the B3LYP/6-311+G(d,p) level of theory.

Table 5-16: Calculated energies of the proposed SCBD isomers formed by caffeine. Energies for the interacting sites have been calculated at the MP2(full)/aug-cc-pCVTZ//B3LYP/6-311+G(d,p) level of theory on N(9), O(2) and O(6) in both monomer moieties, and also on Na. Energies for all remaining atoms have been calculated at the MP2(full)/6-311+(2d,2p)//B3LYP/6-311+G(d,p) level of theory. All energies are reported in kJ mol^{-1}. $\Delta\Delta G^{\circ}_{298}$ is calculated with respect to the lowest energy isomer, **Is**.

Species	ΔH°_{rxn}	ΔS°_{rxn}	ΔG°_{298}	$\Delta\Delta G^{\circ}_{298}$
Is	-126	-104	-94.8	0.0
IIs	-113	-131	-74.3	20.5
IIIs	-111	-111	-78.2	16.6
IVs	-98.3	-127	-60.5	34.3
Vs	-99.7	-131	-60.8	34.0
VIs	-105	-127	-66.7	28.1

Several factors that may simplify the interpretation of the IRMPD spectrum for the SCBD of caffeine relative to the spectrum of the PBD have been described previously. However, the structures and binding energies of the SCBDs of caffeine given in **Table 5-16** leads to the realization of the possibility of more simplification being made.

First, there is the large increase in bond distance between heteroatoms involved in the sodium cation interaction relative to that found in the PBDs of caffeine. The $O-Na^{+}\cdots O$,

$N-Na^{+}\cdots O$ and $N-Na^{+}\cdots N$ distances are 4.28, 4.47 and 4.66 Å, respectively. The $O-Na^{+}\cdots O$ and $N-Na^{+}\cdots N$ bonds share the Na^{+} ion efficiently and are thus characterized by a flat potential well possessing no barrier. The $N-Na^{+}\cdots O$ bond is characterized by an asymmetric double-well potential with the global minimum favouring the oxygen side of the bond. Electronic structure calculation has found that rotation about the sodium cation interaction from the most stable geometry (**Is**) into the most eclipsed configuration in the SCBD of caffeine results in a rise in the electronic energy of only 0.1 kJ mol^{-1}. The essentially negligible increase in electronic energy can be regarded as free rotation about the sodium cation interaction under the experimental conditions, and thus it is reasonable to assume that six isomers of the SCBD of caffeine exist compared to the six pairs of enantiomers for the PBD of caffeine.

The second difference between the formation of the SCBDs and PBDs of caffeine is in relation to which sodium cation-bound monomer is favoured to combine with neutral caffeine to form the SCBD. **Table 5-15** shows that initially the O(2) site of neutral caffeine preferentially interacts with sodium cation, and **Table 5-16** shows that this species also forms the most favourable SCBD, greatly reducing the possibility of forming multiple isomers. The simplified situation for the SCBD does not exist for formation of the PBD of caffeine and a possible explanation for this follows.

It has been shown that the most favourable site of initial protonation of caffeine is located at N(9) (**Table 5-1**); however the most favourable pair of isomers for the PBD of caffeine (**IIIa/b**) does not involve binding between nitrogen atoms. The $N-H^{+}\cdots N$ dimer is

found to be the least probable isomer of the PBD of caffeine. Because N(9) is preferentially protonated it is likely that formation of $N-H^+\cdots O$ PBDs (**Ia/b**) will dominate initially, however, equilibrium between the PBD of caffeine, neutral caffeine and protonated caffeine exists such that a statistical distribution of both oxygen and nitrogen protonated monomers will be formed following dissociation of the PBD. The oxygen protonated caffeine monomers are then able to re-associate with neutral caffeine to form the more favourable $O-H^+\cdots O$ PBD (**IIIa/b)**. Based on energetic considerations, at equilibrium the solution should largely consist of **IIIa/b**, however **Ia/b** will also exist and confirmation of the presence of at least one $N-H^+\cdots O$ PBD has been verified in the IRMPD spectrum of the PBD of caffeine.

5.4.2 Mass-Selected IRMPD of The Sodium Cation-Bound Dimer of Caffeine

The mass-selected IRMPD spectrum of the SCBD of caffeine has been obtained and is given in **Figure 5.38** along with a calculated spectrum including contributions from the lowest energy isomer, **Is**. It is proposed that very little, or no contribution of vibrational intensity is arising from other isomers in the IRMPD spectrum based on the discussion provided above. Comparison of the IRMPD spectrum and the calculated spectrum does not suggest that the consideration of other isomers is necessary. Mass-selected IRMPD of the isolated SCBD of caffeine with *m/z* 411 afforded sodium cationized caffeine with *m/z* 217 as an exclusive product ion. As found with all other PBD spectra, the weak sodium cation interaction in the SCBD of caffeine results in dissociation occurring for even the lowest intensity absorptions generating an IRMPD spectrum spanning the entire observable

frequency range. Assignments of the vibrational intensities for both the IRMPD spectrum and calculated spectrum of **Is** are given in **Table 5-17**.

Based on previously described IRMPD spectra and the results of visualization of vibrational modes with the aid of *GAUSSVIEW 4.1*, assignment of vibrational intensities have been made with less ambiguity than for the PBD spectra presented above. Generally the peaks of the calculated spectrum of **Is** match very well with the IRMPD spectrum with a MAD of 19 cm^{-1}. Much of the difference arises from the degenerate symmetric and asymmetric stretching of the free C(6)=O of each caffeine moiety occurring at 1732 cm^{-1} in the IRMPD spectrum and at 1772 cm^{-1} in the calculated spectrum, a difference of 40 cm^{-1}. This is not unexpected since the free carbonyl stretch in the IRMPD spectrum of protonated caffeine (**II**) located at 1757 cm^{-1} is calculated by a harmonic approximation to occur at 1805 cm^{-1}, a difference of 48 cm^{-1}. Based on the energetic arguments and the results of the IRMPD spectrum it is proposed that the structure of the SCBD of caffeine is best represented by **Is**.

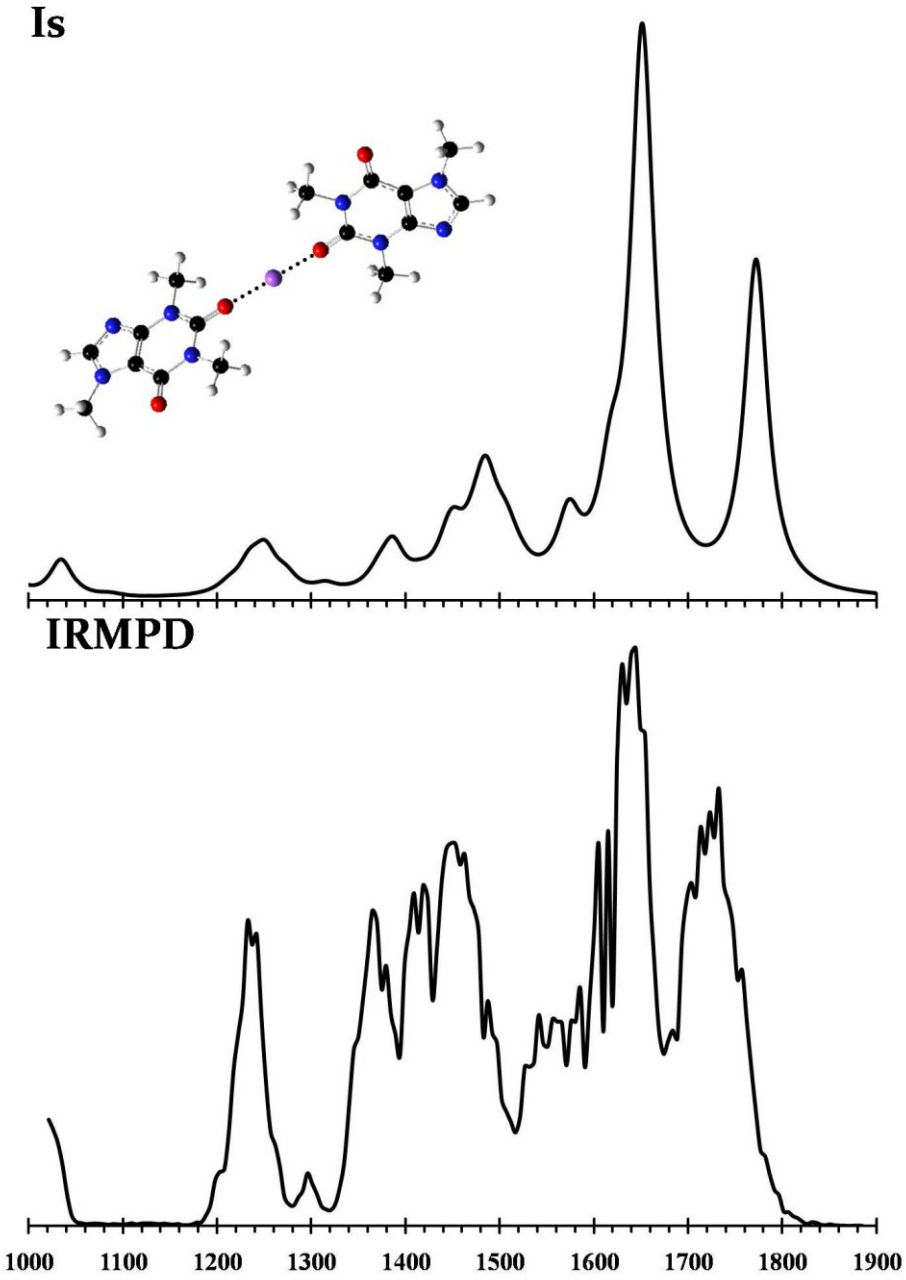

Figure 5.38: IRMPD spectrum of the SCBD of caffeine (bottom) and the spectrum of **Is** determined by calculation at the B3LYP/6-311+G(d,p) level of theory. Harmonic frequencies have been scaled by 0.9679. Intensities for the experimental and calculated spectra are in relative units of IRMPD efficiency and km mol^{-1}, respectively.

Table 5-17: Infrared peak assignments associated with the IRMPD and calculated spectra for the SCBD of caffeine presented in **Figure 5.38**. The frequencies are assigned in units of wavenumbers (cm^{-1}).

Vibrational Mode	IRMPD	Is
***2 x C(6)=O stretch (symm.)**	1732	1772
***2 x C(6)=O stretch (asymm.)**	1732	1772
***** **C(2)=O-Na^+ stretch**	1644	1651
***** **methyl breathing**	1487	1485
	1448	1450
***** **C(8)-H wag**	1232	1251
***** **N(7)-C(8) stretch**	1365	1386
MAD from IRMPD	0	19

5.4.3 Electronic Structure: The Sodium Cation-Bound Dimer of Theophylline

Exactly as described previously for caffeine, theophylline possesses three stable sites for sodium cation interaction located at the N(9), O(2) and O(6) positions. The three SCA values of the sites N(9), O(2) and O(6), along with the associated changes in entropies and Gibbs free energies (**Eq. 5.4**) are given in **Table 5-17**.

Table 5-18: Calculated sodium cation affinities (SCA) and thermodynamic quantities associated with the interaction of sodium cation with theophylline (**Eq. 5.4**). Energies for the interacting sites have been calculated at the MP2(full)/aug-cc-pCVTZ//B3LYP/6-311+G(d,p) level of theory on N(9), O(2) and O(6) in both monomer moieties, and also on Na. Energies for all remaining atoms have been calculated at the MP2(full)/6-311+(2d,2p)//B3LYP/6-311+G(d,p) level of theory. All energies are reported in kJ mol^{-1}.

Site of Sodium Cation Interaction	SCA	ΔS°_{rxn}	ΔG°_{298}	$\Delta\Delta G^{\circ}_{298}$
N(9)	114	-102	-83.8	38.6
O(2)	153	-104	-122	0.0
O(6)	142	-96.2	-113	9.1

It is found that the calculated value of the SCA at O(6) in theophylline is exactly the same as obtained for caffeine, however the sodium cation interaction formed in theophylline is more favourable entropically. The proximity of O(6) to the N(7) methyl moiety in caffeine may result in a weak steric interaction occurring between the O(6) interacting sodium ion and the methyl group. This interaction is absent in theophylline since a hydrogen exists at the N(7) site (**Figure 5.39**).

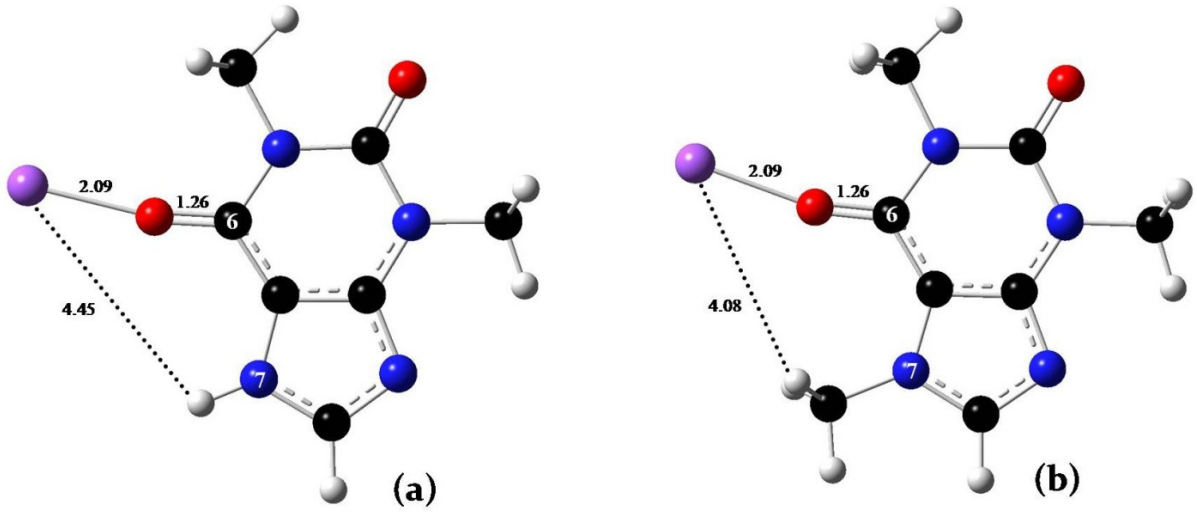

Figure 5.39: Calculated structures of theophylline **(a)** and caffeine **(b)** interacting with Na^+ at the C(6) carbonyl oxygen. The SCA of each species is calculated to be identical; however the interaction of Na^+ with theophylline is favoured entropically. Energies have been obtained at the MP2(full)/aug-cc-pCVTZ//B3LYP/6-311G+(d,p) level of theory for Na, O(6), O(2) and N(9), and all remaining atoms at the MP2(full)/6-311+(2d,2p)//B3LYP//6-311G+(d,p) level of theory with harmonic frequencies scaled by 0.9679.

With three sites of sodium cation interaction available in theophylline, it is possible to form six possible isomers of the SCBD of theophylline and the calculated structures are given in **Figure 5.40**. Thermodynamic quantities for the proposed isomers of the SCBD of theophylline are given in **Table 5-19**.

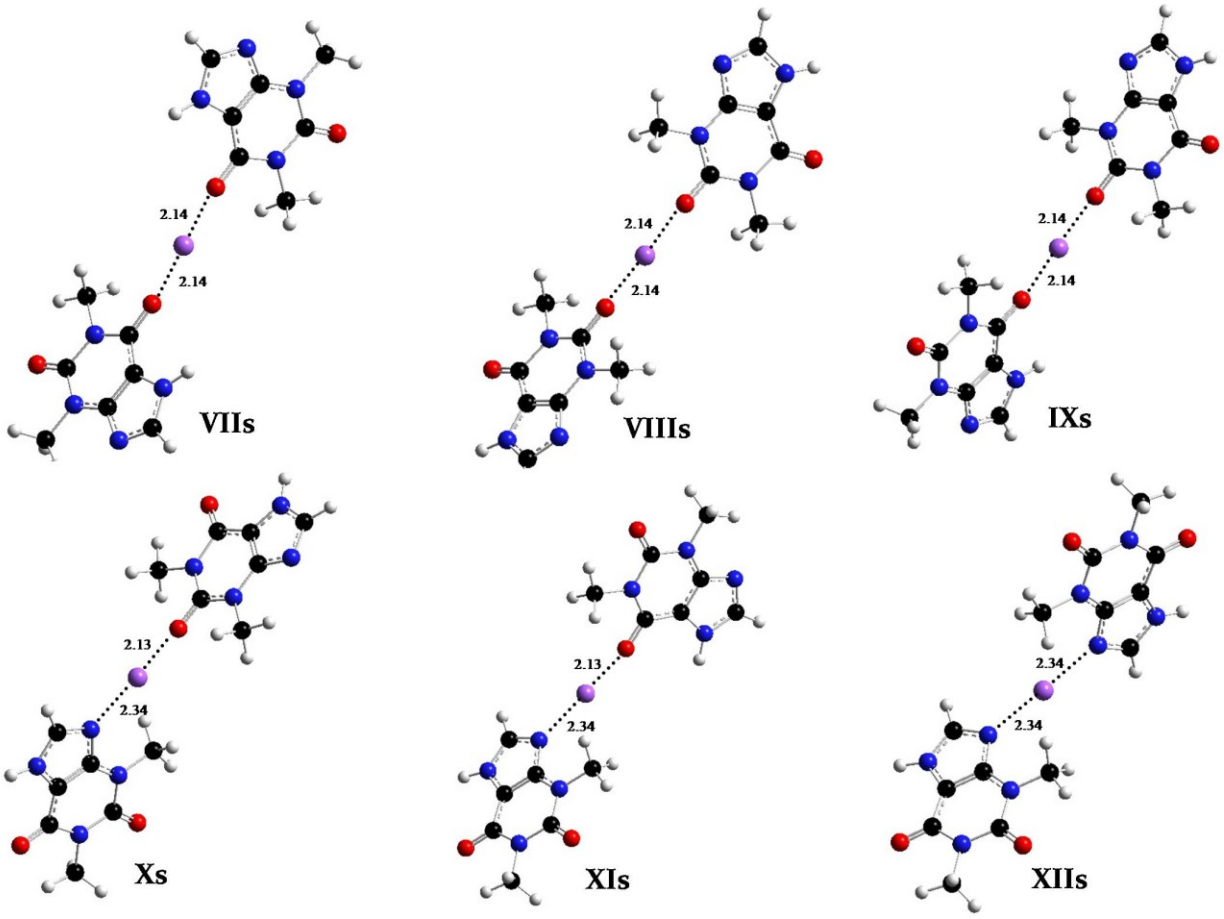

Figure 5.40: Calculated structures of possible isomers of the SCBD of theophylline. Optimized at the B3LYP/6-311+G(d,p) level of theory.

Table 5-19: Calculated energies of the proposed SCBD isomers formed by theophylline. Energies for the interacting sites have been calculated at the MP2(full)/aug-cc-pCVTZ//B3LYP/6-311+G(d,p) level of theory on N(9), O(2) and O(6) in both monomer moieties, and also on Na. Energies for all remaining atoms have been calculated at the MP2(full)/6-311+(2d,2p)//B3LYP/6-311+G(d,p) level of theory. All energies are reported in kJ mol^{-1}. $\Delta\Delta G^{\circ}_{298}$ is calculated with respect to the lowest energy isomer, **VIIIs**.

Species	ΔH°_{rxn}	ΔS°_{rxn}	ΔG°_{298}	$\Delta\Delta G^{\circ}_{298}$
VIIs	-113	-113	-79.1	11.6
VIIIs	-122	-106	-90.6	0.0
IXs	-112	-108	-79.8	10.9
Xs	-90.1	-114	-56.1	34.5
XIs	-90.4	-119	-54.8	35.8
XIIs	-96.3	-123	-59.6	31.0

It is reasonable to assume that the IRMPD spectrum of the SCBD of theophylline should be predominantly based on vibrational intensities arising from isomer **VIIIs**. The IRMPD spectrum of the SCBD of caffeine demonstrated the exclusive formation of the analogous isomer, **Is**. Both isomers **Is** and **VIIIs** are characterized by having the most favourable initial site of sodium cation interaction in the monomer as also being the most favourable site to form the SCBD. For both **Is** and **VIIIs** the formation of the SCBDs are favoured with respect to the enthalpy and entropy change of reaction relative to all other

proposed isomers. This results in **Is** and **VIIIs** existing as the dominant isomers at all temperatures since, at higher temperature entropy, is the principle contribution to the value of Gibbs free energy. The IRMPD spectrum of the SCBD of theophylline will reveal if theophylline is as exclusive as caffeine in formation of the SCBD.

5.4.4 Mass-Selected IRMPD of The Sodium Cation-Bound Dimer of Theophylline

The mass-selected IRMPD spectrum of the SCBD of theophylline has been obtained and is given in **Figure 5.41** along with a calculated spectrum including contributions from the lowest energy isomer, **VIIIs**. The IRMPD spectrum obtained for the SCBD of theophylline is found to be of superior quality, thus greatly simplifying the ability to assign vibrational intensities unambiguously. There appears to be an excellent match between the calculated spectrum of **VIIIs** and the IRMPD spectrum, therefore no other isomers were included as contributors to the spectrum. Mass-selected IRMPD of the isolated SCBD of theophylline at *m/z* 383 afforded sodium cationized theophylline at *m/z* 203 as the exclusive product ion. Due to the high resolution of the spectrum, many more vibrational intensities have been assigned with confidence and are given in **Table 5-20**.

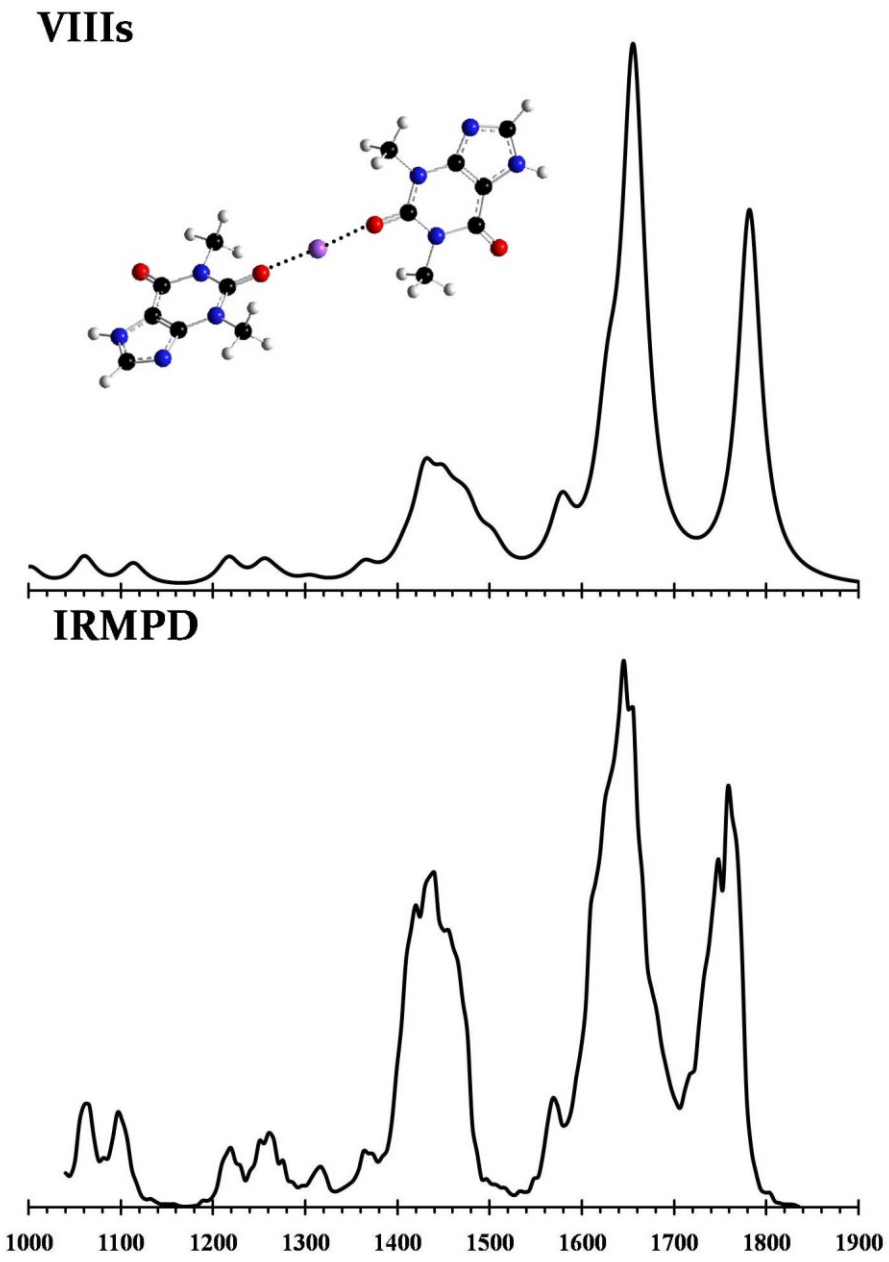

Figure 5.41: IRMPD spectrum of the SCBD of theophylline (bottom) and the spectrum of **Is** determined by calculation at the B3LYP/6-311+G(d,p) level of theory. Harmonic frequencies have been scaled by 0.9679. Intensities for the experimental and calculated spectra are in relative units of IRMPD efficiency and km mol^{-1}, respectively.

Table 5-20: Infrared peak assignments associated with the IRMPD and calculated spectra for the SCBD of theophylline presented in **Figure 5.41**. The frequencies are assigned in units of wavenumbers (cm^{-1}).

Vibrational Mode	IRMPD	VIIIs
***2 x C(6)=O stretch (symm.)**	1758	1781
***2 x C(6)=O stretch (asymm.)**	1758	1781
***** **C(2)=O-Na^+ stretch**	1646	1655
***** **C(2)=O-Na^+ stretch + C(4)=C(5) stretch**	1625	1628
***** **N(7)-H + C(8)-H symm. wag**	1568	1578
	1250	1256
***** **N(7)-H + C(8)-H symm. wag + methyl breathing**	1435	1429
***** **ring breathing**	1363	1364
***** **C(8)-H wag + methyl bending**	1220	1217
***** **N(7)-H + C(8)-H asymm. wag**	1096	1114
***** **methyl rocking**	1061	1060
MAD from IRMPD	0	9

The high quality of the IRMPD spectrum obtained for the SCBD of theophylline allows for the assignment of a large number of vibrational intensities resulting in a MAD of

calculated harmonic frequencies of only 9 cm^{-1} from the IRMPD spectrum. Vibrational intensities associated with the degenerate symmetric and asymmetric free carbonyl (C(6)=O) stretching modes in the SCBD of theophylline and caffeine are red-shifted for caffeine and located in the IRMPD spectra at 1758 and 1732 cm^{-1}, respectively. The calculated harmonic frequencies for these modes in the SCBD of theophylline and caffeine are at 1781 and 1772 cm^{-1} respectively, demonstrating a theoretically predicted red-shift between the dimers as well. The vibrational intensities associated with the carbonyls (C(2)=O-Na^{+}) involved in interaction with the sodium cation are very similar, located at 1646 and 1644 cm^{-1} in the IRMPD spectra of the SCBDs of theophylline and caffeine, respectively. The calculated harmonic frequencies for these modes are at 1655 and 1651 cm^{-1} respectively, implying that very little difference in chemical environment exists between the sodium cation interactions in the dimers. It is intriguing that the free carbonyl frequencies differ so greatly between the two SCBDs and it is difficult to precisely describe what electronic effects are resulting in this observation. Although it is not valid to compare the absolute vibrational frequencies between solution and the gas phase it has been found (in nujol mull) that the C(6)=O stretches are located at 1718 and 1699 cm^{-1} for neutral theophylline and caffeine, respectively demonstrating a similar red-shift for the caffeine C(6)=O stretch in the condensed phase.[148] Generally, substitution of a hydrogen atom with a methyl moiety within the proximity of a carbonyl increases the stretching frequency due to an increase in inductive electron donation.[149] There must not be a significant inductive effect as a result of the substituting N(7)-H in theophylline, with N(7)-CH_3 in caffeine, since this would result in an observed

blue-shift of the C(6)=O stretch in caffeine. There is possibly a through space interaction between the methyl moiety at N(7) in caffeine and the C(6)=O carbonyl oxygen, since a noticeable difference exists in the calculated entropy between the addition of sodium cation to the C(6)=O carbonyl in neutral theophylline and caffeine. It is found that entropy favours addition to the less sterically congested carbonyl oxygen in theophylline, suggesting the possibility of restriction of internal rotation of the methyl moiety located at N(7) in caffeine.

5.4.5 Concluding Remarks

The mass-selected IRMPD spectra of the SCBDs of caffeine and theophylline have been obtained. Both electronic structure calculations and the IRMPD spectra predict the most likely structure of the SCBDs of caffeine and theophylline to exist as **Is** and **VIIIs**, respectively. In both **Is** and **VIIIs** the SCBDs are found to engage in the efficient sharing of Na^+ between the C(2)=O functional groups possessed by each monomer. Binding between the C(2)=O groups has also been observed as the most favourable enantiomeric pair for the PBD of caffeine (**IIIa/b**), and the PBD of theophylline (**XIIa/b**). However the most favourable structure of the PBD of theophylline exists as the unique bidentate isomer **XIIIA**.

The frequencies of the C(2)=O-Na^+ stretch are found to be nearly identical in the IRMPD spectra for both of the SCBDs of caffeine and theophylline at 1644 and 1646 cm^{-1}, respectively. However, the degenerate free C(6)=O symmetric and asymmetric stretches for the SCBDs of caffeine and theophylline found at 1732 and 1758 cm^{-1}, respectively, demonstrating a red-shift for caffeine possibly linked to the proximity of the N(7) methyl moiety absent in theophylline.

Based on the results of electronic structure calculations it was proposed that free rotation about the $O - Na^+ \cdots O$ would result in less stable isomers for the SCBDs of caffeine and theophylline relative to those described for their PBDs. This is confirmed by reduced complexity observed in the IRMPD spectra of both ions allowing for the unambiguous assignment of structures **Is** and **VIIIs** to the IRMPD spectra of the SCBDs of caffeine and theophylline, respectively. Due to the reduced scale of nuclear motion of bonded Na^+ in the IR frequency range it was also proposed that harmonic frequency calculations may perform sufficiently well under these circumstances relative to the presumably anharmonic interactions arising from proton motion in the IHB of the PBDs. This is verified by the low MAD of calculated harmonic frequencies from the IRMPD frequencies of 19 and 9 cm^{-1} for the SCBDs of caffeine and theophylline, respectively.

Chapter 6
A New Electrospray Ion Source for High Pressure Mass Spectrometry

6.1 Introduction

In section 2.4 the technique of high pressure mass spectrometry (HPMS) was introduced and details regarding the current instrumental configuration of the HPMS located in the McMahon laboratory have been provided. The current HPMS design has provided fundamentally important and highly cited experimental data such as the PAs[150, 151] and SCAs[152] of hundreds of small molecules, gas phase S_N2 reactions[153, 154], methyl cation transfer reactions[155], as well as a means to measure the strengths of IHBs in gaseous ionic clusters quantitatively.[4, 64, 80, 156] However, there exists one limitation with regard to the nature of species amenable to study by the current technique, which is an inability to promote certain species of molecules into the gas phase. Generally this is found when molecules possess intermolecular interactions sufficiently strong such that the temperature required to yield a minimal vapour pressure exceeds the decomposition threshold of the species. The energy used to volatize the molecules is delivered in the form of heating a 5 L stainless steel reservoir, where normally liquid phase samples have been introduced by injection through a septum. This technique is perfectly well-suited to small volatile organic compounds, however there exists many small molecules that cannot be fully promoted to the gaseous state by heating. Molecules exhibiting these characteristics include the entire family of naturally

occurring amino acids, small peptides, nucleic acid bases, ionic compounds and methylxanthine species such as caffeine and theophylline, to name but a few. There have been exceptional HPMS experiments relating to the study of cluster ions of several of the species previously described performed successfully.[64, 156-158] However all such experiments require direct introduction of a solid sample of the analyte into the ion source, where gentle heating causes the species to provide a minimally sufficient vapour pressure for equilibrium measurements to be made. The difficulties arising from performing experiments in this manner include: 1. In order to access the ion source, the high vacuum (~ 10^{-7} Torr) chamber in which the ion source is housed must be breached to introduce the solid sample, then pumped down once the ion source has been reassembled, requiring at least one to two days of instrument down time. 2. Following completion of a study involving the use of a solid reagent sample, a residue is deposited within the interior of the ion source and also on the surfaces of the primary ion optics, requiring extensive physical cleaning in order to proceed with a new experiment.

To remove the limitations imposed by the issues described above, it would be desirable to find a method in which gaseous species are produced in a manner that does not require heating. One such technique that fulfills this criteria is electrospray ionization (ESI). The following will provide an overview of the design, assembly and future implementation of a unique pulsed-electrospray ionization high pressure source currently in the last stage of implementation in the McMahon laboratory.

6.2 Electrospray Ionization (ESI)

The first mention of ESI in the literature was that by Dole and coworkers in 1968 in which oligomers of polystyrene were electrosprayed and detected from samples of known molecular weight.[159] It was not until 1982 that Masamichi Yamashita, a post doctoral fellow under the supervision of John B. Fenn, constructed the first working ESI mass spectrometer.[160] A schematic representation of the device is shown in **Figure 6.1**.[161]

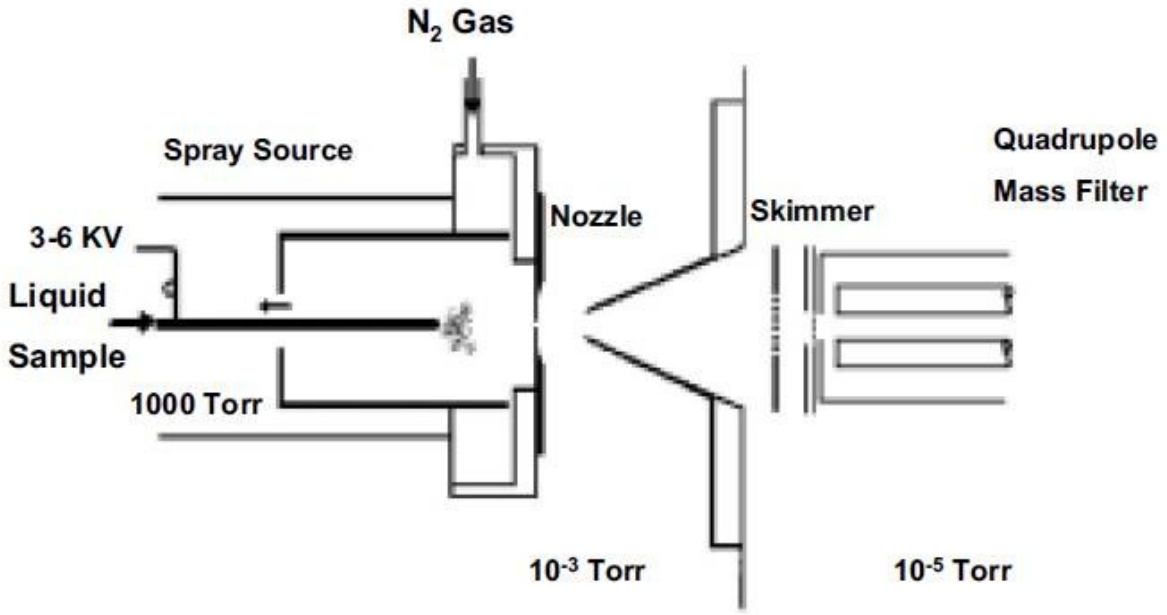

Figure 6.1: Schematic representation of the ESI-MS constructed by Yamashita and Fenn.[161]

The basis of operation of the apparatus shown in **Figure 6.1** is quite simple and begins with the introduction of analyte solution through a stainless steel hypodermic needle to which a static potential of approximately 3 to 6 kV is applied. The needle is placed within a cylindrical electrode and nozzle assembly fixed at ground potential (0 V). This induces the

presence of a strong electric field between the needle tip and the nozzle plate. The nozzle serves as an interface between the high pressure region where the ESI process occurs and the high vacuum region of the mass spectrometer. Due to the pressure differential between the ionization chamber and vacuum region, ions leave the nozzle at supersonic velocities.

There are two models generally accepted for describing the electrospray process, the "charged residue model" (CRM) of Dole[161] and the "ion evaporation model" (IEM) of Iribane and Thomson.[162] Both models incorporate the idea of a "Rayleigh Limit", postulated theoretically by Lord Rayleigh in 1882[163], describing the behaviour expected during the evaporation of solvent from a droplet that possess a net electric charge. The "Rayleigh Limit" is defined as the critical value where the coulomb repulsion of the ions contained within a solvent droplet exceeds the surface tension, causing it to break apart into smaller droplets. The first observation of the "Rayleigh Limit" was by John Zeleny at the University of Minnesota and then at Yale.[164] Zeleny used an apparatus comprised of a 0.92 mm diameter vertical glass tube attached to a reservoir of ethanol and suspended 2 cm above a grounded plate. The ethanol was charged with static electric potentials of 5 and 6 kV and observation of the "Rayleigh Limit" was made between the end of the glass tube and plate by taking a series of high speed (800 shots s^{-1}) photographs of the process. The CRM model postulates that the decomposition of droplets due to evaporation and successive Rayleigh instabilities will ultimately lead to droplets containing only one solute ion. As the final solvent molecules evaporate from the droplet they leave behind only one charged gaseous ion. The IEM model is strikingly similar in all regards to the CRM model; however it does differ in the proposed

mechanism of how single ions are obtained in the gas phase. The IEM model postulates that as a solvent droplet becomes sufficiently small, the electric field strength at the droplet surface is intense enough to "lift" an ion into the gas phase. Within the ESI community there is not a unanimous preference for either mechanism, however Fenn has proposed that the IEM model is more consistent with experimental observations involving small molecules and that the CRM model may be better suited for large molecules.[161]

One very important property of ESI is that it is a "soft" ionization method, implying that it leaves the ions with very little excess internal energy which could result in unimolecular dissociation. This is why ESI is particularly well suited to the study of large, fragile biomolecules and was likely the inspiration for the title of John B. Fenn's Nobel lecture, "Electrospray: Wings for Molecular Elephants".

6.3 Existing Electrospray Ionization High Pressure Ion Sources

There have been two independent designs implementing ESI in conjunction with HPMS reported in the literature. Both designs allow for the measurement of ion-molecule equilibria involving electrosprayed ions. The first[165-167] apparatus was built by Klassen and coworkers and the second[168, 169] was built individually by Wincel. A brief description of both designs and their operation follows.

A schematic representation[165, 167] of the ESI source constructed by Klassen and coworkers is shown in **Figure 6.2** with the initial and slightly modified designs represented by **(a)** and **(b)**, respectively.

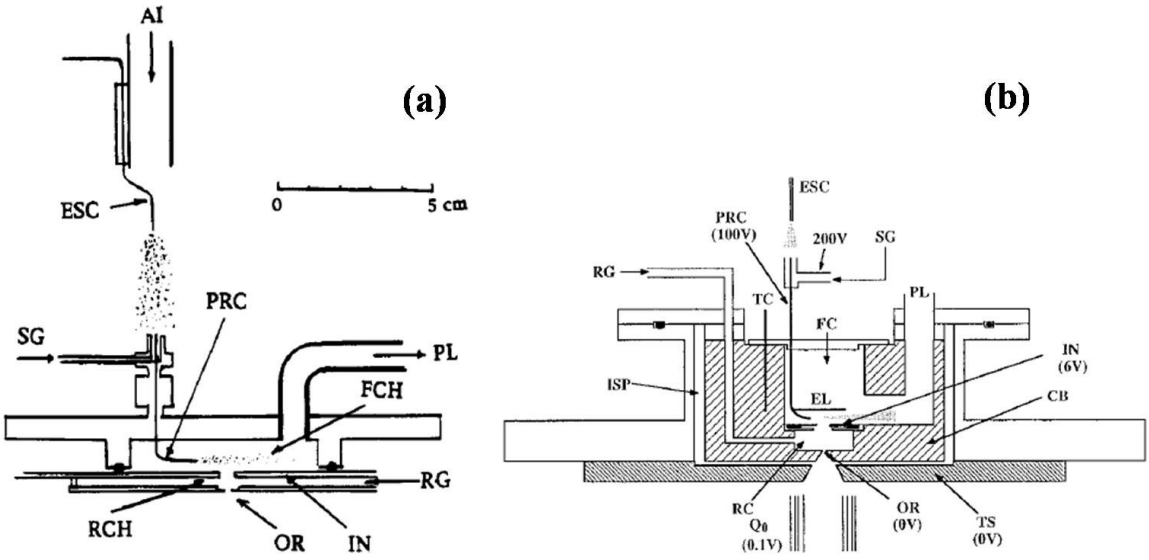

Figure 6.2: Schematic representations of the high pressure ESI sources built by Klassen *et al*. **(a)** The first ion source. The abbreviations shown are as follows: ESC = electrospray capillary (4 kV); SG = source gas tube and sleeve (700 V) through which N_2 gas is flowed in order to suppress the entry of solvent molecules into the pressure reduction capillary, PRC (165 V); FCH = forechamber (165 V) maintained at 10 Torr by pumping lead, PL; IN = interface plate (110 V) separating FCH from the reaction chamber, RCH by a 4 mm diameter orifice; RG = reagent gas mixture which flows through the reaction chamber and into FCH. OR = orifice of 100 μm diameter (100 V) located on the bottom plate of the RCH, where ions deflected from the jet expansion leaving the PRC may exit the source following establishment of ion-molecule equilibria in the RCH. **(b)** The second ion source. Additions differing from the source shown by **(a)** are: CB = copper block containing forechamber (FC) and reaction chamber (RC); TC = thermocouple; ISP = evacuated space for thermal insulation; TS = thermal shield to reduce radiative heating of cryopump surfaces; Q_0 = AC only Brubacker lens, followed by a triple quadrupole assembly, not shown in the diagram.[165, 167]

The operation of the high pressure ESI source shown in **Figure 6.2 (a)** can be described as follows: Solution is provided to the ESC by a motor driven syringe pump (1.5 to

2 μl/min), where the spray containing ions is drawn into the PRC and supersonically jets into the ion source FCH. The ion-containing plume emitted from the PRC is parallel to the bottom of the FCH, and ions are deflected by a potential difference between the PRC and IN towards the 4 mm orifice, where they drift under the presence of a weak electric field (20 V/cm) through the RCH. In the RCH, ion-molecule equilibria is established and a small fraction of ions will reach the orifice, where they effuse out of the RCH and into a triple quadrupole mass spectrometer. A thermocouple is placed firmly on the wall near OR, which is assumed to be at the same temperature as the reactant gas. The apparatus is not temperature-variable and provided equilibrium measurements at room temperature only.

Several of the critical dimensions and flow rates associated with the high pressure ESI source shown in **Figure 6.2 (a)** are as follows: The PRC is comprised of stainless steel, 0.7 mm o.d. (outer diameter), 400 μm i.d. (inner diameter) and 5 cm long. The PRC was strengthened by silver soldering it inside a 1.5 mm o.d. tube. The PRC exit is approximately 3 mm above IN and 1 cm adjacent to the axis of the 4 mm orifice of IN. The widths of the FCH and RCH are 9 and 5 mm, respectively. Typically, a pressure of approximately 10 Torr is maintained in the RCH and FCH regions and is monitored by a capacitance pressure sensor attached to PL. The reagent gas mixture is comprised of 10 Torr of pure nitrogen and 1 to 80 mTorr of analyte which flows from the PRC interface counter current to the spray plume at a rate of ~ 2 L/min. In the spray chamber, dry air is passed over the ESC at a high rate of ~ 60 L/min in order to promote the evaporation of solvent molecules. It was found that the

electrosprayed solutions performed very well when they were composed exclusively of methanol, due to its high volatility.

The modifications made to apparatus **(b)** in **Figure 6.2** consist of the addition of a cylindrical copper block (CB) in which the reaction chamber (RC) and forechamber (FC) are housed. Copper is used due to its excellent heat conducting properties. The CB has cartridge heaters inserted inside of it to allow for temperature variability, which is a necessity for producing van't Hoff plots. A thermocouple (TC) is placed in a narrow channel within the CB.

The apparatus described by Klassen and coworkers was used successfully to obtain hydration energies of a series of protonated amines, diamines and some small peptides.[165-167]

The author and his colleague, Jon Martens, were fortunate enough to have been invited to the Polish Academy of Sciences in Warsaw, Poland by Professor Henryk Wincel to observe the performance of his pulsed electrospray high pressure mass spectrometer in person. The visit was very valuable in informing the design of a similar device for our own high pressure mass spectrometer at the University of Waterloo. The knowledge gained from Professor Wincel, with regard to potential difficulties arising in the design of our own device, has been invaluable.

The apparatus designed and built by Wincel is shown in **Figure 6.3**.[168, 169]

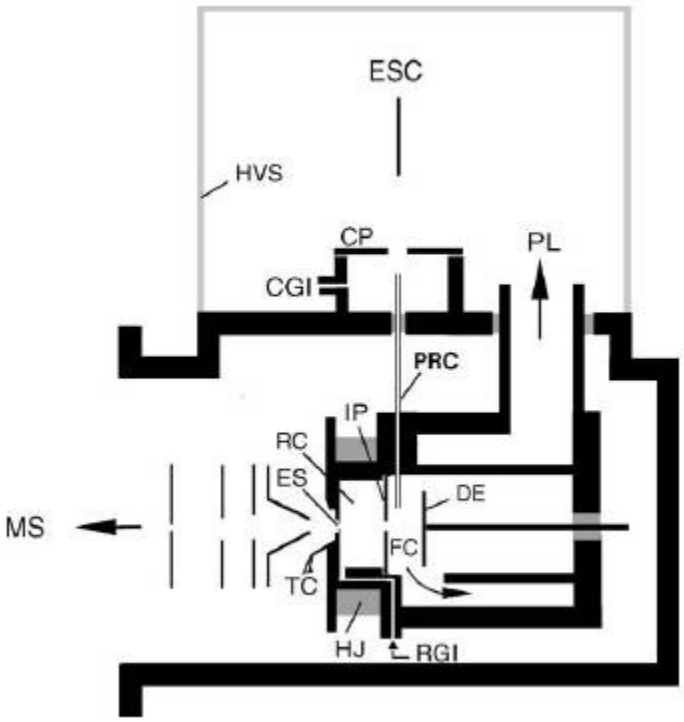

Figure 6.3: Schematic representations of the high pressure ESI source built by Wincel. The abbreviations shown are as follows: ESC = electrospray capillary (4 kV); HVS = high voltage shield; CP = curtain plate; CGI = curtain gas inlet; PL = pumping lead; PRC = pressure reducing capillary (2 kV); FC = forechamber; DE = deflection electrode (2014 to 2050 V); IP = interface plate (2014 to 2016 V); RC = reaction chamber (2 kV); RGI = reactant gas inlet; TC = thermocouple; ES = exit slit (15 μm x 3 mm); HJ = electrically heated jacket. The mass spectrometer here is a single-focusing, 60° magnetic sector instrument.

A description of the design of the apparatus shown in **Figure 6.3** is as follows: Electrosprayed ions are generated at atmospheric pressure by an emitter made from a fused-silica capillary (ESC) with a 15 and 150 μm i.d. and o.d., respectively. The emitter is inserted into a stainless steel capillary where it extends from the tip by 2 mm. The capillary end is

coated with a conductive mixture made from polyimide and graphite. This was done to prevent electrolysis of the solution because the power supply in use has a sufficiently high current to cause this. The problem with electrolysis of the solution is that it produces bubbles of oxygen and hydrogen gas in the line causing sputtering of the emitter. The emitter assembly is fixed to a home-built xyz-translational stage for the purpose of optimizing ion intensities by changing the emitter position with respect to the CP entrance orifice (4 mm). Solutions are delivered to the emitter by a motor-driven syringe pump at a flow rate of 0.8 μL/min, with the solvent consisting exclusively of methanol with analyte concentrations of approximately 10^{-4} M. The emitter tip is positioned approximately 5 mm from the CP orifice where 25 L/h of nitrogen gas flows counter current towards the electrospray plume. Electrosprayed ions are drifted through the curtain gas and into the PRC due to the potential difference between the emitter tip and the PRC.

The design of Wincel`s ion source is similar to that described above for the apparatus built by Klassen and coworkers. However, it possesses two significant improvements. The first is the design of the PRC (500 μm i.d. and 118 mm long), which is resistively heated by applying a small voltage and current (0.5 to 2 V at 1 to 2 amps) in Wincel's design. The PRC in the apparatus built by Wincel is capable of being heated from 80 to 200 $^{\circ}$C and serves to facilitate the desolvation process.[†] The second improvement is the pulsing of the continuous beam of ions exiting the PRC into the RC. This allows for the production of temporal profiles similar to those described in section 2.4.1 (**Figure 2.8)** and, as a result, the equilibrium

[†] Wincel advised that heating of the PRC was the single most important factor contributing to the impressive ion intensities produced by his apparatus.

constant can be obtained as a function of ion intensities at a constant pressure of analyte (**Eq. 2.52**). The apparatus described by Klassen and coworkers is not pulsed and the equilibrium constant is obtained by plotting the simple ratio of ion intensities versus inverse pressure. The linear plot yields a slope equal to the equilibrium constant; however pressure measurements generally have greater uncertainty than intensity measurements, and the data provided by the apparatus designed by Wincel can be considered to be more reliable based on this merit.

The PRC exit is located at distances of 2 and 5 mm, respectively, from the IP and DE. There are short pulses applied between IP and DE with a potential difference of 34 V for 60 μs (700 μs delay with a 10 ns rise time), sampling "slices" of ion packets from the continuous beam emitted from the PRC. The ion intensities are then measured as arrival time distributions (ATD). The time domain of the ATD profiles is normally short due to the presence of a weak electric field (< 33 V/cm) inside the RC, normally between 100 to 1000 μs. In traditional HPMS experiments, temporal profiles obtained in a field free RC of similar dimensions are normally on the order of 10 to 50 ms. In order to obtain the reaction time, the average distribution time (t_{av}) of the ions is obtained from the centre of the ATD profiles. A plot of t_{av} as a function of the inverse of electric field strength (1/E) is linear with an intercept equal to the analyzer time. The analyzer time is the flight time of the ions through the instrument and to the detector. The average residence time of the ions within the RC can be obtained by subtracting the analyzer time from t_{av}. Ions are found to be in equilibrium when the normalized ATD profiles are identical in shape. The ion intensities required for

calculating the equilibrium constant (**Eq. 2.52**) are obtained from the area of the ATD temporal profiles. Data is collected using methods identical to those described in section 2.4.1, but the time scale is significantly shorter. It has been shown by Wincel that for ions drifting through the RC, the presence of electric field strengths below 33 V/cm does not affect the value of the measured equilibrium constant.

Pressure measurements are made in the RGI and PL regions using capacitance pressure sensors and are found to differ by less than 1 mbar. The pressure of the RC is then taken as the average of the two values measured in the RGI and PL regions. The reactant gas mixture required for hydration of ionic species is made by introducing a continuously monitored quantity of water vapour at constant humidity and temperature into pure nitrogen gas.

The temperature of the RC can be varied from room temperature to 300 °C by an electrically heated copper jacket housing the stainless steel RC. Temperature of the RC is monitored by a J-type thermocouple mounted near the ion exit slit.

The pulsed electrospray high pressure ion source constructed by Wincel has been used to provide hydration energies for a variety of alkylamines, amino acids and peptides.[168, 169]

6.4 A New Pulsed Electrospray High Pressure Mass Spectrometer Design

The implementation of a pulsed electrospray high pressure mass spectrometer is currently in progress in the McMahon laboratory. The following will provide a status report regarding what has been achieved thus far, as well as future considerations regarding use of

the new ion source. A schematic representation of the pulsed electrospray high pressure source which has been constructed at the University of Waterloo is shown in **Figure 6.4**.

6.4.1 Electrospray Region

The electrospray emitter assembly, ESE, is a stainless steel (SS) block with dimensions 18 x 23 x 51 mm (**Figure 6.5**). The threaded cylindrical (12.5 mm o.d.) nozzle head is screwed into the tapped end of the ESE block and sealed by an o-ring. The electrospray nozzle head extends 21 mm from the ESE block with an emitter tip length of 3 mm, from which a fused silica capillary (15 μm i.d. and 150 μm o.d.) extends by 1 to 2 mm. The fused silica capillary is fed through a tapped 4 mm orifice located at the back end of the ESE block and sealed by a SS ferrule. The ESE assembly is mounted to an electrically isolating nylon block (14 x 55 x 65 mm), followed by a xyz-translational stage (56 x 56 x 68 mm) with a range of motion of 25.4 mm in three dimensions. Finally, the translational stage is supported by an aluminum bracket (143 x 32 x 19 mm) fixed to the surface of the curtain chamber.

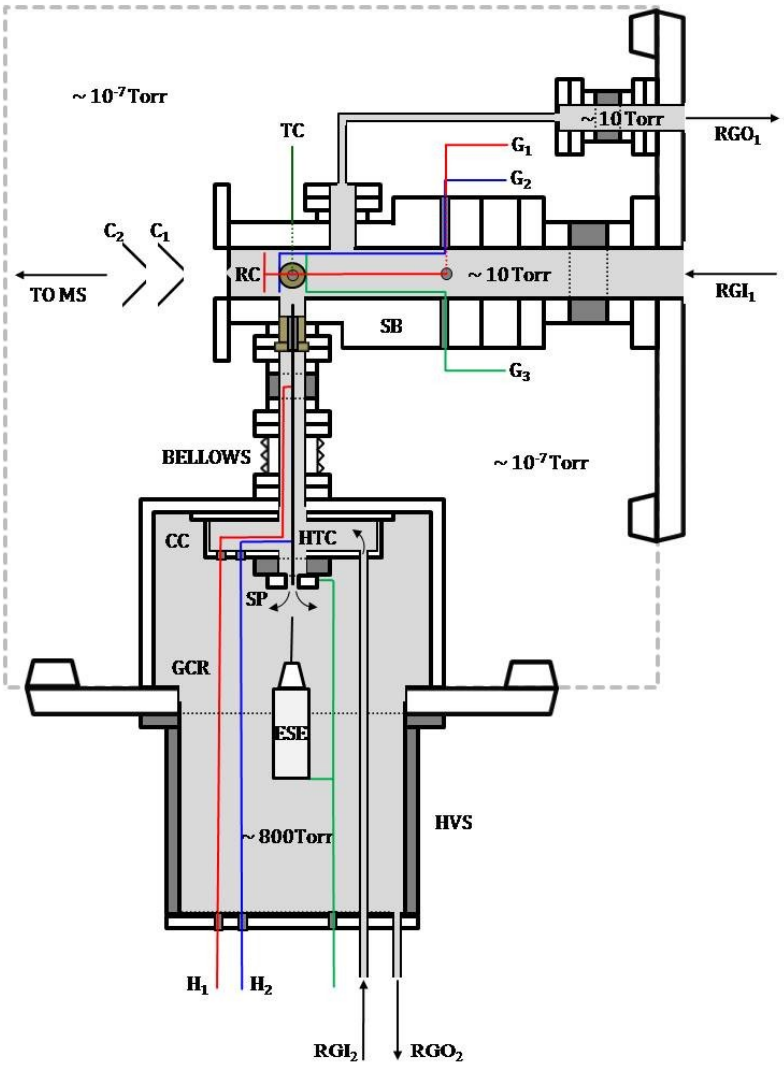

Figure 6.4: Schematic representation of the pulsed electrospray high pressure ion source built at the University of Waterloo. Definition of the abbreviations is as follows: ESE = electrospray emitter assembly (7 to 10 kV); SP = shielding plate (7 to 10 kV); CC = capillary chamber (0 V); GCR = gas confinement region; HVS = high voltage shield (Plexiglas); HTC = heated transfer capillary (3 kV); H_1/H_2 = resistive heating power inputs (0.5 to 2 V at 1 to 2 A, floating at 3kV);); SB = source body (3 kV); RC = reaction chamber (3 kV) 7 mm long with a 100 to 150 μm platinum exit aperture; $G_1/G_2/G_3$ = grids, where G_2 and G_3 (± 2950 to 3050 kV) are used to deflect samples of ions into the RC from the continuous stream emitted from the HTC, and G_1 is a shielding grid maintained at RC/SB potential (3 kV) in order to provide an electric field-free RC. RGI_1/RGO_1 = reagent gas inlet

and outlet for introduction of reagent gas through the SB and into the RC; RGI_2/RGO_2 = reagent gas inlet and outlet for introduction of reagent gas into the capillary chamber and removal of gas from the GCR, respectively (0 V); TC = K-type thermocouple maintained in contact with the reagent gas mixture near the RC (3 kV); C_1/C_2 = skimmer cones leading to ion optics and a double focusing mass spectrometer described previously (section 2.4). The light grey coloured regions represent areas with the same composition of reactant gas (~ 99 % N_2 + 1% solvent species such as ROR', NRR'R", RSR', etc..., with R, R' and R" = H or alkyl moieties). The dark grey regions are composed of electrically insulating materials.

Solution (~ 10^{-4} M) required for electrospraying is provided from a gas-tight glass Hamilton syringe (500 μL) by a motorized pump (Model 11 Plus, Harvard Apparatus) through a fused silica capillary to the ESE assembly, then out of the nozzle exit at flow rates of 0.5 to 1 μL/min. In both studies described previously[165-169], methanol was used as the solvent with great success and the same conditions will be used here initially.

The ESE and CC assembly are mounted and sealed by an o-ring to a SS flange made to fit onto the high vacuum chamber of the existing HPMS described in section 2.4. The SS flange housing the ESE and CC is sealed and isolated from the operator by a cylindrical (165 mm o.d. and 152 mm i.d.) Plexiglas high voltage shield (HVS).

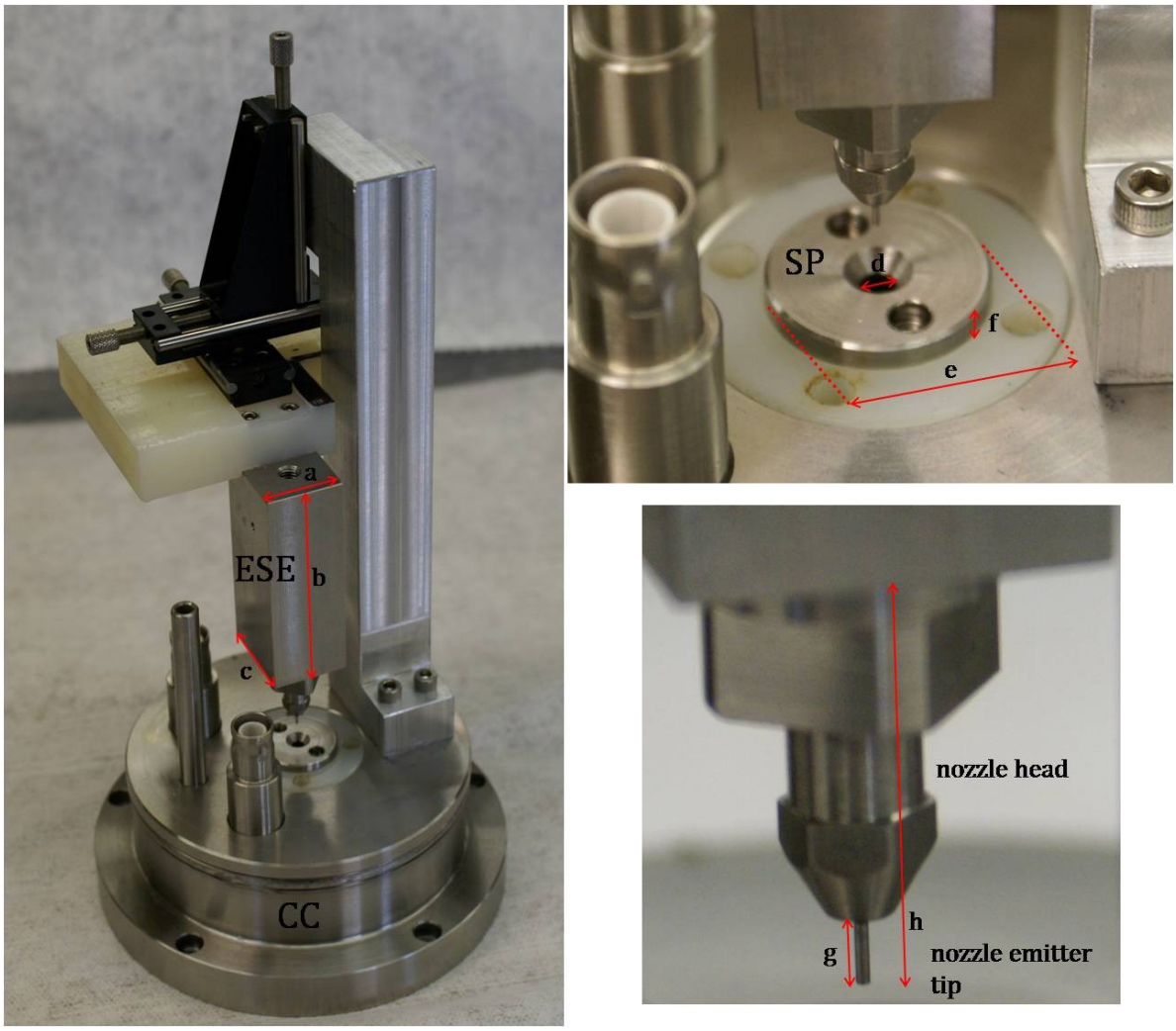

Figure 6.5: Electrospray emitter assembly (ESE). Overall assembly is shown mounted to the capillary cover, CC, with a, b and c = 18, 23 and 51 mm, respectively (left). Close up view of shielding plate, SP, with d, e and f = 3, 19 and 2 mm, respectively (top right). The SP is set in a 31 mm diameter nylon block in order to provide electrical isolation. Close up view of nozzle head and emitter tip with g and h = 3 and 21 mm, respectively (bottom right).

Safe high voltage (SHV) electrical inputs are provided for the heated transfer capillary (H_1 and H_2) and ESE/SP on a SS cover, which serves to provide a gas-tight seal on the HVS.

A small feed-through for the fused silica capillary is located at the centre of the SS cover and is sealed by SS ferrule and a polyetheretherketone (PEEK) sleeve. The reactant gas inlet (RGI_2) for the CC and outlet (RGO_2) for the GCR are also located on the cover, along with thumb screws and handles for ease of removal (**Figure 6.6**).

The region in which the electrospray process occurs is referred to as the gas confinement region (GCR). Unlike the two previous designs, the confinement of this region allows for the use of toxic solvent gases without causing harm to the operator. However, when optimization of the three dimensional position of the ESE is required in the current apparatus, non-toxic solvent species (e.g. water) will be used to avoid dangerous exposure. It is known that use of pure nitrogen at atmospheric pressure in the presence of high voltages can lead to corona discharge,[167] however this issue can be eliminated by introduction of a small percentage of inert, electron capturing species such as CCl_4 or SF_6. The choice of SF_6 is convenient since it exists as gas at ambient temperature.

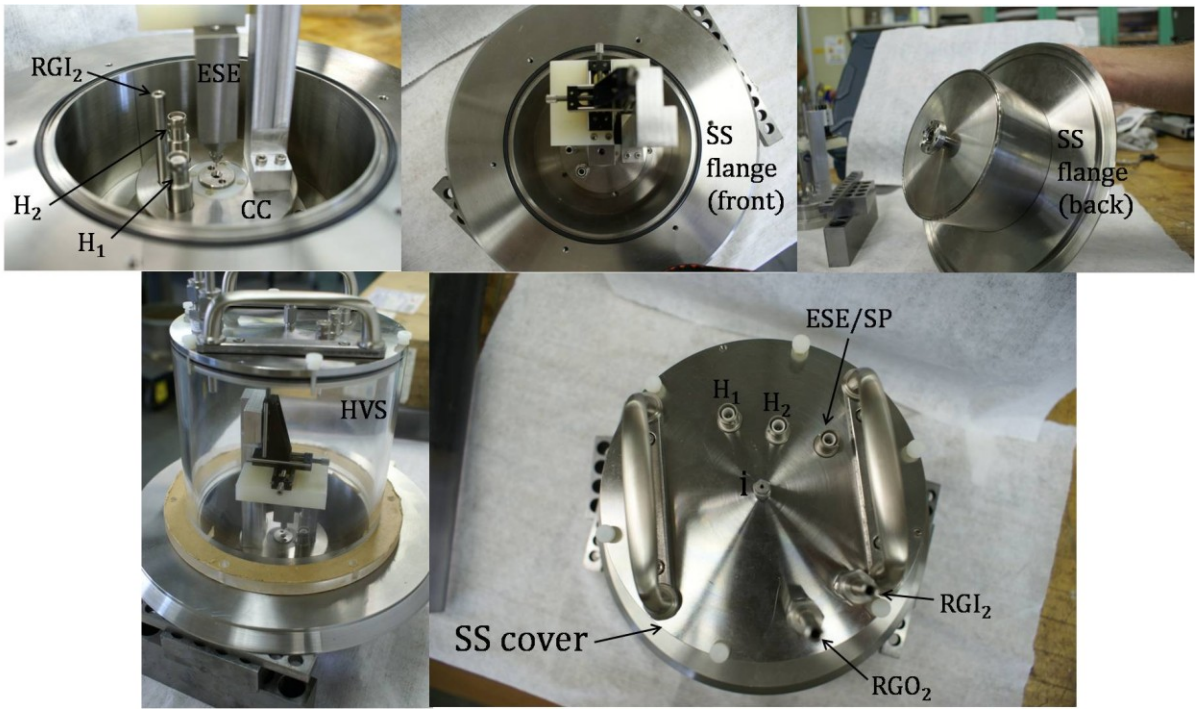

Figure 6.6: Series of images of the GCR. Front of SS flange for mounting assembly into existing HPMS high vacuum chamber (top left). Front top view of SS flange (top centre). Back of SS flange inserted into the high vacuum chamber (top left). The HVS and SS cover mounted to the SS flange forming the gastight housing of the GCR (bottom left). SS cover showing electrical inputs for the HTC (H_1 and H_2), ESE/SP, reactant gas inlet for the CC (RGI_2), reactant gas outlet for the GCR (RGO_2), and input for a fused silica capillary sealed by SS ferrule and PEEK sleeve (i).

Upon exiting the nozzle head emitter of the ESE, solvated ions will encounter a large potential difference between the emitter and HTC of 4 to 7 kV, where they will be drawn into the HTC against a counter current of reactant gas at a flow rate of 25 L/hr. The reactant gas is composed of approximately 99 % N_2 and 1 % solvent vapour. The solvent molecules used to form cluster ions with the ions generated by electrospray could consist of species such as H_2O, ethers, ketones, NH_3, amines, diamines, thiols or sulfides, to name but a few. This short

list of possible solvent species demonstrates the requirement that the GCR be gas-tight and isolated from the laboratory. The SS 6.4 mm o.d. RGO_2 is used to direct the flow of harmful and/or noxious vapour away from the instrument interface through polyethylene tubing and directly into a fume hood exhaust outlet.

6.4.2 Heated Transfer Capillary (HTC) and High Pressure Source Region

Originally it was considered that the SS HTC (500 μm i.d. and 1 mm o.d. at ~ 12 cm in length) exit would be positioned on axis with the RC and platinum exit aperture (100 to 150 μm), in order to provide a greater number density of ions entering the RC. Klassen and coworkers describe using such an on-axis configuration initially; however it was modified to an orthogonal configuration due to the supersonic expansion leaving the capillary, thus altering the gas composition inside the RC.[167] Considering this, an orthogonal positioning of the HTC in relation to the RC is used here (**Figure 6.4**). The coupling of the HTC housing from the GCR to the ion source body (SB) is provided by a cylindrical insulated feed-through and bellows assembly (**Figure 6.7**). The assembly is attached directly by conflat (CF) to the source body and SS flange described previously. A CF seal is very reliable under high vacuum conditions (~ 10^{-14} Torr) and is formed by two edges ("knife edges") of stainless steel being tightened around a circular copper gasket until they cut into it. Such copper gaskets should only be used once in order to give an optimum seal.

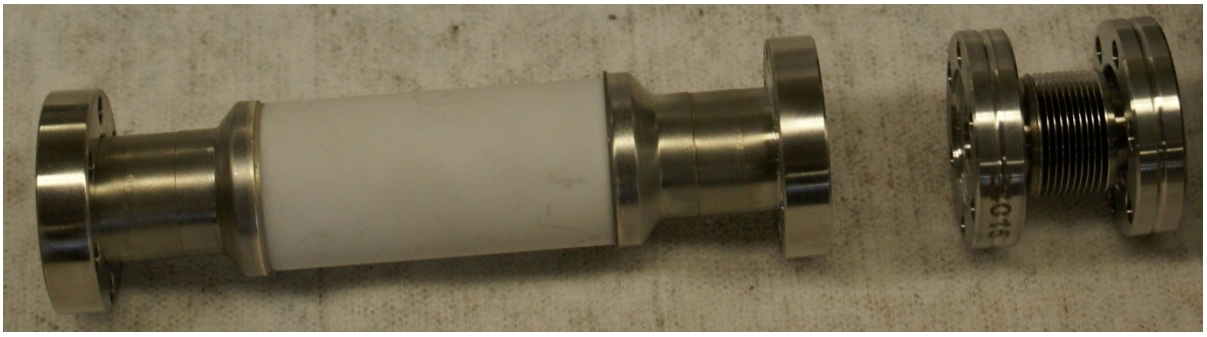

Figure 6.7: Insulated (35 kV) CF feed-through and bellows used to house the HTC and create a junction between the GCR (~ 800 Torr) to the SB (~ 10 Torr). The junction connecting the two regions is suspended in a high vacuum (~ 10^{-7} Torr) region of the mass spectrometer. Reactant gas is only permitted to enter the SB by the HTC.

The HTC is electrically isolated and suspended by a custom made copper gasket which forms a seal on the SB side of the CF feed through shown in **Figure 6.7**. The schematic representation shown in **Figure 6.4** demonstrates this for clarity. The copper gasket, HTC and SB and are shown in **Figure 6.8**. Electrical insulation and support of the HTC inside the copper gasket is provided by a ceramic insulator (Omegabond "700", Omega Engineering Inc.) prepared in the lab and cured by a series of baking and cooling procedures (bake at 180 °F for 4 hours, cool 12 to 24 hours, then bake at 220 °F for 4 hours). This procedure has already been used successfully to produce thermocouples capable of making direct measurements of gas temperature. Once the ceramic has cured it is resistant to temperatures as high as 700 °C. The HTC is heated resistively from 150 to 200 °C by connections made to SHV outputs located on the back face of the CC. An applied voltage ranging from 0.5 to 2 V (1 to 2 A) and floating at SB potential (3 kV) is supplied to the SHV inputs (H_1 and H_2)

located on the front face of the CC. A ceramic sleeve is placed over the HTC for added stability and electrical isolation.

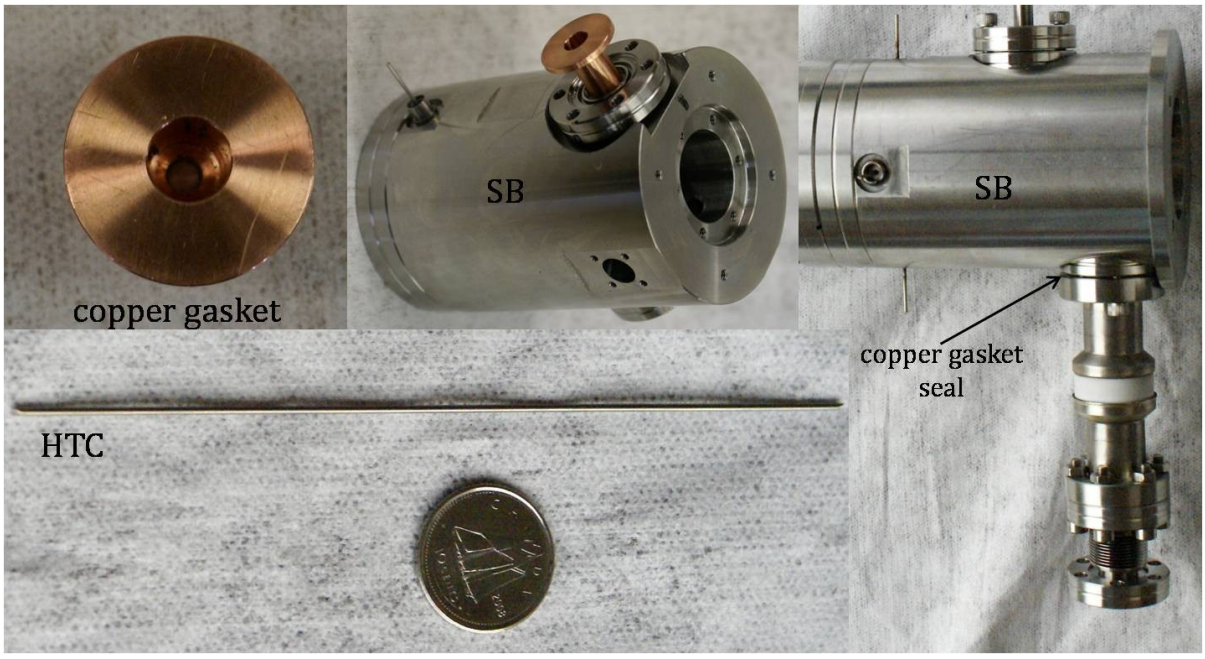

Figure 6.8: Copper gasket used to support and electrically isolate the HTC, as well as form a high vacuum seal (top left). Insertion of the copper gasket into the SB (top centre). The HTC (next to a Canadian dime for scale, bottom centre). Coupling of the insulated feed-through and bellows housing to the SB and high vacuum, sealed by the copper gasket (right).

The expansion of ions leaving the HTC enters the SB between a pair of deflection grids (G_2 and G_3) contained inside the 25.4 mm diameter cylindrical interior of the SS SB. A detailed description of the grid assembly follows. The grid material is composed of 85 % open gold mesh with wire thickness of 20 μm. Gold is selected as a grid material due to its excellent conductive, non-magnetic and chemically inert properties. The grid assembly

consists of three individually powered and electrically isolated circular rings with the gold mesh of each grid "sandwiched" between a SS and ceramic ring (**Figure 6.9**).

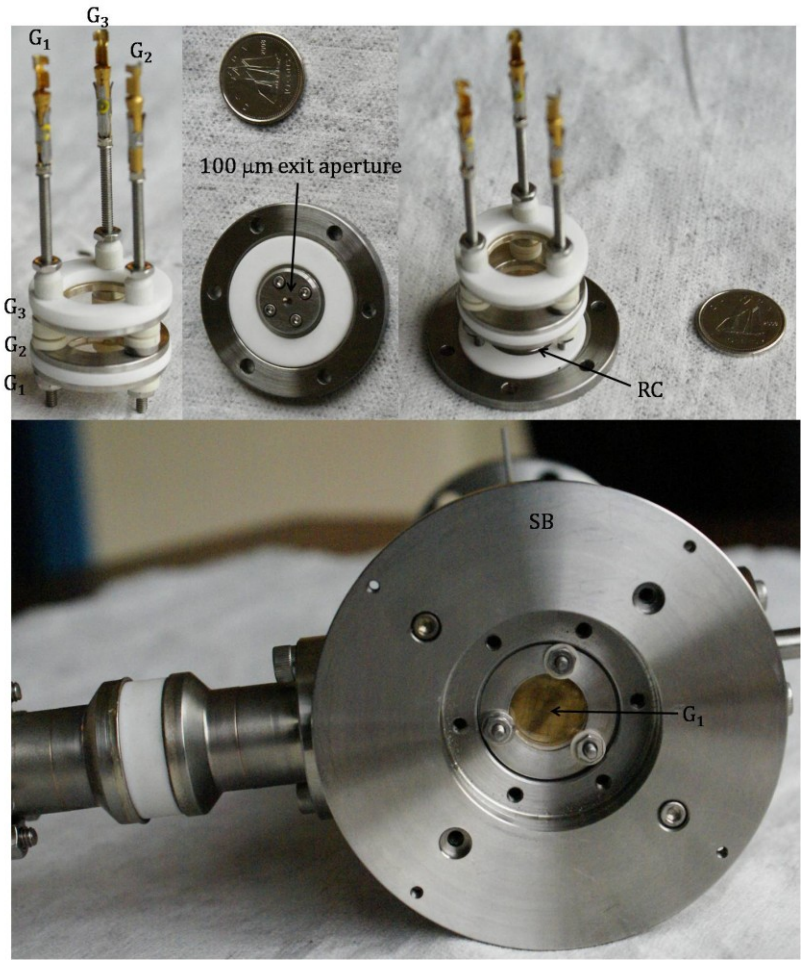

Figure 6.9: Grid assembly. The ceramic and SS rings have o.d. 25 and 24.2 mm, and i.d. 14 and 14 mm, respectively. The thicknesses of the ceramic and SS rings are 2.2 and 1.54 mm, respectively. The total length of the assembly is 64.8 mm. The grids have individually applied voltages *via* three gold plated electrode rods, which also serve to give structural integrity to the assembly (top left). Exit Aperture assembly. The diameters of the outside and platinum aperture disk (100 μm orifice) mount are 38 mm and 12.7 mm, respectively. The thicknesses of the outside and platinum disk mount are 3.15 mm and 4.87 mm, respectively. The ceramic ring serves to electrically isolate the grid electrodes from the front of the SB with o.d. 25.3, i.d. 14.4 and thickness of 1.5 mm (top centre). Grid and

aperture assembly as found inside the SB, with the RC formed by the perpendicular distance (7 mm in length) between G_1 and the platinum aperture disk mount (top right). Front of SB with grid assembly in place (aperture mount removed) where the gold grid, G_1, is visible. The circumferential space between the outside of the ceramic insolating rings of the grid assembly and the interior wall of the SB is 50 μm, allowing for the assembly to be slid in and out of the SB (bottom).

One very important difference between the apparatuses described by both Klassen and Wincel and that described here is the ability to provide an electric field-free RC. This is accomplished by having a three grid system for sampling of the ion beam exiting the HTC. A reaction pulse sequence is proposed (**Figure 6.10**) with time considerations made based on knowledge of time intervals used in pulsed electron beam ionization high pressure mass spectrometry (section 2.4).

The function of the grids is as follows: The HTC exit is situated 3 to 4 mm from the centre axis of the grid assembly between G_2 and G_3. In the "injection" mode, the potentials applied (for ~ 500 μs) to G_2 and G_3 are 3100 and 3050 V, respectively with G_1 fixed at the source potential of 3000 V. The values of the potentials described here are most likely on the high end of the range required, however all grids are variable from zero to ± 100 V centred at 3000 V, and optimized values will be established once the system is operational.[†] In the injection mode the electric potential difference between G_2 and G_3 will orthogonally deflect ions in the direction of G_1, followed by a linear acceleration towards the RC induced by the electric potential difference between G_2 and G_1. Although it provides further acceleration in

[†] The high voltage potential of every ion source component described is variable in order to maximize flexibility of the system.

the direction of the RC, the principle purpose of G_1 is to provide a shielding field, preventing the pulsing fields from entering the RC. This implies that acceleration of ions provided by the electric potential difference between G_1 and G_2 will immediately cease the instant they cross G_1 into the RC. There is no electric potential difference between G_1 and the interior of the RC and thus no electric forces are imposed upon the ions, allowing them to naturally diffuse in a manner analogous to that observed in existing pulsed electron, beam ionization HPMS experiments. Under such conditions, thermochemical equilibrium is rapidly attained by the ions due to the numerous collisions ($\geq 10^6$ collisions s^{-1}) they experience with the bath gas.

The range of times required for ions to diffuse to the walls of the RC is generally between 5 to 50 ms, therefore at least 50 to 100 ms of detection time should be provided between ion injection events into the RC. Ions that have not been injected into the RC during the 500 μs pulse time should not be able to cross G_1 during the detection period. This is of concern since there is a continuous beam of ions being emitted from the HTC exit, and the possibility that some unwanted ions could diffuse into the RC exists. To prevent this from occurring during detection, the magnitude of the electric fields applied to G_2 and G_3 is switched, orthogonally deflecting the ions away from G_1 and towards the reactant gas outlet, RGO_1. This is referred to as the "quench" mode, and under such conditions no ions should enter the RC. There is a rise time of less than 10 ns between pulses, which is essentially instantaneous relative to the transit time of the ions (~ 1 to 10 μs) to the ion source.

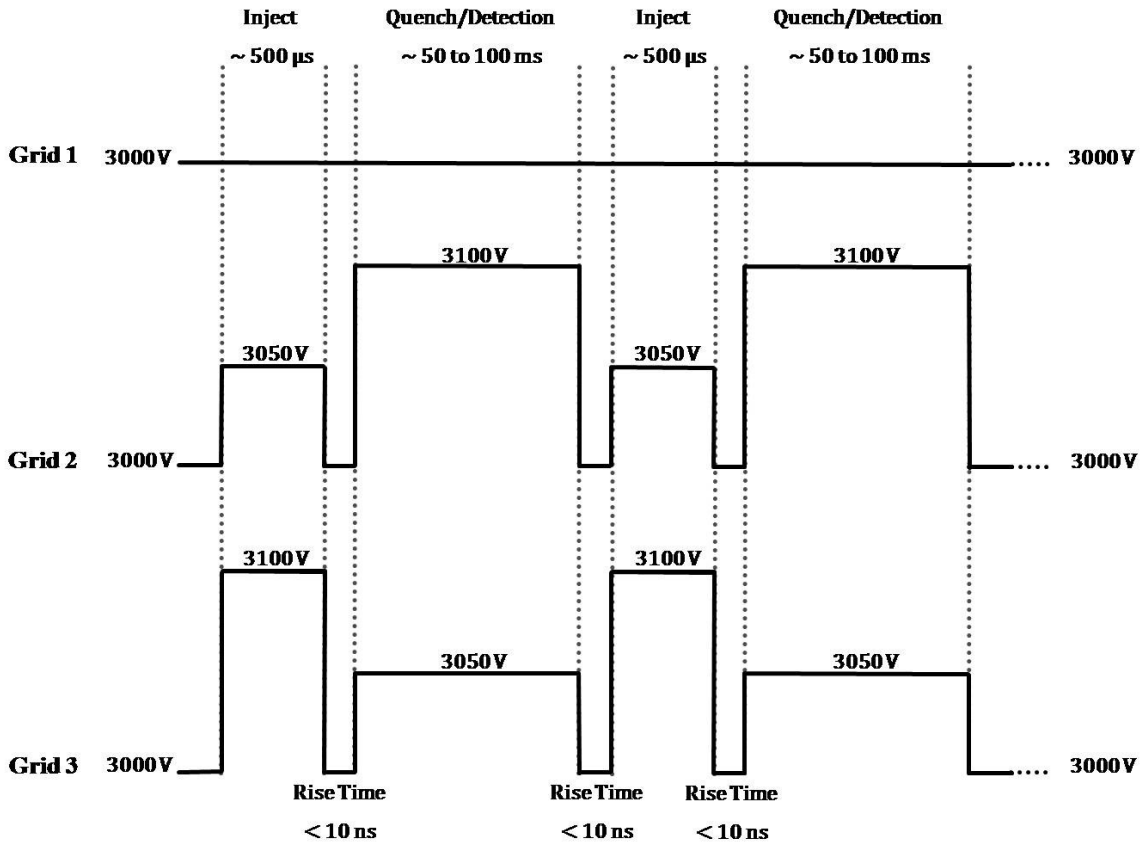

Figure 6.10: Proposed pulse sequence for performing pulsed electrospray ionization HPMS experiments demonstrating one period of injection and quench sequences.

The zero-time of a temporal profile generated by such experiments is initiated when the injection pulse begins. Typically 2000 to 5000 repetitions of the sequence shown in **Figure 6.10** can be made and summed in order to produce temporal profiles similar to those typically observed in HPMS experiments (**Figure 2.8**).

In order to gain insight into the injection and quenching processes described above, simulations have been performed using the software program *SIMION ver. 8.0*. This software

makes use of "potential arrays", which are three dimensional geometric representations of electrodes and magnets created in a visual interface by the user. Typically, the user provides the values of electric potentials to be applied to the potential arrays, then *SIMION* solves for the potentials in the spaces between the electrodes. The potentials between electrodes are determined by solving the Laplace equation (**Eq. 6.1**) by finite difference methods.

$$\nabla^2 V = \nabla \cdot \nabla V = 0 \qquad \textbf{6.1}$$

$$\nabla V = \left(\frac{\partial V}{\partial x}\right) i + \left(\frac{\partial V}{\partial y}\right) j + \left(\frac{\partial V}{\partial z}\right) k = E$$

$$\nabla^2 V = \nabla \cdot E = \frac{\partial E_x}{\partial x} + \frac{\partial E_y}{\partial y} + \frac{\partial E_z}{\partial z} = 0$$

Where V, is the electric potential, E is the electric field strength and ∇^2 is "Del squared", defined previously. *SIMION* refers to this process as "refining" the potential array. Once the potential arrays have been refined they are positioned into an ion optics workbench volume. Ions can be flown within the volume of the workbench and then have their trajectories calculated from the fields experienced inside the potential arrays. The use of *SIMION* allows one to develop "intuition" and to provide an understanding of the behaviour of charged particles in various configurations of electric and magnetic fields.[170]

The simulations of the pulsing modes were created while considering the HTC exit positioned on axis with the grids and RC, however it is more important that the grids function as described previously. A hard-sphere collision model included with *SIMION* was also used

to simulate the presence of gas through which ions should diffuse through. **Figures 6.11** and **6.12** show both the injection and quenching modes of the grid assembly.

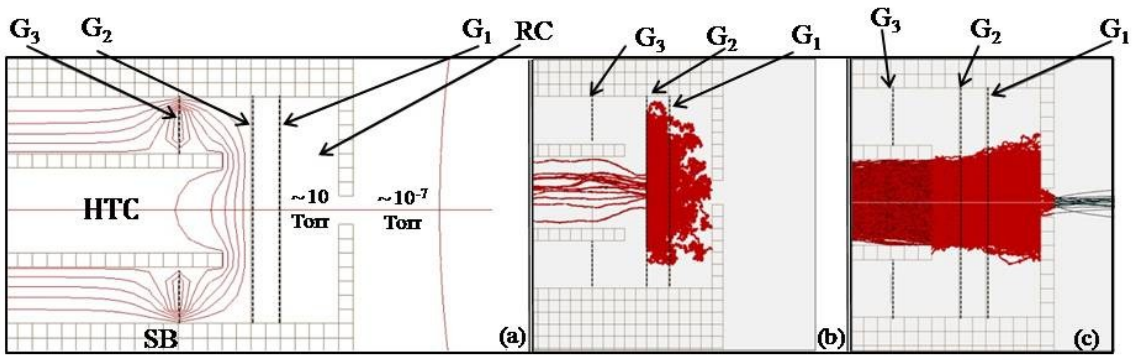

Figure 6.11: Injection mode of grid assembly. **(a)** G_1 = 3150 V, G_2 = G_3 = 3000 V and HTC = 3100 V. The red contour lines represent the shape and range of the electric field generated by the potential differences between G_1, G_2 and the HTC. There is no electric field present in the RC. **(b)** Simulation of ions being injected into the RC showing the diffusion of ions once they enter the RC (10 Torr). **(c)** Same as in **(b)** after thousands of trajectories have been simulated (5 Torr). The black lines emitted from the exit aperture represent ions leaving the ion source and into the mass spectrometer ion optics.

Figure 6.12: Quenching mode of grid assembly. **(a)** G_1 = G_3 = 3000 V, G_2 = 3150 V and HTC = 3150 V. The red contour lines represent the shape and range of the electric field generated by the potential differences between G_1, G_2, G_3 and the HTC. There is no electric field present in the RC. **(b)** Simulation of ions being prevented from entering into the RC showing ions unable to exit the end of the HTC. **(c)** The same as in **(b)** after thousands of trajectories have been simulated. There is not a single ion entering the RC.

The simulations shown by **Figures 6.11** and **6.12** are made using a three dimensional potential array and are provided as two dimensional representations for visual simplicity. The two most important features provided by the simulation are: 1), there are no electric fields present in the RC during operation of the two modes; 2), in the injection mode, ions are able to drift to the exit aperture without the requirement of further acceleration after they pass G_1 into the electric field free RC.

The source body (SB) houses the grid assembly and maintains the temperature and pressure required for the study of ion-molecule equilibria (**Figure 6.13**). The SB is constructed from a cylindrical block of non-magnetic SS with a length and diameter of 105 and 70 mm, respectively. A cylindrical channel extends the axis of the SB with a diameter of 25.4 mm. The back end of the SB is fixed by a CF seal to an electrical isolation feed-through which serves to support the SB and also to provide a channel through which reactant gas may enter the SB and into the RC (RGI_1). The isolation feed-through has length and diameter of 104 and 70 mm, respectively. The front end of the SB has a fixed SS ring-shaped plate with an o.d and i.d. of 82 and 38 mm, respectively from which the first (C_1) and second (C_2) skimmer cones are mounted. The aperture mount shown in **Figure 6.9** is located at the centre of the mounting plate. In order to provide constant pressure conditions inside the RC, a CF sealed SS gas outlet tube (RGO_1) with o.d. and i.d. of 6.35 and 3.64 mm, respectively, is located across from the HTC entrance and approximately 20 mm behind the grid assembly.

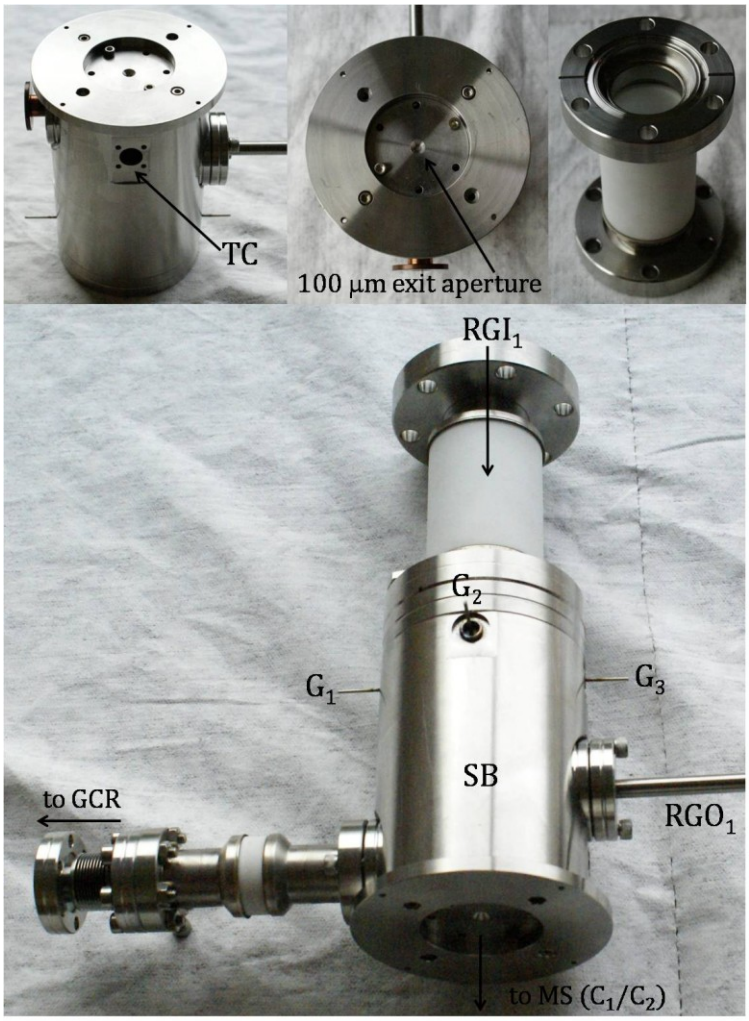

Figure 6.13: Source body (SB). The cylindrically shaped SB is shown with three insulated electrical inputs for powering of the grid assembly ($G_1/G_2/G_3$). All gas entry and exit points are connected by CF in order to provide high vacuum seals (bottom). A cylindrical channel with diameter 9.45 mm perpendicularly intersects the RC space and provides a location for placement of a thermocouple (TC) to measure the gas temperature inside the RC directly. The TC is sealed to the SB by a gold o-ring (top left). Front of the SB displaying the aperture mount and mounting plate for the skimmer cones, C_1 and C_2. The aperture mount is sealed to the SB by a gold o-ring (top centre). Electrical isolation feed through which serves to support the SB and allow reactant gas to flow (RGI_1) through the SB and to the RC (top right).

Constant pressure is maintained in the RC by measuring pressures near the RGI_1 and RGO_1 with capacitance sensors and ensuring they are kept equivalent with electronic mass flow controllers. In practice, the average of the values measured by sensors is taken as the pressure inside the RC. If required, the RGO_1 has a rotary vane pump attached after the flow controller to provide a means for fast gas removal inside the SB. Heating of the SB is facilitated by 600 Watt band heaters applied tightly around the circumference of the SB. It is estimated that a maximum temperature of 300 to 350 °C is possible.

A 50 to 100 L SS vessel for producing and containing the nitrogen reactant gas mixture will be constructed and pressure rated for approximately 2000 Torr. Volatile liquids will be injected into the heated vessel by a septum interface where they are vaporized and can then be clustered with ions produced by electrospray. Nitrogen and gaseous species (e.g. NH_3, H_2S) will be introduced by an attached gas inlet for the same purpose. The reactant gas mixture is then fed to RGI_1 and RGI_2 from the heated 50 to 100 L (calibrated) SS vessel where pressure and temperature are monitored continuously. Pressure is measured by a capacitance sensor and temperature with a thermocouple in direct contact with the gas inside the vessel. If necessary, the gas inlet will also allow for the addition of SF_6 to suppress corona discharge inside the GCR.

6.5 Concluding Remarks

Installation and implementation of a pulsed electrospray high pressure ion source is currently in progress. The structural components of an electrospray interface and ion source body have been built and described. High voltage power supplies and a pulsing unit for operation of the grid assembly are currently under construction. All structural and electronic components will be installed soon when testing of the new apparatus can begin.

When the new ion source is operational, the range of possibilities for the study of ion-molecule reactions in the McMahon laboratory will greatly increase. Electrospray will permit the formation of ions such as the naturally occurring amino acids, small peptides, nucleic acid bases, ionic compounds and methylxanthine species such as caffeine and theophylline, to name but a few. A study of particular interest is to accurately measure the binding energy of the bidentate IHB formed in the PBD of theophylline and ammonia (**XXIX**).

Because the electrospray interface is kept isolated from the operator by the gas confinement region (GCR), the study of cluster-ion equilibria is not limited to hydration chemistry. Other prototypical biological small molecules such as amines and thiols, will be available to use without concern for the toxic, corrosive or sometimes noxious properties of many of these species. Allowing ions to associate with neutral solvent species in the electric field free reaction chamber (RC) will ensure that the values of equilibrium constants determined are truly representative of ions in a state of thermochemical equilibrium.

Bibliography

[1] L. Pauling, The Chemical Bond: A Brief Introduction to Modern Structural Chemistry, Ithaca, New York, **1967**.
[2] S. K. Searles, P. Kebarle *J. Phys. Chem.* **1968**, 72, 742-743.
[3] I. Dzidic, P. Kebarle *J. Phys. Chem.* **1970**, 74, 1466-1474.
[4] J. W. Larson, T. B. McMahon *J. Am. Chem. Soc.* **1982**, 104, 6255-6261.
[5] R. G. Keesee, A. W. Castleman Jr. *J. Phys. Chem. Ref. Data*. **1986**, 15, 1011-1071.
[6] M. Meot-Ner *Chem. Rev.* **2005**, 105, 213-284.
[7] T. D. Fridgen, L. MacAleese, T. B. McMahon, J. Lemaire, P. Maitre *Phys. Chem. Chem. Phys.* **2006**, 8, 955-966.
[8] R. Wu, T. B. McMahon *J. Am. Chem. Soc.* **2007**, 129, 4864-4865.
[9] CRC Handbook of Chemistry and Physics, The Chemical Rubber Co., Clevland, Ohio, **1971**.
[10] K. Norrman, T. B. McMahon *Int. J. Mass Spectrom.* **1999**, 182, 381-402.
[11] M. W. Forbes, M. F. Bush, N. C. Polfer, J. Oomens, R. C. Dunbar, E. R. Williams, R. A. Jockush *J. Phys. Chem. A*. **2007**, 111, 11759-11770.
[12] M. F. Bush, J. Oomens, R. J. Saykally, E. R. Williams *J. Phys. Chem. A*. **2008**, 112, 8578-8584.
[13] N. C. Polfer, J. Oomens, R. C. Dunbar *Chem. Phys. Chem.* **2008**, 9, 579-589.
[14] R. Wu, T. B. McMahon *J. Mass Spectrom.* **2008**, 43, 1641-1648.
[15] R. Wu, T. B. McMahon *Chem. Eur. J.* **2008**, 14, 7765-7770.
[16] R. Wu, T. B. McMahon *J. Mass Spectrom.* **2008**, 43, 1641-1648.
[17] R. Wu, T. B. McMahon *Chem. Phys. Chem.* **2008**, 9, 2826-2835.
[18] M. F. Bush, J. Oomens, E. R. Williams *J. Phys. Chem. A*. **2009**, 113, 431-438.
[19] M. Vala, J. Szczepanski, R. C. Dunbar, J. Oomens, J. D. Steill *Chem. Phys. Lett.* **2009**, 473, 43-48.
[20] R. A. Marta, T. D. Fridgen, T. B. McMahon *J. Phys. Chem. A*. **2007**, 111, 8792-8802.
[21] R. Wu, T. B. McMahon *J. Am. Chem. Soc.* **2007**, 129, 11312-11313.
[22] T. Baer, W. L. Hase, Unimolecular Reaction Dynamics, Oxford University Press, New York, **1996**.
[23] H. M. Frey, G. B. Kistiakowsky *J. Am. Chem. Soc.* **1957**, 79, 6373-6379.
[24] J. N. Butler, G. B. Kistiakowsky *J. Am. Chem. Soc.* **1960**, 82, 759-765.
[25] C. S. Parmenter *J. Phys. Chem.* **1982**, 86, 1735-1750.
[26] J. S. Broadbelt, J. J. Wilson *Mass Spec. Rev.* **2009**, 28, 390-424.
[27] R. H. Petrucci, W. S. Harwood, F. G. Herring, J. D. Madura, General Chemistry Principles and Modern Applications Pearson Prentice Hall, Upper Saddle River, New Jersey, USA, **2007**.
[28] N. G. Basov, E. P. Markin, A. N. Oraevskii, A. V. Pankratov, A. N. Skachkov *JETP Letters*. **1971**, 14, 165-167.
[29] J. Blazejowski, F. W. Lampe *Spectrochimica Acta*. **1987**, 43A, 265-267.

[30] G. C. Baykut, C. H. Watson, R. R. Weller, J. R. Eyler *J. Am. Chem. Soc.* **1985**, 107, 8036-8042.
[31] T. H. Osterheld, T. Baer, J. I. Brauman *J. Am. Chem. Soc.* **1993**, 115, 6284-6289.
[32] L. S. Kassel *J. Phys. Chem.* **1928**, 32, 1065-1079.
[33] R. A. Marcus *J. Chem. Phys.* **1952**, 20, 359-364.
[34] R. A. Marcus *J. Chem. Phys.* **1965**, 43, 2658-2661.
[35] R. A. Marcus, O. K. Rice *J. Phys. Colloid Chem.* **1951**, 55, 894-908.
[36] O. K. Rice, H. C. Ramsperger *J. Am. Chem. Soc.* **1928**, 50, 617-620.
[37] J. A. Zimmerman, C. H. Watson, J. R. Eyler *Anal. Chem.* **1991**, 63, 361-365.
[38] D. P. Little, M. W. Speir, M. W. Senko, P. B. O'Connor, F. W. McLafferty *Anal. Chem.* **1994**, 66, 2809-2815.
[39] J. M. J. Madey, H. A. Schwettman, W. M. Fairbank *IEEE Trans. Nuc. Sci.* **1973**, N S20, 980-983.
[40] D. A. G. Deacon, L. R. Elias, J. M. J. Madey, G. J. Ramian, H. A. Schwettman, T. I. Smith *Phys. Rev. Lett.* **1977**, 38, 892-894.
[41] S. V. Benson, J. Schultz, B. A. Hooper, R. Crane, J. M. J. Madey *Nuclear Instr. and Methods A*. **1988**, A272, 22-28.
[42] R. Graham *Z. Phys.* **1968**, 211, 469-482.
[43] R. Graham *Z. Phys.* **1968**, 210, 319-336.
[44] R. Graham, H. Haken *Z. Phys.* **1968**, 210, 276-302.
[45] K. J. McNeil, C. W. Gardiner *Phys. Rev. A*. **1983**, 28, 1560-1566.
[46] M. D. Reid, P. D. Drummond *Phys. Rev. Lett.* **1988**, 60, 2731-2733.
[47] C. G. Atkins, K. Rajabi, E. A. L. Gillis, T. D. Fridgen *J. Phys. Chem. A*. **2008**, 112, 10220-10225.
[48] E. A. L. Gillis, K. Rajabi, T. D. Fridgen *J. Phys. Chem. A*. **2009**, 113, 824-832.
[49] CLIO *http://clio.lcp.u-psud.fr/clio_eng/FEL.html*. **2009**.
[50] J. A. Hipple, H. Sommer, H. A. Thomas *Phys. Rev.* . **1949**, 76, 1877-1878.
[51] H. Sommer, H. A. Thomas, J. A. Hipple *Phys. Rev.* **1951**, 82, 697-702.
[52] M. B. Comisarow, A. G. Marshall *Chem. Phys. Lett.* **1974**, 25, 282-283.
[53] R. Chen, X. Cheng, D. W. Mitchell, S. A. Hofstadler, Q. Wu, A. L. Rockwood, M. G. Sherman, R. D. Smith *Anal. Chem.* **1995**, 67, 1159-1163.
[54] A. G. Marshall, C. L. Hendrickson, G. S. Jackson *Mass Spec. Rev.* **1998**, 17, 1-35.
[55] H. Paul, H. Steinwedel *USA Patent # 2939952*. **1960**.
[56] R. E. March *J. Mass Spectrom.* **1997**, 32, 351-369.
[57] E. Mathieu *J. Math. Pure Appl.* **1868**, 13, 137.
[58] F. H. Field, J. L. Franklin, F. W. Lampe *J. Am. Chem. Soc.* **1957**, 79, 2419-2429.
[59] D. P. Stevenson, D. O. Schissler *J. Chem. Phys.* **1955**, 23, 1353-1354.
[60] P. Kebarle *J. Am. Soc. Mass Spectrom.* **1992**, 3, 1-9.
[61] P. Kebarle, E. W. Godbole *J. Chem. Phys.* **1962**, 36, 302-305.
[62] P. Kebarle, E. W. Godbole *J. Chem. Phys.* **1963**, 39, 1131-1132.
[63] P. Kebarle, M. A. Hogg *J. Chem. Phys.* **1965**, 42, 668-674.
[64] R. Wu, T. B. McMahon *Can. J. Chem.* **2005**, 83, 1978-1993.

[65] M. J. Frisch, G. W. Trucks, H. B. Schlegel, G. E. Scuseria, M. A. Robb, J. R. Cheeseman, J. A. Montgomery, T. V. Jr., K. N. Kudin, J. C. Burant, J. M. Millam, S. S. Iyengar, J. Tomasi, V. Barone, B. Mennucci, M. Cossi, G. Scalmani, N. Rega, G. A. Petersson, H. Nakatsuji, M. Hada, M. Ehara, K. Toyota, R. Fukuda, J. Hasegawa, M. Ishida, T. Nakajima, Y. Honda, O. Kitao, H. Nakai, M. Klene, X. Li, J. E. Knox, H. P. Hratchian, J. B. Cross, C. Adamo, J. Jaramillo, R. Gomperts, R. E. Stratmann, O. Yazyev, A. J. Austin, R. Cammi, C. Pomelli, J. W. Ochterski, P. Y. Ayala, K. Morokuma, G. A. Voth, P. Salvador, J. J. Dannenberg, V. G. Zakrzewski, A. D. D. S. Dapprich, M. C. Strain, O. Farkas, D. K. Malick, A. D. Rabuck, K. Raghavachari, J. B. Foresman, J. V. Ortiz, Q. Cui, A. G. Baboul, S. Clifford, J. Cioslowski, G. L. B. B. Stefanov, A. Liashenko, P. Piskorz, , I. Komaromi, R. L. Martin, D. J. Fox, T. Keith, M. A. Al-Laham, C. Y. Peng, A. Nanayakkara, M. Challacombe, P. M. W. Gill, B. Johnson, W. Chen, M. W. Wong, C. Gonzalez, J. A. Pople *Gaussian, Inc., Wallingford CT, 2004.* **2004**, Gaussian 03, Revision C.02.
[66] I. N. Levine, Quantum Chemistry, Upper Saddle River, NJ, **2000**.
[67] J. B. Foresman, A. Frisch, Exploring Electronic Structure Methods, Gaussian, Inc., Pittsburgh, PA, **1996**.
[68] J. C. Cramer, Essentials of Computational Chemistry: Theories and Models, John Wiley & Sons Ltd, West Sussex, England, **2008**.
[69] M. Head-Gordon, J. A. Pople, M. J. Frisch *Chem. Phys. Lett.* **1988**, 153, 503-506.
[70] M. J. Frisch, M. Head-Gordon, J. A. Pople *Chem. Phys. Lett.* **1989**, 166, 275-280.
[71] M. J. Frisch, M. Head-Gordon, J. A. Pople *Chem. Phys. Lett.* **1990**, 166, 281-289.
[72] A. D. Becke *Phys. Rev. A*. **1988**, 38, 3098-3100.
[73] A. D. Becke *J. Chem. Phys.* **1993**, 98, 1372-1377.
[74] C. Lee, W. Yang, R. G. Parr *Phys. Rev. B*. **1988**, 37, 785-789.
[75] A. Szabo, N. S. Ostlund, Modern Quantum Chemistry: Introduction to Advanced Electronic Structure Theory, Dover, Mineola, New York, **1996**.
[76] T. H. Dunning Jr. *J. Phys. Chem. A*. **2000**, 104, 9062-9080.
[77] W. Kohn, L. J. Sham *Phys. Rev.* **1965**, 140, A1133-A1138.
[78] A. Gil, S. Simon, L. Rodriguez-Santiago, J. Bertran, M. Sodupe *J. Chem. Theory Comput.* **2007**, 3, 2210-2220.
[79] M. Leopoldini, I. P. Pitarch, N. Russo, M. Toscano *J. Phys. Chem. A*. **2004**, 108, 92-96.
[80] R. J. Nieckarz, N. Oldridge, T. B. McMahon *International Journal of Mass Spectrometry*. **2007**, 267, 338-345.
[81] I. A. B. Topol, S. K.; Russo, N.; Toscano, M. *J. Am. Soc. Mass Spectrom.* **1999**, 10, 318-322.
[82] M. P. Andersson, P. Uvdal *J. Phys. Chem. A*. **2005**, 109, 2937.
[83] D. A. Clabo Jr., W. D. Allen, R. B. Remington, Y. Yamaguchi, H. F. Schaefer III *Chem. Phys.* **1988**, 123, 187-239.
[84] V. Barone *J. Chem. Phys.* **2004**, 120, 3059-3065.
[85] B. Njegic, M. S. Gordon *J. Chem. Phys.* **2006**, 125, 12.
[86] D. M. McQuarrie, Statistical Thermodynamics, Harper & Row, New York, NY, **1973**.
[87] R. Krishnan, J. S. Binkley, R. Seeger, J. A. Pople *J. Chem. Phys.* **1980**, 72, 650-654.

[88] T. Engel, Quantum Chemistry & Spectroscopy, Pearson Education, Inc., San Francisco, CA, **2006**.
[89] M. M. Francl, W. J. Pietro, W. J. Hehre, S. J. Binkley, M. S. Gordon, D. J. Defrees, J. A. Pople *J. Chem. Phys.* **1982**, 77, 3654-3665.
[90] L. A. Curtiss, P. C. Redfern, K. Raghavachari, V. Rassolov, J. A. Pople *J. Chem. Phys.* **1999**, 110, 4703-4709.
[91] T. H. Dunning Jr. *J. Chem. Phys.* **1989**, 90, 1007-1023.
[92] R. A. Kendall, T. H. Dunning Jr., R. H. Harrison *J. Chem. Phys.* **1992**, 96, 6796-6806.
[93] K. A. Peterson, D. E. Woon, T. H. Dunning Jr. *J. Chem. Phys.* **1994**, 100, 7410-7415.
[94] D. E. Woon, T. H. Dunning Jr. *J. Chem. Phys.* **1993**, 98, 1358-1371.
[95] G. Z. Whitten, B. S. Rabinovitch *J. Chem. Phys.* **1963**, 38, 2466-2473.
[96] T. Beyer, D. F. Swinehart *Commun. Assoc. Comput. Machin.* **1971**, 16, 379.
[97] J. I. Steinfeld, J. S. Fransisco, W. L. Hase, Chemical Kinetics and Dynamics, Prentice-Hall, Inc., Upper Saddle River, NJ, **1999**.
[98] K. R. Asmis, N. L. Pivonka, G. Santambrogio, M. K. C. Brummer, D. M. Neumark, L. Woste *Science*. **2003**, 299, 1375-1377.
[99] T. D. Fridgen, L. MacAleese, P. Maitre, T. B. McMahon, P. Boissel, J. Lemaire. **2005**, 7, 2747-2755.
[100] T. D. Fridgen, T. B. McMahon, L. MacAleese, J. Lemaire, P. Maitre *J. Phys. Chem. A*. **2004**, 108, 9008-9010.
[101] R. L. Clair, T. B. McMahon *Can. J. Chem.* **1980**, 58, 863-865.
[102] T. Su, W. J. Chesnavitch *J. Chem. Phys.* **1982**, 76, 5183-5185.
[103] P. Maitre, S. Le Caer, A. Simon, W. Jones, J. Lemaire, H. N. Mestdagh, M. Heninger, G. Mauclaire, P. Boissel, R. Prazeres, F. Glotin, J. M. Ortega *Nuclear Instr. and Methods A* **2003**, 507, 541-546.
[104] J. M. Ortega, F. Glotin, R. Prazeres *Infra. Phys. Tech.* **2006**, 49, 133-138.
[105] R. Prazeres, F. Glotin, C. Insa, D. A. Jaroszynski, J. M. Ortega *Eur. Phys. J. D*. **1998**, 3, 98-93.
[106] R. Prazeres, F. Glotin, J. M. Ortega *Eur. Phys. J. AP*. **2005**, 29, 223-230.
[107] G. Mauclaire, J. Lemaire, P. Boissel, G. Bellec, M. Heninger *Eur. J. Mass Spec.* **2004**, 10, 155-162.
[108] J. Cizek *J. Chem. Phys.* **1966**, 45, 4256-4266.
[109] S. E. Barlow, J. M. Van Doren, V. M. Bierbaum *J. Am. Chem. Soc.* **1988**, 110, 7240-7242.
[110] A. A. Viggiano, R. A. Morris, J. S. Paschkewitz, J. F. Paulson *J. Am. Chem. Soc.* **1992**, 114, 10477-10482.
[111] T. B. McMahon, J. L. Beauchamp *J. Phys. Chem.* **1977**, 81, 593-598.
[112] T. D. Fridgen, J. D. Keller, T. B. McMahon *J. Phys. Chem. A*. **2001**, 105, 3816-3824.
[113] O. Sekiguchi, D. Watanabe, S. Nakajima, S. Tajima, E. Uggerud *Int. J. Mass Spectrom.* . **2003**, 222, 1-9.
[114] S. Tajima, S. Takahashi, O. Sekiguchi *Rapid Comm. Mass Spetrom.* **1999**, 13, 1458-1461.

[115] C. Wesdemiotis, H. Schwarz, H. Budzikiewicz, E. Vogel *Org. Mass Spectrom.* **1981**, 16, 89-91.
[116] M. Carbini, L. Conte, G. Gambaretto, S. Catinella, P. Traldi *Org. Mass Spectrom.* **1995**, 27, 1248-1254.
[117] P. Varnai, L. Nyulaszi, T. Veszpremi, K. Vekey *Chem. Phys. Lett.* **1995**, 233, 340-346.
[118] C. F. Brice, A. P. Smith *Jnt. J. Food Sci. Nutr.* **2002**, 53.
[119] L. Geraets, H. J. J. Moonen, E. F. M. Wouters, A. Bast, G. J. Hageman *Biochemical Pharmacology*. **2006**, 72, 902-910.
[120] Z. He, W. Y. Ma, T. Hashimoto, A. M. Bode, C. S. Yang, Z. Dong *Cancer Res.* **2003**, 63.
[121] K. Marheineke, O. Hyrien *J. Biol. Chem.* **2004**, 279.
[122] J. Vavrova, M. Marekova-Rezacova, D. Vokurkova, S. Szkanderova, J. Psutka *Radiat. Environ. Biophys.* **2003**, 42.
[123] D. B. Davies, D. A. Veselkov, V. V. Kodintsev, M. P. Evstigneev, A. N. Veselkov *Mol. Phys.* **2000**, 23.
[124] D. B. Davis, D. A. Veselkov, L. N. Dijmant, A. N. Veselkov *Eur. Biophys. J.* **2001**, 30.
[125] R. W. Larsen, R. Jasuja, R. Hetzler, P. T. Muraoka, V. G. Andrada, D. M. Jameson *Biophys. J.* **1996**, 70.
[126] M. B. Lyles, I. L. Cameron *Cell Biol. Int.* **2002**, 26.
[127] A. V. Shestopalova *Journal of Molecular Liquids*. **2006**, 127, 113-117.
[128] M. Brenner, R. Berkowitz, N. Marshall, S. R. C. *Clinical Allergy*. **1988**, 18, 143-150.
[129] E. G. Nassif, M. Weinberger, R. Thompson, W. Huntly *New England J. Med.* **1981**, 304, 71-75.
[130] J. W. Jenne *Clinics in Chest Medicine*. **1984**, 5, 645-658.
[131] J. Lemaire, P. Boissel, M. Heninger, G. Mauclaire, G. Bellec, H. Mestdagh, A. Simon, S. L. Caer, J. M. Ortega, F. Glotin, P. Maitre *Phys. Rev. Lett.* **2002**, 89.
[132] J. Bauschlicher, C. W.;, S. R. Langhoff, H. Partridge, J. E. Rice, A. Komornicki *J. Chem. Phys.* **1991**, 95, 5142-5148.
[133] D. Feller, E. D. Glendening, D. E. Woon *J. Chem. Phys.* **1995**, 193, 3526-3542.
[134] K. A. Peterson, T. H. Dunning Jr. *J. Chem. Phys.* **2002**, 117, 10548-10560.
[135] K. A. Peterson, A. K. Wilson, D. E. Woon, T. H. Dunning Jr. *Theor. Chem. Acc.* **1997**, 97, 251-259.
[136] J. P. Williams, N. M. M. Nibbering, B. N. Green, V. J. Patel, J. H. Scrivens *Journal of Mass Spectrometry*. **2006**, 41, 1277-1286.
[137] E. P. Grimsrud, P. Kebarle *J. Am. Chem. Soc.* **1973**, 95.
[138] K. Hiraoka, H. Takimoto *J. Phys. Chem.* **1986**, 90.
[139] J. W. Larson, T. B. McMahon *J. Am. Chem. Soc.* **1982**, 104.
[140] M. Meot-Ner, S. L. W. *J. Am. Chem. Soc.* **1991**, 113.
[141] S. G. Lias, E. P. Hunter *J. Phys. Chem. Ref. Data*. **1998**, 27, 413-656.
[142] J. A. P. Ruttink, P. C. Burgers, L. M. Fell, J. K. Terlouw *J. Phys. Chem. A*. **1998**, 102, 2976-2980.

[143] C. Y. Wong, J. A. P. Ruttink, P. C. Burgers, J. K. Terlouw *Chemical Physics Letters*. **2004**, 387, 204-208.
[144] C. Y. Wong, J. A. P. Ruttink, P. C. Burgers, J. K. Terlouw *Chemical Physics Letters*. **2004**, 390, 176-180.
[145] O. P. Balaj, C. Kapota, J. Lemaire, G. Ohanessian *Int. J. Mass Spectrom.* **2008**, 269, 169-209.
[146] C. Kapota, J. Lemaire, P. Maitre, G. Ohanessian *J. Am. Chem. Soc.* **2004**, 126, 1836-1842.
[147] P. Wang, M. J. Polce, G. Ohanessian, C. Wesdemiotis *J. Mass Spectrom.* **2008**, 43, 485-494.
[148] SDBS *http://riodb01.ibase.aist.go.jp/sdbs/cgi-bin/cre_index.cgi?lang=eng*. **2009**.
[149] R. M. Silverstein, F. X. Webster, D. J. Kiemle, Spectrometric Identification of Organic Compounds, John Wiley & Sons, Inc., Hoboken, NJ, **2005**.
[150] T. B. McMahon, J. E. Szulejko *Int. J. Mass Spectrom. and Ion Proc.* **1991**, 109, 279-294.
[151] J. E. Szulejko, T. B. McMahon *J. Am. Chem. Soc.* **1993**, 115, 7839-7848.
[152] S. Hoyau, K. Norrman, T. B. McMahon, G. Ohanessian *J. Am. Chem. Soc.* **1999**, 121, 8864-8875.
[153] B. Bogdanov, T. B. McMahon *Int. J. Mass Spectrom.* **2005**, 241, 205-223.
[154] C. Li, P. Ross, J. E. Szulejko, T. B. McMahon *J. Am. Chem. Soc.* **1996**, 118, 9360-9367.
[155] J. E. Szulejko, J. J. Fisher, T. B. McMahon *Int. J. Mass Spectrom. and Ion Proc.* **1988**, 83, 147-161.
[156] S. A. Raspopov, T. B. McMahon *J. Mass Spectrom.* **2005**, 40, 1536-1545.
[157] R. J. Nieckarz, C. G. Atkins, T. B. McMahon *Chem. Phys. Chem.* **2008**, 9, 2816-2825.
[158] R. Wu, T. B. McMahon *J. Am. Chem. Soc.* **2007**, 129, 569-580.
[159] M. Dole, L. L. Mack, R. L. Hines *J. Chem. Phys.* **1968**, 49, 2240-2249.
[160] M. Yamashita, J. B. Fenn *J. Phys. Chem.* **1984**, 88, 4451-4459.
[161] J. B. Fenn *Nobel Lecture*. **2002**, 154-184.
[162] J. V. Iribane, B. A. Thomson *J. Chem. Phys.* **1976**, 64, 2287-2294.
[163] L. Rayleigh *Phil. Mag.* **1882**, 14, 184.
[164] J. Zeleny *Phys. Rev.* **1917**, 10, 1-7.
[165] A. T. Blades, J. S. Klassen, P. Kebarle *J. Am. Chem. Soc.* **1996**, 118, 12437-12442.
[166] J. S. Klassen, A. T. Blades, P. Kebarle *J. Am. Chem. Soc.* **1994**, 116, 12075-12076.
[167] J. S. Klassen, A. T. Blades, P. Kebarle *J. Phys. Chem.* **1995**, 99, 15509-15517.
[168] H. Wincel *Int. J. Mass Spectrom.* **2006**, 251, 23-31.
[169] H. Wincel *Chem. Phys. Lett.* **2007**, 439, 157-161.
[170] D. J. Manura, D. A. Dahl, SIMION^{TM} 8.0 User Manual, Idaho National Laboratory, **2006**.

Appendices

Appendix A

Sample of Mathcad 14.0 Worksheet for Calculation of RRKM Rate Constants

RRKM Rate Constant Calculator for Reactant XI passing through TS XVII

Maximum total energy above the ground state of the reactant (cm^{-1})

$E := 21802$

Difference in energy between reactant and TS ground states (cm^{-1})

$Eo := 1413$

Average of most probable angular momentum quantum numbers for reactant and TS at temperature, T

$J := 28$

Physical constants

$T := 298.15$

$c := 2.99792458 \cdot 10^{10}$

$kb := 0.69503879$

$\sigma r := 1 \quad \sigma a := 1$

Reactant rotational constants (GHz)

$$Br := \frac{10^9}{c}\begin{pmatrix} 2.495 \\ 2.798 \\ 7.127 \end{pmatrix}$$

Reactant rotational constants (cm^{-1})

$$Br = \begin{pmatrix} 0.083 \\ 0.093 \\ 0.238 \end{pmatrix}$$

TS rotational constants (GHz)

$$Ba := \frac{10^9}{c}\cdot\begin{pmatrix} 2.707 \\ 2.969 \\ 5.364 \end{pmatrix}$$

TS rotational constants (cm^{-1})

$$Ba = \begin{pmatrix} 0.09 \\ 0.099 \\ 0.179 \end{pmatrix}$$

Vibrational frequencies of reactant

$$\nu := \begin{pmatrix} 54 \\ 93 \\ 134 \\ 300 \\ 380 \\ 466 \\ 484 \\ 512 \\ 625 \\ 724 \\ 1074 \\ 1097 \\ 1185 \\ 1244 \\ 1335 \\ 1408 \\ 1491 \\ 1697 \\ 7803 \\ 2247 \\ 3256 \\ 3631 \\ 3703 \\ 3723 \end{pmatrix}$$

Vibrational frequencies of TS

$$\omega := \begin{pmatrix} 56 \\ 161 \\ 269 \\ 299 \\ 336 \\ 369 \\ 444 \\ 556 \\ 626 \\ 720 \\ 1038 \\ 1064 \\ 1173 \\ 1177 \\ 1330 \\ 1463 \\ 1651 \\ 1735 \\ 3003 \\ 3356 \\ 3577 \\ 3717 \\ 3819 \end{pmatrix}$$

Reactant rotational partition function

$$qrotr := \frac{\sqrt{\pi}}{\sigma r}\cdot(kb\cdot T)^{\frac{3}{2}}\cdot\left[\prod_{i=0}^{2}\left(\frac{1}{Br_i}\right)\right]^{\frac{1}{2}}$$

$qrotr = 1.23 \times 10^{5}$

TS rotational partition function

$$qrota := \frac{\sqrt{\pi}}{\sigma a}\cdot(kb\cdot T)^{\frac{3}{2}}\cdot\left[\prod_{i=0}^{2}\left(\frac{1}{Ba_i}\right)\right]^{\frac{1}{2}}$$

$qrota = 1.322 \times 10^{5}$

Rotational energy of reactant approximated by a symmetric top and rounded to nearest cm-1

$$Er(J,K) := \text{floor}\left[\frac{\sum_{K=-J}^{J}\left[\left(Br_0 + Br_1\right)\cdot\frac{J\cdot(J+1)-K^2}{2} + Br_2\cdot K^2\right]}{2\cdot J+1}\right]$$

Rotational energy of TS approximated by a symmetric top and rounded to nearest cm-1

$$Era(J,K) := \text{floor}\left[\frac{\sum_{K=-J}^{J}\left[\left(Ba_0 + Ba_1\right)\cdot\frac{J\cdot(J+1)-K^2}{2} + Ba_2\cdot K^2\right]}{2\cdot J+1}\right]$$

Summary of rotational energy parameters (cm-1)

$Er(J,K) = 112$ $Era(J,K) = 99$ $\Delta Er := Er(J,K) - Era(J,K)$ $\Delta Er = 13$

Definition of active energy range for TS

$$Ea := \begin{cases} E - Eo - Era(J,K) & \text{if } E > Eo + Era(J,K) \\ 0 & \text{otherwise} \end{cases}$$

$Ea = 2.029 \times 10^{4}$

Exact count sum of states for TS calculated by Beyer-Swinehart Algorithm

$$G := \begin{cases} \text{for } k \in 0..Ea \\ \quad G_k \leftarrow 1 \\ G \end{cases}$$

$$G := \begin{cases} \text{for } j \in 0..\text{rows}(\omega) - 1 \\ \quad \text{continue if } \omega_j > Ea \\ \quad \text{for } i \in \omega_j..Ea \\ \quad\quad G_i \leftarrow G_i + G_{i-\omega_j} \\ G \end{cases}$$

Sum of states at Ea for TS (states)

$G_{Ea} = 1.678 \times 10^{14}$

Definition of active energy range for reactant

$$Ev := \begin{cases} E - Er(J,K) & \text{if } E > Er(J,K) \\ 0 & \text{otherwise} \end{cases}$$

$Ev = 2.169 \times 10^{4}$

Exact count density of states for reactant calculated by Beyer-Swinehart Algorithm

$\rho_0 := 1 \qquad \rho_{Ev} := 0$

$$\rho := \begin{cases} \text{for } j \in 0..\text{rows}(\nu) - 1 \\ \quad \text{continue if } \nu_j > Ev \\ \quad \text{for } i \in \nu_j..Ev \\ \quad\quad \rho_i \leftarrow \rho_i + \rho_{i-\nu_j} \\ \rho \end{cases}$$

Density of states at Ev for reactant (states/cm^{-1})

$\rho_{Ev} = 8.434 \times 10^{11}$

RRKM rate constant calculated at total energy (E) above the ground state of reactant (s^{-1})

$$kt := \frac{G_{Ea}}{\rho_{Ev}} \cdot c \qquad kt = 5.964 \times 10^{12}$$

Finding the most probable angular momentum quantum number (J) for reactant and TS at temperature, T

Set range of angular momentum quantum numbers in order to plot probability distribution of J at temperature, T

$$J := 0 .. 150$$

Probability distribution of J at temperature, T, for reactant

$$Prr(J) := \frac{(2 \cdot J + 1) \cdot e^{-\frac{\sum_{K=-J}^{J} \left[(Br_0 + Br_1) \cdot \frac{J \cdot (J+1) - K^2}{2} + Br_2 \cdot K^2 \right]}{(2 \cdot J + 1) \cdot kb \cdot T}}}{qrotr}$$

Probability distribution of J at temperature, T, for TS

$$Pra(J) := \frac{(2 \cdot J + 1) \cdot e^{-\frac{\sum_{K=-J}^{J} \left[(Ba_0 + Ba_1) \cdot \frac{J \cdot (J+1) - K^2}{2} + Ba_2 \cdot K^2 \right]}{(2 \cdot J + 1) \cdot kb \cdot T}}}{qrota}$$

Plot of probability distribution of J at temperature, T, for reactant (red solid) and TS (blue dashed)

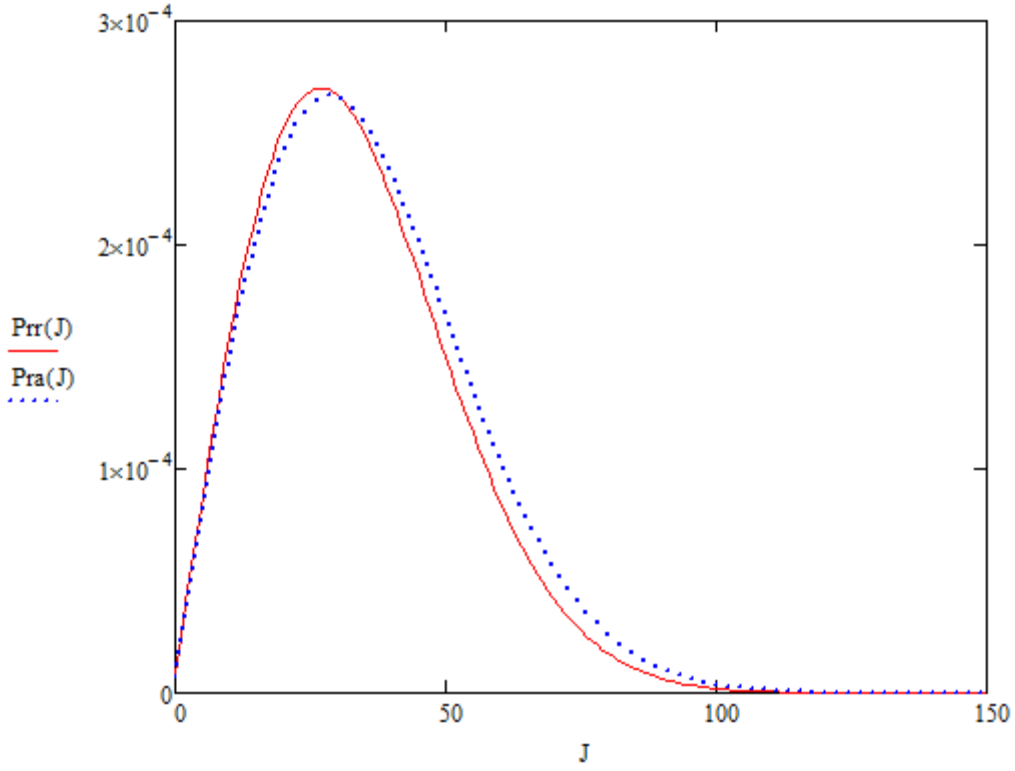

Most probable J value from Probability distribution of J at temperature, T, for reactant

$Psort := \text{for } i \in 0..150$

$Psort_i \leftarrow Prr(i)$ $\quad \max(Psort) = 2.701 \times 10^{-4}$ $\quad Jrmax := 27$

Most probable J value from Probability distribution of J at temperature, T, for TS

$Psort := \text{for } i \in 0..150$

$Psort_i \leftarrow Pra(i)$ $\quad \max(Psort) = 2.666 \times 10^{-4}$ $\quad Jamax := 29$

Appendix B

Samples of GAUSSIAN Input Files for Electronic Structure Calculations

Optimization at the MP2(full)/6-31G(d) level of theory

```
%nprocshared=1
%mem=1500MB
%nosave
%chk=cf2oh.chk
# mp2(full)/6-31g(d) opt=tight scf=tight freq=noraman scale=0.9427

difluoromethanol

0 1
 C              0.20738000    0.00000000    0.37316300
 H              0.18475000    0.00000000    1.46179300
 H             -1.78830100    0.81624300    0.07114400
 O             -1.26889100    0.00000000   -0.13740500
 F              0.68326100   -1.09303200   -0.15243500
 F              0.68326100    1.09303200   -0.15243400
```

Optimization of a transition state at the MP2(full)/6-31G(d) level of theory

%chk=mz69TS1.chk

mp2(full)/6-31g(d) opt=(qst2,noeigentest,maxcycle=200,tight) scf=tight freq=noraman scale=0.9427

protonated difluoromethanol

1 1

C	-0.20738000	0.00000000	0.37316300
H	-0.18475000	0.00000000	1.46179300
H	1.78830100	0.81624300	0.07114500
H	1.78830100	-0.81624400	0.07114400
O	1.26889100	0.00000000	-0.13740500
F	-0.68326100	1.09303200	-0.15243500
F	-0.68326100	-1.09303200	-0.15243400

pbd of difluorocarbene and water *m/z* 69

1 1

C	-0.52151800	-0.00009200	-0.00005400
H	0.60604900	-0.00031100	-0.00010400
H	2.85566000	-0.00277700	0.77519600
H	2.85598600	0.00395100	-0.77496000
O	2.26814100	-0.00035500	-0.00001100
F	-1.18489300	1.06024300	0.00028900
F	-1.18552000	-1.05996200	-0.00025800

Optimization at the B3LYP/6-311+G(d,p) level of theory

%nosave
%mem=1500mb
%nprocshared=1
B3LYP/6-311+G(d,p) freq nosymm opt=tight scf=tight scale=0.9679

Title Card Required

1 1

C	1.22861400	-1.54619600	0.00444700
N	-0.16985100	-1.39084500	0.00166200
C	-0.71214500	-0.13114800	0.00264900
C	0.08297900	0.99428100	0.00231800
C	1.52625900	0.95730100	-0.00409600
N	1.99192000	-0.36980900	0.00088800
O	1.75192300	-2.65335000	0.00736400
O	2.25848500	1.94474600	-0.01467400
C	-0.99942300	-2.57926600	-0.00163000
H	-1.61643800	-2.62286100	0.90523400
H	-1.61849800	-2.61405800	-0.90764500
H	-0.33421600	-3.44217100	-0.00662000
C	3.44777500	-0.58608500	-0.00134200
H	3.73324600	-1.14897900	0.88705900
H	3.73100100	-1.15063600	-0.88946400
H	3.91754000	0.39440000	-0.00308900
N	-2.03895100	0.20769300	0.00783800
N	-0.77684200	2.06305700	0.00272700
C	-2.02986200	1.55883900	0.00560600
H	-2.90867900	2.19013400	0.01110400

C	-0.39523700	3.47848000	0.00395400
H	0.19922200	3.69080700	-0.88334400
H	-1.30813900	4.07353100	0.00332500
H	0.19710000	3.68991700	0.89295900
Na	-3.81937100	-1.25810600	-0.01038900

Optimization of a transition state at the B3LYP/6-311+G(d,p) level of theory

freq=noraman B3LYP/6-311+G(d,p) opt=(qst3,noeigentest,maxcycle=200,tight) scf=tight scale=0.9679

protonated theophylline at purine nitrogen 7

1 1

C	1.35929300	0.84625400	0.00013400
N	0.03442700	1.38637100	0.00027000
C	-1.00172000	0.52384500	0.00012700
C	-0.85695600	-0.83770200	-0.00014900
C	0.43527400	-1.49500500	-0.00031400
N	1.48025500	-0.55393700	-0.00016000
O	2.31537500	1.57477400	0.00027500
O	0.58269500	-2.69653400	-0.00055600
C	-0.15084600	2.84491500	0.00058400
H	-0.68462400	3.16066500	-0.89875500
H	-0.68447400	3.16030000	0.90014100
H	0.83806400	3.29577900	0.00059300
C	2.87032900	-1.06216000	-0.00029800
H	3.38894500	-0.70237200	-0.88773800
H	3.38895300	-0.70285200	0.88733200
H	2.82262500	-2.14685400	-0.00058900
N	-2.36098000	0.77677600	0.00021700
N	-2.12598600	-1.37795100	-0.00022000
C	-3.02484200	-0.40368300	0.00000200
H	-4.09618500	-0.51831700	0.00001200
H	-2.81035800	1.68408700	0.00041100
H	-2.32471000	-2.37395300	-0.00041100

protonated theophylline at oxygen C6

1 1

C	1.28977800	0.92072400	-0.00000100
N	-0.03320200	1.40642000	-0.00000500
C	-1.05409100	0.52062300	-0.00000200
C	-0.87815900	-0.85828300	-0.00000200
C	0.41561000	-1.37229700	-0.00000200
N	1.44794800	-0.50241000	-0.00000500
O	2.24934400	1.64157400	0.00000900
O	0.69041300	-2.65445800	0.00000200
C	-0.25763600	2.86433500	-0.00000100
H	-0.80592200	3.15346000	-0.89831800
H	-0.80585700	3.15346700	0.89835300
H	0.71413800	3.34977600	-0.00003800
C	2.85891900	-0.96560900	-0.00000100
H	3.35596500	-0.57720300	-0.88717400
H	3.35594000	-0.57727700	0.88721900
H	2.87041000	-2.05004600	-0.00004600
N	-2.39692300	0.70878800	0.00000000
N	-2.09076500	-1.51536700	0.00000300
C	-2.97695400	-0.56757100	0.00000200
H	-4.04915500	-0.69393700	0.00000400
H	-2.89705000	1.58773200	0.00000300
H	-0.13073400	-3.17645100	0.00000200

TS

1 1

C	1.28977800	0.92072400	-0.00000100
N	-0.03320200	1.40642000	-0.00000500
C	-1.05409100	0.52062300	-0.00000200
C	-0.87815900	-0.85828300	-0.00000200
C	0.41561000	-1.37229700	-0.00000200
N	1.44794800	-0.50241000	-0.00000500
O	2.24934400	1.64157400	0.00000900
O	0.69041300	-2.65445800	0.00000200
C	-0.25763600	2.86433500	-0.00000100
H	-0.80592200	3.15346000	-0.89831800
H	-0.80585700	3.15346700	0.89835300
H	0.71413800	3.34977600	-0.00003800
C	2.85891900	-0.96560900	-0.00000100
H	3.35596500	-0.57720300	-0.88717400
H	3.35594000	-0.57727700	0.88721900
H	2.87041000	-2.05004600	-0.00004600
N	-2.39692300	0.70878800	0.00000000
N	-2.09076500	-1.51536700	0.00000300
C	-2.97695400	-0.56757100	0.00000200
H	-4.04915500	-0.69393700	0.00000400
H	-2.89705000	1.58773200	0.00000300
H	-0.93948938	-2.67229717	-0.00000080

Single point energy calculation at the MP2/aug-cc-pVTZ level of theory

%rwf=caffeinenh44c.rwf
%scr=caffeinenh44c.scr
%chk=caffeinenh44c.chk
%mem=3GB
%NoSave
%NProc=4
mp2/aug-cc-pVTZ scf=tight

PBD of ammonia and caffeine

1 1

C	-1.28405900	-1.57519000	0.00010600
N	0.12816400	-1.41398400	0.00318500
C	0.63720200	-0.15801700	-0.00089700
C	-0.14230000	0.97174000	-0.00045700
C	-1.58944600	0.92327800	0.00184300
N	-2.05865600	-0.40495500	0.00274100
O	-1.78173400	-2.67324800	-0.00316600
O	-2.31419300	1.89686400	0.00267100
C	0.98178000	-2.60682200	-0.00624600
H	1.54907900	-2.66111300	-0.93807300
H	1.65636800	-2.59265400	0.85211400
H	0.32946200	-3.47299100	0.06435900
C	-3.52050900	-0.62313000	0.00277200
H	-3.80610700	-1.18388700	-0.88620200
H	-3.80464200	-1.19137200	0.88740300
H	-3.99772000	0.35194100	0.00711800
N	1.95203700	0.24329600	-0.00351900

N	0.71805300	2.06008800	-0.00202200
C	1.96144400	1.59467000	-0.00382500
H	2.85048300	2.20301200	-0.00518700
C	0.32106100	3.47960500	-0.00166900
H	-0.27450800	3.68495800	0.88556100
H	1.22401500	4.08713500	-0.00274200
H	-0.27660200	3.68489000	-0.88750300
H	2.84423400	-0.34345000	-0.00342200
N	4.40472800	-1.12573000	0.00705800
H	4.40711200	-2.01469400	-0.48973600
H	5.13105600	-0.56199100	-0.43150400
H	4.73388400	-1.32653400	0.94991000

Single point energy calculation at the MP2/aug-cc-pVQZ level of theory

%rwf=/scratch/ramarta/XIq.rwf
%scr=/scratch/ramarta/XIq.scr
%NoSave
%mem=3000MB
%chk=/scratch/ramarta/XIq.chk
%NProc=4
mp2/aug-cc-pVQZ scf=tight

the pbd of difluoromethanol and water

1 1

C	0.96859100	0.01466700	-0.35251300
H	1.68571800	-0.01060200	-1.17016100
H	-1.32350800	-0.46880100	0.00473000
H	0.27272800	-1.84608300	-0.28276100
O	-0.05637800	-0.95066900	-0.51041900
F	0.29694500	1.18718800	-0.33534400
F	1.56929400	-0.17302300	0.82613800
O	-2.21907200	-0.01300600	0.36957100
H	-2.97640000	-0.12813200	-0.24757000
H	-2.06263100	0.94753400	0.52047200

Single point energy calculation at the CCSD(T)/aug-cc-pVTZ level of theory

```
%rwf=/scratch/ramarta/cf2h2as.rwf
%scr=/scratch/ramarta/cf2h2as.scr
%mem=3000MB
%chk=/scratch/ramarta/cf2h2as.chk
%NProc=4
%NoSave
# ccsd(t)/aug-cc-pvtz scf=tight

fluoroform

0 1
 C
 H              1          B1
 F              1          B2    2          A1
 F              1          B3    2          A2    3          D1    0
 H              1          B4    2          A3    3          D2    0

  B1           1.08392469
  B2           1.35542753
  B3           1.35542753
  B4           1.08392485
  A1         108.68853168
  A2         108.68853168
  A3         113.59960096
  D1        -117.74882936
  D2         121.12558532
```

Single point energy calculation at the MP2/6-311+(2d,2p) level of theory

%rwf=/scratch/ramarta/caffeinepbd33a.rwf
%scr=/scratch/ramarta/caffeinepbd33a.scr
%mem=3000MB
%chk=/scratch/ramarta/caffeinepbd33a.chk
%NProc=4
mp2/6-311+G(2d,2p) scf=tight

caffeine pbd with O-H--O bond

1 1

H	0.73165800	2.65697900	0.76339800
O	1.43188400	3.43854900	0.82411200
C	1.63328900	4.09561100	1.91836800
N	2.03467400	5.37380600	1.76797300
N	1.49978900	3.53763400	3.14713100
C	2.30231100	6.11591100	2.90717100
C	2.17585700	5.97358300	0.42453000
C	1.72045800	4.24283500	4.41024000
C	1.16747900	2.10125000	3.25466000
C	2.14282900	5.58171400	4.17109200
N	2.71667300	7.39538900	2.94497100
H	2.94708800	5.44760800	-0.13632900
H	1.22789000	5.91052200	-0.10694900
H	2.46019400	7.01206400	0.56935200
O	1.55498000	3.67735400	5.46640800
H	1.26572300	1.83554100	4.30295600
H	0.14876200	1.91482200	2.92112400
H	1.86627800	1.51834100	2.65528400

N	2.48613600	6.60603500	5.03568600
C	2.81760000	7.65550800	4.24560700
C	2.49664900	6.56218000	6.50125200
H	3.13162200	8.60334200	4.65656400
H	3.18328100	5.79004700	6.84584900
H	2.82331500	7.53396300	6.86749700
H	1.49678700	6.34571700	6.87535300
O	-0.32171300	1.72776100	0.55501200
C	-0.82314200	1.11097400	-0.41746400
N	-2.15905500	0.83497200	-0.40420100
N	-0.06067200	0.69161200	-1.48486300
C	-2.71242600	0.14034200	-1.46442600
C	-2.99027600	1.27435500	0.72668300
C	-0.54650200	-0.02890500	-2.64150100
C	1.38199400	0.97675300	-1.44512400
C	-1.94747300	-0.27294600	-2.53670200
N	-4.00757500	-0.21009300	-1.60245100
H	-2.64440300	0.80693200	1.64835900
H	-2.93864900	2.35805200	0.82779100
H	-4.01126700	0.96755500	0.51582700
O	0.20364200	-0.35096900	-3.54053500
H	1.82712100	0.49309700	-2.30985900
H	1.56381600	2.05038600	-1.49846200
H	1.81716300	0.57385400	-0.53067500
N	-2.83523200	-0.91792100	-3.38247200
C	-4.04075600	-0.84623700	-2.77010400
C	-2.53097900	-1.54967100	-4.66798000
H	-4.93020600	-1.27321000	-3.20872800
H	-1.80643400	-2.35126000	-4.52888600
H	-3.45554300	-1.95700500	-5.07419200

Single point energy calculation at the MP2(full)/aug-cc-pCVTZ/6-311+G(2d,2p) level of theory

%rwf=/scratch/ramarta/caffna3ge.rwf
%scr=/scratch/ramarta/caffna3ge.scr
%mem=3000MB
%chk=/scratch/ramarta/caffna3ge.chk
%NProc=4
mp2(full)/gen scf=tight

Title Card Required

1 1

C	0	1.33856700	-0.05502400	-0.00036300
N	0	0.58039600	-1.19016400	-0.00048100
C	0	-0.80001000	-1.07803400	-0.00025600
C	0	-1.42735200	0.15123100	-0.00006400
C	0	-0.72318600	1.39151500	-0.00022400
N	0	0.70743400	1.16988700	-0.00036000
O	0	2.58907900	-0.12937700	-0.00028700
O	0	-1.18340600	2.51439700	-0.00023800
C	0	1.22241700	-2.51088400	-0.00056900
H	0	1.83765700	-2.63017000	-0.89293200
H	0	1.83738700	-2.63044400	0.89195000
H	0	0.43138700	-3.25636900	-0.00078500
C	0	1.55905400	2.36736600	-0.00066100
H	0	2.18455100	2.38762700	0.89270700
H	0	2.18487400	2.38686300	-0.89381000
H	0	0.89904200	3.23020400	-0.00111600
N	0	-1.68258600	-2.09680500	-0.00011000

N	0	-2.78187800	-0.13866100	0.00022000
C	0	-2.86672800	-1.48978000	0.00020200
H	0	-3.81676700	-2.00280500	0.00039000
C	0	-3.89042400	0.81906200	0.00100600
H	0	-3.83887500	1.45043500	-0.88513600
H	0	-4.82410400	0.25889700	-0.00076500
H	0	-3.84042200	1.44732100	0.88947300
Na	0	4.67839200	-0.13674900	0.00135600

H C 18 2 6 0
6-311+G(2d,2p)
****
Na 0
S 14 1.00
423000.0000000 0.180618D-04
63340.0000000 0.140430D-03
14410.0000000 0.738438D-03
4077.0000000 0.311182D-02
1328.0000000 0.112081D-01
478.6000000 0.352828D-01
186.2000000 0.959897D-01
76.9200000 0.213735D+00
33.3200000 0.348688D+00
15.0000000 0.324566D+00
6.8690000 0.112633D+00
2.6830000 0.706797D-02
1.1090000 0.598010D-03
0.0601500 -0.530870D-05
S 14 1.00
423000.0000000 -0.440653D-05

63340.0000000 -0.343443D-04
14410.0000000 -0.180114D-03
4077.0000000 -0.763900D-03
1328.0000000 -0.275248D-02
478.6000000 -0.886016D-02
186.2000000 -0.247939D-01
76.9200000 -0.605995D-01
33.3200000 -0.116446D+00
15.0000000 -0.162437D+00
6.8690000 -0.438891D-01
2.6830000 0.337917D+00
1.1090000 0.561347D+00
0.0601500 0.406754D-02
S 14 1.00
423000.0000000 0.663019D-06
63340.0000000 0.515769D-05
14410.0000000 0.271250D-04
4077.0000000 0.114635D-03
1328.0000000 0.415118D-03
478.6000000 0.132978D-02
186.2000000 0.375595D-02
76.9200000 0.914025D-02
33.3200000 0.179859D-01
15.0000000 0.251477D-01
6.8690000 0.763522D-02
2.6830000 -0.614589D-01
1.1090000 -0.115721D+00
0.0601500 0.626406D+00
S 1 1.00
0.4540000 1.0000000

```
S   1   1.00
     0.0238200            1.0000000
S   1   1.00
     4.1890000            1.0000000
S   1   1.00
     0.6260000            1.0000000
S   1   1.00
     0.0066500            1.0000000
P   8   1.00
   243.3000000             0.224392D-02
    57.3900000             0.173997D-01
    18.1000000             0.774125D-01
     6.5750000             0.219102D+00
     2.5210000             0.378522D+00
     0.9607000             0.394902D+00
     0.3512000             0.160424D+00
     0.0982700             0.233311D-02
P   8   1.00
   243.3000000            -0.222401D-03
    57.3900000            -0.174277D-02
    18.1000000            -0.775456D-02
     6.5750000            -0.225187D-01
     2.5210000            -0.384330D-01
     0.9607000            -0.450177D-01
     0.3512000            -0.192132D-01
     0.0982700             0.182697D+00
P   1   1.00
     0.0373400            1.0000000
P   1   1.00
     0.0150000            1.0000000
```

```
P   1   1.00
     1.5690000           1.0000000
P   1   1.00
     0.5120000           1.0000000
P   1   1.00
     0.0070000           1.0000000
D   1   1.00
     0.1367000           1.0000000
D   1   1.00
     0.0636000           1.0000000
D   1   1.00
     5.4040000           1.0000000
D   1   1.00
     1.5300000           1.0000000
D   1   1.00
     0.0223000           1.0000000
F   1   1.00
     0.1397000           1.0000000
F   1   1.00
     3.4650000           1.0000000
F   1   1.00
     0.0714000           1.0000000
****
8 7 0
S   8   1.00
  15330.0000000           0.0005080
   2299.0000000           0.0039290
    522.4000000           0.0202430
    147.3000000           0.0791810
     47.5500000           0.2306870
```

```
     16.7600000              0.4331180
      6.2070000              0.3502600
      0.6882000             -0.0081540
S   8   1.00
  15330.0000000              -0.0001150
   2299.0000000              -0.0008950
    522.4000000              -0.0046360
    147.3000000              -0.0187240
     47.5500000              -0.0584630
     16.7600000              -0.1364630
      6.2070000              -0.1757400
      0.6882000              0.6034180
S   1   1.00
      1.7520000              1.0000000
S   1   1.00
      0.2384000              1.0000000
S   1   1.00
      7.8450000              1.0000000
S   1   1.00
     21.0320000              1.0000000
S   1   1.00
      0.0737600              1.0000000
P   3   1.00
     34.4600000              0.0159280
      7.7490000              0.0997400
      2.2800000              0.3104920
P   1   1.00
      0.7156000              1.0000000
P   1   1.00
      0.2140000              1.0000000
```

```
P   1   1.00
     15.1590000           1.0000000
P   1   1.00
     57.4370000           1.0000000
P   1   1.00
      0.0597400           1.0000000
D   1   1.00
      2.3140000           1.0000000
D   1   1.00
      0.6450000           1.0000000
D   1   1.00
     15.8580000           1.0000000
D   1   1.00
      0.2140000           1.0000000
F   1   1.00
      1.4280000           1.0000000
F   1   1.00
      0.5000000           1.0000000
****
17 0
S   8   1.00
  11420.0000000            0.0005230
   1712.0000000            0.0040450
    389.3000000            0.0207750
    110.0000000            0.0807270
     35.5700000            0.2330740
     12.5400000            0.4335010
      4.6440000            0.3474720
      0.5118000           -0.0085080
S   8   1.00
```

```
 11420.0000000           -0.0001150
  1712.0000000           -0.0008950
   389.3000000           -0.0046240
   110.0000000           -0.0185280
    35.5700000           -0.0573390
    12.5400000           -0.1320760
     4.6440000           -0.1725100
     0.5118000            0.5999440
S   1   1.00
     1.2930000            1.0000000
S   1   1.00
     0.1787000            1.0000000
S   1   1.00
     5.9520000            1.0000000
S   1   1.00
    16.2010000            1.0000000
S   1   1.00
     0.0576000            1.0000000
P   3   1.00
    26.6300000            0.0146700
     5.9480000            0.0917640
     1.7420000            0.2986830
P   1   1.00
     0.5550000            1.0000000
P   1   1.00
     0.1725000            1.0000000
P   1   1.00
    11.8710000            1.0000000
P   1   1.00
    44.8490000            1.0000000
```

```
P   1   1.00
     0.0491000          1.0000000
D   1   1.00
     1.6540000          1.0000000
D   1   1.00
     0.4690000          1.0000000
D   1   1.00
    14.2000000          1.0000000
D   1   1.00
     0.1510000          1.0000000
F   1   1.00
     1.0930000          1.0000000
F   1   1.00
     0.3640000          1.0000000
****
```

Appendix C

Samples of Conceptual and Working Drawings for Electrospray Design

Electrospray Emitter Assembly (ESE)

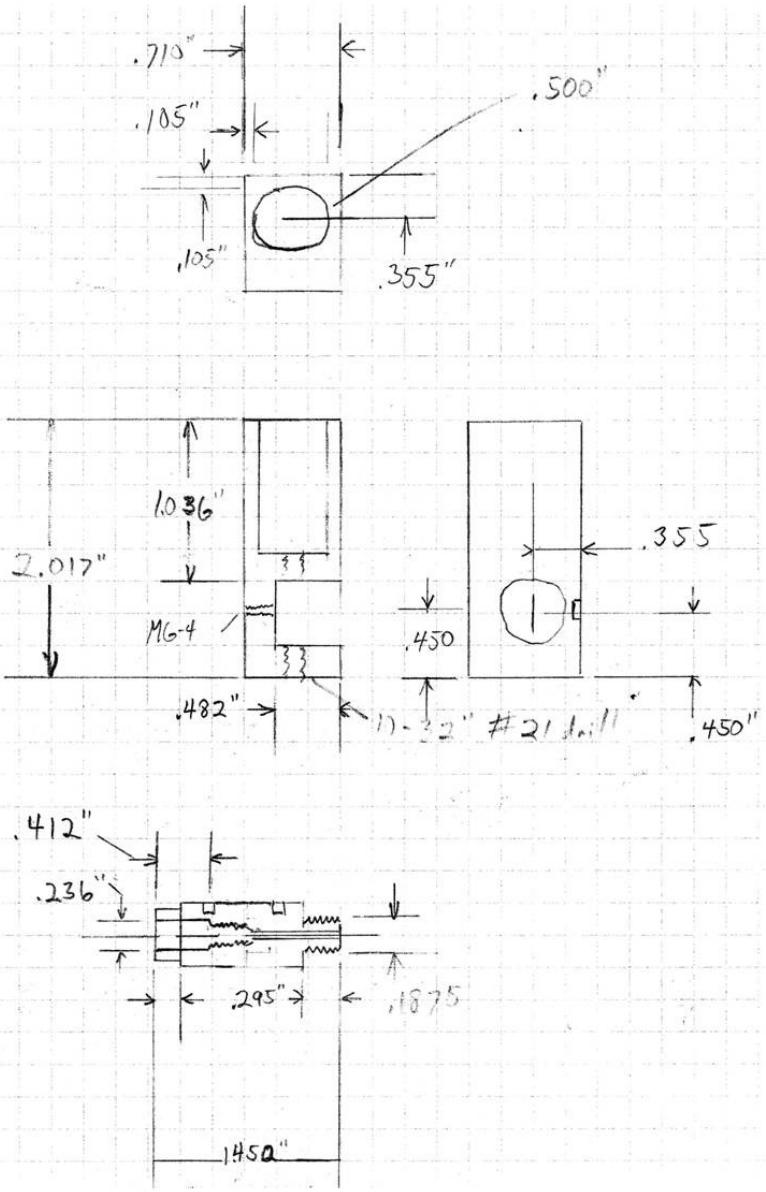

Capillary Cover (CC)

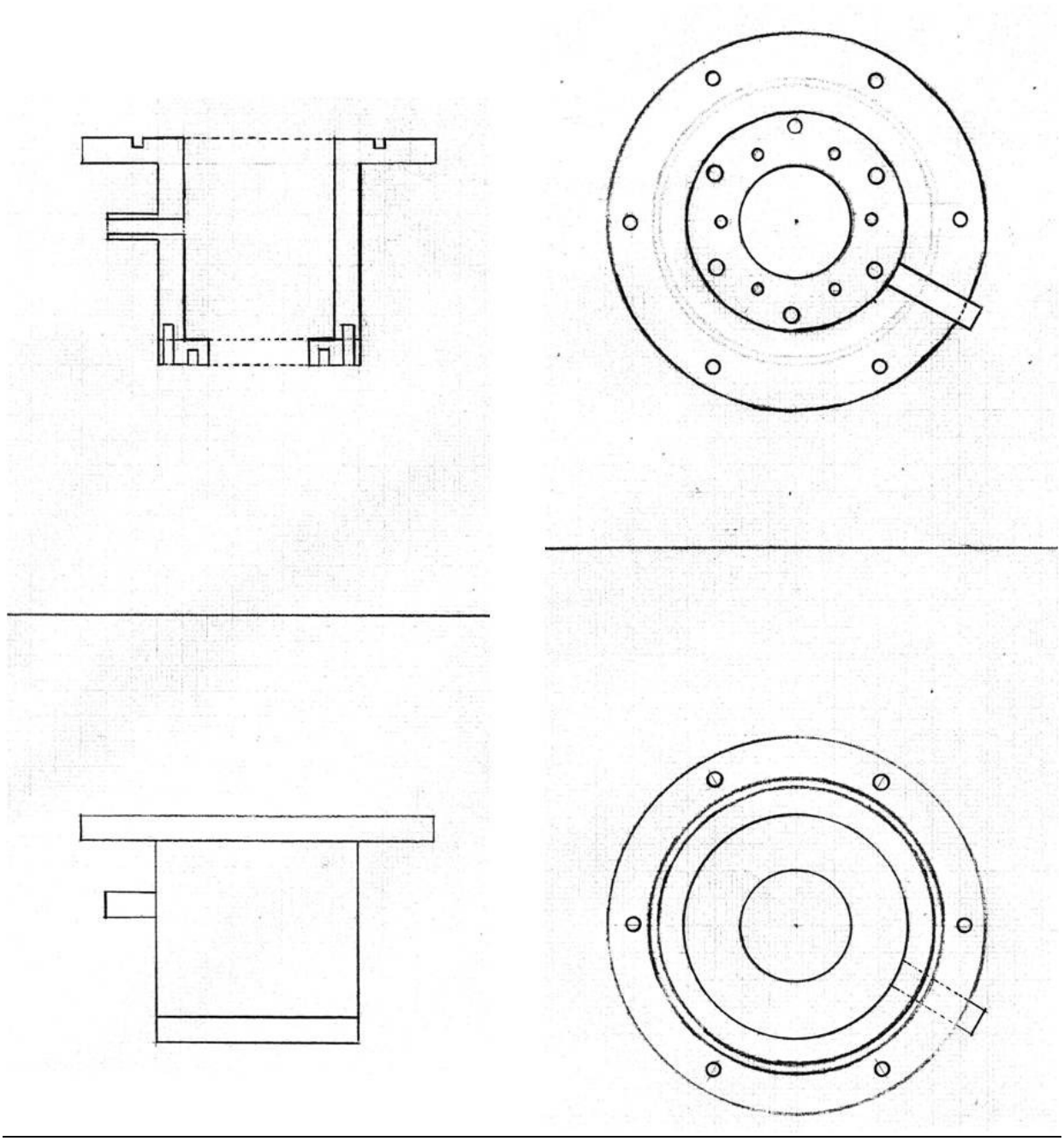

Shielding Plate (SP)

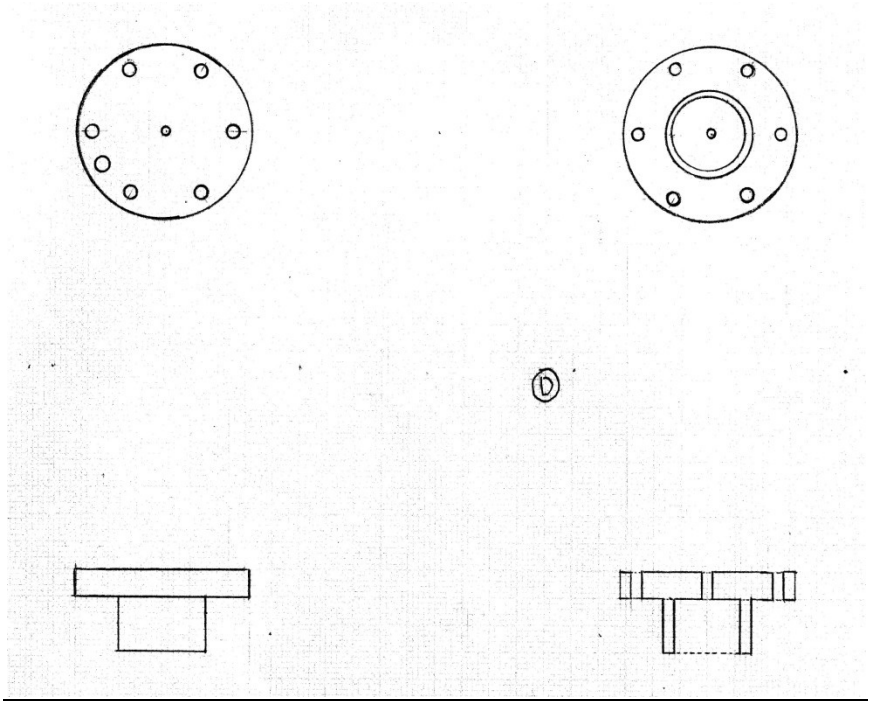

Capillary Mount

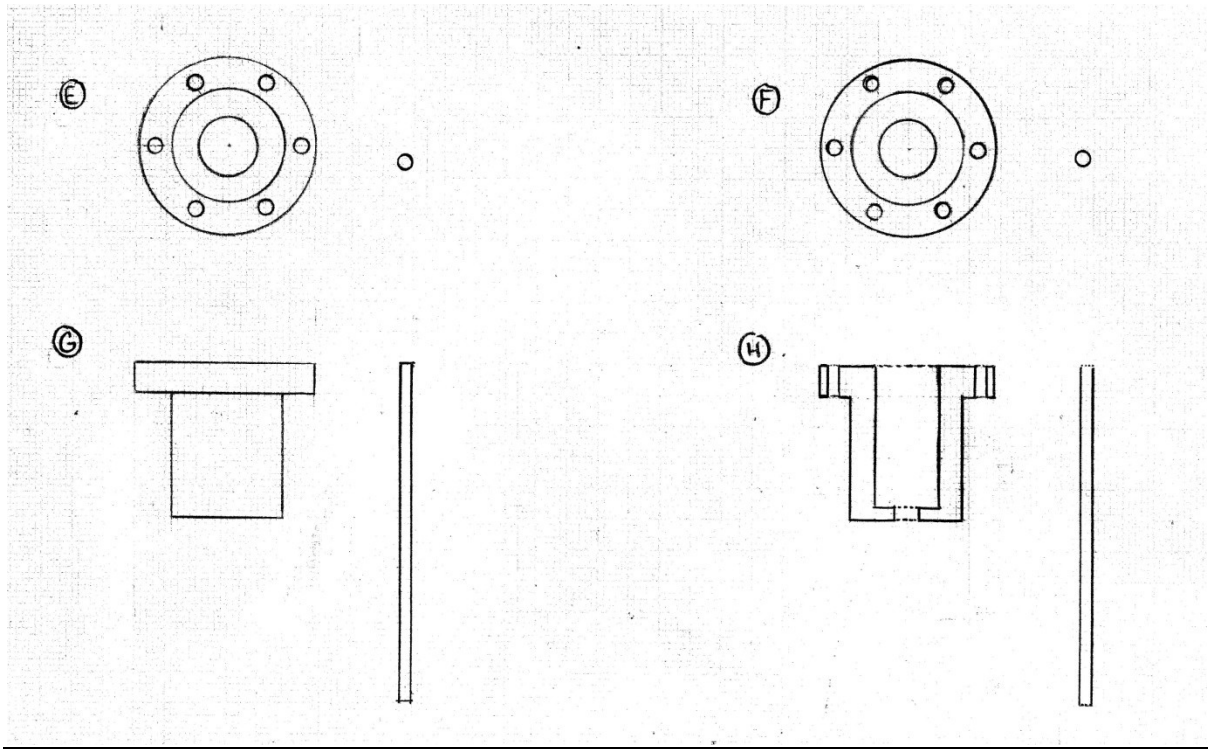

Stainless Steel Flange

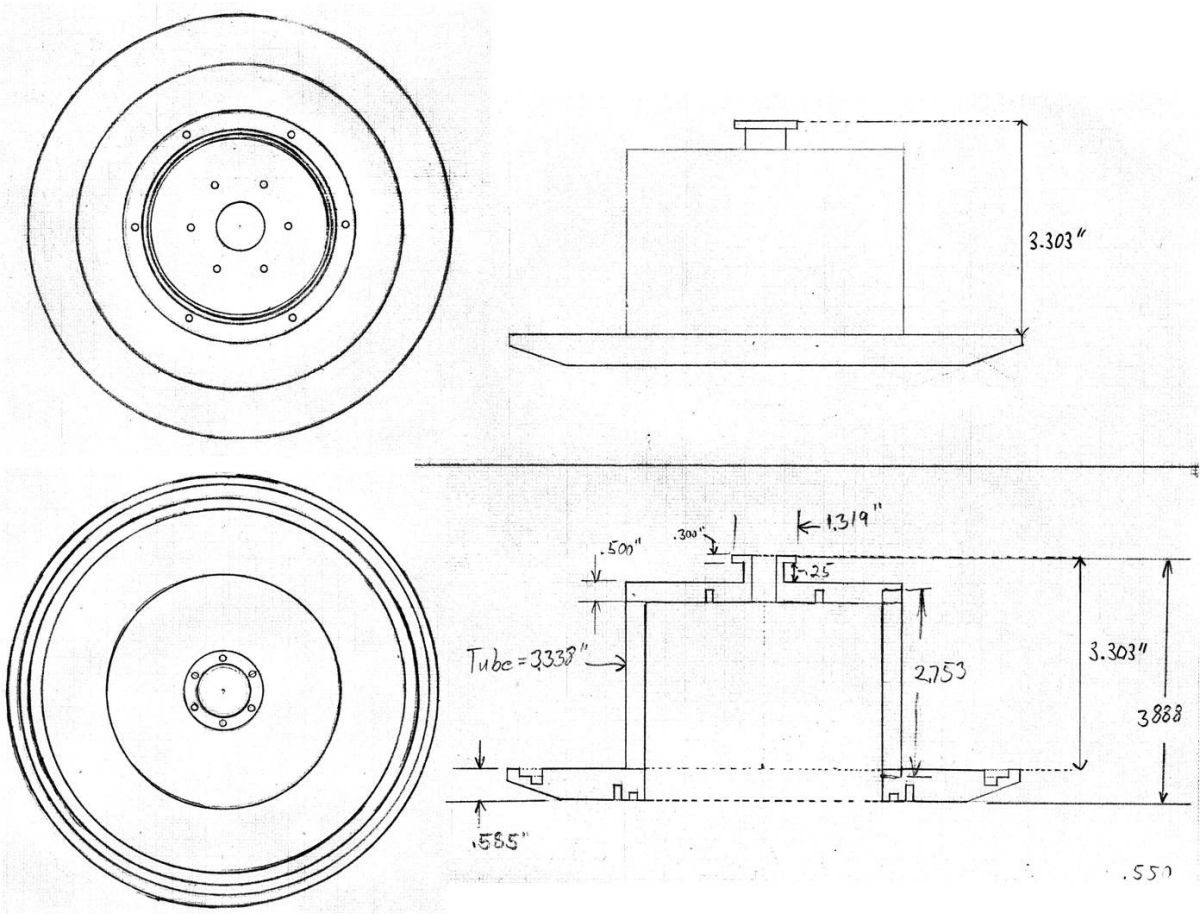

High Voltage Shield (HVS)

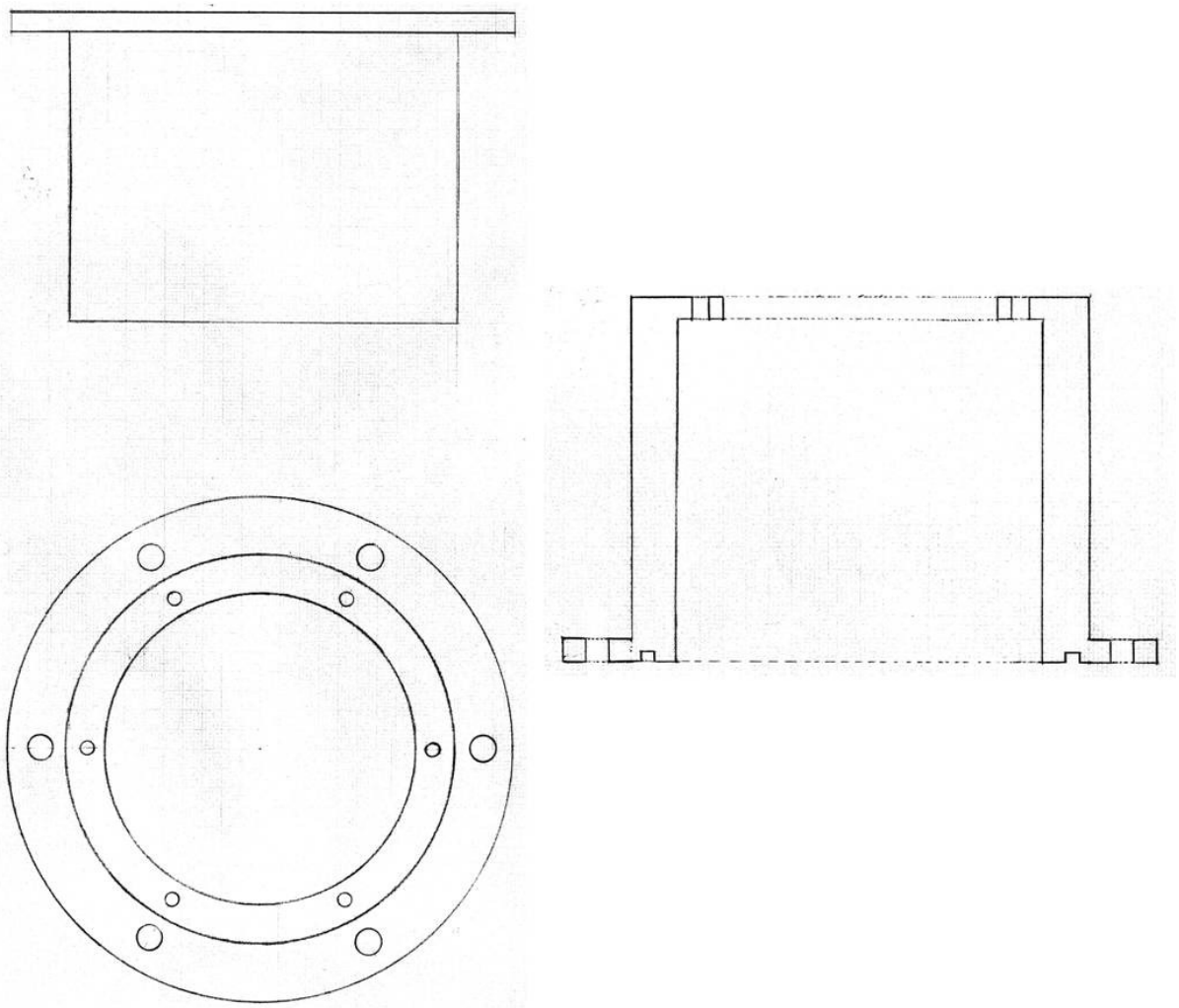

Source Body (SB)

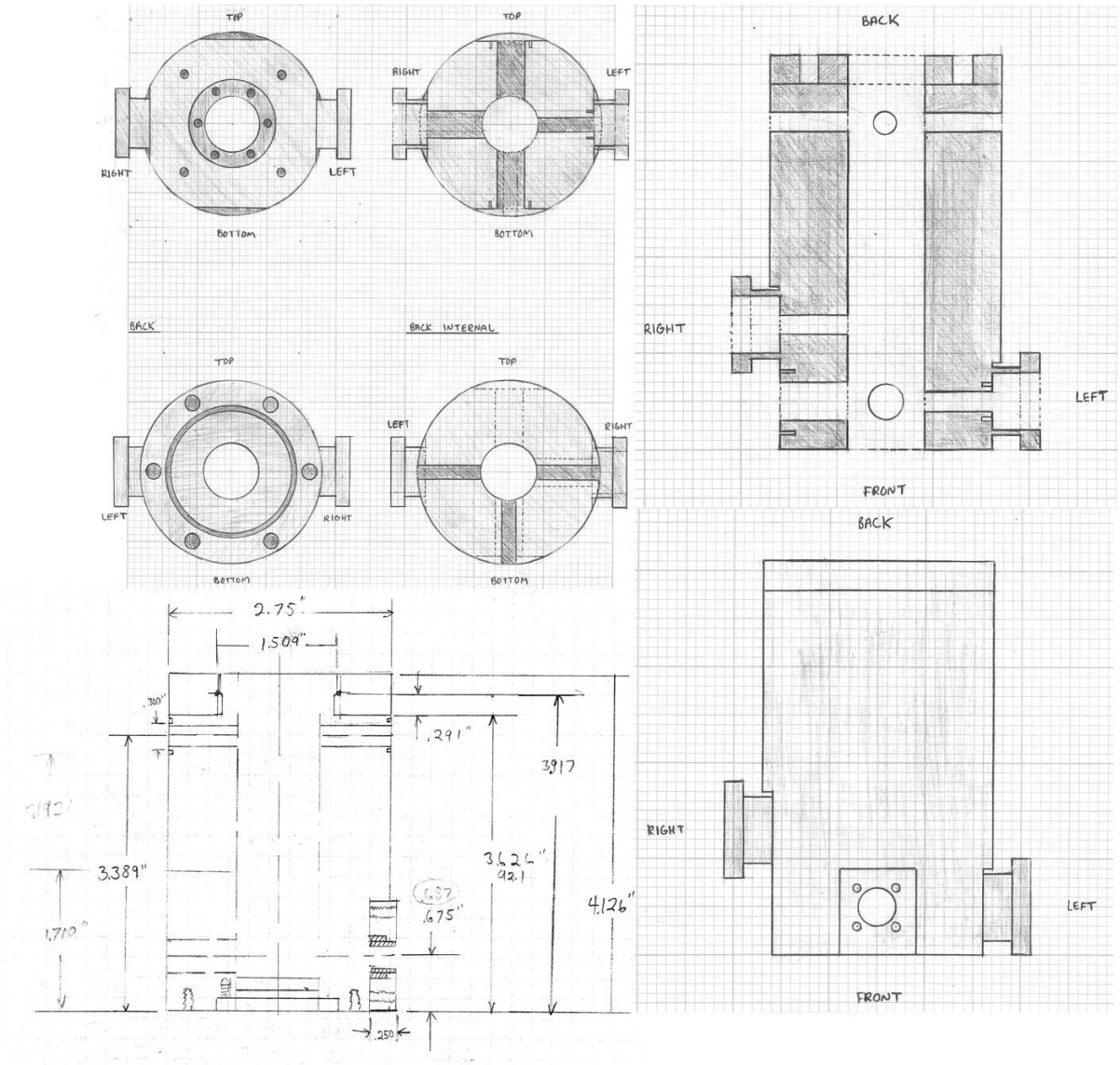

Platinum Aperture Mount

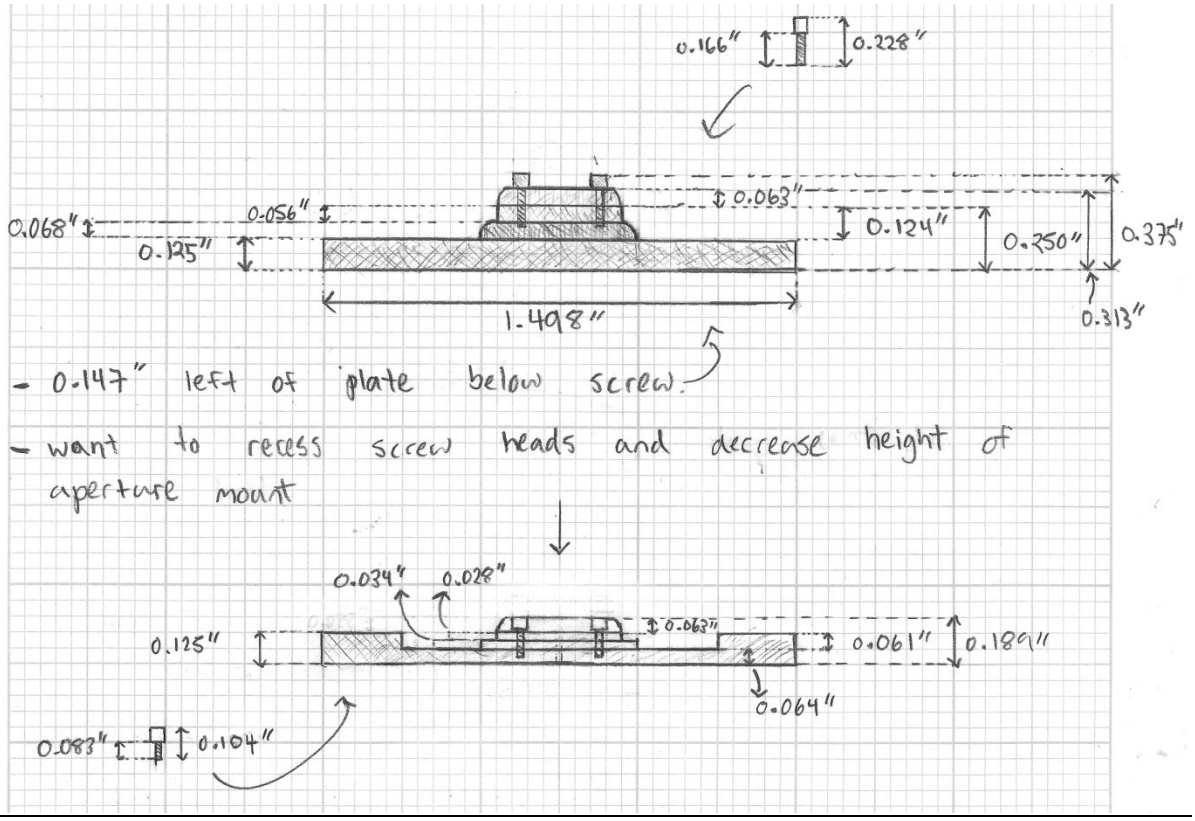

Grid Assembly

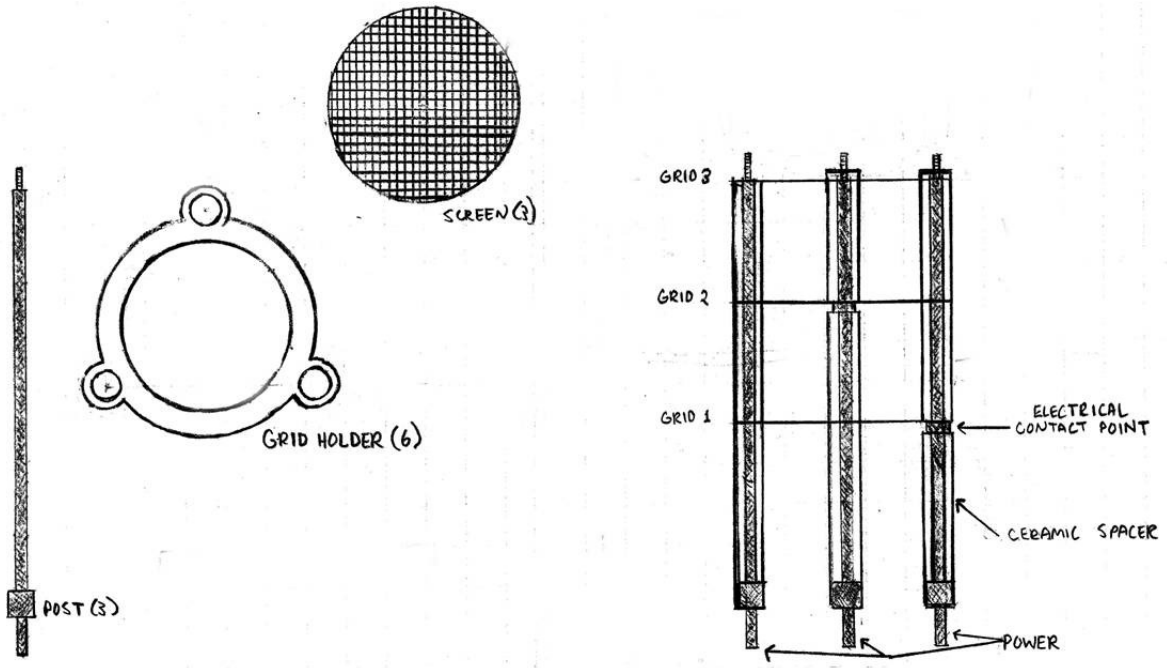

Concept Design 1a

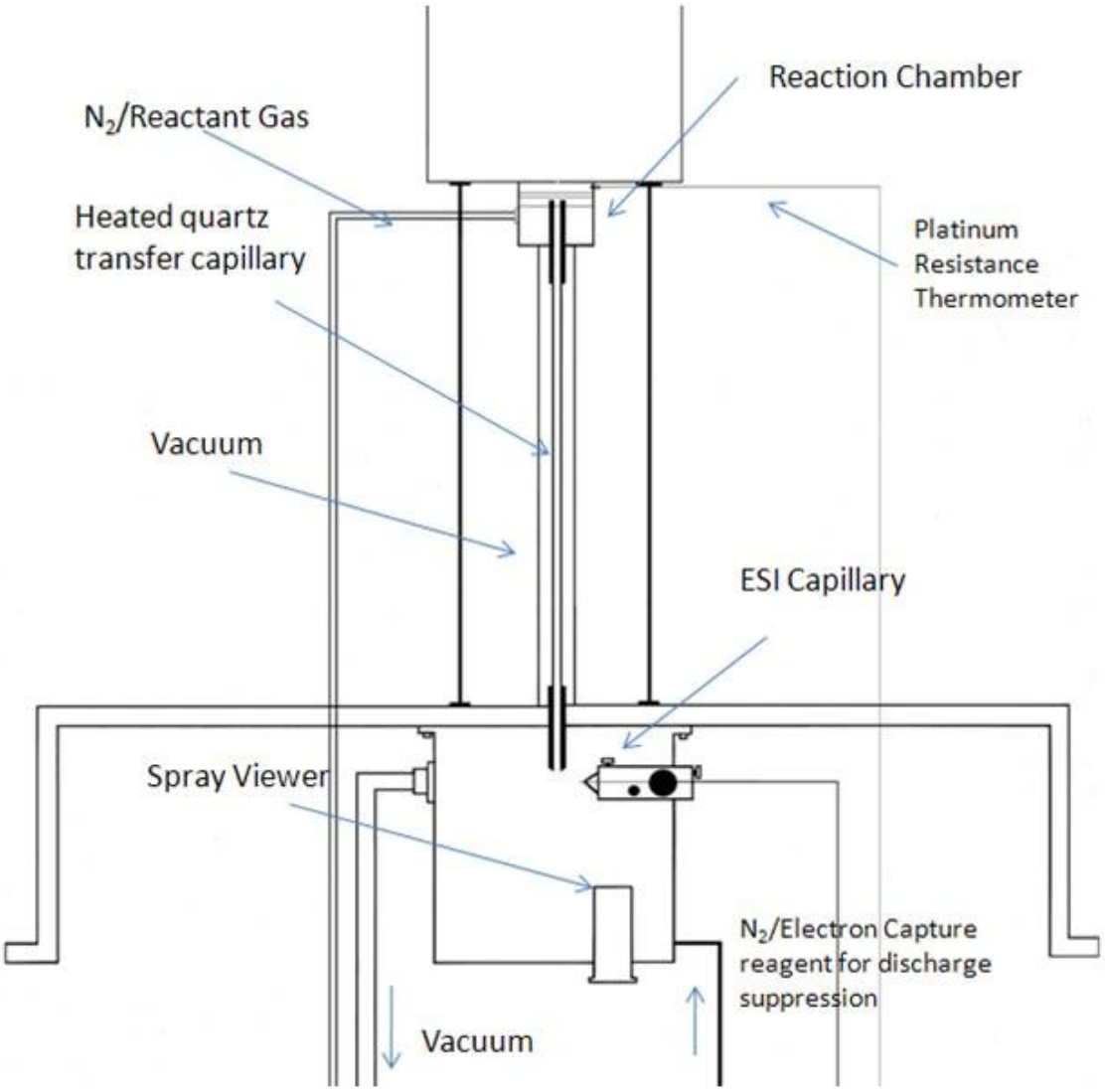

Concept Design 1b

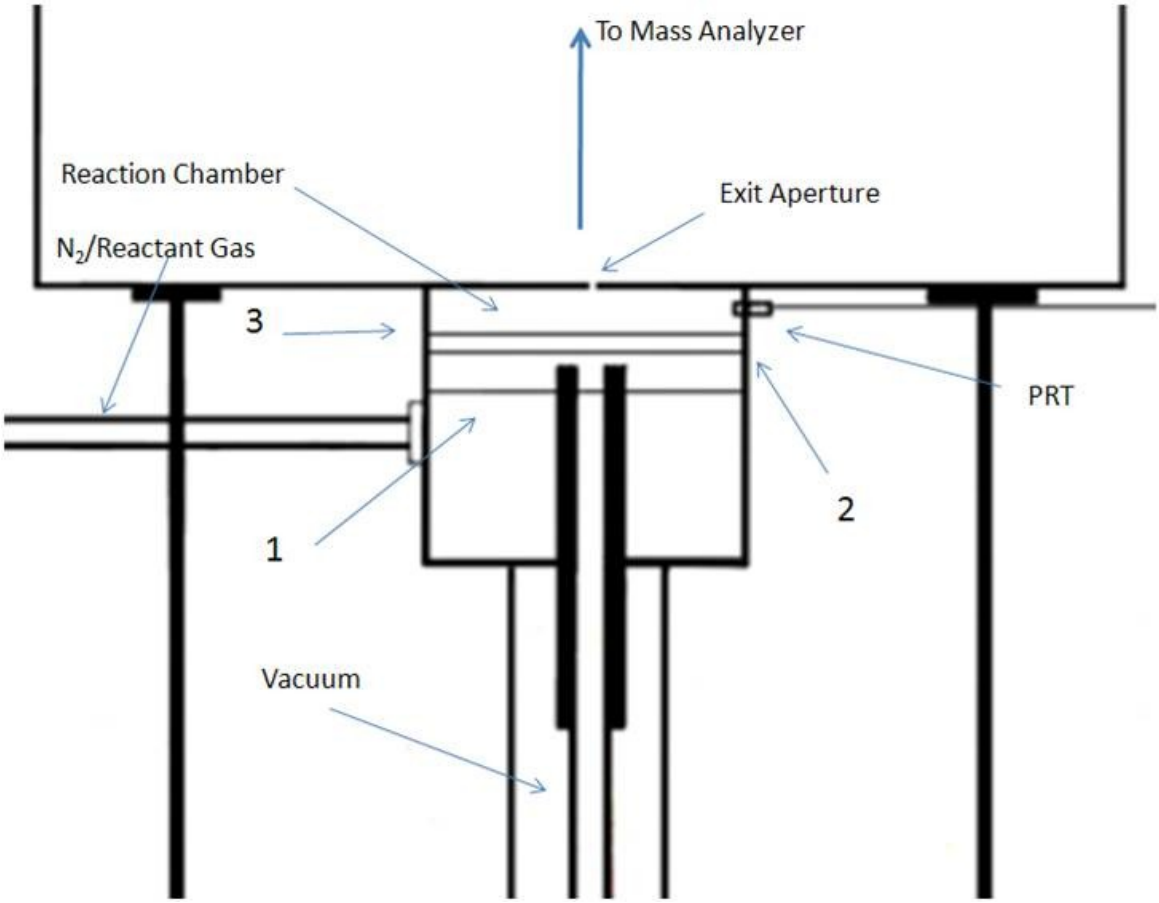

Concept Design 1c

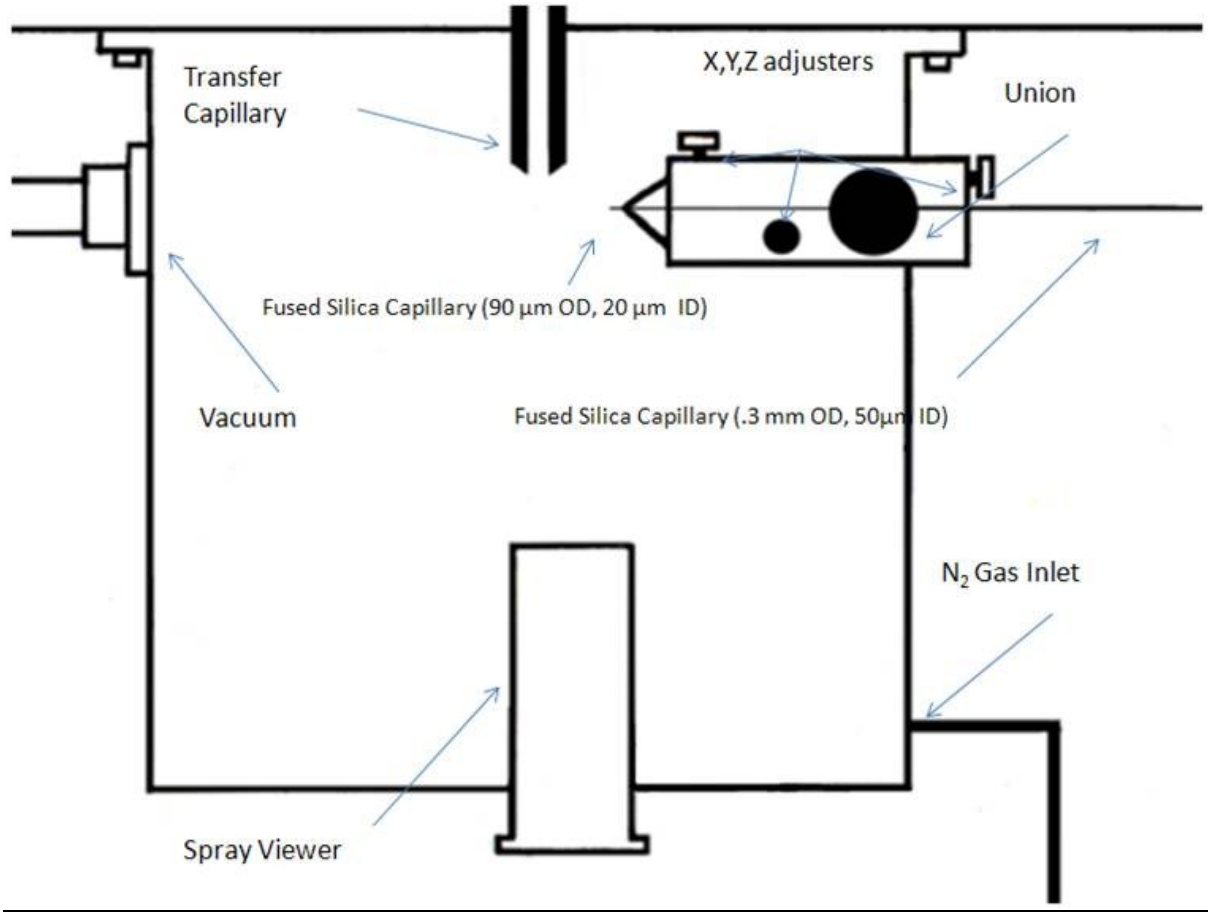

Concept Design 2